UNIVERSITY OF SOUTHAMPTON

Faculty of Engineering and Physical Sciences
School of Physics and Astronomy

Perspectives on Wilson Loops in Strongly-Coupled Yang-Mills Theories

by

Jack David Holden
MPhys MASt
ORCiD: 0000-0002-0946-2282

A thesis for the degree of
Doctor of Philosophy

October 2023

University of Southampton

Abstract

Faculty of Engineering and Physical Sciences
School of Physics and Astronomy

Doctor of Philosophy

Perspectives on Wilson Loops in Strongly-Coupled Yang-Mills Theories

by Jack David Holden

Strongly-coupled Yang-Mills theories encompass many of the most intriguing open problems in physics, including colour confinement, the internal structure of neutron stars, and a full comprehension of gauge/gravity duality. We continue the research programme, conducted over many decades, of exploring the physics of strongly coupled gauge theories, giving special attention to the use of Wilson loops as probes of the physics of gauge theories.

We examine in particular a newly-recognised phase of Yang-Mills theories known as 'partial confinement'. This is postulated to appear in the crossover region of the quark-gluon plasma and to take an important role in gauge/gravity duality.

We present evidence that flux tubes form in the confined sector of the partially confined phase. This is the first direct evidence for any statement about the dynamics of the partially confined phase.

We furthermore argue that the partially confined phase can be distinguished from the totally confined and deconfined phases with the use of global symmetries. This permits the first acknowledgement of the partially confined phase in $SU(N)$ gauge groups of finite N, and offers more prospects for understanding the physics of any manifestation of the partially confined phase in quantum chromodynamics.

Finally, we employ the AdS/CFT correspondence to examine renormalization group flows in strongly coupled gauge theories on spherical defects harbouring hypermultiplets of Dirac fermions and their scalar superpartners. We find that these defects flow in the infrared to line operators that we determine to be Wilson and Wilson-'t Hooft loops. We thus find a new UV completion of Wilson-'t Hooft loops, simultaneously discovering an interesting example of cross-dimensional renormalisation group flows on defects. There is hope that our results can be adapted to allow experimental realisation in spherical graphene and fullerenes.

Contents

Declaration of Authorship

I declare that this thesis and the work presented in it is my own and has been generated by me as the result of my own original research.

I confirm that:

1. This work was done wholly or mainly while in candidature for a research degree at this University;
2. Where any part of this thesis has previously been submitted for a degree or any other qualification at this University or any other institution, this has been clearly stated;
3. Where I have consulted the published work of others, this is always clearly attributed;
4. Where I have quoted from the work of others, the source is always given. With the exception of such quotations, this thesis is entirely my own work;
5. I have acknowledged all main sources of help;
6. Where the thesis is based on work done by myself jointly with others, I have made clear exactly what was done by others and what I have contributed myself;
7. Parts of this work have been published as:

Signed:.. Date:..................

Acknowledgements

I would like to express my deep thanks to my supervisor, Andy O'Bannon, who accommodated my unusual circumstances as a remote PhD student, patiently explained many topics in physics, guided me through the postdoctoral application process, and even listened to me practice talks on some evenings and weekends. I would like to thank him for his encouragement when I was pursuing my own ideas, for his willingness to entertain and discuss my musings, and for directing me to relevant areas in the literature that I could not have found without him.

I am likewise very grateful to my 'unofficial supervisor', Masanori Hanada, with whom I have enjoyed many long sessions discussing physics, often benefitting from his unique perspective and approach. He has proposed many projects and introduced me to the very interesting topic of partial deconfinement. He also greatly encouraged me when pursuing my own investigations. I am moreover thankful for his social dexterity and skill at introducing me to other physicists.

I express gratitude to my other collaborators, John Estes, Vaibhav Gautam, Diego Gutiez, Carlos Hoyos, Matthew Knaggs, Matthew Lippert, Enrico Rinaldi, and Ronnie Rogers, for their help in completing the work contained here. I am especially grateful to Ronnie his assistance with the use of Mathematica, finding solutions to differential equations, and formatting plots nicely.

I would like to thank my examiners, Nick Evans and Pavel Buividovich, for agreeing to conduct my viva and for carefully reading through this manuscript.

I am grateful to my sisters, Amy and Charlotte, for their continual kindness towards me and their faithful fulfilment of their sororal duties. I also thank Louis, my cat, for spending more time by my side over the course of my PhD than anyone else, and for his general research assistance. I regret that I must now work alone.

Finally, I must express extreme gratitude to my parents. They have made many personal sacrifices to provide for me, in their home, an environment in which I can do my work. They have also granted me companionship, great patience, and endless support.

To my parents

Chapter 1

Introduction

Quantum field theory (QFT) provides the best available framework for describing elementary particles. A class of QFTs known as Yang-Mills theories have proben to be the most successful QFTs at modelling nature. The Standard Model of particle physics is composed of Yang-Mills theory of three components (more precisely, irreducible representations), $SU(3) \times SU(2) \times U(1)$. Moreover, some Yang-Mills theories are believed to furnish a description of theories of quantum gravity via gauge/gravity duality.

However, having accurate elementary descriptions in the form of these Yang-Mills equations is not sufficient for understanding or performing computations on the Standard Model or mathematical models of quantum gravity in all circumstances - in particular, when the coupling of the gauge fields is large. The formation of nuclear matter via the confinement of quarks, the internal structure of neutron stars, and a full understanding of AdS/CFT are all enticing mysteries that remain unsolved, despite good reasons to believe they are fully and accurately described on an elementary level by particular Yang-Mills theories, due to the strong coupling of the respective theories.

Much work has been conducted over the last five decades to expand our understanding of Yang-Mills theories at strong coupling. This thesis is an attempt to further these efforts. We will employ an extensive set of techniques in an attempt to make general inferences about a newly-recognised *partially deconfined* phase, thought to be exhibited by gauge theories at strong coupling. We will argue for universal properties concerning global symmetries and the dynamics of such a phase. This could see direct application to the crossover region of quantum chromodynamics (QCD) and promises to increase our understanding of the mapping of degree of freedom under gauge/gravity duality. In addition, we will employ holographic methods to explore renormalization group flows on spherical defects in strongly-coupled gauge theories, finding that these defects flow to Wilson loops in the infrared (IR). This could be utilised to understand graphene and fullerenes.

1.1 Gauge theories and Wilson loops

Yang-Mills theories are a special instance of gauge theories, which are theories constructed under the principle of gauge invariance. Gauge theories arise naturally when attempting to construct a manifestly Lorentz-invariant Lagrangian in $3+1$ dimensions for a massless spin 1 particle while satisfying unitarity [1]. However, even before the notion of the 'unitarity' existed in physical models or the group-theoretic approach of Wigner was realised, a simple example of a gauge theory was known from Maxwell's equations for electromagnetism, and closely analogous ideas appear in the equations and Riemann manifold structure underlying General Relativity. Gauge theories can be motivated by an attempt to generalise Maxwell theory of a photon to allow for interactions between gauge bosons, or equivalently to gauge invariance under more general symmetry groups. Generalising Maxwell theory seems a natural candidate to search for new self-consistent theories that might describe nature.

Maxwell theory can be characterised as a theory in which the Lagrangian description contains an apparent local $U(1)$ symmetry. The group $U(1)$ is the simplest version of a class of continuous groups - more precisely, groups that are also manifolds - known as Lie groups. To enable us to a construct a Lagrangian that is symmetric under more general Lie groups, we seek a set of objects that transform covariantly under the group.

Consider a field $\phi(x)$ that transforms in some representation of the gauge group as $\phi(x) \to h(x)\phi(x)$, where $h(x)$ is an element of the representation that varies smoothly across spacetime. The derivative $\partial_\mu \phi(x)$ does not transform covariantly under the group. This is for the same reason that an arbitrary separation $\phi(y) - \phi(x)$ is not invariant under the group transformation: it maps to $h(y)\phi(y) - h(x)\phi(x)$, and thus varies for different choices of the function h. To obtain a gauge invariant expression, we introduce the Wilson line, $W(x, y)$, with the defining property,

$$h(x)W(x,y)h(y)^{-1} \tag{1.1}$$

Then, we can define $W(x,y)\phi(y) - \phi(x)$, which transforms like $\phi(x)$ under an arbitrary gauge transformation. We can use this to construct a derivative operator D_μ that transforms covariantly,

$$D_\mu \phi(x) \equiv \lim_{\delta x^\mu \to 0} \frac{W(x, x+\delta x)\phi(x+\delta x) - \phi(x)}{\delta x^\mu} \tag{1.2}$$

which has the property,

$$D_\mu \phi(x) \to h(x) D_\mu \phi(x). \tag{1.3}$$

Any Lie group element continuously connected to the identity can be expressed as

$$h = \exp\{i \sum \alpha^a T^a\} \tag{1.4}$$

for some real numbers α and generators of the group T^a. Since we want the point-operator $W(x,x)$ to act as the identity, we can express the Wilson line locally as,

$$W(x, x+\delta x) = 1 + igA^a_\mu T^a_R + O(\delta x^2) \tag{1.5}$$

for expansion parameter A^a_μ and the generators T^a_R in an appropriate Lie algebra representation. Using (1.4) to expand $h(x) = 1 + i\alpha^a T^a$, we see that (1.3) can be satisfied if we assert that the field $A^a_\mu(x)$ transforms under gauge transformations as,

$$A^a_\mu(x) \to A^a_\mu(x) + \frac{1}{g}\partial_\mu \alpha^a(x) - f^{abc}\alpha^b(x)A^c_\mu(x) \tag{1.6}$$

for f^{abc} structure constants of the Lie Algebra. Thus, we have obtained an expression for a derivative object that transforms locally as a Lie Group representation.

From now on, we will often suppress Lie algebra indices and write the Lie-algebra valued field defined by $A_\mu(x) = A^a_\mu(x)T^a$.

The expansion (1.5) can be extended to obtain a closed-form expression for the Wilson line at finite separations of the endpoints,

$$W_{\mathcal{C}}(x,y) = \mathcal{P}\exp\left\{ig\int_x^y A_\mu(z)dz^\mu(\mathcal{C})\right\}, \tag{1.7}$$

where $\mathcal{C}$ is a particular path in spacetime along which we take the integration variable z and $\mathcal{P}$ is the path-ordering operator, defined as sorting the operators in ascending order of their position along the path $\mathcal{C}$, analogous to the time ordering operator in Dyson's equation. This path ordering operator is required as the generators do not commute. Note that expectation values of physical quantities such as $\langle\phi(x)W_{\mathcal{C}}(x,y)\phi(y)\rangle$ will depend on exactly which path $\mathcal{C}$ is chosen. We can construct a gauge-invariant quantity by taking the path $\mathcal{C}$ to be a loop, $W_{\mathcal{C}}(x,x)$, and tracing over the gauge indices, thereby obtaining a *Wilson loop*. However, we want our theory to be local, and would like to build a manifestly-local Lagrangian. Loops extended in spacetime are not local. We can, though, imagine taking an infinitesimally small Wilson loop, which we can obtain by Taylor expanding (1.7),

$$W^{\text{loop}}_{\partial\Sigma} = 1 + ig\oint_{\partial\Sigma} A_\mu dx^\mu + O(g^2) = 1 + ig\int_\Sigma F_{\mu\nu}d\sigma^{\mu\nu} + O(g^2) \tag{1.8}$$

where we have used Stokes' theorem to introduce the local field $F_{\mu\nu}$. Consistent with the notion of a small loop, we can also obtain $F_{\mu\nu}$ by taking,

$$F_{\mu\nu} = \frac{i}{g}[D_\mu, D_\nu]. \tag{1.9}$$

We can now write down gauge-invariant, Lorentz-invariant, manifestly-local Lagrangians with kinetic terms for the gauge fields. The simplest is,

$$\mathcal{L} = -\frac{1}{4}F^a_{\mu\nu}F^{a\mu\nu} \tag{1.10}$$

with a denoting the Lie algebra index, and with an implied trace over all repeated indices. If we choose the gauge group to be $U(1)$, this reduces to Maxwell theory. For more general gauge groups, we obtain a Yang-Mills theory. It is conventional to describe operators that transform nontrivially under the gauge group as being *charged under colour*, with the index a spanning colour 'space'.

However, when we try to use this Lagrangian in a quantum theory, treating all degrees of freedom as physical, we encounter an obstacle. Any field A^a_μ that can be written as a gradient, $A^a_\mu = \partial_\mu \Lambda^a(x,t)$, carries zero action or energy. This would mean that fields of arbitrary frequency can be exchanged without any energetic cost [2]. Similarly, it can be shown that the Green's function for these fields are not single-valued [1]. To circumvent such pathologies, we can impose the condition that field configuration related by $A^a_\mu \to A^a_\mu + \partial_\mu \Lambda^a(x,t) + \cdots$ should be considered physically identical, i.e. that local gauge transformations describe the same physical configuration. Thus, when taking the path integral in the quantised theory, we do not integrate over configurations that are equivalent under such local gauge transformations. The local gauge 'symmetry' should therefore be considered a *redundancy in our description* of the physical theory, rather than a physical symmetry itself.

To this basic theory, we can add matter. For example, consider

$$\mathcal{L}_{\text{QCD}} - \frac{1}{4}F^a_{\mu\nu}F^{a\mu\nu} + \sum_q \bar{\chi}^q_i \left(i\gamma^\mu (D_\mu)_{ij} - \delta_{ij} m_q\right) \chi^q_j \tag{1.11}$$

for the gauge group $SU(3)$, with fermions χ and $\bar{\chi}$ in the fundamental and anti-fundamental representations, Dirac matrices γ^μ, colour indices i and j running from 1 to 3, and a summation over the six quark flavours indices q with quark masses m_q. The summation over the colour indices a, i and j is here implicit. This is the Lagrangian for QCD.

1.2 Thermal gauge theory

We rarely have total information about a physical system, and generally only control a few variables in a macroscopic ensemble such as temperature, total energy, chemical potential, or total charge. All physical measurements must then be statistical in nature. We know that the statistical information of a system is encoded in the partition function, which in quantum systems is,

$$Z_{\text{thermal}} = \operatorname{Tr} e^{-\beta H} \tag{1.12}$$

for inverse temperature β and Hamiltonian H, with the trace taken over a basis of quantum states. It is possible to express this as a path integral. To do this, we start with the path integral partition function of QFT,

$$Z = \int_{\phi_i, \chi_i}^{\phi_f, \chi_f} \exp\left\{ i \int_0^T dt \int d^3x \mathcal{L}[\phi, \chi] \right\} \tag{1.13}$$

for total time T, bosonic fields ϕ, fermionic fields χ, Lagrangian $\mathcal{L}$, and initial and final field configurations ϕ_i, χ_i and ϕ_f, χ_f, respectively [3]. Taking this expression and setting $T \to -i\beta$ and $\phi_i = \phi_f$, $\chi_i = -\chi_f$ [1] gives us a path integral expression of the same form as $\operatorname{Tr} e^{-\beta H}$. This means that we can introduce a temperature $1/\beta$ to a QFT by Wick rotating to Euclidean time and then compactifying this by compactifying onto a circle of circumference β, with periodic boundary conditions for bosons and antiperiodic boundary conditions for fermions.

We can easily add chemical potentials μ_i associated with $U(1)$ charges Q_i by generalising to,

$$Z = \operatorname{Tr} e^{-\beta H - \sum_i \mu_i Q_i} = \int_{\phi_i, \chi_i}^{\phi_i, -\chi_i} \exp\left\{ - \int_0^\beta d\tau \int d^3x \mathcal{L}[\phi, \chi] - \sum_i \mu_i Q_i \right\} \tag{1.14}$$

Many of the most important open questions in physics can be reduced to the challenge of computing the integral on the right-hand side of this equation, and its derivatives in β and μ_i, for particular theories in the strong coupling regime.

The expression (1.14) describes the statistical system in the grand canonical ensemble since we control temperature and chemical potential. We can Legendre transform to enter into alternative descriptions. Particularly relevant to us will be the microcanonical ensemble, in which we fix total energy instead of temperature. This can significantly affect what physical information we can probe. To understand this,

---

[1] The necessity of antiperiodic boundary conditions for fermions can be seen by expanding the exponent in powers of Grassman numbers. Periodic boundary conditions would give use the graded trace, $\operatorname{Tr}(-1)^F e^{-\beta H}$, for fermion number F, which does have utility in supersymmetric systems, as we will see in Chapter 3.

look at Fig. 1.1. The curves show the free energy extrema at each value of the energy and temperature. The dotted saddle has negative heat capacity and is therefore never favoured when we fix temperature: either the upper or the lower saddle will always be dominant. However, if we fix energy at some value between the phases denoted by the two solid-lines, this dotted-line saddle can become stable and dominant. In other words, it becomes the free energy minimum under the constraint of fixed energy. The relevance of this to us will be transparent in Sec. 1.3.

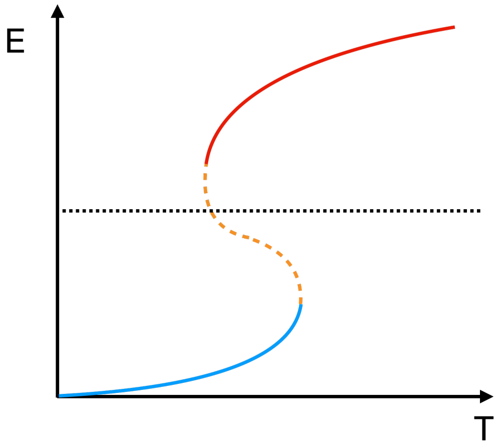

FIGURE 1.1: Saddles for a first order phase transition in the canonical ensemble. In the canonical ensemble, in which we fix temperature, the local mininma of the free energy are the solid blue and red lines. A first order phase transition occurs when the free energy of one of these minima becomes lower than that of the other. The dashed orange line has negative heat capacity and must therefore be unstable. It is a saddle point but not a local minimum of the free energy in the canonical ensemble. In contrast, in the microcanonical ensemble, we fix energy. At energies between the red and blue saddles, such as that denoted by the dotted black line, the dashed orange saddle *is* now a local minimum of the free energy and can be stable and dominant.

1.3 Confinement and deconfinement

The phenomenon of confinement is the most salient feature and most interesting open problem in Yang-Mills theories and QCD in particular. This is the statement that colour-charged matter, such as individual quarks and gluons, cannot appear as asymptotic states [4; 3; 5; 6; 7]. This is observed empirically by the fact that the measured spectrum of QCD consists only of colour-neutral bound states, i.e. hadrons, such as mesons and baryons, whereas isolated quarks or gluons are not observed. However, the confined phase generally lies in the strong coupling, non-perturbative regime of the theory, where an analytic understanding is not yet possible. Lattice computations have confirmed that the property of confinement emerges from the equations (1.9) and (1.11), but offer little explanation as to *why* it is happening, and certainly no mathematical rigorous proof that it does so.

The dynamical origin of confinement is universally acknowledged to be *chromoelectric flux tube* formation [4; 3; 5]. This is most easily described in the case of a quark and its anti-quark forming a meson. Quarks source the non-abelian analogue of electric flux, known as chromoelectric flux, which obeys Gauss' law. In the confined phase, this chromolectric flux is concentrated into a thin tube that stretches between the quark-antiquark pair. By Gauss' Law, the tension of this flux tube cannot dissipate along its length. Consequently, the total energy of the string grows linearly with its length, i.e. the separation of the particles.

This simple picture of confinement by flux tube formation is confirmed by lattice computations and rare examples of Yang-Mills theories for which confinement is analytically tractable, such as Seiberg-Witten theory and the Polyakov model[8; 9]. Yet there is no agreement about why these flux tubes form in pure Yang-Mills or QCD, and, again, no mathematical proof.

In the deconfined phase, by contrast, quarks and gluons are liberated to move somewhat independently over short differences, forming a plasma known as the quark-gluon plasma (QGP). Understanding the transition between confined and deconfined phases is of crucial importance for the physics of heavy ion collisions, neutron stars, and the early universe. For example, the universe was dominated by the QGP for some time microseconds after the Big Bang until the temperature lowered enough for confinement of quarks into nuclear matter [10]. In pure Yang-Mills, this is a first order transition. In QCD, it is commonly believed not to be a strict transition, but rather a smooth crossover. This assumption will be reexamined in Sec.1.3

The confined phase can be distinguished from the deconfined phase in many ways. For example, in the 't Hooft limit of infinite number of colours N, the confined phase typically has entropy of order N^0, arising from glueballs and other gauge-singlet degrees of freedom, while the deconfined phase typically has entropy of order N^2, arising from deconfined gluons and other adjoint degrees of freedom. Such behavior is generic, appearing for example in the strongly-coupled large-N gauge theories of holography [11], as well as weakly-coupled gauge theories on spatial spheres, described by matrix models [12; 13], among others.

In pure Yang-Mills theory at zero temperature, we can also probe the potential resulting from linear flux directly using the Wilson loops. A Wilson Loop in the fundamental representation can be thought of as the trajectory of a nondynamical quark taken around the designated path $\mathcal{C}$. Inserting the Wilson loop allows us to measure the potential between a probe quark and an anti-quark in a gauge invariant and precise way [3]. To see this, consider taking $\mathcal{C}$ to be a rectangle in spacetime, describing a quark-antiquark pair created at an instance of time, propagated through time at fixed spatial location, and then annihilated. This can be described in the

(Wick-rotated) Hamiltonian formalism as,

$$\langle W(C)\rangle = \langle 0|F(L)e^{-H\tau}F(L)^{\dagger}|0\rangle, \tag{1.15}$$

where $F(L)$ is the operator that annihilates a nondynamical (i.e. very massive) quark-antiquark pair separated by a distance L. Consider now taking $L \to \infty$ and $T \to \infty$. Since the Hamiltonian H measures the energy of the state, for a state with linear confinement, we expect $H \sim V(L) \sim \sigma L$, for some string tension σ, to become the dominant contribution. Therefore, in the confining phase, we expect,

$$\langle W(\mathcal{C})\rangle \sim e^{-\sigma\tau L} = e^{-\sigma A(\mathcal{C})} \tag{1.16}$$

i.e. the area $A(\mathcal{C})$ of the loop $\mathcal{C}$ appears at leading order in the exponent of the expectation value. This property holds for more general paths $\mathcal{C}$, and hence this signature of confinement is known as the area law. When the potential energy from the quark-antiquark pair grows more slowly than the separation L, as in the deconfined phase, we instead expect contributions local to the path to dominate, yielding a *perimeter* law. Note that, at finite temperature, we cannot take the strict $T \to \infty$ limit, since the (Euclidean) time direction has the finite (anti-)periodicity β, and hence this prescription becomes mathematically inexact.

This characterisation also cannot be extended to Yang-Mills theories with dynamical matter in the fundamental representation, such as QCD. The linear flux between quarks persists only for a finite separation of the quark-antiquark pair. When the energy contained in the string is sufficient, additional quark-antiquark pairs can be produced from the vacuum. The strict $L \to \infty$ limit therefore cannot be taken.

In fact, the flux tubes can be broken whenever the symmetry under the centre of the gauge group (the subgroup that commutes with all other elements in the group) is explicitly broken, as achieved by the presence of dynamical quarks. The flux tube can be considered as being protected by the centre symmetry; it is the unbroken centre symmetry that prevents the tube from breaking and leads to the linear potential. Similarly, deconfinement in pure Yang-Mills, or Yang-Mills with only adjoint matter, is concomitant with the spontaneous breaking of centre symmetry, as this signifies the ability of flux tubes to break down. Centre symmetry offers one of the most precise and useful definitions of confinement, and is applicable at finite temperature. We will therefore discuss it extensively, along with its order parameter, the Polyakov loop, in the following subsection.

1.3.1 Polyakov loop

The Polyakov loop is a fundamental-representation Wilson loop taken around the thermal circle, which renders it topologically nontrivial. It can be expressed by,

$$P(x) = \frac{1}{N} \operatorname{Tr} \mathcal{P} \exp\left\{ ig \int_0^\beta d\tau A_\mu(x,\tau) \right\} \tag{1.17}$$

where we have chosen to normalise by the N appearing in $SU(N)$. The Polykov loop is charged under the centre symmetry. In theories with a centre symmetry, its expectation value, $P \equiv \langle P \rangle$, is zero in the confined phase and non-zero in the deconfined phase. This can be argued as follows.

As a type of Wilson loop, the Polyakov loop can be thought of as inserting a quark along the designated path, the temporal circle. We can therefore express the insertion of a quark and antiquark, held at fixed point in space and separated by a distance L, by

$$\langle P(x) P^\dagger(x+L) \rangle \sim e^{-V(L)\beta} \tag{1.18}$$

where the asymptotic identification with the exponential potential and inverse temperaturefollows the same argument used to obtain (1.16). Now consider taking $L \to \infty$. By the cluster decomposition principle, the expectation value for the Polyakov loop should factorise, yielding,

$$\lim_{L\to\infty} \langle P(x) P^\dagger(x+L) \rangle \to |\langle P(x) \rangle|^2 \tag{1.19}$$

Combined with (1.18), we deduce,

$$\langle P \rangle \sim e^{-V(L)\beta/2} \sim e^{-F_{\text{quark}}}, \tag{1.20}$$

where we have interpreted a single Polyakov loop as the insertion of an individual quark with accompanying free energy F_{quark}. In a confining phase, with potential between quarks linear in their separation, we expect $V(L) \to \infty$, and thus $\langle P(x) \rangle \to 0$. In a deconfined phase, by contrast, we expect $V(L)$ to be finite even as $L \to \infty$, and thus $\langle P(x) \rangle$ should be finite and non-zero. This implies that the Polyakov loop is an order parameter for confinement, zero when confining and non-zero when deconfining. A Polyakov loop expectation value of zero indicates that the insertion of an isolated quark would cost an infinite amount of free energy, $F_{\text{quark}} \to \infty$.

As noted in Sec 1.2, as bosons, the gauge fields $A_\mu(x)$ must be periodic over the compact thermal direction. A standard gauge transformation $\Omega(x,\tau)$ has the property of periodicity $\Omega(x,\tau) = \Omega(x,\tau+\beta)$, which of course leaves the periodicity of gauge fields intact. However, we can extend the notion of gauge transformations to include *improper* gauge transformations. These have the property $\hat{\Omega}(x,\tau) = h\hat{\Omega}(x,\tau+\beta)$, for

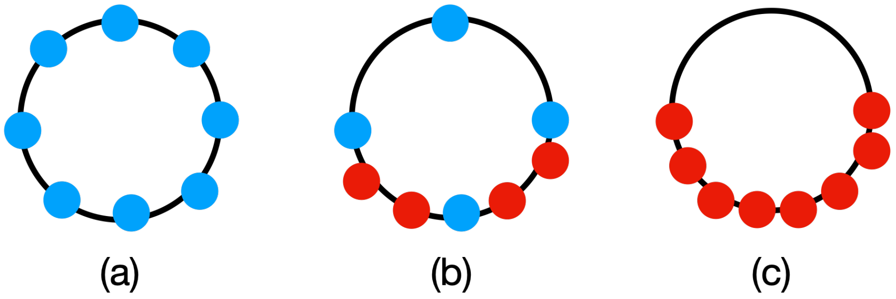

FIGURE 1.2: Eigenvalues, $\psi_i = \exp\{i\alpha_i\}$, of the gauge holonomies around the thermal cricle, represented on the unit circle, in the classical or weak coupling limit. The sum, $\sum \psi_i = \sum \exp(i\alpha_i)$ gives the Polyakov loop. (a) The confined phase, with centre-symmetric distribution invariant under $\psi_i \to e^(2\pi ik/N)\psi_i$, $k \in \mathbb{Z}$, and vanishing Polyakov loop expectation value, $P = \sum \psi_i = 0$. (b) The partially confined phase. A subset of the eigenvalues (blue) are uniformly distributed, corresponding to the confined sector and not contributing to the value of P, while the other eigenvalues (red) correspond to the deconfined sector and have no uniformly-distributed subsection. P is non-zero. (c) The completely deconfined phase, with no uniformly-distributed subset. P is non-zero. Outside of the semiclassical limit, we must also consider fluctuations.

h an element in the centre of the gauge group. Gauge fields $A_\mu(x)$ retain periodicity under this gauge transformation since the fields transform in the adjoint , and, by definition, the centre is the kernel of the adjoint action. Since $\hat{\Omega}(x,\tau)$ still describes a gauge transformation everywhere locally, all local operators are unaffected by this improper gauge transformation. Likewise, topologically trivial Wilson lines transform trivially under its action. However, the Polyakov loop *does* transform nontrivially under the the improper gauge transformation $\hat{\Omega}(x,\tau)$.

To see this explicitly, perform the improper gauge transformation on the definition (1.17),

$$P(x) \to P'(x) = \mathrm{Tr}\,\mathcal{P}\hat{\Omega}(x,\tau)\exp\left\{ig\int_0^\beta d\tau A_\mu(x,\tau)\right\}\hat{\Omega}^\dagger(x,0) \tag{1.21}$$

$$= h\,\mathrm{Tr}\,\mathcal{P}\Omega(x,0)\exp\left\{ig\int_0^\beta d\tau A_\mu(x,\tau)\right\}\Omega^\dagger(x,0) \tag{1.22}$$

$$= hP(x) \tag{1.23}$$

Therefore, the Polyakov loop transforms as $P(x) \to hP(x)$ under the centre symmetry. We can gain more insight by diagonalising the holonomy and the central elements of the gauge group. Any element of the centre of $SU(N)$ can then be written as a complex number multiplying the identity, $e^{2\pi ik/N}\mathbf{1}$, for $k \in \mathbb{Z}$. Meanwhile, the holonomy eigenvalues ψ_i also consist of a set of complex numbers on the unit circle, which can be written in terms of the phases $\alpha_i \in [-\pi,\pi)$ via $\psi_i = e^{i\alpha_i}$. We can obtain the Polyakov loop from the eigenvalues of the holonomy by summation over all eigenvalues, $\sum_i e^{i\alpha_i}$. The eigenvalues are gauge-invariant up to permutation of their labels.

The centre symmetric configuration is invariant under the action of $e^{2\pi ik/N}$, and is therefore uniformly distributed. In the semiclassical or weak coupling limit, such configurations are depicted by the left panel of Fig. 1.2. (Beyond the semiclassical limit, we must also average over fluctuations, but the essential understanding is the same.) The action of the centre can be visualised as the rotation of the circle by the angle $e^{2\pi ik/N}$. This configuration is clearly invariant under this operation, thus demonstrating the symmetry. It is clear that the Polyakov loop expectation value associated with this configuration, $P = \sum_{i=0}^{N-1} e^{i\alpha_i}$, must vanish due to this symmetry.

In contrast, the deconfined phase is shown in the right panel of Fig. 1.2. There is no symmetry under the action of the centre, or rotation of the circle, indicating that the centre symmetry is broken. Concomitantly, the Polyakov loop $P = \sum_{i=0}^{N-1} e^{i\alpha_i}$ is nonzero.

It is possible to have a configuration in which some eigenvalues are uniformly distributed while the others are not part of any uniformly-distributed sector. This is depicted in the central panel of Fig. 1.2. It suggests a phase that shares properties of both the confined and the deconfined phase. The phase described by this configuration will be the subject of the next section.

1.4 Partial deconfinement

In recent years, evidence has emerged that, quite generally in large-N gauge theories, a partially-confined, or equivalently partially-deconfined, phase can appear between the completely-confined and completely-deconfined phases [14; 15; 16; 17; 18; 19; 20; 21]. More specifically, in $SU(N)$ gauge theories at large N a phase can appear in which only an $SU(M)$ sub-sector deconfines, where as the energy E increases, M increases from $M = 0$ to $M = N$, at which points the phase connects to the completely-confined and completely-deconfined phases, respectively. We will often simply refer to the partially deconfined phase as "the partial phase", and will continue to refer to the "completely-deconfined" and "completely-confined" phases simply as "deconfined" and "confined".

In the partial phase, confined and deconfined degrees of freedom coexist, similar to the coexistence of liquid water and ice at water's freezing temperature. However, unlike water, in the partial phase the coexistence occurs in the "internal" colour space, where interactions are non-local, and hence can lead to non-trivial T dependence.[2] In fact, the underlying physics is more similar to Bose-Einstein condensate (BEC), where the confined and deconfined phases are like the superfluid and normal fluid phases, respectively, and the partial phase is like a two-fluid phase of N bosons split between

---

[2] In QCD, the change of the ratio between the numbers of flavors and confined colour degrees of freedom can lead to a nontrivial T dependence, even in the free limit [18].

$N - M$ in the superfluid and M in the normal fluid. The similarity to a BEC can be made precise, because a BEC can be treated in terms of gauge theory: the indistinguishability of the N bosons means their permutation symmetry, S_N, is gauged [20].

Crucially, in the large-N limit, the partial phase can be characterised in a gauge-invariant manner by making use of the Polyakov loop eigenvalues introduced in Sec. 1.3.1. In the large-N limit these eigenvalues can be treated as a continuum, and their distribution, $\rho(\psi)$, provides precise definitions of the confined, partial, and deconfined phases. Cartoons of $\rho(\psi)$ in these three phases appear in Fig. 1.3 for gauge group $SU(N)$, where the eigenvalues are all complex phases distributed on $\psi \in [-\pi, \pi]$. These correspond to the densities of the configurations depicted in Fig. 1.2 taken to the continuum limit.

In the confined phase, shown in Fig. 1.3 (a), the distribution is uniform: $\rho(\psi) = \frac{1}{2\pi}$ when properly normalised. Recall that the centre symmetry acts as a permutation of the eigenvalues, which in Fig. 1.3 is a discrete translational symmetry acting horizontally, so a constant $\rho(\psi)$ preserves the centre symmetry. Correspondingly, the Polyakov loop expectation value vanishes, $P = 0$, because upon taking the trace, all the phases cancel one another. In the partial phase, shown in Fig. 1.3 (b), $\rho(\psi)$ becomes non-uniform, indicating spontaneous breaking of the centre symmetry, and correspondingly, $P \neq 0$. The distribution remains ungapped, however, meaning eigenvalues appear for all possible values on the interval $\psi \in [-\pi, \pi]$. Crucially, $\min\left[\rho(\psi)\right] = \frac{1}{2\pi}\left(1 - \frac{M}{N}\right)$ provides a gauge-invariant definition of the size M of the deconfined subsector [20]. In the deconfined phase, shown in Fig. 1.3 (c), the distribution is non-uniform, so again centre symmetry is spontaneously broken and $P \neq 0$, but now the distribution is gapped, as some eigenvalues near $-\pi$ and π disappear.

The order of the transition from confined to deconfined phase depends on the detailed dynamics of each particular gauge theory. The two logical possibilities are either first order, or second order or higher, i.e. continuous. By extension, where the partial phase appears in the thermodynamic phase diagram depends on detailed dynamics. For each of the two logical possibilities, Fig. 1.4 shows cartoons of the Polyakov loop expectation value as a function of T. In the first order case, depicted in Fig. 1.4 (a), the partial phase is the thermodynamically unstable phase between the confined and deconfined phases. In this case, in the free energy the partial phase is the local maximum between two local minima, and the transition occurs when the local minima exchange roles as the global minimum. In the continuous case, depicted in Fig. 1.4 (b), the partial phase is a stable phase that connects the confined and deconfined phases. The same theory can exhibit both cases depending on the details of the parameters, such as quark mass. In either case, the partial phase connects to the

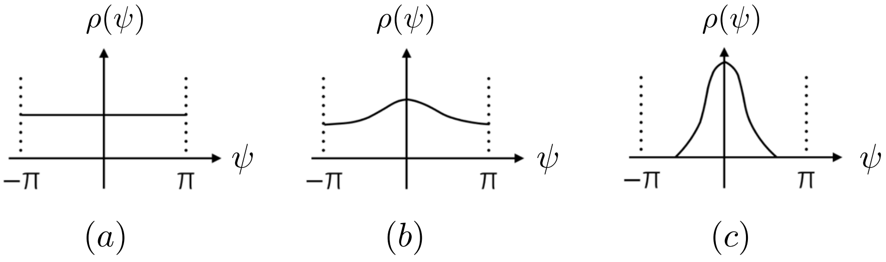

FIGURE 1.3: Schematic depictions of the eigenvalue distributions, $\rho(\psi)$, of the path-ordered exponential of the gauge holonomy around the thermal circle in a Euclidean gauge theory, in the 't Hooft large-N limit. We assume an $SU(N)$ gauge group, so the eigenvalues are complex phases distributed on $\psi \in [-\pi, \pi]$. For such theories with a centre symmetry, $\rho(\psi)$ provides a gauge-invariant way to distinguish three phases, as follows. (a) The confined phase, in which $\rho(\psi)$ is uniform, so the centre symmetry is unbroken, and hence the Polyakov loop expectation value vanishes, $P = 0$. (b) The partial phase, in which $\rho(\psi)$ is non-uniform, so the centre symmetry is spontaneously broken and $P \neq 0$. However, $\rho(\psi)$ is ungapped. (c) The deconfined phase, in which $\rho(\psi)$ is non-uniform, so again the centre symmetry is broken and $P \neq 0$, but now $\rho(\psi)$ is gapped. (a) and (b) are separated by a Hagedorn transition, while (b) and (c) are separated by a Gross-Witten-Wadia (GWW) transition.

confined phase via a Hagedorn transition[3], characterised by an exponential growth of the density of states when approaching the transition from the confined phase, and connects to the deconfined phase via a Gross-Witten-Wadia (GWW) transition, a transition defined by the appearance of the gap in $\rho(\psi)$. The order of the GWW transition depends on the details of the dynamics.[4]

The concept of partial phases was originally motivated by holography, to explain the field theory dual to certain phase transitions in the bulk gravity theory [14; 24]. For instance, the small black hole phase in global AdS$_5$ is conjectured to be dual to a partial phase in $\mathcal{N} = 4$ SYM on $S^1 \times S^3$. If this is the case, then the point at which the specific heat of the AdS black hole phase becomes negative would be a GWW point.

Partial confinement might also be invoked to describe the thermodynamic behaviour of the QGP in QCD. Lattice computations at zero charge density show that the is no first or second order confinement/deconfinement transition in the QGP. Instead, there appears to be a smooth crossover between the phases. It is plausible that this 'crossover' actually represents a partially confined phase, interpolating between the

---

[3] This is expected to be a generic statement for theories at large N. The Hagedorn transition indicates the endpoint of the fully confined phase and the onset of the quark-gluon plasma phase, and therefore a phase that shares at least some properties of the deconfined phase. The Hagedorn transition appears explicitly between the confined phase and what we identify as the partially-deconfined phase in [12; 13] using perturbative field theory calculations in $\mathcal{N} = 4$ SYM. In theories with a holographic dual, at zero string coupling, the Hagedorn transition manifests as strings with Hagedorn behaviour, typically connecting a string gas phase (confinement) with a small black hole phase (in our interpretation, partial confinement). Since the Hagedorn transition is a description pertaining strictly only to free strings, the definition loses precision in theories at finite N, but is still a useful characterisation.

[4] The original example of the GWW transition [22; 23] was in two-dimensional lattice Yang-Mills theory, and the transition was of third order.

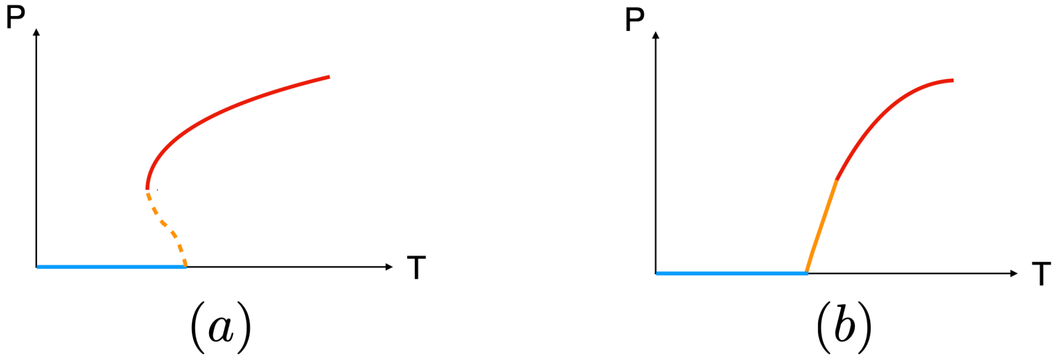

FIGURE 1.4: Schematic depiction of the Polyakov loop expectation value, P, as a function of temperature T for a confinement/deconfinement transition that is (a) first order or (b) second order or higher, i.e. continuous. The blue, orange and red curves represent the confined, partial, and deconfined phases, respectively. Either situation is a logical possibility, and are thought to be parametrically connected though quark number and mass.

confined and deconfined phases. If this is the case, we might expect that there is a transition of third order or higher, which is a possibility that has not yet been discounted. This interpretation of the crossover region could synthesise the relationship between chiral symmetry breaking[5] and deconfinement in the QGP, which has been a longstanding mystery in physics. This will be explained in Chapters 2 and 3.

1.5 Outline of this thesis

In this chapter, we have introduced the partially confined phase, which we expect to appear as a generic feature of strongly-coupled gauge theories. Some natural questions remain that we have been omitted from the discussion. This is because direct evidence concerning their resolution was lacking prior to the work presented in this thesis.

The first question concerns the dynamics of the partially confined phase. We have discussed flux tube formation and linear confinement in the confined phase, and the dissolution of flux tubes in the deconfined phase. How does flux tube formation manifest in the partially confined phase, if at all? In Chapter 2, we will argue that the colours of the gauge group can be separated into a confined and a deconfined sectors, and that the confined sector exhibits linear confinement, implying flux tube formation in this part of the gauge group. This could allow us to identify a signature of the partially confined phase that could be measured in the QGP.

---

[5] The finite quark masses in QCD explicitly break chiral symmetry. By 'chiral symmetry breaking' here, we refer to the theory in the limit of massless quarks. We then considering QCD as a perturbation of this theory with messy remnants of the chiral symmetry breaking

The second question concerns potential characterisations of the partially confined phase in terms of global symmetries. We have described an order parameter to distinguish between the confined and deconfined phases, namely the Polyakov loop. However, we have not discussed whether any order parameter exists to distinguish the partially confined phase. Moreover, the characterisation we have given in terms of the distribution of the Polyakov loop eigenvalue distribution (which is not strictly gauge invariant and thus not an order parameter) applies only at large N, and we would like to extend the notion of partial confinement to finite N. These problems will be addressed in Chapter 3.

We shift focus somewhat in Chapter 4. Employing the AdS/CFT correspondence, we examine renormalization group flows on a class of $2+1$-dimensional spherical defects carrying hypermultiplets of Dirac fermions and their scalar superpartners in strongly-coupled $\mathcal{N}=4$ SYM, finding that these flow to $0+1$ dimensional Wilson-'t Hooft loops in the infrared. We thus uncover a new ultraviolet completion of the Wilson-'t Hooft loops, with hopes of applying our results to spherical graphene and fullerenes. We speculate that these novel descriptions of Wilson loops could be employed in gauge/gravity duality as probes to investigate the partially confined phase.

Finally, we offer concluding remarks in Chapter 5.

Chapter 2

Linear confinement in the partially-deconfined phase

2.1 Introduction

A natural question proceeding from the discussion of partial confinement in the introduction of this thesis concerns the *dynamics* of the the partially confined phase, and specifically the nature of any linearly-confining flux tubes. Prior to the research that is the focus of this chapter, only kinematic properties of the partially confined phase had been explored, primarily based on the N-dependence of the free energy and entropy. We expect, however, that another characterization of confinement — that we cannot separate quarks without forming a color singlet — is valid for the confined sector in the partially-deconfined phase as well. Up until now, there had been no direct confirmation of this idea. In this chapter, we make solid progress regarding this point.

As a concrete example, we consider pure Yang-Mills theory, which for $N \geq 3$ exhibits a first-order confinement/deconfinement transition. There is a partially-deconfined saddle separating two minima of the free energy (completely-confined phase and completely-deconfined phase); see Fig. 2.1. Along this partially-deconfined saddle, the size of the deconfined sector, M, varies, growing from zero near the completely confined saddle to N near the completely deconfined saddle. Although this saddle is thermodynamically unstable, it is connected to the stable saddle in QCD as $\frac{N_f}{N}$ or quark mass are varied[1] and we expect qualitative similarity between stable and unstable saddles. In the string-condensation picture, only the SU(M) chromo-electric strings are condensed. If we take a probe quark and antiquark from the deconfined sector, then they can interact with condensed strings and should not have the confinement potential. On the other hand, if we take probes from the confined sector,

---

[1] Pure Yang-Mills can be regarded as the heavy-quark-mass limit or $\frac{N_f}{N} \to 0$ limit.

we expect the linear confinement potential, because there are no condensed strings in this sector.

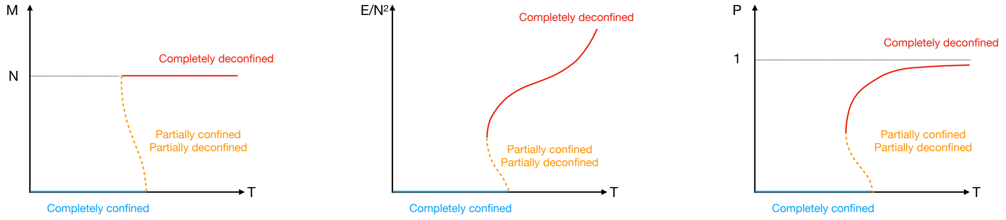

FIGURE 2.1: Sketches of the temperature dependence of M, $\frac{E}{N^2}$ and P for the pure Yang-Mills theory. Blue, orange and red lines are completely-confined phase, partially-deconfined saddle (equivalently, partially-confined saddle) and completely-deconfined phase. The partially-deconfined saddle is the maximum of free energy at fixed temperature. The size of the deconfined sector, M, varies along the partially-deconfined saddle, growing from zero near the completely confined saddle to N at the completely deconfined saddle. This is shown explicitly in the leftmost figure. See Ref. [16] for other examples including a thermodynamically stable partially-deconfined phase.

We will test this statement by using a gauge fixing that separates confined and deconfined sectors in a controlled manner. Specifically, we will consider the strong-coupling lattice gauge theory at finite temperature and study the two-point function of the Polyakov loop. There are several reasons we consider this theory. First of all, partial deconfinement is a generic property of gauge theories with confinement/deconfinement transition including this model. Secondly, we can use the Eguchi-Kawai equivalence (large-N volume reduction) which makes our numerical simulation tractable. Furthermore, for this particular setup, we can make a few analytic predictions assuming the formation of the flux tube in the confined sector, and we can confirm the prediction numerically. Recall from Sec. 1.3.1 that the Polyakov loop two-point function decays exponentially in the completely-confined phase as

$$\langle \mathrm{Tr}\mathcal{P}(\vec{x}) \cdot \mathrm{Tr}\mathcal{P}(\vec{y}) \rangle \sim e^{-\beta\sigma|\vec{x}-\vec{y}|}, \tag{2.1}$$

where, again, $\beta = T^{-1}$ is the inverse temperature and σ is the string tension. We will perform a gauge fixing such that colors split into the confined and deconfined sectors, respectively, and define the Polyakov loops in those sectors, $\mathrm{Tr}\mathcal{P}_{\mathrm{con}}(\vec{x})$ and $\mathrm{Tr}\mathcal{P}_{\mathrm{dec}}(\vec{x})$. Then, we show that $\mathrm{Tr}\mathcal{P}_{\mathrm{con}}(\vec{x})$ exhibits the exponential decay

$$\langle \mathrm{Tr}\mathcal{P}_{\mathrm{con}}(\vec{x}) \cdot \mathrm{Tr}\mathcal{P}_{\mathrm{con}}(\vec{y}) \rangle \sim e^{-\beta\sigma|\vec{x}-\vec{y}|} \tag{2.2}$$

with the same string tension σ. We also show that

$$\langle \mathrm{Tr}\mathcal{P}_{\mathrm{con}}(\vec{x}) \cdot \mathrm{Tr}\mathcal{P}_{\mathrm{dec}}(\vec{y}) \rangle \sim e^{-\beta\sigma|\vec{x}-\vec{y}|}. \tag{2.3}$$

We interpret the relations (2.2) and (2.3) as consequences of the formation of flux tubes and linear confinement in the confined sector. For the strong-coupling lattice gauge theory, we confirm these relations quantitatively, including the concrete value of the string tension σ and the overall constant factor.

This chapter is organized as follows. In Sec. 2.2, we use the operator formalism to explain partial deconfinement in the current setting. In Sec. 2.3, we define the lattice action and set the simulation strategy. In Sec. 2.4, we determine the size of the deconfined sector M at each simulation point by using the relation between M and the phase distribution of the Polyakov loop [20]. In Sec. 2.5, we provide evidence of the linear confinement potential in the confined sector of the partially-deconfined phase. Theoretical considerations are provided in Sec. 2.5.1. Then, numerical evidence is given in Sec. 2.5.2. We define the Wilson loop equivalent to the two-point function of the Polyakov loop, and study it by using the Eguchi-Kawai equivalence in the large-N limit.

2.2 Theoretical background

Hamiltonian formulation

The meaning of partial deconfinement in the context of this chapter is clearer if we look directly at quantum states by working in the operator formalism. In this section, we describe the partially-deconfined phase by using the Hamiltonian formulation by Kogut and Susskind [25]. We consider the (3+1)-d Yang-Mills theory with U(N) gauge group[2]. The adaptation of this theory to the path-integral formalism, as actually used in our simulations, is described in Sec. 2.3. The purpose of this section is to explain aspects of partial deconfinement using the string condensation picture [26; 27].

The Kogut-Susskind Hamiltonian consists of the electric and magnetic terms,

$$\hat{H} = \hat{H}_{\mathrm{E}} + \hat{H}_{\mathrm{B}}. \tag{2.4}$$

The electric part of the Hamiltonian becomes

$$\hat{H}_{\mathrm{E}} = \frac{1}{2} \sum_{\vec{n}} \sum_{\mu=1}^{3} \sum_{a=1}^{N^2} \left(\hat{E}^{a}_{\mu,\vec{n}} \right)^2 . \tag{2.5}$$

---

[2] In the central part of this chapter, we will be working in the large N limit. In this case, differences in formulae and quantities between SU(N) and U(N)=U(1)× SU(N) differ only by terms suppressed by $1/N$. However, many formulae can be written more compactly when using the U(N) gauge group, which makes its use more convenient here and throughout this chapter.

The magnetic term (plaquette) is dropped in the strong coupling limit [27]. The commutation relations are

$$[\hat{U},\hat{U}]=\left[\hat{U},\hat{U}^{\dagger}\right]=\left[\hat{U}^{\dagger},\hat{U}^{\dagger}\right]=0. \tag{2.6}$$

$$\left[\hat{E}^{a}_{\mu,\vec{n}},\hat{U}_{\nu,\vec{n}'}\right]=\delta_{\mu\nu}\delta_{\vec{n}\vec{n}'}\tau_a\hat{U}_{\nu,\vec{n}'},\qquad \left[\hat{E}^{a}_{\mu,\vec{n}},\hat{U}^{\dagger}_{\nu,\vec{n}'}\right]=-\delta_{\mu\nu}\delta_{\vec{n}\vec{n}'}\hat{U}^{\dagger}_{\nu,\vec{n}'}\tau_a, \tag{2.7}$$

$$\left[\hat{E}^{a}_{\mu,\vec{n}},\hat{E}^{b}_{\nu,\vec{n}'}\right]=-if^{abc}\delta_{\mu\nu}\delta_{\vec{n}\vec{n}'}\hat{E}^{c}_{\nu,\vec{n}'}, \tag{2.8}$$

where f^{abc} is the structure constant of U(N), and

$$\sum_{a=1}^{N^2}\tau^a_{pq}\tau^a_{rs}=\frac{\delta_{ps}\delta_{qr}}{N},\qquad \sum_{a=1}^{N^2}(\tau^a\tau^a)_{pq}=\delta_{pq}. \tag{2.9}$$

The ground state of this string-coupling lattice gauge theory Hamiltonian $|\mathrm{g.s.}\rangle$ satisfies $\hat{E}^{a}_{\mu,\vec{n}}|\mathrm{g.s.}\rangle=0$ for any a,μ and $\vec{n}$. Hence, let us use the notation $|E=0\rangle$ to denote the ground state.

The operator $\hat{U}_{\mu,\vec{n}}$ is interpreted as the coordinate of the group manifold U(N) for the link variable on the site $\vec{n}$ in the μ-direction. The operators $\hat{U}$ and $\hat{E}$ are defined on the extended Hilbert space $\mathcal{H}_{\mathrm{ext}}$ that contains gauge non-singlet modes. A convenient basis of $\mathcal{H}_{\mathrm{ext}}$ is the coordinate representation,

$$\mathcal{H}_{\mathrm{ext}}=\otimes_{\mu,\vec{n}}\mathcal{H}_{\mu,\vec{n}}\sim\otimes_{\mu,\vec{n}}\left(\oplus_{g\in\mathrm{U}(N)}|g\rangle_{\mu,\vec{n}}\right), \tag{2.10}$$

where

$$\hat{U}_{\mu,\vec{n}}|g\rangle_{\mu,\vec{n}}=g|g\rangle_{\mu,\vec{n}}\qquad g\in\mathrm{U}(N). \tag{2.11}$$

More precisely, we will consider only the Hilbert space of square-integrable wave functions on U(N): $\mathcal{H}_{\mu,\vec{n}}=L^2(\mathrm{U}(N))$, where $L^2(\mathrm{U}(N))$ is the set of square-integrable functions from U(N) to $\mathbb{C}$. The ground state is the constant mode,

$$|E=0\rangle=\otimes_{\mu,\vec{n}}|E=0\rangle_{\mu,\vec{n}},\qquad |E=0\rangle_{\mu,\vec{n}}=\frac{1}{\sqrt{\mathrm{volU}(N)}}\int_{\mathrm{U}(N)}dg|g\rangle_{\mu,\vec{n}}. \tag{2.12}$$

Namely, the wave function $\langle g|E=0\rangle$ is constant.

Let $G=\prod_{\vec{n}}[\mathrm{U}(N)]_{\vec{n}}$ be the group of all local gauge transformations. Gauge transformation by $\hat{\Omega}=\otimes_{\vec{n}}\hat{\Omega}_{\vec{n}}$ is defined by

$$\hat{\Omega}\left(\otimes_{\mu,\vec{n}}|g\rangle_{\mu,\vec{n}}\right)=\otimes_{\mu,\vec{n}}\left(\hat{\Omega}_{\vec{n}}|g\rangle_{\mu,\vec{n}}\right)=\otimes_{\mu,\vec{n}}|\Omega_{\vec{n}}g\Omega_{\vec{n}}^{-1}\rangle_{\mu,\vec{n}}. \tag{2.13}$$

Note that the ground state is gauge-invariant:

$$\hat{\Omega}|E=0\rangle = |E=0\rangle. \tag{2.14}$$

We can define the projection operator to the gauge-invariant Hilbert space $\mathcal{H}_{\text{inv}}$ as

$$\hat{\pi} = \frac{1}{\text{Vol}G}\int_G d\Omega\hat{\Omega}, \tag{2.15}$$

where the integral is taken by using the Haar measure. By using this projection operator, canonical partition function at temperature T can be written in two ways as

$$Z(T) = \text{Tr}_{\mathcal{H}_{\text{inv}}}\left(e^{-\hat{H}/T}\right) = \text{Tr}_{\mathcal{H}_{\text{ext}}}\left(\hat{\pi}e^{-\hat{H}/T}\right). \tag{2.16}$$

The latter expression is directly related to the path-integral formalism with gauge field A_t, as shown in Appendix 2.C. The U(N)-element Ω corresponds to the Polyakov loop in the path-integral formalism [20]. The insertion of $\hat{\pi}$ means we should identify the states connected by gauge transformation, as we identify field configurations connected by gauge transformation in the classical theory. In other words, all states on the gauge orbit are physically equivalent. This makes the meaning of 'gauge fixing' in the extended Hilbert space clear: it selects a point from the gauge orbit, just as in the path-integral formalism or even in the classical theory. In the SU(M)-deconfined phase, we can take a gauge such that the upper-left $M \times M$ block is deconfined, as in Fig. 2.2.

Strings and Interactions

A closed string is created by the Wilson loop $\hat{W}_C^{(\text{closed})} = \text{Tr}(\hat{U}_{\mu,\vec{n}}\hat{U}_{\nu,\vec{n}+\hat{\mu}}\cdots)$, where the product of $\hat{U}$'s in the trace is taken along the closed path C. An open string is created by the open Wilson line along an open path C', denoted by $\hat{W}_{C'}^{(\text{open})}$, which is a product of $\hat{U}$'s without trace. The closed string is gauge invariant.

Suppose that there is a closed loop without self-intersection (i.e. no link appears twice). Then, the state $|W_C^{(\text{closed})}\rangle \equiv \hat{W}_C^{(\text{closed})}|0\rangle$ is an energy eigenstate, and the energy is $\frac{L}{2}$, where L is the length of the loop (i.e., the number of links consisting the loop). This can be seen as follows. Firstly, note that

$$\sum_a \left(\hat{E}^a_{\mu,\vec{n}}\right)^2 \hat{W}_C^{(\text{closed})}|E=0\rangle = \sum_a \left[\hat{E}^a_{\mu,\vec{n}}, \left[\hat{E}^a_{\mu,\vec{n}}, \hat{W}_C^{(\text{closed})}\right]\right]|E=0\rangle. \tag{2.17}$$

$\hat{E}^a_{\mu,\vec{n}}$ commutes with $\hat{W}_C^{(\mathrm{closed})}$ unless the latter contains $\hat{U}_{\mu,\vec{n}}$ or $\hat{U}^\dagger_{\mu,\vec{n}}$. When $\hat{U}_{\mu,\vec{n}}$ is contained,

$$\begin{aligned}\sum_a \left[\hat{E}^a_{\mu,\vec{n}}, \left[\hat{E}^a_{\mu,\vec{n}}, \hat{W}_C^{(\mathrm{closed})}\right]\right] |E=0\rangle &= \sum_a \mathrm{Tr}\left(\left[\hat{E}^a_{\mu,\vec{n}}, \left[\hat{E}^a_{\mu,\vec{n}}, \hat{U}_{\mu,\hat{n}}\right]\right] \hat{U}_{\nu,\hat{n}+\hat{\mu}} \cdots\right) |E=0\rangle \\ &= \sum_a \mathrm{Tr}\left(\tau^a\tau^a \hat{U}_{\mu,\hat{n}}\hat{U}_{\nu,\hat{n}+\hat{\mu}} \cdots\right) |E=0\rangle \\ &= C_R^{(2)} \mathrm{Tr}\left(\hat{U}_{\mu,\hat{n}}\hat{U}_{\nu,\hat{n}+\hat{\mu}} \cdots\right) |E=0\rangle \\ &= C_R^{(2)} \hat{W}_C^{(\mathrm{closed})} |E=0\rangle, \end{aligned} \tag{2.18}$$

where $C_R^{(2)} \equiv \sum_a \tau^a\tau^a$ is the quadratic Casimir operator. For $U(N)$, we have $C_R^{(2)} = 1$, which we will assume from now on. The above equation holds also when $\hat{U}^\dagger_{\mu,\hat{n}}$ is contained. Therefore, $\hat{H}_{\mathrm{E}}|W_C^{(\mathrm{closed})}\rangle = \frac{L}{2}|W_C^{(\mathrm{closed})}\rangle$. The same holds for any multi-string states, including closed or open strings, as long as there is no intersection.

Next, suppose a link $\hat{U}_{\mu,\vec{n}}$ appears twice in the loop, while other links appear only once. Let us write such a loop as $\mathrm{Tr}(\hat{V}_1\hat{U}_{\mu,\vec{n}}\hat{V}_2\hat{U}_{\mu,\vec{n}})$. Then,

$$\begin{aligned}&\sum_a \left[\hat{E}^a_{\mu,\vec{n}}, \left[\hat{E}^a_{\mu,\vec{n}}, \mathrm{Tr}(\hat{V}_1\hat{U}_{\mu,\vec{n}}\hat{V}_2\hat{U}_{\mu,\vec{n}})\right]\right] |E=0\rangle \\ &= 2\mathrm{Tr}(\hat{V}_1\hat{U}_{\mu,\vec{n}}\hat{V}_2\hat{U}_{\mu,\vec{n}})|E=0\rangle + 2\sum_a \mathrm{Tr}(\hat{V}_1[\hat{E}^a_{\mu,\vec{n}}, \hat{U}_{\mu,\vec{n}}]\hat{V}_2[\hat{E}^a_{\mu,\vec{n}}, \hat{U}_{\mu,\vec{n}}])|E=0\rangle \\ &= 2\mathrm{Tr}(\hat{V}_1\hat{U}_{\mu,\vec{n}}\hat{V}_2\hat{U}_{\mu,\vec{n}})|E=0\rangle + 2\sum_a \mathrm{Tr}(\hat{V}_1\tau^a\hat{U}_{\mu,\vec{n}}\hat{V}_2\tau^a\hat{U}_{\mu,\vec{n}})|E=0\rangle \\ &= 2\mathrm{Tr}(\hat{V}_1\hat{U}_{\mu,\vec{n}}\hat{V}_2\hat{U}_{\mu,\vec{n}})|E=0\rangle + \frac{2}{N}\mathrm{Tr}(\hat{V}_1\hat{U}_{\mu,\vec{n}})\mathrm{Tr}(\hat{V}_2\hat{U}_{\mu,\vec{n}})|E=0\rangle. \end{aligned} \tag{2.19}$$

Therefore,

$$\begin{aligned}&\hat{H}_E\left(\mathrm{Tr}(\hat{V}_1\hat{U}_{\mu,\vec{n}}\hat{V}_2\hat{U}_{\mu,\vec{n}})|E=0\rangle\right) \\ &= \frac{L}{2}\mathrm{Tr}(\hat{V}_1\hat{U}_{\mu,\vec{n}}\hat{V}_2\hat{U}_{\mu,\vec{n}})|E=0\rangle + \frac{1}{N}\mathrm{Tr}(\hat{V}_1\hat{U}_{\mu,\vec{n}})\mathrm{Tr}(\hat{V}_2\hat{U}_{\mu,\vec{n}})|E=0\rangle. \end{aligned} \tag{2.20}$$

The second term can be understood as the splitting of a string into two strings. In the same manner, we can show that two strings can be joined to form one string at an intersection,

$$\begin{aligned}&\hat{H}_E\left(\mathrm{Tr}(\hat{V}_1\hat{U}_{\mu,\vec{n}})\mathrm{Tr}(\hat{V}_2\hat{U}_{\mu,\vec{n}})|E=0\rangle\right) \\ &= \frac{L}{2}\mathrm{Tr}(\hat{V}_1\hat{U}_{\mu,\vec{n}})\mathrm{Tr}(\hat{V}_2\hat{U}_{\mu,\vec{n}})|E=0\rangle + \frac{1}{N}\mathrm{Tr}(\hat{V}_1\hat{U}_{\mu,\vec{n}}\hat{V}_2\hat{U}_{\mu,\vec{n}})|E=0\rangle. \end{aligned} \tag{2.21}$$

In general, such splitting and joining can take place at any intersection.

Confinement

Let us consider low-energy gauge-invariant states consisting of a small number of closed strings with total length $L \sim N^0$. Then, there is at most order N^0 number of intersections. The interaction (splitting or joining) at each intersection is suppressed by $\frac{1}{N}$, and hence the interaction is negligible at large N. The energy of the system is simply $\frac{L}{2}$. Such states are in the confined phase.

If we introduce a probe quark-antiquark pair connected by the open Wilson line, the energy increases linearly as $E_{q\bar{q}} = \frac{L}{2}$. This leads to the linear confinement potential.

Deconfinement and string condensation

In the deconfined phase [26; 27], long strings with length of order N^2 condense. There are many intersections, and thus the $1/N$-suppressed interactions accompanying each intersection pile up and become non-negligible as a whole. Intuitively, if we introduce a short open string, it interacts with a condensed long string and forms a long open string, which allows us to separate quark and antiquark without making the string longer.

Partial deconfinement

Let $\hat{U}_{\text{dec}}$ be the SU(M)-subsector. The SU(M)-deconfined states can be constructed by acting with long traces of $\hat{U}_{\text{dec}}$'s on $|E = 0\rangle$ [17].[3] By using the Wilson loops restricted to the SU(M)-subsector

$$\hat{W}_{\text{dec},C} = \text{Tr}_{SU(M)}(\hat{U}_{\text{dec};\mu,\vec{n}}\hat{U}_{\text{dec};\nu,\vec{n}+\hat{\mu}}\cdots), \tag{2.22}$$

we can construct multi-string states

$$\hat{W}_{\text{dec},C}\hat{W}_{\text{dec},C'}\cdots|E = 0\rangle, \tag{2.23}$$

and then we can take a linear combination of such states. Such states are SU(M)-invariant, but not SU(N)-invariant. If we want to get an SU(N)-invariant state, we can act with the projector $\hat{\pi}$. We write the projection operator $\hat{\pi}$ explicitly as

$$Z(T) = \frac{1}{\text{Vol}(G)} \int_G d\Omega \text{Tr}_{\mathcal{H}_{\text{ext}}} \left(\hat{\Omega} e^{-\hat{H}/T} \right). \tag{2.24}$$

Let $\hat{U}_{\text{con}}$ be the other $N^2 - M^2$ elements. Operators that consist of a number $L \sim O(N^0)$ of $\hat{U}_{\text{con}}$'s increase the energy by $\frac{L}{2}$. They cannot be joined to the condensed

---

[3] See Refs. [24; 28; 29] for more general characterization.

strings. The energy eigenstate remains an energy eigenstate. Naturally, we expect that the color flux in the confined sector forms a flux tube and exhibits the linear potential $E_{q\bar{q}} = \frac{L}{2}$ while the deconfined sector does not. We will discuss this later, together with numerical results.

2.3 Methods

We will perform our simulations on a lattice-discretized model of U(N) Yang-Mills theory. Our simulations will involve constraining specific quantities so that we can remain in the partially-deconfined phase, and also so that we can separate the confined and deconfined sectors. Specifically, we use the Eguchi-Kawai model, which is equivalent to U(N) Yang-Mills theory in the large-N limit. The introduction of the constraints amounts to the study of the microcanonical ensemble rather than canonical ensemble, plus gauge fixing. Simulations of lattice gauge theories in the microcanonical ensemble (where the energy is fixed, instead of the temperature) [30] play a very important role in the numerical study of phase transitions [31].

2.3.1 The lattice regularization

2.3.1.1 Path-integral formulation

To set up our lattice model, we will begin with the path integral formulation. We consider Yang-Mills theory on a d-dimensional spatial lattice with continuous time t. We will focus on $d = 3$. Let $\vec{n}$ be the spatial points labeled by d integers, and $U_{\mu,\vec{n}}(t)$ be the U(N) link variable on the link connecting $\vec{n}$ and $\vec{n} + \hat{\mu}$. Here, $\hat{\mu}$ is the unit vector along the μ-direction. The gauge transformation is defined by

$$U_{\mu,\vec{n}}(t) \to \Lambda_{\vec{n}}^{-1}(t) U_{\mu,\vec{n}}(t) \Lambda_{\vec{n}+\hat{\mu}}(t). \tag{2.25}$$

Here $\Lambda_{\vec{n}}(t)$ and $\Lambda_{\vec{n}+\hat{\mu}}(t)$ are $N \times N$ unitary matrices that describe the local gauge transformation at points $\vec{n}$ and $\vec{n} + \hat{\mu}$, respectively. We introduce a gauge field $A_{\vec{n}}(t)$ that transforms as

$$A_{\vec{n}}(t) \to \Lambda_{\vec{n}}^{-1}(t) A_{\vec{n}}(t) \Lambda_{\vec{n}}(t) + i\Lambda_{\vec{n}}^{-1}(t) \partial_t \Lambda_{\vec{n}}(t). \tag{2.26}$$

The covariant derivative $D_t U_{\mu,\vec{n}}$, which transform as $D_t U_{\mu,\vec{n}} \to \Lambda_{\vec{n}}^{-1}(D_t U_{\mu,\vec{n}}) \Lambda_{\vec{n}+\hat{\mu}}$, is defined by

$$D_t U_{\mu,\vec{n}} = \partial_t U_{\mu,\vec{n}} - iA_{\vec{n}} U_{\mu,\vec{n}} + iU_{\mu,\vec{n}} A_{\vec{n}+\hat{\mu}}. \tag{2.27}$$

We will work in the strong coupling limit, by which we mean that the action contains only the electric term and not the magnetic term [4]. Hence the Euclidean action at temperature $T = \beta^{-1}$ is[5]

$$S = \frac{1}{2g^2} \sum_{\vec{n}} \int_0^\beta dt \mathrm{Tr} \left((D_t U_{\mu,\vec{n}}(t))(D_t U_{\mu,\vec{n}}(t))^\dagger \right). \tag{2.28}$$

The operator $\hat{\Omega}$ in (2.24) corresponds to the Polyakov loop in the path-integral formalism [20] (see Appendix 2.C). In the large-N limit, the distribution of the phases of the Polyakov loop is related to the symmetry of the typical quantum states dominating the partition function. The size of the deconfined sector M can be determined from the distribution of the phases [20], as explained in Sec. 2.4.

2.3.1.2 Eguchi-Kawai reduction

In the large-N limit, some features of the strong-coupling lattice gauge theory do not depend on the lattice size. Therefore, we can use the single-site model, which is called the Eguchi-Kawai model, to learn about the infinite-volume theory. We use conventions close to those in Ref. [32].

In the Eguchi-Kawai model, we have only one spatial point, so we drop $\vec{n}$ from the expressions for the strong-coupling lattice gauge theory. We will employ the gauge field A and unitary link variables U_μ, both of which are function of (Euclidean) time t. The gauge transformation is defined by

$$U_\mu \to \Lambda^{-1} U_\mu \Lambda \tag{2.29}$$

and

$$A \to \Lambda^{-1} A \Lambda + i \Lambda^{-1} \partial_t \Lambda. \tag{2.30}$$

The covariant derivative $D_t U_\mu$, which transform as $D_t U_\mu \to \Lambda^{-1}(D_t U_\mu)\Lambda$, is defined by

$$D_t U_\mu = \partial_t U_\mu - i[A, U_\mu]. \tag{2.31}$$

The Euclidean action is

$$S = \frac{1}{2g^2} \int_0^\beta dt \mathrm{Tr}(D_t U_\mu)^2. \tag{2.32}$$

---

[4] Empirically, many of the features of the lattice theory and confinement are the same in this strong coupling limit as the continuum theory, which justifies this approach.

[5] We use the same symbol S for the action and entropy, assuming the risk of confusion is low.

This action is invariant under the global (i.e. t-independent) $\mathrm{U}(1)^d$ center symmetry generated by

$$U_\mu \to e^{i\theta_\mu} U_\mu. \tag{2.33}$$

As long as this symmetry is unbroken, the Eguchi-Kawai model and infinite-volume lattice are equivalent, in the sense that various properly-normalized quantities agree. This is the so-called Eguchi-Kawai equivalence [33].[6]

In the strong coupling limit, the center symmetry is not spontaneously broken. To confirm this in our simulations as a sanity check, we calculated the Wilson loop wrapped on the spatial direction,

$$\frac{1}{N n_t d} \sum_{\mu,d} |\mathrm{Tr} U_{\mu,t}|. \tag{2.34}$$

If the center symmetry is not broken, this quantity should be zero up to $1/N$-suppressed terms. Our simulations affirmed this.

2.3.1.3 Gauge fixing

To make the separation to confined and deconfined phases easier, we take the static diagonal gauge (used in Ref. [21] for the same purpose),

$$A = \frac{1}{\beta} \cdot \mathrm{diag}(\alpha_1, \cdots, \alpha_N), \qquad -\pi < \alpha_i \leq \pi. \tag{2.35}$$

Associated with this gauge fixing, we add the Faddeev-Popov term

$$S_{\text{F.P.}} = -\sum_{i<j} 2 \log \left| \sin\left(\frac{\alpha_i - \alpha_j}{2}\right) \right| \tag{2.36}$$

to the action. This fixes $\mathrm{SU}(N)$ down to S_N. In Sec. 2.3.2, we explain how the confined and deconfined phases can be separated by fixing the residual S_N symmetry appropriately.

---

[6] In the original work by Eguchi and Kawai, all dimensions including time are reduced to a point. In most references, 'Eguchi-Kawai model' and 'Eguchi-Kawai equivalence' are used for the original setup.

2.3.1.4 Lattice regularization for the time dimension

Finally, we place this theory on the lattice in the time direction, too, with the below action:

$$S = \frac{N}{2a} \sum_{\mu=1}^{d} \sum_{t=1}^{n_t} \mathrm{Tr}\left(\mathbf{1}_N - U_{\mu,t} V U^{\dagger}_{\mu,t+1} V^{\dagger} \right) + \text{h.c.} + S_{\text{F.P.}}, \tag{2.37}$$

where $V = \mathrm{diag}(e^{i\alpha_1/n_t}, \cdots, e^{i\alpha_N/n_t})$. Here a is the lattice spacing, and $\beta = an_t$ is the inverse temperature, $\beta = T^{-1}$. This is the lattice action we use in our simulations. We will focus on $d = 3$. (We will make one more alteration by adding terms that constrain the Polyakov loop; see Sec. 2.3.2.)

2.3.2 Polyakov loop and constrained simulations

The Polyakov loop under the gauge fixing described above is $P = \frac{1}{N}\mathrm{Tr}\mathcal{P}$, where

$$\mathcal{P} = \mathrm{diag}(e^{i\alpha_1}, \cdots, e^{i\alpha_N}). \tag{2.38}$$

This is the quantity we will measure in the standard (unconstrained) simulation. In addition, we will run two kinds of constrained simulation that make use of this definition of the Polyakov loop.

2.3.2.1 The microcanonical ensemble and constrained simulation of the first kind

Via the Euclidean path integral, we can study the thermodynamic properties of a theory in the canonical ensemble, in which temperature T is the controlling parameter. If the confinement/deconfinement phase transition is of first order, however, it is more convenient to study the microcanonical ensemble, in which the energy E is the controlling parameter [34] .

In canonical thermodynamics, temperature is fixed and free energy is minimized. In microcanonical thermodynamics, energy is fixed and entropy is maximized. Usually, the partially-deconfined phase is unstable in the canonical ensemble, but can be stable in the microcanonical ensemble. If the spatial volume is large and the transition is of first order, the partially-deconfined phase will be unstable even in the microcanonical ensemble. Some part of space is occupied by the completely-deconfined phase while the rest is filled by the completely-confined phase, and the partially-deconfined phase is realized only at the interface of these two phases. When the spatial volume is small, such a spatial splitting can be avoided. This is sometime exemplified by gauge theories compactified on a sphere. For matrix models, including the Eguchi-Kawai model, spatial splitting cannot take place because ‘space’ is just a single point. The large-N volume independence connects the partially-deconfined phase in the Eguchi-Kawai, which is microcanonically stable, to the partially-deconfined phase of large-volume theory which is not stable even in microcanonical thermodynamics. The Polyakov loop P increases monotonically with E (Fig. 2.1). Hence, by fixing P we also fix E and can access the information of the microcanonical ensemble .

In general, using the Hamiltonian to define and fix the energy of quantum ensembles leads to difficulties and ambiguities due to quantum fluctuations. Here, however, we are in the large N limit, and can hence neglect such fluctuations. Instead, we have argued that, in the thermodynamic limit, fixing some macroscopic variable (in this case, the Polyakov loop) should amount to fixing the energy of the system (modulo difficulties that can follow from the energy being multi-valued with respect to this variable, which need not trouble us here due to the aforementioned monotonicity of the Polyakov loop). The work presented in this chapter does not depend on the precise meaning of energy in this system.

For the first constrained simulation, we add the following term to fix the Polyakov loop:

$$\Delta S = \begin{cases} \frac{g_{\rm P}}{2}\left(|P| - (P_{\rm fix} + \delta)\right)^2 & (|P| > P_{\rm fix} + \delta) \\ 0 & (P_{\rm fix} - \delta \le |P| \le P_{\rm fix} + \delta) \\ \frac{g_{\rm P}}{2}\left(|P| - (P_{\rm fix} - \delta)\right)^2 & (|P| < P_{\rm fix} - \delta) \end{cases} \tag{2.39}$$

We take $g_{\rm P}$ sufficiently large, so that the value of $|P|$ is fixed to a small window $P_{\rm fix} - \delta \le |P| \le P_{\rm fix} + \delta$. The purpose of this constraint is to probe the partially-confined saddle, which is otherwise unstable in the canonical ensemble. Essentially, we use the density-of-state method by fixing P, and hence E. The size of the deconfined sector $SU(M)$ will depend on our choice of $|P|$. The precise relation is explained in Sec. 2.4. Note that the constraint term (2.39) does not require a specific gauge choice (although we took the static diagonal gauge) and hence we can extract information from the microcanonical thermodynamics in a gauge-invariant manner.

2.3.2.2 Fixing of residual gauge symmetry and constrained simulation of the second kind

For the second kind of constrained simulation, we want to take this SU(M)-partially-deconfined phase and separate the confined and the deconfined degrees of freedom. As we will explain in Sec. 2.4, this can be achieved by, firstly, taking the static diagonal gauge, and then fixing the remaining S_N gauge redundancy down to $\mathrm{S}_M\times\mathrm{S}_{N-M}$ by reordering the eigenvalues such that the $N - M$ confined eigenvalues $\alpha_{M+1}, \cdots, \alpha_N$ constitute a uniform distribution. With this gauge fixing, we separate N^2 color degrees of freedom into the deconfined sector ($M \times M$ upper-left block) and the confined sector, as depicted in Fig. 2.2 [21].

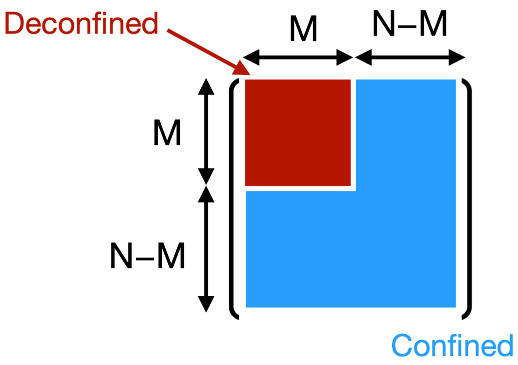

FIGURE 2.2: In the partially-deconfined phase (equivalently, partially-confined phase), color degrees of freedom split into the confined and deconfined sectors. In this paper, we use M to denote the size of the deconfined sector.

The most obvious approach to fixing S_N in this way is, after having performed the constrained simulation of first kind, to sort the resulting α's appropriately. Here, we take another approach which is technically simpler. We define

$$P_{\mathrm{dec}} = \frac{1}{M}\sum_{j=1}^{M} e^{i\alpha_j} \tag{2.40}$$

and

$$P_{\mathrm{con}} = \frac{1}{N-M}\sum_{j=M+1}^{N} e^{i\alpha_j}. \tag{2.41}$$

We want to fix P_{dec} and P_{con} to be P_{fix} and 0, respectively. Hence we will add

$$\Delta S_{\mathrm{dec}} = \begin{cases} \frac{g_P}{2}\left(|P_{\mathrm{dec}}| - (P_{\mathrm{fix}}+\delta)\right)^2 & (|P_{\mathrm{dec}}| > P_{\mathrm{fix}}+\delta) \\ 0 & (P_{\mathrm{fix}}-\delta \le |P_{\mathrm{dec}}| \le P_{\mathrm{fix}}+\delta) \\ \frac{g_P}{2}\left(|P_{\mathrm{dec}}| - (P_{\mathrm{fix}}-\delta)\right)^2 & (|P_{\mathrm{dec}}| < P_{\mathrm{fix}}-\delta) \end{cases} \tag{2.42}$$

and

$$\Delta S_{\mathrm{con}} = \begin{cases} \frac{g_P}{2}\left(|P_{\mathrm{con}}| - \delta\right)^2 & (|P_{\mathrm{con}}| > \delta) \\ 0 & (|P_{\mathrm{con}}| \le \delta), \end{cases} \tag{2.43}$$

taking g_P sufficiently large. Fixing $P = \frac{M}{N}P_{\mathrm{dec}} + \frac{N-M}{N}P_{\mathrm{con}}$ ensures we are on the partially-confined saddle, while fixing P_{con} to zero and P_{dec} to nonzero enforces the gauge fixing. Note that $P_{\mathrm{con}} = 0$ does not necessarily guarantee the uniform phase distribution in the confined sector unless the relationship between M and P_{fix} is set correctly following the procedures explained in Sec. 2.4. With the correct choice of M and P_{fix}, this constraint is equivalent to the constraint of the first kind plus permutations of phases. Some explicit checks are provided in Appendix 2.A.

2.4 The size of the deconfined sector in the partially-deconfined phase

In this section, we explain how we can separate confined and deconfined sectors. The starting point is the relationship between the operator formalism and the path-integral formalism discussed in Appendix 2.C.

The canonical partition function is written as (2.24). Let us write the expression again:

$$Z(T) = \frac{1}{\text{Vol}(G)} \int_G d\Omega \text{Tr}_{\mathcal{H}_{\text{ext}}} \left(\hat{\Omega} e^{-\hat{H}/T} \right) . \tag{2.44}$$

For the microcanonical ensemble, we can obtain a similar expression for the density of states by inserting the projection operator $\hat{\pi} = \frac{1}{\text{Vol}(G)} \int_G d\Omega \hat{\Omega}$. As explained in Appendix 2.C, this Ω corresponds to the Polyakov loop in the path-integral formalism [20].

An energy eigenstate $|E\rangle \in \mathcal{H}_{\text{ext}}$ contributes to the partition function as

$$\frac{e^{-E/T}}{\text{Vol}(G)} \int_G d\Omega \, \langle E| \, \hat{\Omega} \, |E\rangle \, . \tag{2.45}$$

The SU(M)-partially-deconfined states are characterized by invariance under SU$(N-M) \subset$ SU(N) [20]. Namely,

$$\hat{\Omega} \, |E\rangle = |E\rangle \ , \qquad \Omega \in \text{SU}(N-M) \subset \text{SU}(N) \tag{2.46}$$

for SU(M)-deconfined states. Specifically, by choosing the SU($N-M$) to correspond to the lower-right $(N-M) \times (N-M)$-block, we can choose the SU(M)-deconfined sector to be the upper-left $M \times M$-block as in Fig. 2.2. This choice of embedding of SU($N-M$) into SU(N) fixes SU(N) down to SU$(M) \times$ SU$(N-M)$. Ω takes the following form:

$$\Omega = \begin{pmatrix} \mathcal{P}_{\text{dec}} & 0 \\ 0 & \mathcal{P}_{\text{con}} \end{pmatrix} . \tag{2.47}$$

Here, $\mathcal{P}_{\text{con}}$ can be any element of SU($N-M$), and the generic phase distribution in this part is uniform in the limit of $N-M \to \infty$. The phases of $\mathcal{P}_{\text{dec}}$ and $\mathcal{P}_{\text{con}}$ are $\alpha_1, \cdots, \alpha_M$ and $\alpha_{M+1}, \cdots, \alpha_N$, respectively. From these, we can determine the distribution of the phases $\rho_{\text{dec}}(\alpha)$ and $\rho_{\text{con}}(\alpha)$. The latter is constant,

$$\rho_{\text{con}}(\alpha) = \frac{1}{2\pi}, \tag{2.48}$$

while the former is not and its smallest value is zero. For the model under consideration, we can fix center symmetry in such a way that

$$\rho_{\text{dec}}(\pm\pi) = 0. \tag{2.49}$$

The full distribution is

$$\begin{aligned}\rho(\alpha) &= \left(1 - \frac{M}{N}\right) \cdot \rho_{\text{con}}(\alpha) + \frac{M}{N} \cdot \rho_{\text{dec}}(\alpha) \\ &= \frac{1}{2\pi} \cdot \left(1 - \frac{M}{N}\right) + \frac{M}{N} \cdot \rho_{\text{dec}}(\alpha). \end{aligned} \tag{2.50}$$

See Fig. 2.3. Constrained simulation of the second kind enforces this separation by constraining P_{dec} to be the appropriate value for each M and setting P_{con} to be zero. In the large-N limit, this is equivalent to the constrained simulation of the first kind plus sorting of the phases, because the distribution becomes continuous and sample-by-sample fluctuation is suppressed.

For our numerical analysis via the Euclidean path integral, we prefer the Polyakov loop to have the form (2.47) at any Euclidean time t so that the SU(M)-deconfined sector is always in the upper-left $M \times M$-block. The static diagonal gauge is suitable for this purpose: because the gauge field A_t is constant, the Polyakov loop does not depend on Euclidean time t. (If A_t is not static, the Polyakov loop can depend on t, although the phases do not.) By appropriately fixing the residual S_N symmetry, we can have the same embedding visualized in Fig. 2.2 at any t.

The model under consideration has a first-order confinement/deconfinement transition around $T_c = \frac{1}{2\log(2d-1)}$ [32]. It is easy to see the two-state signal when N is not too large. When N is large, we can see one of two phases depending on the initial configuration for the simulation.

In order to determine the size of deconfined sector for each N, let us take P to be real and positive (i.e., $P = |P|$) configuration-by-configuration, by using the U(1) center symmetry. For each fixed value of P, we collect many samples to determine the distribution of the phases α, denoted by $\rho(\alpha)$. Because of (2.49) and (2.50), the minimum value of $\rho(\alpha)$ (which should be at $\alpha = \pm\pi$) is related to the size of the deconfined sector M by [20]

$$\rho(\pm\pi) = \frac{1}{2\pi}\left(1 - \frac{M}{N}\right).$$

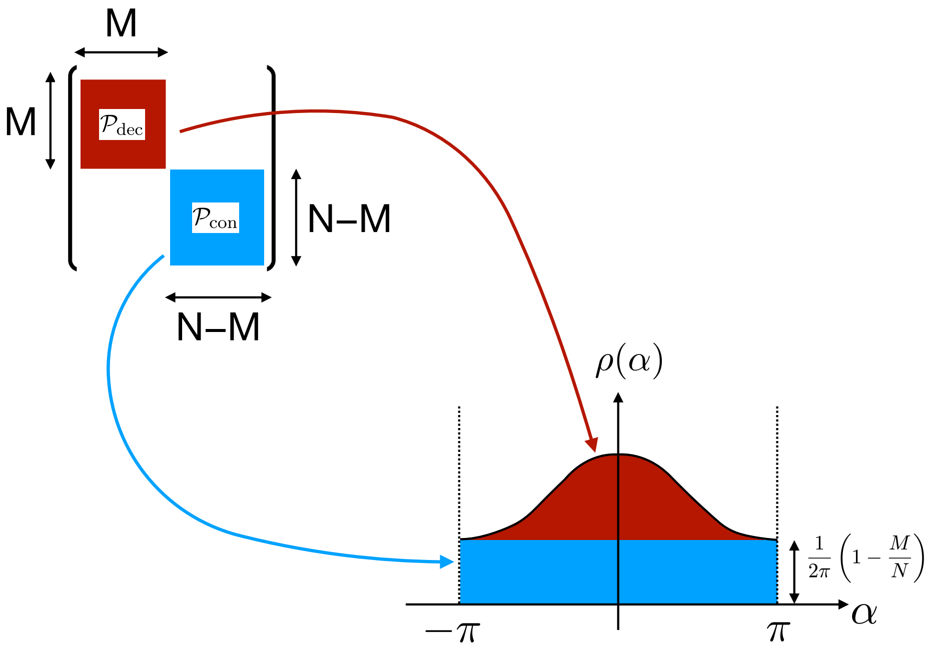

FIGURE 2.3: Sketches of the distribution of the phases of Polyakov loop in the partially-deconfined phase. Constant offset comes from the confined Polyakov loop $\mathcal{P}_{\rm con}$ while the non-uniform part comes from the deconfined Polyakov loop $\mathcal{P}_{\rm dec}$.

Note that this relation is precise in the large-N limit. After determining M for each P and N, we can perform the constrained simulation of the second kind with $P_{\rm dec} = \frac{N}{N-M}P(M)$.

The constrained-simulation methods that we use in this work are essentially the same as the one used in Ref. [21]. The only difference is that the models studied in Ref. [21] had the simpler relation $P = \frac{M}{2N}$, which does not hold in the model under consideration in this work. Therefore, we must determine the relationship between P and M by numerically determining $\rho(\pm\pi)$ in the constrained simulation of the first kind.

In general, $\rho(\alpha)$ can be written as

$$\rho(\alpha) = \frac{1}{2\pi} + \sum_{k=1}^{\infty} \tilde{\rho}_k \cos(k\alpha). \tag{2.51}$$

We determine the coefficients $\tilde{\rho}_k$ based on the simulation data, by using a Bayesian inference procedure with the likelihood of the data α given by Eq. (2.51).

Each of the n_{config} configurations contains N phases $\alpha_1, \cdots, \alpha_N$. At large N, we expect any two samples to have exactly the same distribution. More precisely, the difference between any two samples can be made arbitrarily small by taking N large enough. The distribution of the phases then cannot depend strongly on any precise details of the sample, such as the precise value of the other phases. Following, therefore, this usual assumption of the self-averaging nature of the system at large N, we suppose that each α_i is obtained with a probability $\rho(\alpha_i)$, regardless of the values of the other phases. Then, for a given model distribution $\rho(\alpha)$ specified by a fixed set of coefficients $\{\tilde{\rho}_k\}$, the probability that $\{\alpha\} = (\alpha_1, \cdots, \alpha_N)$ is obtained is simply the product of the individual phases probabilities:

$$\prod_{i=1}^{N} \rho(\alpha_i). \tag{2.52}$$

Taking into account all configurations (assumed to be independent), we obtain the likelihood function for the data $\{\alpha\}$, given the parameters $\{\tilde{\rho}_k\}$:

$$L(\{\alpha^{(1)}\}, \cdots, \{\alpha^{(n_{\text{config}})}\} | \{\tilde{\rho}_k\}) = \prod_{n=1}^{n_{\text{config}}} \prod_{i=1}^{N} \rho(\alpha_i^{(n)}). \tag{2.53}$$

We use Bayes rule to compute the posterior distribution over the parameters $\{\tilde{\rho}_k\}$ given a set of observations corresponding to the data $\{\alpha^{(1)}\}, \cdots, \{\alpha^{(n_{\text{config}})}\}$. In practice, we need to truncate the Fourier expansion in Eq. (2.51) at some order Λ, setting $\tilde{\rho}_k = 0$ for $k > \Lambda$, and we choose a uniform prior distribution centered around zero and with bounds ± 0.1. At fixed order Λ we compute the posterior over exactly Λ parameters by using a dynamical Nested Sampling algorithm [35; 36] implemented in the python library `ultranest` [37].

Ultimately, we do not care about the values of the model parameters $\{\tilde{\rho}_k\}$, but we want to use their posterior distribution to sample all models $\rho(\alpha)$ that are compatible with the data. With these samples we have direct access to the expectation value of $\rho(\pi) = \frac{1}{2\pi}\left(1 - \frac{M}{N}\right)$, hence to the expectation value of M and its corresponding error bar, given by the 16% and 84% quantiles of the posterior predictive distribution.

We tried a few different values of the Fourier expansion order Λ and found that results are consistent within error bars for $\Lambda \in \{2, 3, 4, 5\}$. For our analysis we choose to consider $\Lambda = 3$ out of simplicity.

The values of M for $T = 0.29$ obtained this way are summarized in Table 2.1. For each fixed N and P, there is a weak dependence on the lattice size n_t.

In this work, we are trying to study the partially-deconfined saddle. The temperature of the saddle changes slightly with P, while we varied P at fixed T. We are implicitly

P	N	n_t	M
0.2	16	16	$7.44^{+0.12}_{-0.11}$
		24	$7.62^{+0.15}_{-0.16}$
		32	$7.56^{+0.11}_{-0.12}$
	24	16	$10.99^{+0.18}_{-0.18}$
		24	$11.13^{+0.19}_{-0.19}$
		32	$11.12^{+0.22}_{-0.22}$
	32	16	$14.51^{+0.21}_{-0.19}$
		24	$14.77^{+0.22}_{-0.22}$
		32	$14.91^{+0.21}_{-0.23}$
	64	16	$28.70^{+0.31}_{-0.31}$
		24	$29.04^{+0.31}_{-0.34}$
		32	$29.06^{+0.29}_{-0.29}$
	96	16	$42.78^{+0.40}_{-0.38}$
		24	$43.19^{+0.48}_{-0.49}$
0.25	16	16	$10.06^{+0.09}_{-0.10}$
		24	$9.99^{+0.13}_{-0.13}$
		32	$10.18^{+0.14}_{-0.15}$
	24	16	$14.85^{+0.17}_{-0.16}$
		24	$14.92^{+0.17}_{-0.17}$
		32	$15.18^{+0.11}_{-0.12}$
	32	16	$19.52^{+0.18}_{-0.15}$
		24	$19.81^{+0.22}_{-0.23}$
		32	$19.92^{+0.19}_{-0.18}$
	64	16	$38.19^{+0.30}_{-0.28}$
		24	$38.77^{+0.37}_{-0.36}$
		32	$39.11^{+0.33}_{-0.34}$
	96	16	$56.50^{+0.35}_{-0.34}$
		24	$57.43^{+0.42}_{-0.40}$

TABLE 2.1: P vs M at $T = 0.29$. The central value of M is the median of the posterior predictive distribution. The lower and upper bound are the 16% and 84% quantiles, respectively.

P	N	M at $T = 0.29$	M at $T = 0.30$	M at $T = 0.31$
0.2	16	$7.62^{+0.15}_{-0.16}$	$7.75^{+0.15}_{-0.15}$	$7.83^{+0.16}_{-0.16}$
	24	$11.13^{+0.19}_{-0.19}$	$11.31^{+0.19}_{-0.20}$	$11.68^{+0.19}_{-0.20}$
	32	$14.77^{+0.22}_{-0.22}$	$15.03^{+0.20}_{-0.20}$	$15.23^{+0.22}_{-0.22}$
0.25	16	$9.99^{+0.13}_{-0.13}$	$10.36^{+0.15}_{-0.14}$	$10.59^{+0.14}_{-0.14}$
	24	$14.92^{+0.17}_{-0.17}$	$15.61^{+0.17}_{-0.16}$	$15.95^{+0.16}_{-0.17}$
	32	$19.81^{+0.22}_{-0.23}$	$20.50^{+0.18}_{-0.16}$	$21.07^{+0.20}_{-0.19}$

TABLE 2.2: P vs M at three different temperatures for $n_t = 24$. The central value of M is the median of the posterior predictive distribution. The lower and upper bound are the 16% and 84% quantiles, respectively.

assuming that a slight difference of temperature does not have a significant effect if P is fixed. The validity of this assumption requires that the saddle is insensitive with respect to the temperature. To test this, we looked at the value of M for different values of temperature at fixed P. See Table 2.2 for the relation between P and M for $T = 0.29, 0.30$ and $T = 0.31$. The dependence on temperature is rather mild (mostly compatible within error bars). Hence, we assume other quantities such as the string tension are not sensitive to the small change of temperature. We leave an explicit confirmation of this assumption as a future work.

2.5 Flux tube in partially-deconfined phase

2.5.1 Theoretical expectations

In this section, we demonstrate (2.2) and (2.3) using Eguchi-Kawai equivalence. The Eguchi-Kawai model is easier for numerical purposes, but the lack of the spatial dimensions forces us to rewrite the two-point functions on the left-hand side of (2.2) and (2.3) to slightly different forms. We define the temporal Wilson loop with temporal extent $0 < t_0 \leq \beta$ and spatial extent L in the lattice unit, as shown in See Fig. 2.4. When $t_0 = \beta$ (Fig. 2.5), it is equivalent to the two-point function of the Polyakov loop, as we will see shortly. Thanks to Eguchi-Kawai equivalence, we can calculate this Wilson loop by using the Eguchi-Kawai model.

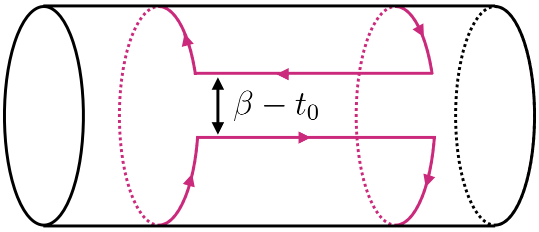

FIGURE 2.4: The temporal Wilson loop $W_\mu(L, t_0)$ considered in this work. A spatial Wilson line with length L is created, goes through Euclidean time evolution around the temporal circle, and is then annihilated. By exchanging the role of time and space, we can interpret this also as the propagation of an open string along the compactified space over Euclidean time L. We will focus on the case of $t_0 = \beta$.

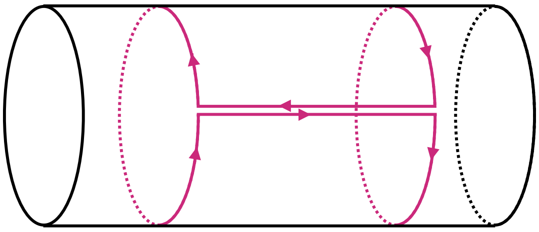

FIGURE 2.5: Temporal Wilson loop $W_\mu(L,\beta)$. Such a Wilson loop is equivalent to the two-point function of Polyakov loops.

Let us elucidate the physical meaning of this loop. Let $F^\dagger$ be a creation operator for two heavy probe particles ϕ and χ connected by a Wilson line [3],

$$\hat{F}^\dagger_\mu(\vec{x},L) = \hat{\phi}^\dagger_a(\vec{x})\hat{U}_{\mu,ab}(\vec{x},\vec{x}+L\hat{\mu})\hat{\chi}^\dagger_b(\vec{x}+L\hat{\mu}). \tag{2.54}$$

Then $W_\mu(L,t_0)$ is

$$\begin{aligned} W_\mu(L,t_0) &= \frac{1}{Z(\beta)}\sum_i \langle E_i| e^{-(\beta-t_0)\hat{H}}\hat{F}_\mu e^{-t_0\hat{H}}\hat{F}^\dagger_\mu |E_i\rangle \\ &= \frac{1}{Z(\beta)}\sum_i e^{-\beta E_i}\langle E_i|\hat{F}_\mu e^{-t_0(\hat{H}-E_i)}\hat{F}^\dagger_\mu |E_i\rangle\,. \end{aligned} \tag{2.55}$$

Note that the contribution from the mass of the probes is subtracted.

Let us write $F^\dagger_\mu |E_i\rangle$ as a linear combination of the energy eigenstates,

$$\hat{F}^\dagger_\mu |E_i\rangle = \sum_j c_{ij} |E_j\rangle\,. \tag{2.56}$$

Then,

$$W_\mu(L,t_0) = \frac{1}{Z(\beta)}\sum_{i,j} e^{-\beta E_i}|c_{ij}|^2 e^{-t_0(E_j-E_i)}. \tag{2.57}$$

Suppose the sum over all the states can be replaced by a typical energy eigenstate $|E_i\rangle$. Then,

$$W_\mu(L, t_0) \sim \sum_j |c_{ij}|^2 e^{-t_0(E_j - E_i)}. \tag{2.58}$$

If the minimum excitation above E_i increases linearly with L, we have $W_\mu(L, t_0) \sim e^{-cL}$, with some constant c. We expect this to happen in the confined sector, i.e., we expect $W_{\mu,\mathrm{con}}(L, t_0) \sim e^{-cL}$. If only the low-energy states contribute, we should have $c \propto t_0\sigma$, where σ is called the string tension. In the Eguchi-Kawai model, by using the Polyakov line

$$\mathcal{P} \equiv \mathrm{diag}(e^{i\alpha_1}, \cdots, e^{i\alpha_N}), \tag{2.59}$$

we can write $W_\mu(L, \beta)$ as

$$W_\mu(L, \beta) = \left\langle \mathrm{Tr}\left(\mathcal{P}(U_\mu(t))^L \mathcal{P}^\dagger (U_\mu(t)^\dagger)^L\right)\right\rangle. \tag{2.60}$$

We can see the exponential decay of $W_\mu(L, \beta)$ in Fig. 2.6 for the completely-confined case.

$\frac{1}{N} W_\mu(L, \beta)$ is equivalent to the two-point function of Polyakov loops, i.e.,

$$\frac{1}{N} W_\mu(L, \beta) = \langle \mathrm{Tr}\mathcal{P}(\vec{x}) \cdot \mathrm{Tr}\mathcal{P}(\vec{x} + L\hat{\mu})\rangle. \tag{2.61}$$

Here $\hat{\mu}$ is the unit vector along the μ-th dimension. One way to see this is to exchange the roles of temporal and spatial directions. Namely, we interpret the μ-direction to be imaginary time. $W_\mu(L, t_0)$ is interpreted as the propagation along the imaginary time direction of an open string with length t_0 stretched along the spatial circle with circumference β. When $t_0 = \beta$ and the color factors (Chan-Paton factors) at the endpoints of the open string are summed over, we get a closed string, or equivalently, the Polyakov loop. The $1/N$ factor arises between (2.60) and (2.61) because of the insertion of the additional trace on the right hand side of (2.61) as we ‘split the string’ into two independent strings and are free to take an independent trace over each.

To see the properties of the confined and deconfined sectors separately, we define the Polyakov line in the deconfined sector,

$$\mathcal{P}_{\mathrm{dec}} \equiv \mathrm{diag}(e^{i\alpha_1}, \cdots, e^{i\alpha_M}, 0, \cdots, 0), \tag{2.62}$$

and that in the confined sector,

$$\mathcal{P}_{\mathrm{con}} \equiv \mathrm{diag}(0, \cdots, 0, e^{i\alpha_{M+1}}, \cdots, e^{i\alpha_N}). \tag{2.63}$$

By using these, we can define the counterparts of two-point functions in the lattice gauge theory $\langle\mathcal{P}_{\rm dec}(\vec{x})\mathcal{P}_{\rm dec}(\vec{y})\rangle$, $\langle\mathcal{P}_{\rm con}(\vec{x})\mathcal{P}_{\rm con}(\vec{y})\rangle$ and $\langle\mathcal{P}_{\rm con}(\vec{x})\mathcal{P}_{\rm dec}(\vec{y})\rangle$ as

$$W_{\mu,{\rm dec}}(L,\beta)\equiv\left\langle{\rm Tr}\left(\mathcal{P}_{\rm dec}(U_\mu(t))^L\mathcal{P}^\dagger_{\rm dec}(U_\mu(t)^\dagger)^L\right)\right\rangle, \tag{2.64}$$

$$W_{\mu,{\rm con}}(L,\beta)\equiv\left\langle{\rm Tr}\left(\mathcal{P}_{\rm con}(U_\mu(t))^L\mathcal{P}^\dagger_{\rm con}(U_\mu(t)^\dagger)^L\right)\right\rangle. \tag{2.65}$$

and

$$W_{\mu,{\rm mix}}(L,\beta)\equiv\left\langle{\rm Tr}\left(\mathcal{P}_{\rm con}(U_\mu(t))^L\mathcal{P}^\dagger_{\rm dec}(U_\mu(t)^\dagger)^L\right)\right\rangle. \tag{2.66}$$

We can also define $W_{\mu,{\rm dec}}(L,t_0)$, $W_{\mu,{\rm con}}(L,t_0)$ and $W_{\mu,{\rm mix}}(L,t_0)$ in a similar manner.

Because $\frac{1}{N}W_\mu(L,\beta)$ is equivalent to the two-point function of Polyakov loops, and because the connected part of the two-point function is suppressed at long distance ($L\to\infty$), we will have

$$\lim_{L\to\infty}\frac{1}{N}W_\mu(L,\beta)=|\langle P\rangle|^2. \tag{2.67}$$

We expect $W_{\mu,{\rm con}}(L,\beta)$ and $W_{\mu,{\rm mix}}(L,\beta)$ to vanish at large L, and hence we expect

$$\lim_{L\to\infty}\frac{1}{N}W_{\mu,{\rm dec}}(L,\beta)=|\langle P\rangle|^2. \tag{2.68}$$

We expect that $W_{\mu,{\rm con}}(L,\beta)$ and $W_{\mu,{\rm mix}}(L,\beta)$ vanish in a very specific manner. We expect the exponential decay at long distance with the same string tension as the confined sector, i.e., we expect

$$\frac{1}{N}W_{\mu,{\rm con}}(L,\beta)=C_{\rm con}(N,M)\cdot\exp\left(-\sigma L\beta\right) \tag{2.69}$$

and

$$\frac{1}{N}W_{\mu,{\rm mix}}(L,\beta)=C_{\rm mix}(N,M)\cdot\exp\left(-\sigma L\beta\right)\ . \tag{2.70}$$

To obtain (2.70), we can interpret the μ-direction to be the Euclidean time. Then, closed string in the confined sector is created by $\mathcal{P}_{\rm con}$ and propagate distance L. Then it is annihilated by $\mathcal{P}_{\rm dec}$. It is natural to expect that $\mathcal{P}_{\rm dec}$ contains a small but nonzero contribution from the lightest mode in $\mathcal{P}_{\rm con}$ because there is no reason that it is forbidden, and hence, we expect to see the propagation of the closed string in the confined sector that is associated with the decay factor $\exp\left(-\sigma L\beta\right)$.

In the strong-coupling lattice gauge theory, with our normalization,

$$\sigma = \frac{1}{2}. \tag{2.71}$$

Note that the large-N limit should be taken first. Approximately, we expect $C_{\rm con}(N,M) \simeq \left(1 - \frac{M}{N}\right)^2$ and $C_{\rm mix}(N,M) \simeq \frac{M}{N}\left(1 - \frac{M}{N}\right)$. To give a stronger constraint on $C_{\rm con}(N,M)$ and $C_{\rm mix}(N,M)$, let us assume that these factors do not depend on the size of the loops along the temporal direction, i.e.,

$$\frac{1}{N} W_{\mu,\rm con}(L,t_0) = C_{\rm con}(N,M) \cdot \exp\left(-\sigma L t_0\right) \tag{2.72}$$

and

$$\frac{1}{N} W_{\mu,\rm mix}(L,t_0) = C_{\rm mix}(N,M) \cdot \exp\left(-\sigma L t_0\right) \ . \tag{2.73}$$

By definition, the sum of $W_{\mu,\rm con}(L,t_0=0)$ and $W_{\mu,\rm mix}(L,t_0=0)$ can be written as

$$\begin{aligned} W_{\mu,\rm con}(L,t_0=0) + W_{\mu,\rm mix}(L,t_0=0) &= \left\langle \mathrm{Tr}\left(\Pi_{\rm con}(U_\mu(t))^L \mathbf{1}_N (U_\mu(t)^\dagger)^L\right)\right\rangle \\ &= \left\langle \mathrm{Tr}\left(\Pi_{\rm con}\right)\right\rangle \\ &= N - M, \end{aligned} \tag{2.74}$$

where $\Pi_{\rm con} = \mathrm{diag}(\underbrace{0,\cdots,0}_{M},\underbrace{1,\cdots,1}_{N-M})$. Therefore,

$$C_{\rm con}(N,M) + C_{\rm mix}(N,M) = 1 - \frac{M}{N}\ , \tag{2.75}$$

if $C_{\rm con}(N,M)$ and $C_{\rm mix}(N,M)$ do not depend on t_0. In Sec. 2.5.2, we will confirm this relation numerically.

2.5.2 Simulation results

In this subsection, we will show the simulation results. The expectation values of $W(L)$ used for the analyses are shown in Tables 2.9, 2.10, 2.11, and 2.12.

Completely-confined phase

Let us start with the unconstrained simulation at $T = 0.25$, where temperature is sufficiently low such that the completely-confined phase is obtained in the large-N limit. We took the lattice size $n_t = 24$, and studied $N = 16, 24, 32, 48, 64, 96$ and 128. We took the average over all spatial dimensions $\mu = 1,2,3$ and studied $W = \frac{1}{3}\sum_{\mu=1}^{3} W_\mu$. As we can see in the first panel of Fig. 2.6, the N-dependence of

$\frac{1}{N}W(L)$ can be fitted well to the fitting ansatz $\frac{1}{N}W(L) = a(L) + \frac{b(L)}{N^2}$. We used $N \geq 24$ to perform the extrapolation to $N = \infty$. We could achieve reliable extrapolations at $L = 1, 2, 3$ and 4. For $L \geq 5$, larger N are needed for reliable extrapolations.

Because the Eguchi-Kawai reduction is valid at $N = \infty$, we can compare the large-N extrapolated values with the theoretical expectation (2.69) and $\sigma = \frac{1}{2}$, $\beta = \frac{1}{T} = 4$, and $M = 0$, i.e., $\frac{1}{N}W(L, \beta = 4) = \exp(-2L)$. Note that $C_{\text{con}}(N, M = 0) = 1$, because of (2.75) and $C_{\text{mix}}(N, M = 0) = 0$. In the second panel of Fig. 2.6, $\frac{1}{N}W(L)$ for each N and the large-N extrapolation are shown for $L = 1, 2, 3, 4, 5$. By fitting the large-N extrapolated results at $1 \leq L \leq 4$ to the ansatz $a(L) = \exp(-cL + d)$, we obtained $c = 2.0887(30)$ and $d = 0.0011(31)$. Small deviations from $\exp(-2L)$ would be finite-n_t effects.

We can also probe the confined phase at $T = 0.29$ by constraining P to its confined value, $P = 0$, as shown in Fig. 2.7. This is more comparable to the constrained simulation, described below, that we perform at $T = 0.29$ to probe the partial phase, but is here applied to examining the familiar completely-confined phase with its well-established theory and predictions.

For this, we took the large-N and continuum ($n_t \to \infty$) limit at each L by performing a weighted least-squares regression with the ansatz $\frac{1}{N}W_{\text{con}}(L; n_t) = a_{\text{con}}(L) + \frac{b_{1,\text{con}}(L)}{N^2} + \frac{b_{2,\text{con}}(L)}{n_t} + \frac{b_{3,\text{con}}(L)}{n_t N^2}$. The weights were derived from the error bars of the Monte-Carlo observables, where the integrated autocorrelation time measured by the Madras-Sokal algorithm [38] is taken into account. Then $a_{\text{con}}(L)$ gives the extrapolated value in the $N, n_t \to \infty$ limit. Fitting the ansatz $a_{\text{con}}(L) = \exp(-c_{\text{con}}L + d_{\text{con}})$, we obtain $c_{\text{con}} = 1.738(29)$ and $d_{\text{con}} = 0.022(31)$. This is consistent with the theoretical expectation $e^{\sigma\beta L} = e^{-\frac{1}{2\times 0.29}L} \simeq e^{-1.724L}$.

Partially-deconfined phase

In Fig. 2.8, we show W_{con} at $T = 0.29$, $P = 0.2$ and $P = 0.25$, which corresponds to $\frac{M}{N} \simeq 0.50$ and $\frac{M}{N} \simeq 0.61$. We performed a two-dimensional weighted least-squares regression to take the large N and continuum ($n_t \to \infty$) limits simultaneously. Note that it is more difficult to take the large-N limit at larger L, and/or when either M or $N - M$ is small.

Motivated by (2.69) with $C_{\text{con}}(N, M) \simeq \left(1 - \frac{M}{N}\right)^2$, we normalized the loop as $\frac{1}{N}W_{\text{con}}(L) \times \left(1 - \frac{M}{N}\right)^{-2}$. We will compare the loop normalized this way to $e^{\sigma\beta L} = e^{-\frac{1}{2\times 0.29}L} \simeq e^{-1.724L}$.

The large-N and continuum extrapolations were estimated at each L by performing a weighted least-squares regression with the ansatz

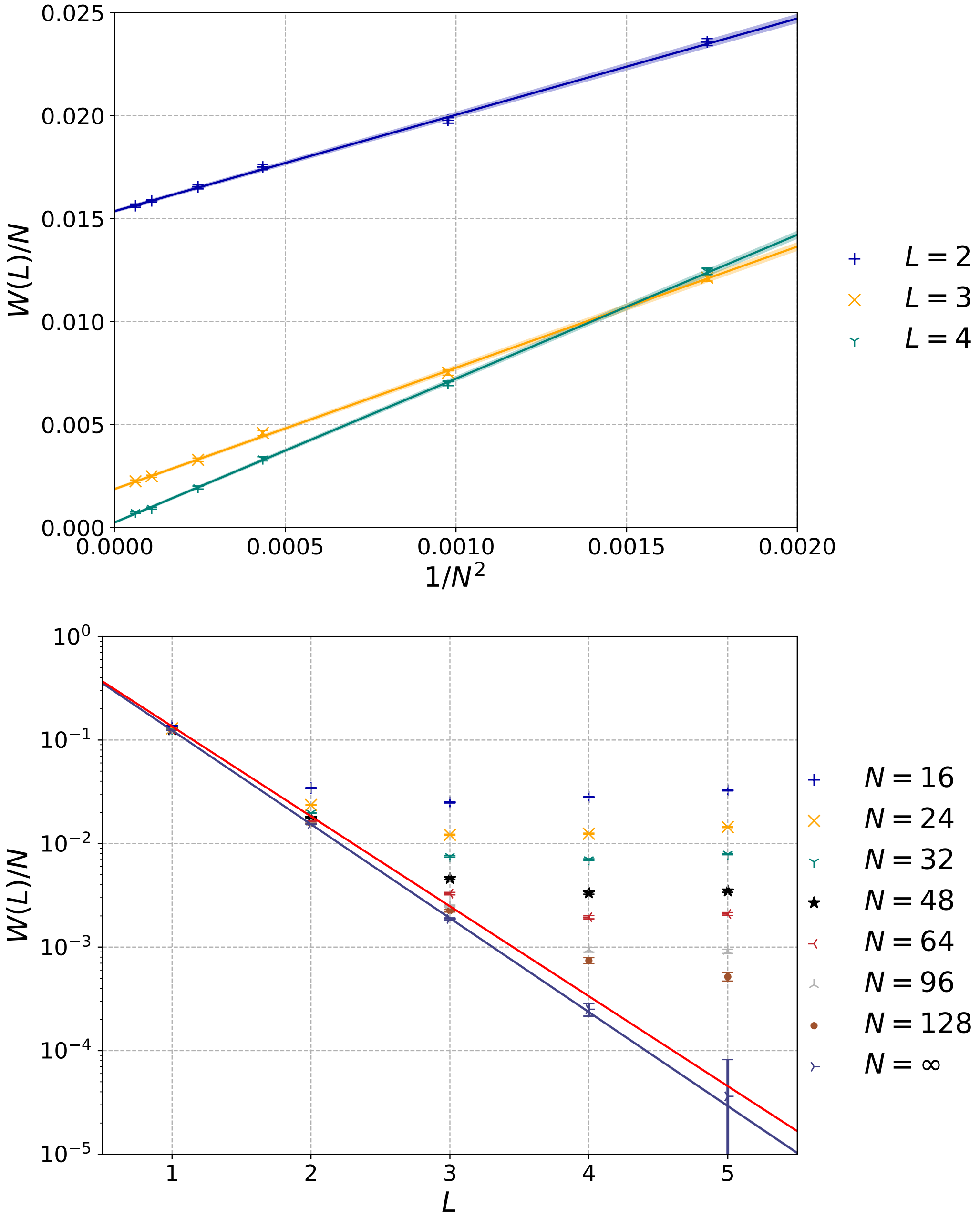

FIGURE 2.6: $T = 0.25$ and $n_t = 24$, without constraint. Temperature is sufficiently low such that the completely-confined phase is realized automatically. For the extrapolation to $N = \infty$, we used data points at $N = 24, 32, 48, 64, 96, 128$ for $L = 1, 2, 3, 4$ and $N = 48, 64, 96, 128$ for $L = 5$. We used the fitting ansatz $\frac{1}{N}W(L) = a(L) + \frac{b(L)}{N^2}$. By fitting the large-$N$ extrapolated results at $1 \leq L \leq 4$ by the ansatz $a(L) = \exp(-cL + d)$, we obtained $c = 2.0887(30)$ and $d = 0.0011(31)$. This fit is shown by the blue line. The red line is $\exp(-2L)$, which is the theoretical expectation for long distance (large L) and continuum limit ($n_t = \infty$). A small disagreement would be finite-n_t effects.

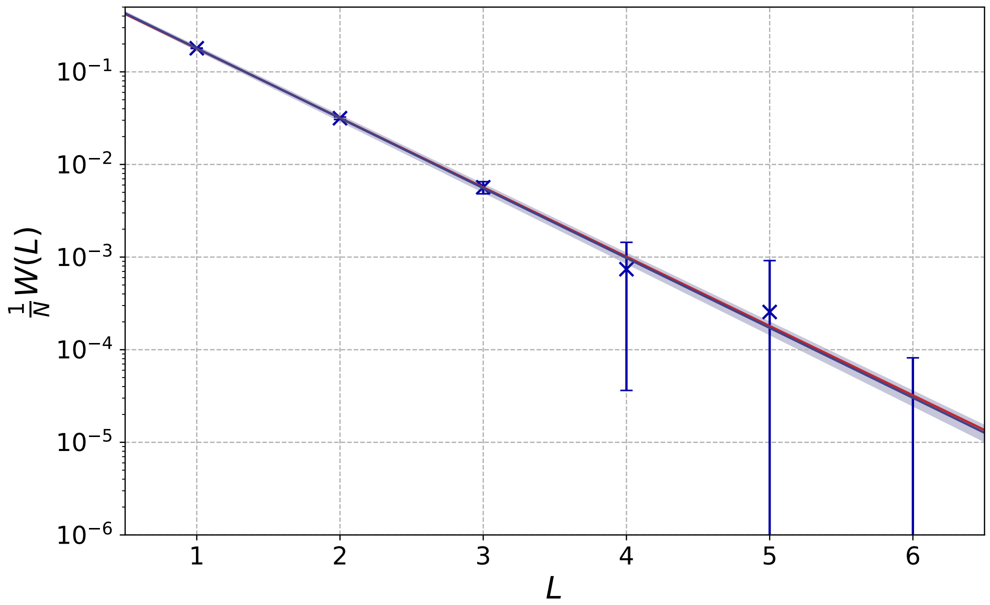

FIGURE 2.7: $T = 0.29$ with the constraint $P = 0$, allowing us to probe the completely-confined phase near the transition. We have extrapolated to the large N limit using $N = 7, 10, 16, 24, 32$, and to the continuum limit using $n_t = 16, 24, 32$ for each N, using the 2D interpolation $\frac{1}{N}W_{\text{con}}(L) = a_{\text{con}}(L) + \frac{b_{1,\text{con}}(L)}{N^2} + \frac{b_{2,\text{con}}(L)}{n_t} + \frac{b_{3,\text{con}}(L)}{n_t N^2}$. We fitted these interpolated values $a_{\text{con}}(L)$ for $1 \leq L \leq 4$ to the ansatz $a_{\text{con}}(L) = \exp(-c_{\text{con}}L + d_{\text{con}})$, yielding $c_{\text{con}} = 1.738(29)$ and $d_{\text{con}} = 0.022(31)$. The fit is shown along with error bounds by the blue line. The theoretical prediction ($c_{\text{con}} = 1.724$, and $d_{\text{con}} = 0$ for $M = 0$) is given by the red line, which is mostly obscured by the fit.

$\frac{1}{N}W_{\text{con}}(L) \times \left(1 - \frac{M}{N}\right)^{-2} = a_{\text{con}}(L) + \frac{b_{1,\text{con}}(L)}{N(N-M)} + \frac{b_{2,\text{con}}(L)}{n_t} + \frac{b_{3,\text{con}}(L)}{n_t N(N-M)}$ [7]. Then $a_{\text{con}}(L)$ gives the extrapolated value of the Wilson loop in the $N, n_t \to \infty$ limit.

We plotted $a_{\text{con}}(L)$ in Fig. 2.8. We can perform one final linear regression with the ansatz $\log(a_{\text{con}}(L)) = -c_{\text{con}}L + d_{\text{con}}$ to check the area law. Fitting to $L \leq 4$, we obtain $c_{\text{con}} = 1.729(17)$ and $c_{\text{con}} = 1.724(23)$ for $P = 0.2$ and $P = 0.25$, respectively, in good agreement with the theoretical expectation, 1.724. The values of d were $d_{\text{con}} = 0.086(20)$ and $d_{\text{con}} = 0.127(28)$. That they are not zero is not a problem; what we expect instead is (2.75), which we will confirm shortly.

The mixed-correlator $W_{\text{mix}}(L)$ is shown in Fig. 2.9. Motivated by (2.70) with $C_{\text{mix}}(N, M) \simeq \frac{M}{N}\left(1 - \frac{M}{N}\right)$, we normalized the loop as $\frac{1}{N}W_{\text{mix}}(L) \times \left[\frac{M}{N}\left(1 - \frac{M}{N}\right)\right]^{-1}$. We used a similar process as described for W_{con} above, but using this different normalisation. We find $c_{\text{mix}} = 1.731(21)$ and $c_{\text{mix}} = 1.708(20)$ for $P = 0.2$ and $P = 0.25$, respectively, in good agreement with the theoretical expectation, 1.724. The

---

[7] In the completely-confined phase, we used N^2 in the denominators of the regression. For the partial phase, we used $N(N - M)$ instead. We found that our data was much closer to being linear in $\frac{1}{N(N-M)}$, both for data points taken at the same P but which differed slightly in M/N, and also when combining points at different P and thus very different values of M/N.

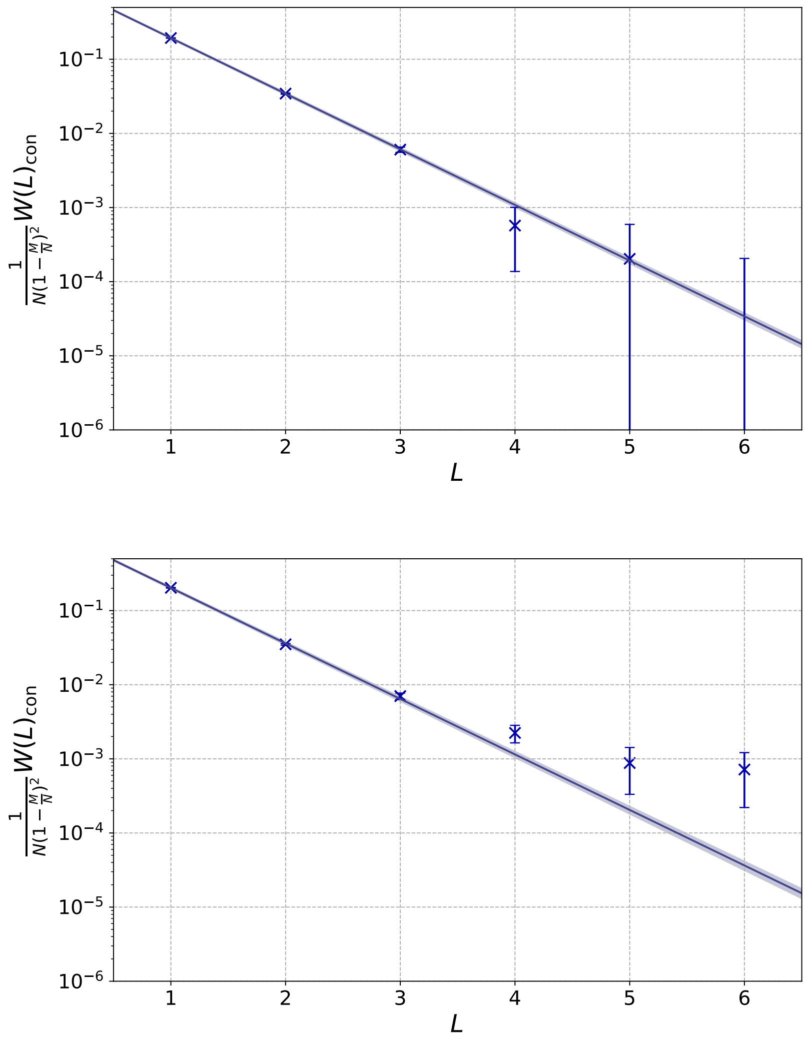

FIGURE 2.8: Confined subsector Wilson loop, $W_{\rm con}$, at $T = 0.29$, for $P = 0.2$ and $P = 0.25$, respectively. We have extrapolated to the large N limit using $N = 24, 32, 64$, and to the continuum limit using $n_t = 16, 24, 32$ for each N, using the 2D interpolation $\frac{1}{N(1-\frac{M}{N})^2}W_{\rm con}(L) = \gamma_{\rm con}(L) + \frac{\beta_1}{N^2} + \frac{\beta_2}{n_t} + \frac{\beta_2}{n_t N^2}$. We fitted these interpolated values $\gamma_{\rm con}(L)$ for $1 \leq L \leq 4$ to the ansatz $\gamma_{\rm con}(L) = \exp(-c_{\rm con}L + d_{\rm con})$ and obtained $c_{\rm con} = 1.729(17)$ and $c_{\rm con} = 1.724(23)$ for $P = 0.2$ and $P = 0.25$, respectively. The fit is shown along with error bounds by the blue line.

values of d_{mix} were $d_{\text{mix}} = -0.076(24)$ and $d_{\text{mix}} = -0.109(23)$. Again, that they are not zero is not a problem; we will confirm (2.75) next.

In Fig. 2.10, $\frac{W_{\text{con}}+W_{\text{mix}}}{N-M}$ is plotted. It is consistent with $e^{-1.724L}$ including the overall normalization factor. We obtained $c = 1.733(19)$ and $d = 0.021(22)$ for $P = 0.20$, and $c = 1.718(18)$ and $d = -0.006(21)$ for $P = 0.25$. Now d is consistent with zero.

To contrast with all of these, we also plotted the deconfined-correlator, W_{dec}, in Fig. 2.11. Here, there is a total absence of any confining behaviour, in easy agreement with our conjecture.

We observe that the confined-sector Wilson loop values for $L \geq 4$ in the lower panel of Fig. 2.8 all lie above the fitted line, indicating the presence of systematic errors. These errors likely stem from imprecision in the separation between the confined and deconfined sectors when constructing the confined-sector Wilson loop. This is a difficulty we anticipate at finite N. Consequently, we see behaviour more redolent of the deconfined sector at larger values of L.

In summary, we have observed that numerical data is consistent with nontrivial theoretical predictions made about partial confinement, i.e., (2.69), (2.70), and (2.75). In particular, the agreement between $W_{\text{con}} + W_{\text{mix}}$ and the theoretical prediction could be confirmed without even performing a fit, as shown in Fig. 2.10. Although our data is not good enough to determine the values of Wilson loops at $L \geq 5$ at this moment, in principle we can study arbitrary large L by taking N larger and collecting sufficiently many statistics in Monte Carlo simulations.

Comments on temperature dependence

In the model under consideration, the partially-deconfined saddle is the maximum of the free energy. The distribution of Polyakov line phases at the saddle changes with temperature. Therefore, strictly speaking, we need to study multiple values of T, choosing the value of P exactly on top of the saddle. However, we explicitly confirmed that the expected behaviors (2.69), (2.70), and (2.75) at $T = 0.29$ at $P = 0$, 0.20 and 0.25, which suggests that this relation holds near the critical point regardless of the value of P, and hence also on the partially-deconfined saddle. It is straightforward to perform the more complete analyses if more computational resources are available. We will leave it for future work. See also comments at the end of Sec. 2.4.

2.6 Conclusion and discussion

In this chapter, we presented evidence for the formation of a flux tube and linear confinement potential in the confined sector of the partially-deconfined saddle of pure

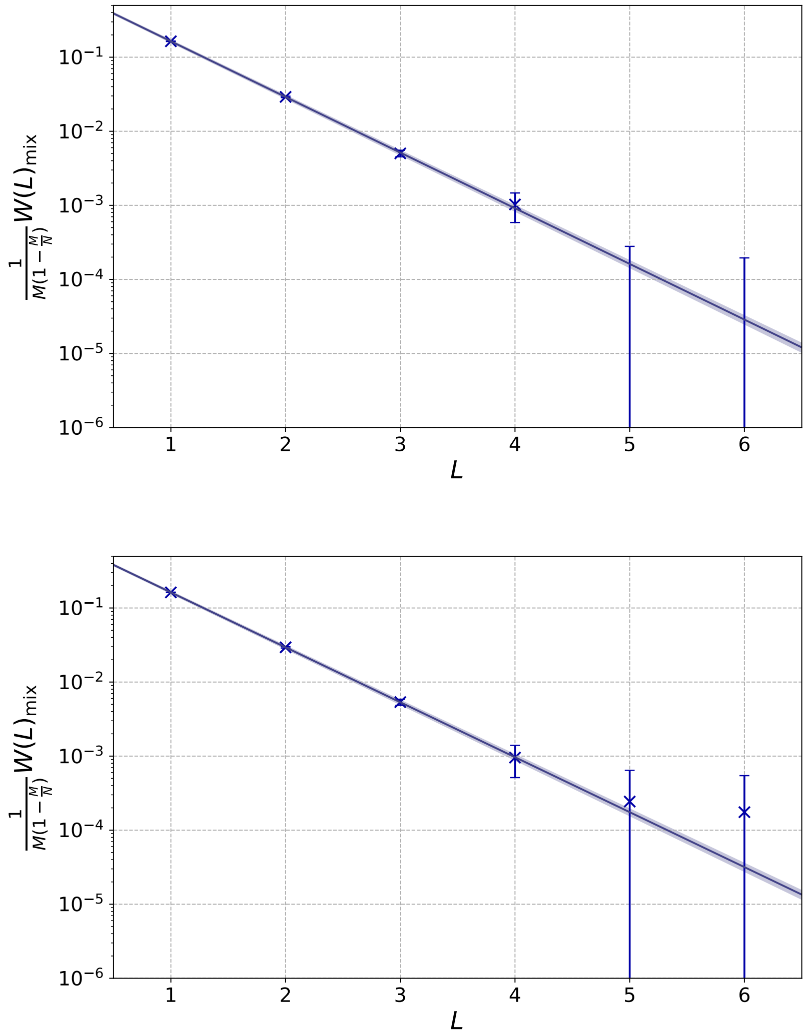

FIGURE 2.9: Mixed subsector Wilson loop, W_{mix}, at $T = 0.29$, for $P = 0.2$ and $P = 0.25$, respectively. We have extrapolated to the large N limit using $N = 24, 32, 64$, and to the continuum limit using $n_t = 16, 24, 32$ for each N, using the 2D interpolation $\frac{1}{M(1-\frac{M}{N})}W_{\text{mix}}(L) = \gamma(L) + \frac{\beta_1}{N^2} + \frac{\beta_2}{n_t} + \frac{\beta_2}{n_t N^2}$. We fitted the interpolated values $\gamma(L)$ for $1 \leq L \leq 4$ to the ansatz $\gamma(L) = \exp(-cL + d)$. We find $c_{\text{mix}} = 1.731(21)$ and $c_{\text{mix}} = 1.708(20)$ for $P = 0.2$ and $P = 0.25$, respectively. The fit is shown along with error bounds by the blue line.

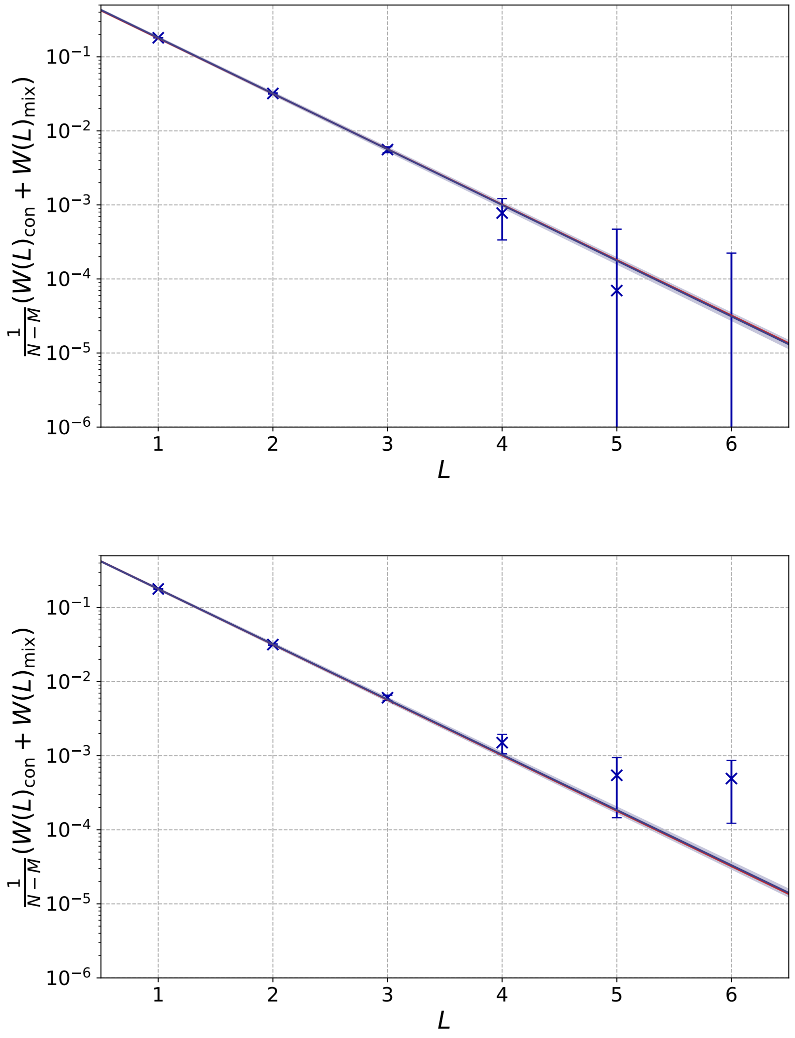

FIGURE 2.10: Combined mixed and confined subsector Wilson loop, $W_{\text{con}} + W_{\text{mix}}$, at $T = 0.29$, for $P = 0.2$ and $P = 0.25$, respectively. We have extrapolated to the large N limit using $N = 24, 32, 64$, and to the continuum limit using $n_t = 16, 24, 32$ for each N, using the 2D interpolation $\frac{1}{M-N}(W_{\text{con}} + W_{\text{mix}})(L) = \gamma(L) + \frac{\beta_1}{N^2} + \frac{\beta_2}{n_t} + \frac{\beta_2}{n_t N^2}$. We fitted these interpolated values $\gamma(L)$ for $1 \leq L \leq 4$ to the ansatz $\gamma(L) = \exp(-cL + d)$. We obtained $c = 1.733(19)$ and $d = 0.021(22)$ for $P = 0.20$, and $c = 1.718(18)$ and $d = -0.006(21)$ for $P = 0.25$. The fit is shown along with error bounds by the blue line. The theoretical prediction is shown by the red and is mostly obscured by the fit.

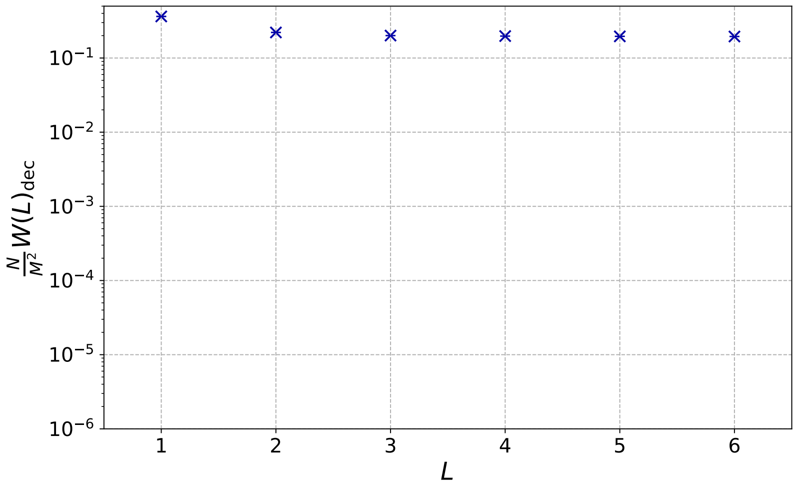

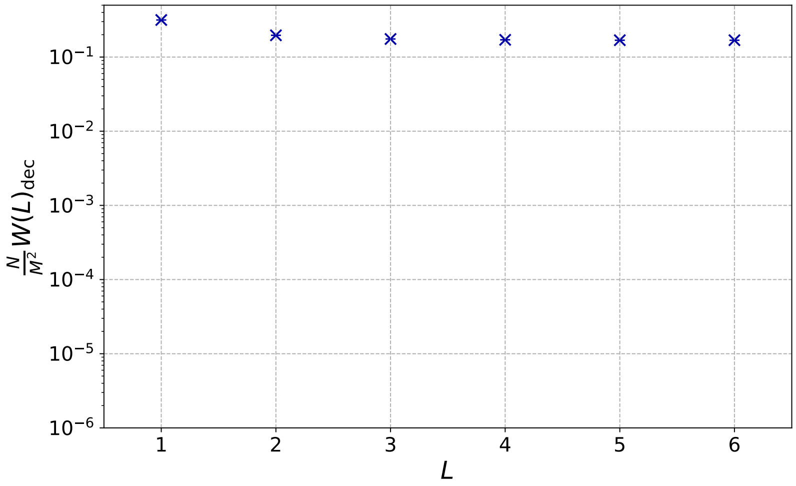

FIGURE 2.11: Deconfined subsector Wilson loop, W_{dec}, at $T = 0.29$, for $P = 0.2$ and $P = 0.25$, respectively. We used the same scale as in Figs. 2.8, 2.9, and 2.10. The potential is clearly nonconfining, and no fitting was attempted

Yang-Mills theory by taking strongly-coupled lattice gauge theory as a concrete example.

It is natural to ask whether our findings are an artefact of the strong-coupling limit taken for our lattice model. The strong-coupling limit allowed us to perform Eguchi-Kawai reduction, greatly enhancing the efficiency of computation. Lattice computations performed outside of this limit, with a full lattice extended in spacetime, could check that our results apply more generally, but would require vastly more resources.

It would also be interesting to investigate how to our results can be extended to finite N. It is not clear how flux tubes will behave at at energy scales that lie between the total deconfinement of an $SU(M)$ sector and that of $SU(M+1)$, for example. Again, to check this on the lattice demands that we depart from the the regime in which Eguchi-Kawai reduction can be employed.

The culmination of these considerations would be to understand the behaviour of flux tubes in a partially confined phase of QCD. We might find consequences for the spectrum and observations in QCD that could confirm the picture of the crossover region as a partially deconfined phase. We might expect, for instance, the formation of bound states of quarks, analogous to pions, in the confined sector. This is supported by an argument advanced in Ref. [18], which posits that quarks in the confined sector must form a bound state in order to satisfy the 't Hooft anomaly matching associated with chiral symmetry breaking in that sector.

In the holographic calculation of the Wilson loop [39], our results imply that different worldsheets are preferred in the confined and deconfined sectors. We have not yet understood how our results affect the conventional computations on the gravity side.

2.A Constrained simulations of the first kind and second kind

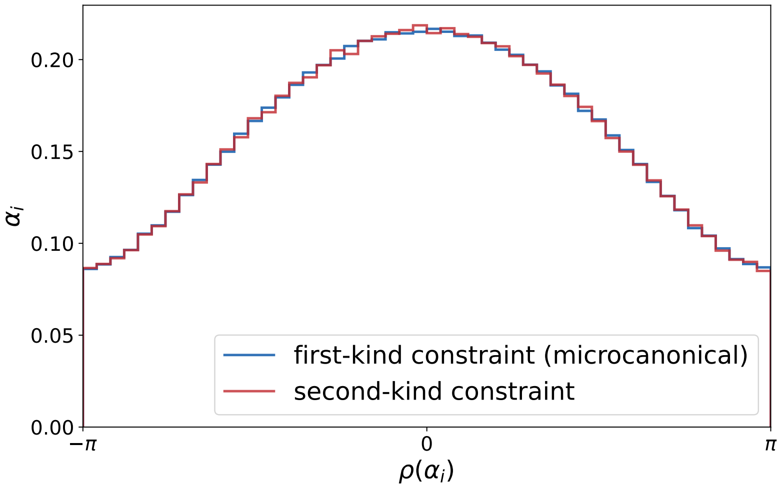

FIGURE 2.12: Polyakov loop phase distributions for $N = 64$, $n_t = 32$, $P = 0.2$, for constraints of the first and second kind.

A potential objection to our approach might be the apparent unnaturalness of the constraint simulation of the second kind. Here, we justify the second constraint as being equivalent to fixing some of the gauge redundancy that remains after having taken static diagonal gauge. The second constraint imposes uniformity on some subset $N - M$ of the eigenvalues of the Polyakov loop. In a general configuration at finite N outputted by the Monte-Carlo simulation under the constraint of the first kind, a subset of eigenvalues is not guaranteed to be exactly uniformly distributed in this way. However, at large N, the constraint of the second-kind and fixing of residual gauge symmetry should be equivalent, with fluctuations away from the mean value being suppressed. If the Polyakov eigenvalue distributions are identical between the microcanonical (first-kind constrained) and second-constrained simulation, we can use our method as an effective gauge fixing in the large-N limit. As we can see from Fig. 2.12, constrained simulations with the 1st and 2nd constraints indeed give the same distribution of the Polyakov-loop phases. Furthermore, as we can see Fig. 2.13, the distributions of $\alpha_1, \cdots, \alpha_M$ and $\alpha_{M+1}, \cdots, \alpha_N$ exhibit the kind splitting depicted in Fig. 2.3.

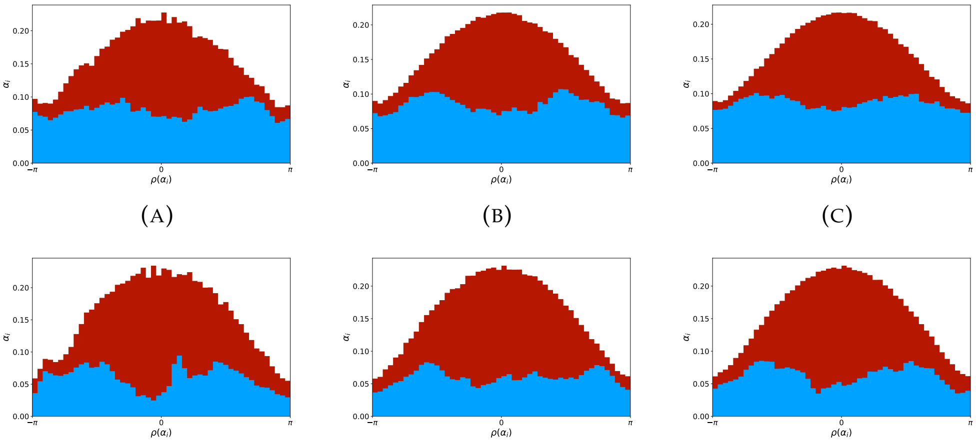

(A) (B) (C)

(D) (E) (F)

FIGURE 2.13: Polyakov loop phase distributions for $N = 32$ and $N = 64$, $n_t = 24$, $P = 0.2$ (top) and $P = 0.25$ (bottom), for constraints of the second kind. In addition to the distribution of all phases, the 'deconfined part' $(\alpha_1, \cdots, \alpha_M)$ and 'confined part' $(\alpha_{M+1}, \cdots, \alpha_N)$ are shown.

We can also check that the confined Polyakov loop correlator exhibits an area law in the microcanonical ensemble, without the imposition of uniformity on the confined subsector that is done in the constrained simulations of the second kind. We reasoned that the Wilson loop obtained in the constrained simulation of the first kind must be the sum of the contributions from W_{con}, W_{dec} and W_{mix}, and that the constrained simulation of second kind separates these pieces neatly. One may wonder whether this method of explicit separation does something more and spoils the partially-deconfined saddle. As a consistency check, we can subtract the deconfined-sector Wilson loop computed from the second-kind simulations from the first-kind Wilson loop to obtain a quantity with an area law, as expected from the confined and mixed sectors. More advantageously, we can calculate,

$$W_{\text{subtracted}} = W_{\text{full,1st}} - W_{\text{dec,2nd}} - W_{\text{mix,2nd}}. \tag{2.76}$$

This $W_{\text{subtracted}}$ should be the sum of W_{con} and W_{mix}, and hence, $W_{\text{subtracted}} = (N - M)\exp(-\sigma L \beta)$ is expected.

This demonstrates that the linear potential is not the result of an artifical imposition of uniformity on the eigenvalues, but is present even in the constrained simulations of the first kind. We also find by this analysis that the constraint of the second kind approximates the gauge-fixed microcanonical ensemble well even at $N = 16$.

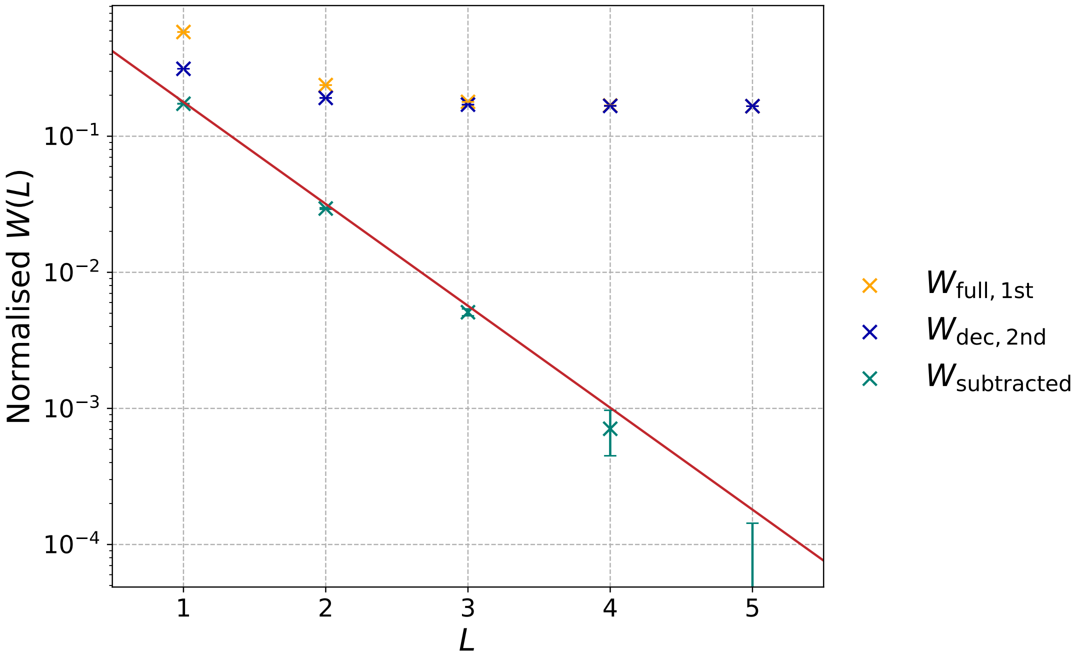

FIGURE 2.14: The complete Wilson loop from first-kind simulations, the deconfined Wilson loop from second-kind simulations, and their difference, $n_t = 32$ and $T = 0.29$, extrapolated to large N. Note that the continuum limit has not been taken.

In Fig. 2.14, we plotted $W_{\text{subtracted}}$. As expected, by subtracting the contribution from the deconfined sector, we find confining behaviour matching that of the mixed and confined subgroups from second-kind simulations.

2.B Stability of the extrapolations

Small N effects

We collected data for $N = 16, 24, 32, 64$. For the large-N extrapolation of W_{con} (respectively, W_{mix}), we should use only the data points with sufficiently large $N - M$ (respectively, M and $N - M$). However, for $P = 0.25$, the $N = 16$ data seemed to present a source of systematic error from finite N, M, and $N - M$ effects. In particular, for $N = 16$ and $P = 0.25$ we have $N - M = 6$. Such errors would not be captured by the error bars. We can measure the contribution to the systematic error by removing data at different values of N from the interpolation. The effect of this on the fitting parameter c is shown in Tables 2.3, 2.4, and 2.5.

P	all N	rmv. $N = 16$	rmv. $N = 24$	rmv. $N = 32$	rmv. $N = 64$
0.2	1.7248(59)	1.7343(74)	1.7271(59)	1.7221(64)	1.718(11)
0.25	1.7117(64)	1.7215(82)	1.7122(64)	1.7133(72)	1.692(12)

TABLE 2.3: Values of c for $W_{\text{con}} + W_{\text{mix}}$ with data for different N removed. With $n_t = 16$.

P	all N	rmv. $N = 16$	rmv. $N = 24$	rmv. $N = 32$	rmv. $N = 64$
0.2	1.7281(55)	1.7335(66)	1.7288(55)	1.7229(58)	1.729(11)
0.25	1.7170(78)	1.732(10)	1.7193(79)	1.7195(86)	1.682(15)

TABLE 2.4: Values of c_{con} for W_{con} with data for different N removed. With $n_t = 16$.

P	all N	rmv. $N = 16$	rmv. $N = 24$	rmv. $N = 32$	rmv. $N = 64$
0.2	1.7340(67)	1.7346(83)	1.7341(68)	1.7338(74)	1.737(13)
0.25	1.7066(72)	1.7116(91)	1.7059(72)	1.7062(80)	1.692(14)

TABLE 2.5: Values of c_{mix} for W_{mix} with data for different N removed. With $n_t = 16$.

P	all N	rmv. $N = 16$	rmv. $N = 24$	rmv. $N = 32$	rmv. $N = 64$
0.2	1.730(15)	1.733(19)	1.730(15)	1.729(17)	1.729(28)
0.25	1.703(14)	1.718(18)	1.703(14)	1.709(16)	1.663(27)

TABLE 2.6: Values of c for $W_{\text{con}} + W_{\text{mix}}$ with data for different N removed. Without $n_t = 16$.

It is easy to understand how the $N = 16$ data is distorting the results when we attempt a linear fit. We demonstrate this in Fig. 2.15. The small value of $N - M$ causes the $N = 16$ point to be far separated from the others on the x axis. Consequently, it has a large effect on the linear fit. There is also clear non-linear behaviour. For $P = 0.2$, $N - M$ is larger, and this explains why the distortion is not so severe. We could have attempted a quadratic fit, but we see from Fig. 2.15 that this does not significantly reduce the uncertainty, and potentially increases it. Therefore, we performed the large-N extrapolations in the main text without using $N = 16$.

Small n_t effects

We see a similar issue with respect to $n_t = 16$. In Table 2.3 and Table 2.4, we see that c for $P = 0.25$ is smaller than the theoretical value 1.724, whether $N = 16$ is removed or not. We attribute this to the use of $n_t = 16$. If we plot points at $n_t = 16, 24$ and 32 with fixed N and L by taking $\frac{1}{n_t}$ as the horizontal axis, we can see that those three points are not always on a straight line and a linear fit is often very bad. This happens for both $P = 0.2$ and $P = 0.25$. For the analyses in the main text, we did not include $n_t = 16$ for either $P = 0.2$ or $P = 0.25$. The effect of removing $n_t = 16$ can be seen by comparing Tables 2.3, 2.4, 2.5 with Tables 2.6, 2.7, 2.8.

P	all N	rmv. $N = 16$	rmv. $N = 24$	rmv. $N = 32$	rmv. $N = 64$
0.2	1.742(14)	1.729(17)	1.741(14)	1.737(16)	1.779(29)
0.25	1.701(18)	1.724(23)	1.702(18)	1.707(19)	1.596(35)

TABLE 2.7: Values of c_{con} for W_{con} with data for different N removed. Without $n_t = 16$.

P	all N	rmv. $N = 16$	rmv. $N = 24$	rmv. $N = 32$	rmv. $N = 64$
0.2	1.721(17)	1.731(21)	1.719(17)	1.731(19)	1.691(31)
0.25	1.702(16)	1.708(20)	1.702(16)	1.703(17)	1.703(31)

TABLE 2.8: Values of c_{mix} for W_{mix} with data for different N removed. Without $n_t = 16$.

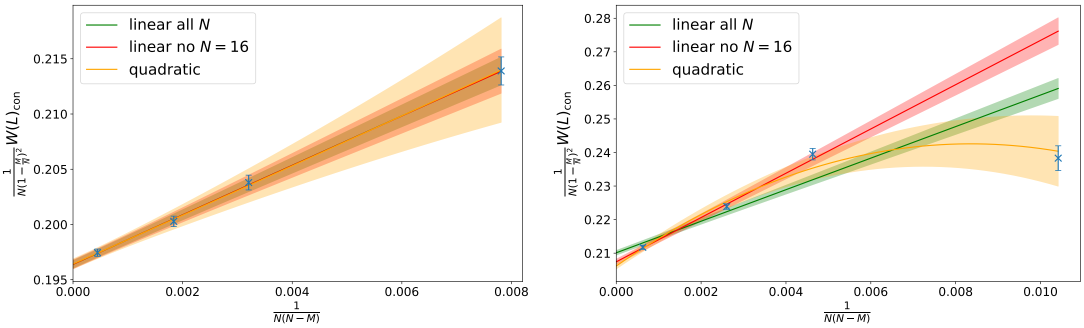

FIGURE 2.15: Performing the large N extrapolation for the confined subsector $P = 0.2$ (left) and $P = 0.25$ (right) for $L = 1$. The continuum limit $n_t \to \infty$ has been taken. We try a linear fit of all points (green), a linear fit that ignores $N = 16$ (red), and a quadratic fit of all points (orange). The destabilising effect of the $N = 16$ (rightmost) point in the $P = 0.25$ linear extrapolation is obvious and can be attributed to the small value $N - M = 6$.

2.C Gauge fixing condition and separation of confined and deconfined sectors

As a starter, let us recall how the operator formalism and path-integral formalism are related (see e.g., [40] for the case of Hermitian variables). The thermal partition function of the Eguchi-Kawai model is

$$\begin{aligned}
Z(T) &= \frac{1}{[\mathrm{volU}(N)]^{n_t}} \int \left(\prod_{k=1}^{n_t} dg_k\right) \mathrm{Tr}_{\mathcal{H}_{\mathrm{ext}}}\Big(\hat{g}_{(n_t)} e^{-\frac{H(\hat{E},\hat{U})}{Tn_t}} \hat{g}^{-1}_{(n_t-1)}\hat{g}_{(n_t-1)} \\
&\quad e^{-\frac{H(\hat{E},\hat{U})}{Tn_t}} \hat{g}^{-1}_{(n_t-2)}\hat{g}_{(n_t-2)} \cdots \hat{g}^{-1}_{(1)}\hat{g}_{(1)} e^{-\frac{H(\hat{E},\hat{U})}{Tn_t}}\Big) \\
&= \frac{1}{[\mathrm{volU}(N)]^{n_t}} \int \left(\prod_{k=1}^{n_t} dg_{(k)}\right) \int \left(\prod_{k=1}^{n_t} dU_{(k)}\right) \\
&\quad \langle U_{(n_t)}|\hat{g}_{(n_t)} e^{-\frac{H(\hat{E},\hat{U})}{Tn_t}} \hat{g}^{-1}_{(n_t-1)}|U_{(n_t-1)}\rangle \\
&\quad \times \langle U_{(n_t-1)}|\hat{g}_{(n_t-1)} e^{-\frac{H(\hat{E},\hat{U})}{Tn_t}} \hat{g}^{-1}_{(n_t-2)}|U_{(n_t-2)}\rangle \\
&\quad \times \cdots \times \langle U_{(1)}|\hat{g}_{(1)} e^{-\frac{H(\hat{E},\hat{U})}{Tn_t}} |U_{(n_t)}\rangle. \qquad (2.77)
\end{aligned}$$

For $H(\hat{E},\hat{U}) = \frac{1}{2}\mathrm{Tr}\hat{E}^2 + V(\hat{U})$, we can rewrite each term in the product as follows.

$$\begin{aligned}
&\langle U_{(k)}|\hat{g}_{(k)} e^{-\frac{H(\hat{E},\hat{U})}{Tn_t}} \hat{g}^{-1}_{(k-1)}|U_{(k-1)}\rangle \\
&= \langle g^{-1}_{(k)}U_{(k)}g_{(k)}| e^{-\frac{H(\hat{E},\hat{U})}{Tn_t}} |g^{-1}_{(k-1)}U_{(k-1)}g_{(k-1)}\rangle \\
&= e^{-\frac{1}{Tn_t}V(g^{-1}_{(k-1)}U_{(k-1)}g_{(k-1)})} \langle g^{-1}_{(k)}U_{(k)}g_{(k)}| e^{-\frac{1}{2Tn_t}\mathrm{Tr}\hat{E}^2} |g^{-1}_{(k-1)}U_{(k-1)}g_{(k-1)}\rangle. \qquad (2.78)
\end{aligned}$$

By using

$$i\epsilon \equiv \log\left(g^{-1}_{(k)}U_{(k)}g_{(k)}g^{-1}_{(k-1)}U^{-1}_{(k-1)}g_{(k-1)}\right), \qquad (2.79)$$

we can relate $|g^{-1}_{(k-1)}U_{(k-1)}g_{(k-1)}\rangle$ and $|g^{-1}_{(k)}U_{(k)}g_{(k)}\rangle$ as

$$|g^{-1}_{(k)}U_{(k)}g_{(k)}\rangle = e^{i\mathrm{Tr}(\epsilon\hat{E})}|g^{-1}_{(k-1)}U_{(k-1)}g_{(k-1)}\rangle, \qquad (2.80)$$

and hence,

$$\begin{aligned}
&\langle g^{-1}_{(k)}U_{(k)}g_{(k)}| e^{-\frac{1}{2Tn_t}\mathrm{Tr}\hat{E}^2} |g^{-1}_{(k-1)}U_{(k-1)}g_{(k-1)}\rangle \\
&= \langle g^{-1}_{(k-1)}U_{(k-1)}g_{(k-1)}| e^{-\frac{1}{2Tn_t}\mathrm{Tr}\hat{E}^2 - i\mathrm{Tr}(\epsilon\hat{E})} |g^{-1}_{(k-1)}U_{(k-1)}g_{(k-1)}\rangle \\
&= \langle U| e^{-\frac{1}{2Tn_t}\mathrm{Tr}\hat{E}^2 - i\mathrm{Tr}(\epsilon\hat{E})} |U\rangle, \qquad (2.81)
\end{aligned}$$

where U can be any element of the unitary group.[8] Up to a normalization constant, this can be written by using trace over the Hilbert space as

$$\begin{aligned}
&\mathrm{Tr}\exp\left(-\frac{1}{2n_tT}\sum_a \hat{E}_a^2 + i\sum_a \epsilon^a \hat{E}_a\right)\\
&= e^{-\frac{n_tT}{2}\mathrm{Tr}\epsilon^2} \times \mathrm{Tr}\exp\left(-\frac{1}{2n_tT}\sum_a (\hat{E}_a - in_tT\epsilon_a)^2\right). \qquad (2.82)
\end{aligned}$$

The second term ($\mathrm{Tr}\cdots$) becomes constant in the limit of $n_tT \to \infty$ when $n_tT\epsilon^2$ is of order one (which is justified because of the first term $e^{-\frac{n_tT}{2}\mathrm{Tr}\epsilon^2}$), because the sum over momentum modes can be identified with usual integral in flat space. Omitting the second term and by approximating ϵ^2 by $|g_{(k)}^{-1}U_{(k)}g_{(k)} - g_{(k-1)}^{-1}U_{(k-1)}g_{(k-1)}|^2$, we obtain

$$\begin{aligned}
&e^{-\frac{n_tT}{2}\mathrm{Tr}[|g_{(k)}^{-1}U_{(k)}g_{(k)} - g_{(k-1)}^{-1}U_{(k-1)}g_{(k-1)}|^2]} e^{-V(g_{(k)}^{-1}U_{(k)}g_{(k)})/(Tn_t)}\\
&\simeq e^{-L[D_t(g_{(k)}^{-1}U_{(k)}g_{(k)}),(g_{(k)}^{-1}U_{(k)}g_{(k)})]/(Tn_t)}\\
&= e^{-L[D_tU_{(k)},U_{(k)})]/(Tn_t)}. \qquad (2.83)
\end{aligned}$$

Here we used

$$g_{(k-1)}g_{(k)}^{-1} \equiv e^{-iA_{(k)}/(n_tT)}, \qquad (2.84)$$

and

$$U_{(k)} - (g_{(k-1)}g_{(k)}^{-1})^{-1}U_{(k-1)}(g_{(k-1)}g_{(k)}^{-1}) \simeq \frac{D_tU_{(k)}}{n_tT}. \qquad (2.85)$$

By taking $n_t \to \infty$ limit, we obtain

$$Z(T) = \int [dA][dU]e^{-\int dtL[D_tU,U]}. \qquad (2.86)$$

Note that $g_{(n_t)}$ is the Polyakov loop. In the static diagonal gauge,

$$g_{(k)} = \mathrm{diag}(e^{ik\theta_1/n_t}, \cdots, e^{ik\theta_N/n_t}). \qquad (2.87)$$

In the confined sector, the distribution of the phases of the Polyakov loop is uniform [20]. We fix the S_N permutation symmetry such that the phase distribution does indeed satisfy this property. This guarantees the neat separation into confined and deconfined sectors at $t = \beta$ (equivalently, $t = 0$).

Let us use the trace cyclicity in the extended Hilbert space and shift the initial time. In the static diagonal gauge, this does not change the Polyakov loop. Therefore, exactly

---

[8] Because $\mathrm{Tr}\hat{E}^2$ commutes with the shift on the group manifold, the first line could be $\langle Wg_{(k)}^{-1}U_{(k)}g_{(k)}|e^{-\frac{1}{2Tn_t}\mathrm{Tr}\hat{E}^2}|Wg_{(k-1)}^{-1}U_{(k-1)}g_{(k-1)}\rangle$, where W is an arbitrary element of $\mathrm{U}(N)$.

the same separation into confined and deconfined sectors holds at any t.

2.D Simulation algorithm

Several aspects of the simulation algorithm used for this study are similar to the one used in Ref. [41], which was originally developed in unpublished work by one of the authors (MH), Takashi Kaneko, Jun Nishimura, and Asato Tsuchiya in 2013. Gauge configurations are generated using the Hybrid Monte-Carlo algorithm [42].

The lattice action we consider is, before adding the constraint term for the Polyakov loop,

$$S = \frac{N}{2a}\sum_{\mu=1}^{d}\sum_{t=1}^{n_t}\mathrm{Tr}\left(\mathbf{1}_N - U_{\mu,t}VU^{\dagger}_{\mu,t+1}V^{\dagger}\right) + \text{h.c.} + S_{F.P.}, \tag{2.88}$$

where $V = \mathrm{diag}(e^{i\alpha_1/n_t}, \cdots, e^{i\alpha_N/n_t})$. Here, a is the lattice spacing and $\beta = an_t$ is the inverse temperature, $\beta = T^{-1}$. We will focus on $d = 3$. The Polyakov line phases $\alpha_{1,2,\cdots,N}$ are constrained to be

$$-\pi < \alpha_i \leq \pi. \tag{2.89}$$

The Faddeev-Popov term $S_{F.P.}$ is given by

$$S_{F.P.} = -\sum_{i<j} 2\log\left|\sin\left(\frac{\alpha_i - \alpha_j}{2}\right)\right|. \tag{2.90}$$

If we just impose the constraint $-\pi < \alpha_i \leq \pi$ as it is, then the simulation is not very efficient – the 'center of mass' $(\sum_i \alpha_i)/N$ randomly moves and hits $\pm\pi$. For this reason, we use the following trick.

Firstly, let us recall that α_i and $\tilde{\alpha}_i \equiv \alpha_i - C$ give the same weight for any C. Here, C must satisfy $\min(\tilde{\alpha}_i) + C > -\pi$ and $\max(\tilde{\alpha}_i) + C \leq \pi$, because of the condition $-\pi < \alpha_i \leq \pi$. Hence C must sit in $(-\pi - \min(\tilde{\alpha}_i), \pi - \max(\tilde{\alpha}_i)]$, whose interval is $2\pi - \mu$, where $\mu \equiv \max(\tilde{\alpha}_i) - \min(\tilde{\alpha}_i)$. Therefore, we can replace the integral over α_i with that over $\tilde{\alpha}_i$, with an additional Boltzmann weight

$$w(\mu) = \begin{cases} 2\pi - \mu & (\mu < 2\pi) \\ 0 & (\mu \geq 2\pi). \end{cases} \tag{2.91}$$

N	$W(1)$	$W(2)$	$W(3)$	$W(4)$	$W(5)$
16	0.13755(41)	0.03427(40)	0.02506(39)	0.02809(38)	0.03269(38)
24	0.12955(19)	0.02357(17)	0.01213(16)	0.01244(16)	0.01442(15)
32	0.12674(17)	0.01977(13)	0.00752(13)	0.00700(11)	0.00791(11)
48	0.12548(17)	0.01751(13)	0.00460(12)	0.00334(10)	0.003483(96)
64	0.12505(13)	0.016542(97)	0.003288(88)	0.001946(74)	0.002086(68)
96	0.124261(79)	0.015867(63)	0.002493(52)	0.000944(49)	0.000910(42)
128	0.124144(98)	0.015631(76)	0.002248(63)	0.000742(51)	0.000517(48)

TABLE 2.9: Wilson loop for $L = 1, 2, 3, 4, 5$, unconstrained, $n_t = 24$, $T = 0.25$.

For numerical calculations, this is not very nice because of the singularity at $\mu = 2\pi$. Instead, in the molecular evolution stage of the HMC algorithm, we use

$$\tilde{w}(\mu) = \begin{cases} 2\pi - \mu + \varepsilon & (\mu < 2\pi) \\ \varepsilon e^{-g_\alpha(\mu - 2\pi)} & (\mu \geq 2\pi), \end{cases} \tag{2.92}$$

with a large enough g_α (say g_α=100) and $\varepsilon = g_\alpha^{-1}$. For the Metropolis test, we use $w(\mu)$ instead of $\tilde{w}(\mu)$. The detailed balance condition is not violated and the correct path-integral weight is reproduced; see e.g., Ref. [43].

Permutation of Polyakov line phases in the constrained simulation of second kind

When ΔS_{dec} and ΔS_{con} are added, the S_N permutation symmetry is explicitly broken to $\mathrm{S}_M \times \mathrm{S}_{N-M}$. The ordering of the α's — say $\alpha_{i_1} < \alpha_{i_2} < \alpha_{i_3} < \cdots$ — does not change (or very rarely changes) in the HMC simulation, which can cause a problem when the permutation symmetry is explicitly broken. To avoid this problem, we choose α_i and α_j randomly from the deconfined and confined sectors and perform a permutation using the Metropolis algorithm. Note that the i-th and j-th rows and columns in U_μ have to be exchanged, too. We do this 10 times after each HMC steps. This method is the same as the one used in Ref. [21].

P	N	n_t	$W(1)$	$W(2)$	$W(3)$	$W(4)$	$W(5)$
0.2	16	16	0.19720(56)	0.04844(32)	0.03111(27)	0.03531(24)	0.04399(23)
		24	0.20151(44)	0.05014(31)	0.03150(27)	0.03588(24)	0.04466(23)
		32	0.20688(71)	0.05279(33)	0.03250(27)	0.03627(25)	0.04480(23)
	24	16	0.18633(31)	0.03648(18)	0.01522(15)	0.01498(13)	0.01772(13)
		24	0.19048(26)	0.03914(18)	0.01619(15)	0.01541(13)	0.01835(12)
		32	0.19626(35)	0.04076(19)	0.01656(16)	0.01549(14)	0.01850(12)
	32	16	0.18234(22)	0.03325(13)	0.01070(11)	0.00875(10)	0.010341(91)
		24	0.18740(25)	0.03521(15)	0.01139(12)	0.00888(11)	0.01047(10)
		32	0.19162(22)	0.03640(14)	0.01173(11)	0.009082(98)	0.010560(92)
	64	16	0.17677(13)	0.029452(90)	0.006087(77)	0.002606(65)	0.002500(60)
		24	0.18392(22)	0.03170(12)	0.006751(89)	0.003008(82)	0.002580(71)
		32	0.18703(16)	0.032779(98)	0.006974(80)	0.002905(67)	0.002640(62)
0.25	16	16	0.2227(41)	0.05909(47)	0.04191(39)	0.04820(34)	0.05954(32)
		24	0.2257(11)	0.06278(44)	0.04272(36)	0.04798(33)	0.05964(31)
		32	0.22946(87)	0.06356(45)	0.04280(37)	0.04818(34)	0.05931(32)
	24	16	0.20105(64)	0.04231(37)	0.02091(31)	0.02186(28)	0.02626(26)
		24	0.21621(80)	0.04765(40)	0.02205(33)	0.02212(28)	0.02672(26)
		32	0.21863(93)	0.04878(39)	0.02327(31)	0.02226(29)	0.02645(26)
	32	16	0.19751(38)	0.03760(20)	0.01382(17)	0.01228(14)	0.01447(13)
		24	0.20707(68)	0.04061(24)	0.01455(19)	0.01256(16)	0.01503(14)
		32	0.21059(38)	0.04224(21)	0.01556(17)	0.01279(15)	0.01490(13)
	64	16	0.18902(31)	0.03223(18)	0.00721(14)	0.00351(13)	0.00380(12)
		24	0.19792(33)	0.03484(15)	0.00780(12)	0.003743(98)	0.003560(89)
		32	0.20000(29)	0.03546(14)	0.00828(11)	0.004051(94)	0.003723(87)

TABLE 2.10: W_{con} for $L = 1, 2, 3, 4, 5$, constrained, $T = 0.29$.

P	N	n_t	$W(1)$	$W(2)$	$W(3)$	$W(4)$	$W(5)$
0.2	16	16	0.13990(48)	0.02331(27)	0.00490(21)	0.00277(19)	0.00344(17)
		24	0.14753(37)	0.02590(26)	0.00598(21)	0.00303(19)	0.00356(17)
		32	0.14991(55)	0.02700(26)	0.00601(21)	0.00315(19)	0.00401(17)
	24	16	0.14023(36)	0.02299(17)	0.00422(14)	0.00149(13)	0.00146(11)
		24	0.14921(25)	0.02529(18)	0.00494(14)	0.00155(13)	0.00181(11)
		32	0.14864(33)	0.02598(17)	0.00490(15)	0.00183(13)	0.00155(12)
	32	16	0.14380(21)	0.02357(13)	0.00407(11)	0.001061(97)	0.000705(88)
		24	0.15052(23)	0.02533(15)	0.00464(12)	0.00098(11)	0.000932(95)
		32	0.15165(21)	0.02624(13)	0.00468(11)	0.001279(93)	0.000807(84)
	64	16	0.14602(14)	0.023551(93)	0.003613(78)	0.000382(71)	-0.000016(65)
		24	0.15021(27)	0.02512(12)	0.004036(95)	0.000452(80)	0.000090(75)
		32	0.15327(17)	0.02607(10)	0.004283(83)	0.000645(72)	0.000065(64)
0.25	16	16	0.13695(84)	0.02376(27)	0.00531(22)	0.00275(19)	0.00354(18)
		24	0.14873(49)	0.02639(27)	0.00559(22)	0.00311(20)	0.00402(18)
		32	0.15251(45)	0.02780(28)	0.00648(23)	0.00347(20)	0.00382(18)
	24	16	0.14656(39)	0.02502(26)	0.00480(21)	0.00180(19)	0.00157(17)
		24	0.14711(50)	0.02594(25)	0.00530(21)	0.00172(18)	0.00172(16)
		32	0.15323(41)	0.02773(26)	0.00584(21)	0.00191(19)	0.00167(16)
	32	16	0.14674(22)	0.02455(13)	0.00443(11)	0.001313(97)	0.000991(91)
		24	0.15044(30)	0.02625(15)	0.00466(12)	0.00118(11)	0.001140(97)
		32	0.15446(20)	0.02732(14)	0.00523(11)	0.00139(10)	0.000989(90)
	64	16	0.14876(21)	0.02429(13)	0.00388(11)	0.000710(98)	0.000189(90)
		24	0.15305(19)	0.02606(10)	0.004208(88)	0.000703(74)	0.000110(66)
		32	0.15572(18)	0.027028(99)	0.004563(80)	0.000816(71)	0.000190(65)

TABLE 2.11: W_{mix} for $L = 1, 2, 3, 4, 5$, constrained, $T = 0.29$.

P	N	n_t	$W(1)$	$W(2)$	$W(3)$	$W(4)$	$W(5)$
0.2	16	16	0.31420(51)	0.19824(28)	0.18637(25)	0.19100(22)	0.19865(21)
		24	0.31659(41)	0.19991(30)	0.18692(24)	0.19110(22)	0.19882(21)
		32	0.32003(52)	0.20061(29)	0.18713(24)	0.19126(22)	0.19927(21)
	24	16	0.33554(37)	0.21962(20)	0.20452(17)	0.20506(15)	0.20854(14)
		24	0.33592(29)	0.22067(19)	0.20486(17)	0.20536(15)	0.20895(13)
		32	0.34119(37)	0.22169(20)	0.20528(17)	0.20555(15)	0.20885(14)
	32	16	0.32265(26)	0.20719(14)	0.19100(12)	0.19007(11)	0.19192(10)
		24	0.32574(25)	0.20918(16)	0.19166(13)	0.19041(12)	0.19206(11)
		32	0.32924(24)	0.20992(14)	0.19185(12)	0.19072(11)	0.192287(95)
	64	16	0.32819(16)	0.21602(11)	0.198914(93)	0.196599(80)	0.196673(80)
		24	0.33471(53)	0.21786(13)	0.19951(12)	0.19681(10)	0.196764(92)
		32	0.33630(20)	0.21869(11)	0.199764(96)	0.196940(84)	0.196834(77)
0.25	16	16	0.30670(34)	0.19424(23)	0.18135(19)	0.18456(17)	0.19108(16)
		24	0.30748(33)	0.19576(23)	0.18229(19)	0.18534(17)	0.19154(17)
		32	0.30880(33)	0.19676(23)	0.18264(19)	0.18571(18)	0.19191(16)
	24	16	0.29786(28)	0.18699(20)	0.17150(17)	0.17095(15)	0.17347(14)
		24	0.30475(37)	0.18914(21)	0.17190(17)	0.17158(15)	0.17376(14)
		32	0.30477(29)	0.18926(22)	0.17214(17)	0.17185(15)	0.17418(14)
	32	16	0.29571(16)	0.18425(11)	0.167607(92)	0.166404(79)	0.167424(75)
		24	0.30153(20)	0.18604(12)	0.16829(10)	0.166629(91)	0.167586(88)
		32	0.30259(16)	0.18686(11)	0.168547(90)	0.166706(79)	0.167646(75)
	64	16	0.29883(16)	0.18903(11)	0.171897(94)	0.169310(87)	0.169291(81)
		24	0.30404(15)	0.190567(90)	0.172290(74)	0.169675(74)	0.169527(63)
		32	0.30702(16)	0.191836(92)	0.172973(74)	0.169992(67)	0.169785(68)

TABLE 2.12: W_{dec} for $L = 1, 2, 3, 4, 5$, constrained, $T = 0.29$.

Chapter 3

Global symmetries and partial deconfinement

3.1 Introduction

In Sec. 1.3, we proposed that the partially confined phase could be identified in the large N limit by the distribution of eigenvalues $\rho(\psi)$. Because the centre symmetry is preserved in the confined phase and broken in the partial and deconfined phases, the Polyakov loop expectation value, P, can act as an order parameter to distinguish the former from the latter. Meanwhile, the gap in $\rho(\psi)$ can distinguish between the partial and deconfined phases. However, this gap is not associated with any symmetry, and hence is not an order parameter. The question therefore arises of whether any order parameter can distinguish the partial and deconfined phases.[1] To date, the only proposals for such order parameters are in holography, and rely in part on arguments about black holes (namely Gregory-Laflamme instabilities of small black holes in AdS) [44; 15], but a completely generic proposal remains absent.

In this chapter, we propose an order parameter that can distinguish the partial and deconfined phases. In short, we argue that if a global symmetry is spontaneously broken in the confined phase and preserved in the deconfined phase, then that global symmetry should be broken in the partial phase. As a result, the transition from the deconfined to the partial phase should be accompanied by spontaneous breaking of the global symmetry, and hence these two phases can be distinguished by an order parameter. We present two examples in which this occurs, and then argue that such behaviour is generic.

---

[1] An intuitive way to understand this transition in terms of symmetry is to relate it to the breaking and restoration of gauge symmetry [17; 20; 24]. However, recall that gauge symmetry is a sort of redundancy, unlike a global symmetry. Here we want to find a more conventional (and less-controversial) characterisation, based on global symmetry.

Our first example is $\mathcal{N} = 1$ supersymmetric (SUSY) Yang-Mills (SYM) theory with gauge group $SU(N)$ on $S^1 \times \mathbb{R}^3$ with periodic boundary conditions for both the gluons and gluino, and with a non-zero gluino mass. We also introduce a non-zero θ-angle, $\theta = \pi$, in which case a mixed CP-centre symmetry anomaly forces CP symmetry to be spontaneously broken in the confined phase [45]. When $\theta = 0$, CP symmetry is preserved in both the confined and deconfined phases [45]. We work at weak coupling, in the so-called Abelian large-N limit, which is distinct from the 't Hooft large limit, as we discuss in section 3.2. We also present some finite-N numerical results, though we consider relatively large $N \geq 30$.

Our second example is a strongly-coupled $SU(N)$ YM theory on S^1 times a three-dimensional spatial lattice. We work in the 't Hooft large-N limit and employ Eguchi-Kawai reduction to a single site in space. We then add quarks in a probe limit, so that to leading approximation the centre symmetry is not explicitly broken, while chiral symmetry is spontaneously broken in the confined phase but restored in the deconfined phase.

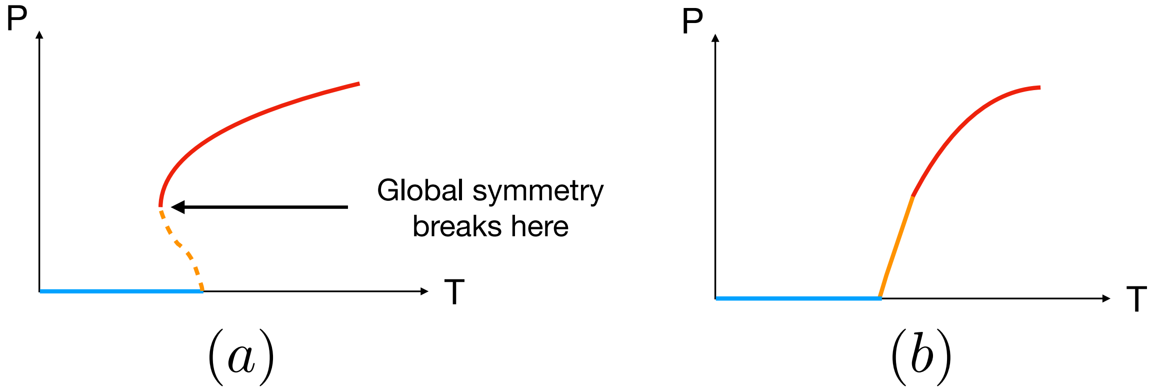

FIGURE 3.1: Schematic depiction of the Polyakov loop expectation value, P, as a function of temperature T for a confinement/deconfinement transition that is (a) first order or (b) second order or higher, i.e. continuous. The blue, orange and red curves represent the confined, partial, and deconfined phases, respectively. The theories we study in this paper have first-order transitions, as in (a). We find that the global symmetry that is spontaneously broken in the confined phase, namely CP or chiral symmetry, is also broken in the partial phase. As a result, the transition from the deconfined to partial phases is characterised by the spontaneous breaking of this global symmetry, as indicated in (a).

In each case we perform numerical calculations, which for the lattice YM theory are in the 't Hooft large-N limit, while for $\mathcal{N} = 1$ SYM, some are genuine finite-N calculations. In each case, we reproduce known results for the confinement/deconfinement transition, which is first order in both theories, so that P behaves as shown in Fig. 3.1 (a). Our new results are numerical evaluations for the unstable saddles connecting the confined and deconfined phases, where we identify the partial phase using the Polyakov eigenvalue distribution. We also numerically compute the order parameters for CP and chiral symmetries, respectively, and show that in each case this global symmetry is spontaneously broken in the partial phase. As a result, in the transition from deconfined to partial phase, the global symmetry breaks spontaneously, as we have indicated in Fig. 3.1 (a).

In short, our two examples share the following behaviour. In the confined phase, the centre symmetry is preserved but another global symmetry, namely CP or chiral symmetry, is spontaneously broken. In the deconfined phase, the centre symmetry is spontaneously broken, but the other global symmetry is preserved. In the partial phase, both symmetries are spontaneously broken. In these examples, we therefore prove that the partial phase is distinguished by global symmetries from both the confined and deconfined phases, and in particular, we identify an order parameter to distinguish the deconfined and partial phases, as mentioned above.

Furthermore, we conjecture that such behaviour may be generic, and can be used to identify, or even define, partial phases, in theories with both a centre symmetry and a global symmetry that is spontaneously broken in the confined phase but preserved in the deconfined phase. Specifically, the partial phase could be defined as the phase in which both of these symmetries are spontaneously broken. Such a definition, using symmetries alone, would obviously have advantages. In particular, such a definition could apply for any N, not just the large-N limit. Indeed, our finite-N numerical results for $\mathcal{N} = 1$ SYM provide some compelling evidence for this.

However, we can provide more general plausibility arguments for this conjecture. For instance, we expect that whatever strong-coupling physics breaks chiral symmetry in a confined phase should occur also in a partial phase's confined subsector. As a result, if chiral symmetry is preserved in the deconfined phase, then chiral symmetry can provide an order parameter distinguishing deconfined and partial phases. Anomalies may provide a more rigorous argument, being independent of coupling strengths and invariant under renormalisation group flows, including flows induced by T. For an anomaly-matching argument that chiral symmetry should be partially broken in the partial phase, see ref. [18]. Another example is $\mathcal{N} = 1$ SYM with $\theta = \pi$, where an anomaly forces CP symmetry to be spontaneously broken at $T = 0$ [45]. As a result, as we raise T, CP symmetry must remain spontaneously broken in the confined phase. Presumably, in the partial phase the same anomaly arguments extend to the confined subsector, and hence CP symmetry must be spontaneously broken, as indeed we observe. Such arguments should generalise to any theory where an anomaly forces spontaneous symmetry breaking in the confining vacuum: we expect the symmetry to remain spontaneously broken in any $T > 0$ phase that has a confined subsector, and if the symmetry is preserved in the deconfined phase, then this symmetry can provide an order parameter distinguishing deconfined and partial phases.

This chapter is organised as follows. In Sec. 3.2 we study mass-deformed $\mathcal{N}=1$ SYM on $S^1\times\mathbb{R}^3$, in Sec. 3.3 we study the EK reduction of strongly-coupled YM with probe quarks, and in Sec. 3.4 we conclude with a summary and outlook for future research. Two appendices contain technical results useful for our study of $\mathcal{N}=1$ SYM.

3.2 Weakly-coupled, softly-broken massive $\mathcal{N}=1$ SYM on $S^1\times\mathbb{R}^3$

In this section, we consider $\mathcal{N}=1$ $SU(N)$ SYM on Euclidean $S^1\times\mathbb{R}^3$, with a non-zero gluino mass, which breaks SUSY. The action for this theory is

$$S_{\text{SYM}}=\int dx_0\, d^3\vec{x}\left[\frac{1}{4g^2}\text{tr}(F_{\mu\nu}F^{\mu\nu})-\frac{i\theta}{8\pi^2}\text{tr}(F_{\mu\nu}\tilde{F}^{\mu\nu})+\frac{2i}{g^2}\text{tr}(\bar{\Psi}\bar{\sigma}^{\mu}D_{\mu}\Psi)+\frac{m}{g^2}(\text{tr}(\Psi\Psi)+\text{c.c.})\right], \tag{3.1}$$

with x_0 the S^1 coordinate, $\vec{x}$ the $\mathbb{R}^3$ coordinates, g the gauge coupling, θ the theta-angle, $F_{\mu\nu}$ the field strength of the $SU(N)$ gauge field A_μ, called the gluon, where $\mu,\nu=0,1,2,3$, $\tilde{F}_{\mu\nu}$ the Hodge dual of $F_{\mu\nu}$, Ψ an adjoint Weyl fermion, called the gluino, where $D_\mu\Psi=\partial_\mu\Psi+i[A_\mu,\Psi]$, and m the gluino mass.

If $m=0$ then the theory has $\mathcal{N}=1$ SUSY. Although the fields in the action are then massless, a mass gap is dynamically generated at the scale Λ, given at two-loop order by [46; 47]

$$\Lambda^3\equiv\frac{4\pi}{3N}M_{\text{PV}}^3\,\text{Im}\,\tau(M_{\text{PV}})\exp\left[\frac{2\pi i\,\tau(M_{\text{PV}})}{N}\right], \tag{3.2a}$$

$$\tau\equiv\left(\frac{4\pi\, i}{g^2}+\frac{\theta}{2\pi}\right), \tag{3.2b}$$

with M_{PV} a Pauli-Villars mass and $\tau(M_{PV})$ the running coupling in eq. (3.2b) evaluated at M_{PV}. If $m\neq 0$, then all SUSY is broken, and in particular if $m\to\infty$ then the theory reduces to pure $SU(N)$ YM theory.

The theory in eq. (3.1) has a $\mathbb{Z}_N$ centre symmetry for all values of N, g, θ, and m, and has CP symmetry for all N, g, and m, but only for certain values of θ. To see why, recall that the term $\frac{1}{8\pi^2}\text{tr}(F\tilde{F})$ in eq. (3.1) is CP-odd and topological, and that the integral of this term takes integer values. As a result, θ is periodic, $\theta\sim\theta+2\pi$, and transforms under CP as $\theta\to-\theta$. The theory thus has CP symmetry only when $\theta=0$ or $\theta=\pi$ mod 2π. In what follows, for brevity we will restrict to $\theta\in[0,\pi]$, leaving the 2π periodicity implicit.

The theory in eq. (3.1) has a mixed CP-centre symmetry anomaly. Assuming that the vacuum is gapped and confining for all θ, when $\theta=\pi$ this anomaly forces the vacuum to break CP symmetry spontaneously [45], an effect known as the Dashen phenomenon [48].

We denote the S^1 circumference as L. If we write the generating functional of connected correlation functions as a path integral, we have two options for boundary conditions around the S^1. First are "thermal" boundary conditions, namely a periodic boundary condition for the gluon and an anti-periodic boundary condition for the gluino. The resulting path integral computes correlators in a thermal state at temperature $T = 1/L$. For example, the path integral with no operator insertions gives the partition function, i.e. the exponential of minus the free energy over T. If we could compute such a path integral, then we could identify phase transitions from the free energy. However, such a path integral is prohibitively difficult to calculate: perturbative methods are unreliable because deconfinement occurs when $T \sim \Lambda$ and so the theory is strongly coupled, and lattice methods are unreliable because we want $\theta = \pi$, but any $\theta \neq 0$ has a "sign problem" due to the i multiplying θ in eq. (3.1), which comes from the Wick rotation to Euclidean signature.

Following ref. [49], we thus choose the second option for boundary conditions, namely periodic boundary conditions around the S^1 for *both* the gluon and gluino. These boundary conditions preserve SUSY, which at first may not seem helpful. If SUSY is preserved then the path integral with no operator insertions is a Witten index [50; 51], which counts SUSY ground states. For gauge group $SU(N)$, this theory's Witten index is simply $SU(N)$'s dual Coxeter number, N. Moreover, the Witten index is invariant under any continuous deformation that preserves SUSY, including continuous changes in $1/L$. As a result, no phase transitions can occur as a function of $1/L$: the theory is always in a confined phase, with centre symmetry preserved, and CP symmetry preserved when $\theta = 0$, explicitly broken when $\theta \in (0, \pi)$, and spontaneously broken when $\theta = \pi$.

However, following ref. [49], we will break SUSY softly by introducing a small gluino mass, $m \ll \Lambda$, so that the path integral is no longer a Witten index, and in particular can vary as a function of $1/L$, allowing for the possibility of phase transitions. Actually, strictly speaking, given our boundary conditions, any changes in symmetries will be *quantum* phase transitions, occurring at $T = 0$, and hence arising from quantum rather than thermal fluctuations. Nevertheless, again following ref. [49], to guide our intuition we will think of $1/L$ as temperature, treat the path integral as a measure of "free energy", and refer to any symmetry changes simply as "phase transitions".

Crucially, when $m \ll \Lambda$, SUSY still provides enough control to compute the path integral, at least in combination with approximations that we will describe in detail in sec. 3.2.1, including L small enough to justify perturbation theory in $g(1/L) \ll 1$, and energy small enough to justify an effective description, i.e. to integrate out all but the lightest modes. In these limits, for any N and θ a deconfinement transition occurs as L shrinks, so that centre symmetry breaks spontaneously at some critical L, i.e. some critical "temperature". The deconfinement transition is first order when $N > 2$ and second order when $N = 2$ [52]. When $\theta = 0$ or $\theta = (0, \pi)$, CP symmetry is unchanged in the deconfinement transition, remaining preserved or explicitly broken, respectively. However, when $\theta = \pi$, CP symmetry is restored at some critical L, which for $N > 2$ is the same critical L as deconfinement, but when $N = 2$ is a *smaller* critical L. Indeed, the main result of ref. [49] is that when $N = 2$, as L shrinks deconfinement occurs before CP restoration, producing, for some range of L, a phase with spontaneously broken centre *and* CP symmetries. From our perspective, this is a partial phase.

In sec. 3.2.1 we will work in the limits mentioned above: $m \ll \Lambda$, small L, and low energy. In particular, following refs. [53; 54; 47; 52; 55; 56] we will perform a dimensional reduction on the S^1, retaining sufficiently light modes, and obtaining an effective theory on $\mathbb{R}^3$. If we then take the so-called Abelian large-N limit, explained below, then the extrema of that effective theory's potential give the free energy of the original theory on $S^1 \times \mathbb{R}^3$. In sec. 3.2.2, we will review known solutions for locally stable minima describing the confined phase for any N, and the deconfined phase in the Abelian large-N limit. In sec. 3.2.3 we will present novel solutions for locally unstable maxima describing the partial phase in the Abelian large-N limit. Our main result will be that in the partial phase, $\mathrm{tr}(F_{\mu\nu}\tilde{F}^{\mu\nu})$ has a non-zero expectation value, $\langle \mathrm{tr}(F_{\mu\nu}\tilde{F}^{\mu\nu}) \rangle \neq 0$, indicating spontaneous breaking of CP symmetry. As a result, $\langle \mathrm{tr}(F_{\mu\nu}\tilde{F}^{\mu\nu}) \rangle$ provides a gauge-invariant order parameter distinguishing the deconfined and partial phases.

3.2.1 The Effective Theory on $\mathbb{R}^3$

In this subsection we will briefly review the derivation of the effective theory of refs. [52; 54; 47; 55], reviewed recently in ref. [56]. The derivation consists of Kaluza-Klein (KK) reducing all fields on the S^1 and integrating out all modes except the lightest modes, thus obtaining an effective theory of these light modes in $\mathbb{R}^3$. Our goal is to derive this effective theory's (bosonic) potential, $\mathcal{V}$, whose extrema give the free energy of the original theory on $S^1 \times \mathbb{R}^3$. We will begin with $m = 0$, and exploit the full power of SUSY to derive the effective theory in $\mathbb{R}^3$. We will then break SUSY softly, by introducing $m \ll \Lambda$, and compute $\mathcal{V}$ to order m, and in the limit of weak coupling, as mentioned above.

In the KK reduction from $S^1 \times \mathbb{R}^3$ to $\mathbb{R}^3$, the gluon's S^1 component, A_0, reduces to a KK tower of adjoint scalars in $\mathbb{R}^3$, including a massless adjoint scalar. In fact, we can gauge away the massive adjoint scalars: via gauge transformations we make A_0 constant over the S^1. We can also gauge transform A_0 to be diagonal in $SU(N)$. Doing so makes the Polyakov loop operator diagonal, with each diagonal entry being pure phase,

$$\langle \mathcal{P} e^{i \oint dx_0 A_0} \rangle = \langle e^{iLA_0} \rangle = \begin{pmatrix} e^{i\phi_0} & & \\ & \ddots & \\ & & e^{i\phi_{N-1}} \end{pmatrix}, \tag{3.3}$$

where $\mathcal{P}$ denotes path-ordering, each phase ϕ_i is 2π periodic, $\phi_i \sim \phi_i + 2\pi$ for $i = 0, \ldots, N-1$, and because the gauge group is $SU(N)$, $\sum_{i=0}^{N-1} \phi_i \equiv 0 \bmod 2\pi$. The only remaining gauge invariance is the Weyl group, which for $SU(N)$ is the permutation group, S_N. We use S_N permutations to order the phases,

$$0 \leq \phi_{N-1} \leq \phi_{N-2} \leq \cdots \leq \phi_0 \leq 2\pi, \tag{3.4}$$

modulo their periodic identifications. With these choices we have fixed the gauge completely. We next collect these phases into an N-component vector,

$$\boldsymbol{\phi} = (\phi_0, \phi_1, \cdots, \phi_{N-1}), \tag{3.5}$$

which in the effective theory on $\mathbb{R}^3$ is an adjoint Higgs field.

In the KK reduction, the gluon's spatial components reduce to a KK tower of vector fields in $\mathbb{R}^3$, including massless $SU(N)$ gauge fields and their massive KK partners. The gluino reduces to a KK tower of fermionic fields, which when $m = 0$ are the superpartners of the vector fields and the adjoint Higgs field, $\boldsymbol{\phi}$. We integrate out all the massive KK fields, obtaining an effective theory of the massless fields alone, namely the massless $SU(N)$ vector, a massless three-dimensional Dirac fermion, and $\boldsymbol{\phi}$, which together comprise a three-dimensional $\mathcal{N} = 2$ vector multiplet.

A non-trivial Higgs field $\boldsymbol{\phi}$ breaks the gauge group $SU(N)$ to a subgroup. Following refs. [52; 54; 47; 55; 56], we assume that all the phases ϕ_i are distinct, so that the gauge group breaks to the maximal Abelian subgroup, $SU(N) \to U(1)^{N-1}$. Such a vacuum is generic, compared to vacua where some ϕ_i are the same, and hence $SU(N)$ breaks to a subgroup with at least one non-Abelian factor. In the maximal Abelian case, the off-diagonal entries of the $SU(N)$ gauge field, also known as the W-bosons, acquire masses $\geq \frac{2\pi}{NL}$, whereas the diagonal gauge field entries comprise a number N of massless $U(1)$ gauge fields in $\mathbb{R}^3$. We integrate out the W-bosons, obtaining an effective theory of the massless fields alone, namely the N $U(1)$ gauge fields, the adjoint Higgs field $\boldsymbol{\phi}$, and their fermionic superpartners. These fields interact with coupling strength $g(\frac{2\pi}{NL})$, that is, the running coupling "frozen" at the scale of the lightest W-boson. As mentioned above, we assume $\frac{2\pi}{NL} \gg \Lambda$, so that $g(\frac{2\pi}{NL}) \ll 1$. Henceforth, g will always denote $g(\frac{2\pi}{NL})$.

Again following refs. [52; 54; 47; 55; 56], we collect the N $U(1)$ gauge fields into an N-component vector of Abelian gauge fields, $\boldsymbol{A}$. We then Hodge dualise in $\mathbb{R}^3$ to obtain an N-component scalar field, $\boldsymbol{\sigma}$, the "scalar photon". Explicitly, we define $\boldsymbol{\sigma}$ via $d\boldsymbol{\sigma} \equiv \frac{4\pi L}{g^2}(*d\boldsymbol{A})$. Both $\boldsymbol{\phi}$ and $\boldsymbol{\sigma}$ come from a compact gauge group, so the components of each are 2π periodic.

The massless sector now consists of $\boldsymbol{\sigma}$, $\boldsymbol{\phi}$, and their fermionic superpartners. Together, these comprise a number N of three-dimensional $\mathcal{N} = 2$ chiral superfields. We collect these into an N-component $\mathcal{N} = 2$ chiral superfield, $\mathbf{X} = (X_0, X_1, \dots, X_{N-1})$, whose lowest component is an N-component complex scalar, $\boldsymbol{z}$, built from $\boldsymbol{\phi}$ and $\boldsymbol{\sigma}$:

$$\boldsymbol{z} \equiv i\left[\tau(\boldsymbol{\phi} - \boldsymbol{\phi}_W) + \boldsymbol{\sigma}\right], \tag{3.6}$$

where $\boldsymbol{\phi}_W$ is proportional to the $SU(N)$ Weyl vector: $(\boldsymbol{\phi}_W)_j = \frac{2\pi}{N}(N-1-j)$ for $j = 0, 1, \dots, N-1$. SUSY requires the bosonic part of the effective action to take the form [54]

$$S_{eff} = \int d^3\vec{x}\left[\mathcal{K}(\boldsymbol{X}, \boldsymbol{X}^\dagger)|_{\Theta\Theta\bar{\Theta}\bar{\Theta}} + \mathcal{W}(\boldsymbol{X})|_{\Theta\Theta} + \bar{\mathcal{W}}(\boldsymbol{X}^\dagger)|_{\bar{\Theta}\bar{\Theta}}\right], \tag{3.7}$$

where Θ and $\bar{\Theta}$ are the fermionic coordinates of superspace, $\mathcal{K}(\boldsymbol{X}, \boldsymbol{X}^\dagger)$ is the Kähler potential, and $\mathcal{W}(\boldsymbol{X})$ is the superpotential. The bosonic potential is then

$$\mathcal{V} = \left(\frac{\partial^2\mathcal{K}}{\partial d\boldsymbol{z}\,\partial d\boldsymbol{z}^\dagger}\right)^{-1}\left|\frac{\partial\mathcal{W}}{\partial\boldsymbol{z}}\right|^2. \tag{3.8}$$

In the effective theory of refs. [52; 47; 55; 56], the Kähler potential includes a trivial, classical contribution, plus perturbative loop corrections. In what follows, we will need only the trivial, classical contribution, for which the bosonic fields' kinetic terms are simply

$$\mathcal{K}(\boldsymbol{X}, \boldsymbol{X}^\dagger)|_{\Theta\Theta\bar{\Theta}\bar{\Theta}} = \frac{g^2}{16\pi^2 L}|d\boldsymbol{z}|^2 = \frac{1}{g^2 L}|d\boldsymbol{\phi}|^2 + \frac{g^2}{16\pi^2 L}|d\boldsymbol{\sigma} + \frac{\theta}{2\pi}d\boldsymbol{\phi}|^2. \tag{3.9}$$

Generically, in any SUSY theory the superpotential, $\mathcal{W}$, is a sum of two contributions, one perturbative and one non-perturbative. In this case, the classical superpotential vanishes, and SUSY non-renormalisation theorems subsequently guarantee that all perturbative contributions vanish.

The non-perturbative contribution to $\mathcal{W}$ is non-zero due to so-called monopole-instantons, which come from the KK reduction of instantons. Monopole-instantons have non-zero Chern number, and hence non-zero topological charge, and an index theorem then implies that they have two fermionic zero modes [57]. They can therefore contribute to $\mathcal{W}$. The resulting form of $\mathcal{W}$ is determined, up to an overall constant, by holomorphy in $\boldsymbol{X}$, single-valuedness under the periodic shifts in σ, and the R-symmetry. A calculation of Ψ's two-point correlator then fixes the overall constant. Detailed discussions of the monopole-instantons and their contribution to $\mathcal{W}$, appear in refs. [52; 54; 47; 55; 57; 56]. We only need the final result for $\mathcal{W}$, which is

$$\mathcal{W}(\boldsymbol{X}) = \frac{LM_{\rm PV}}{g^2}\left(\sum_{j=0}^{N-1} e^{(X_j - X_{j+1})} + e^{2\pi i\tau + (X_0 - X_1)}\right). \tag{3.10}$$

The monopole-instanton operators are

$$M_j \equiv \exp\left((z_j - z_{j+1}) + i\frac{\theta}{N}\right), \tag{3.11}$$

where for $j = N-1$ we define $z_{j+1} = z_N \equiv z_0$. Crucially, the M_j are not all independent: their definition in eq. (3.11) implies the constraint,

$$M_0 \times M_1 \times \cdots \times M_{N-1} = e^{i\theta}. \tag{3.12}$$

Evaluating $\mathcal{W}$ in eq. (3.10) on the lowest component of $\boldsymbol{X}$ shows explicitly how the monopole-instantons contribute:

$$\mathcal{W}(\boldsymbol{z}) = \frac{LM_{\rm PV}}{g^2}\, e^{-i\frac{\theta}{N}}\left[\sum_{j=0}^{N-1} M_j + e^{2\pi i\tau} M_0\right]. \tag{3.13}$$

Plugging $\mathcal{K}$ from eq. (3.9) and $\mathcal{W}$ from eq. (3.13) into eq. (3.8) gives us the bosonic potential,

$$\begin{aligned} \mathcal{V} &= \mathcal{V}_0 \sum_{j=0}^{N-1} |M_j - M_{j-1}|^2, && (3.14a)\\ &= \mathcal{V}_0 \sum_{i=0}^{N-1}\left[M_j M_j^* - M_j M_{j-1}^* - M_{j-1} M_j^* + M_{j-1} M_{j-1}^*\right], && (3.14b) \end{aligned}$$

where the overall constant is most compactly written in terms of Λ in eq. (3.2a),

$$\mathcal{V}_0 \equiv \frac{9\,N^2}{(4\pi)^2}\frac{L^3\,\Lambda^6}{g^2}. \tag{3.15}$$

Although the superpotential $\mathcal{W}$ in eq. (3.13) received contributions from individual monopole-instantons, M_j, the bosonic potential $\mathcal{V}$ in eq. (3.14) receives contributions only from bound states of monopole-instantons with anti-monopole-instantons, such as $M_j M_j^*$. These so-called "bions" have zero net topological charge, and hence have no fermionic zero modes. A microscopic analysis shows that these bions are held together by fermion exchange [58].

Using eqs. (3.6) and (3.11) we can determine how the monopole-instantons M_j transform under centre and CP symmetries. A centre symmetry transformation simply permutes the Polyakov line phases, $\phi_j \to \phi_{j+1}$, with $\phi_{N+1} \equiv \phi_0$. A CP symmetry transformation sends $\theta \to -\theta$, leaving everything else in M_j unchanged. We thus find

$$\begin{aligned} \text{centre:} \quad & M_j \to M_{j+1}, \\ \text{CP:} \quad & M_j \to M_j^*. \end{aligned}$$

As a result, centre symmetry is preserved only when all the M_j take the same value, and CP symmetry is preserved only when all the M_j are real-valued. The bion contributions to $\mathcal{V}$ in eq. (3.14) provide a repulsive interaction for the ϕ_j, and hence ultimate produce centre symmetry and confinement. The potential in eq. (3.14) also clearly preserves CP symmetry.

We now introduce a small gaugino mass, $m \ll \Lambda$, to break SUSY softly. In this case, we can write $\mathcal{V}$ as a sum of two contributions, one perturbative and one non-perturbative, where each contribution consists of the SUSY result plus terms scaling with powers of m.

When $m \ll \Lambda$, the perturbative contribution to $\mathcal{V}$ (sometimes called the Gross-Pisarski-Yaffe potential [59]) becomes non-zero, but turns out to be $\mathcal{O}(m^2 \mathcal{V}_0 \, g^6 \, N^2)$ [49; 52; 47]. In our limit $g \ll 1$, this will be sub-leading compared to the non-perturbative contribution described below, so we will henceforth ignore the perturbative contribution to $\mathcal{V}$.

When SUSY is broken, the non-perturbative contribution to $\mathcal{V}$ again comes from monopole-instantons with no fermion zero modes. However, m lifts the fermion zero modes of the monopole-instantons and anti-monopole instantons, M_j and M_j^*, so that these can now contribute individually, rather than only via bions. In other words, (anti-)monopole-instantons with non-zero topological charge can now contribute. Indeed, to leading non-trivial order in m, the result of refs. [52; 47; 55] for the bosonic potential is

$$\mathcal{V} = \mathcal{V}_0 \sum_{j=0}^{N-1} |M_j - M_{j-1}|^2 - \mathcal{V}_0 \, \frac{\gamma}{2} \left[1 - \frac{g^2 \, N}{(4\pi)^2} \, \log\left(M_j^* M_j \right) \right] \left(M_j + M_j^* \right), \tag{3.16}$$

where we have defined

$$\gamma \equiv \frac{32\pi^2}{3N^2} \frac{m}{L^2 \Lambda^3}, \tag{3.17}$$

which is a measure of the inverse circumference, L. In what follows, we will treat γ as a proxy for temperature, or more precisely, because $\gamma \propto L^{-2}$, as a proxy for T^2. We will also re-scale the bosonic potential by $\mathcal{V}_0$,

$$V \equiv \mathcal{V} / \mathcal{V}_0, \tag{3.18}$$

and henceforth we will work only with the re-scaled bosonic potential, V, rather than $\mathcal{V}$.

While the bion contributions to V provide a repulsive interaction for the ϕ_j, thus encouraging centre symmetry and confinement, in contrast, the individual monopole-instanton contributions provide an attractive interaction for the ϕ_j, encouraging them to bunch up and break centre symmetry, signaling deconfinement. As the "temperature" γ increases, the latter contributions increase until a deconfinement transition occurs that is first order when $N > 2$ and second order when $N = 2$, as mentioned above [49; 52; 47; 55; 56].

We will work with coupling g sufficiently weak that the kinetic terms, including those for the bosons in eq. (3.9), are negligible, and the potential in eqs. (3.16) and (3.18) reduces to

$$V = \sum_{j=0}^{N-1} |M_j - M_{j-1}|^2 - \frac{\gamma}{2} \sum_{j=0}^{N-1} \left(M_j + M_j^* \right) . \tag{3.19}$$

Eq. (3.19) is the effective action that we will use in all that follows. The weak-coupling limit also justifies a saddle-point approximation, where for us the extrema of the effective action are the extrema of V in eq. (3.19), subject to the constraint in eq. (3.12). These extrema coincide with the "free energy" of the mass-deformed $\mathcal{N} = 1$ SU(N) super Yang-Mills on $\mathbb{R}^3 \times \mathrm{S}^1$, so we will use the symbol V to denote this free energy as well.

This effective action is valid for any N, however for a precise definition of the partial phase we need a continuous eigenvalue spectrum, which requires $N \to \infty$. Crucially, as observed in ref. [47], this effective theory breaks down in the standard 't Hooft large-N limit, $N \to \infty$ with $g^2 N$ is fixed, because the W-boson masses, which are $\propto 1/(NL)$, approach zero. In the 't Hooft large-N limit we would thus need to modify the effective action to include these "extra" massless degrees of freedom.

Instead of the 't Hooft large-N limit, following refs. [47; 49] we will take the so-called *Abelian* large-N limit: $N \to \infty$ with the W-boson masses fixed, so that in particular $L \propto 1/N \to 0$, that is, we shrink the S^1. The hierarchy of scales thus remains $m \ll \Lambda \ll 2\pi/(NL)$. To emphasise how the 't Hooft and Abelian large-N limits are different: the former has $g \propto 1/N^2 \to 0$ with any L, while the latter has any g with $L \propto 1/N \to 0$. In other words, the 't Hooft large-N limit says nothing about L, while the Abelian large-N limit says nothing about g.

3.2.2 Review: Confined and Deconfined Phases

In this subsection we will discuss the two extrema of the effective theory with action V in eq. (3.19) that were discovered in ref. [49]. These extrema are minima describing the confined and deconfined phases. In the next subsection we will present our new results for the maximum that connects these minima, and which describes the partial phase.

A central challenge in extremising V in eq. (3.19) is implementing the constraint in eq. (3.12). We can deal with this constraint in several ways. A simple approach is to treat M_0 as a function of $M_1, M_2, \cdots, M_{N-1}$, as $M_0 = \frac{e^{i\theta}}{M_1 \times \cdots \times M_{N-1}}$. In that case, for $j > 0$, we easily find $\frac{\partial M_0}{\partial M_j} = -\frac{M_0}{M_j}$. The saddle-point equation, $\frac{\partial V}{\partial M_j} = 0$, can then be written as

$$2M_j^* - M_{j+1}^* - M_{j-1}^* + \frac{M_0}{M_j}\left(M_1^* - M_0^*\right) + \frac{M_0}{M_j}\left(M_{N-1}^* - M_0^*\right) - \frac{\gamma}{2} + \frac{\gamma}{2}\frac{M_0}{M_j} = 0. \quad (3.20)$$

3.2.2.1 Confined phase

Ref. [49] found the saddle point solution of eq. (3.20) describing the confined phase, valid for any N (not just large N):

$$M_0 = M_1 = M_2 = \cdots = M_{N-1} = e^{i\theta/N}. \quad (3.21)$$

The free energy of the confined phase is then

$$V|_{\text{conf}} = -N\gamma\cos(\theta/N). \quad (3.22)$$

To see that the solution in eq. (3.21) describes the confined phase, we use the definitions of z_j and M_j in eqs. (3.6) and (3.11), respectively, to find an expression for the Polyakov loop phases ϕ_j in terms of the M_j,

$$\phi_j - \phi_{j+1} = \frac{2\pi}{N} - \frac{g^2}{4\pi}\log|M_j|. \quad (3.23)$$

In eq. (3.21), $|M_j| = 1$ for all j, hence from eq. (3.23) we have $\phi_j - \phi_{j+1} = \frac{2\pi}{N}$. This saddle-point solution therefore possesses a uniform Polyakov phase distribution, and thus unbroken centre symmetry, indicating that this is indeed the confined phase. The distribution is normalised, having height $\frac{1}{2\pi}$.

As an order parameter for the CP symmetry we will use $\frac{\partial V}{\partial\theta}$, which in the effective theory is proportional to the expectation value of a CP-odd operator, namely the instanton density: $\frac{\partial V}{\partial\theta} \propto \langle\text{tr}(F_{\mu\nu}\tilde{F}^{\mu\nu})\rangle$. From eqs. (3.21) and (3.22) we find

$$\left.\frac{\partial V}{\partial\theta}\right|_{\text{conf}} = \gamma\sin\left(\theta/N\right). \quad (3.24)$$

When $\theta = 0$, the CP symmetry is not explicitly broken, and the M_j in eq. (3.21) are purely real, hence CP symmetry is not spontaneously broken. Correspondingly,

$\frac{\partial V}{\partial \theta}\Big|_{\text{con}} = 0$. When $\theta \in (0, \pi)$, CP symmetry is explicitly broken, and unsurprisingly, all the M_j in eq. (3.21) are complex, and $\frac{\partial V}{\partial \theta}\Big|_{\text{con}} \neq 0$. When $\theta = \pi$, the CP symmetry is not explicitly broken, but all the M_j's in eq. (3.21) are complex, hence CP symmetry is spontaneously broken. Correspondingly, $\frac{\partial V}{\partial \theta}\Big|_{\text{con}} = \gamma \sin(\pi/N) \neq 0$.

The results above are valid for any N. If we take the Abelian large-N limit, then remembering from eq. (3.17) that $\gamma \propto N^{-2}$, we find that $V|_{\text{conf}} \sim N^{-1}$, while $\frac{\partial V}{\partial \theta}\Big|_{\text{conf}} \sim N^{-3}$. These large-$N$ scalings are in fact generic, as we will see below.

3.2.2.2 Deconfined phase

Following ref. [49], we find the saddle point solution describing the deconfined phase only in the Abelian large N limit, as follows.

To deal with the constraint in eq. (3.12), we will assume that M_0 is much smaller than all the other M_j, that is, $M_0 \ll M_j$ for all $j > 0$. As we will see later, this is self-consistent only for sufficiently large temperature γ. With this assumption, the saddle-point equation as written in eq. (3.20) simplifies to

$$2M_j^* - M_{j+1}^* - M_{j-1}^* - \frac{\gamma}{2} = 0. \tag{3.25}$$

To solve eq. (3.25), we take all the M_j's to be real-valued, which among other things ensures that the solution will preserve CP symmetry. We also take the Abelian large-N limit with N sufficiently large to justify a continuum approximation, and retain only contributions at leading order in N. Specifically, we treat $t \equiv \frac{j}{N} - \frac{1}{2}$ as a continuous "time" parameter, and we use a notation $X(t) \equiv M_j$. Using the periodicity $X(t) = X(t+1)$ we can take $t \in [-1/2, 1/2]$. Furthermore, since our temperature parameter $\gamma \propto N^{-2}$ from eq. (3.17), we also define for convenience a re-scaled temperature parameter that will remain order N^0 in the Abelian large-N limit,

$$\tilde{\gamma} \equiv N^2 \gamma. \tag{3.26}$$

With these approximations and definitions, eq. (3.25) becomes a simple second-order, linear, ordinary differential equation,

$$X''(t) = -\frac{\tilde{\gamma}}{2}, \tag{3.27}$$

where $X'(t) \equiv \frac{dX}{dt}$. The solution of eq. (3.27) is quadratic in t,

$$X(t) = A + Bt - \frac{\tilde{\gamma}}{4} t^2, \tag{3.28}$$

with integration constants A and B. Plugging the solution in eq. (3.28) and our approximations and definitions into the effective action V in eq. (3.19), we find

$$V = \frac{1}{N}\int_{-1/2}^{+1/2} |X'|^2 dt - \frac{\tilde{\gamma}}{N}\int_{-1/2}^{+1/2} X dt + X(-1/2)^2 + X(1/2)^2. \tag{3.29}$$

The last two terms come from $|M_1 - M_0|^2$ and $|M_{N-1} - M_0|^2$, which have to be treated separately because we assumed M_0 to be an outlier. Assuming that X is of order N^0, the first two terms in eq. (3.29), i.e. the terms involving integrals over t, are actually sub-leading in N, while the last two terms are dominant. We already minimised the former by solving eq. (3.27), so to be consistent we must also minimise the latter, meaning we take

$$X(-1/2) = X(1/2) = 0. \tag{3.30}$$

These boundary conditions fix the integration constants A and B, so that the saddle-point solution in eq. (3.28) becomes

$$X(t) = \frac{\tilde{\gamma}}{16}\left(1 - 4t^2\right). \tag{3.31}$$

The corresponding free energy is

$$V|_{\text{deconf}} = -\frac{1}{48}\frac{\tilde{\gamma}^2}{N}. \tag{3.32}$$

This conforms to the generic behaviour $V \sim N^{-1}$ mentioned at the end of sec. 3.2.2.1.

We now need to check when $M_0 \ll M_j$ for $j > 0$, and hence the solution is self-consistent. To do so, we follow ref. [49], and estimate M_0 by integrating $\log(X(t))$ over $t \in [-1/2, 1/2]$, which gives the continuum version of $\sum_{j>0} \ln M_j$, and then exponentiating and using $M_0 = e^{i\theta}/(M_1 \dots M_N)$ to obtain

$$M_0 \simeq \frac{e^{i\theta}}{N}\left(\frac{4e^2}{\tilde{\gamma}}\right)^{N-1}, \tag{3.33}$$

where because we assumed all the M_j are real, including M_0, in eq. (3.33) $\theta = 0$ or π. For M_0 to be vanishingly small, we demand $\frac{4e^2}{\tilde{\gamma}} < 1$, or equivalently $\tilde{\gamma} > 4e^2 = 29.556\cdots$. In other words, we need the temperature $\tilde{\gamma} \equiv N^2\gamma$ to be sufficiently large, as advertised.

Let us now show that the centre symmetry is spontaneously broken. Eq. (3.33) gives

$$-\frac{g^2}{4\pi}\ln|M_0| \sim -\frac{g^2}{4\pi} N \log\left(\frac{4e^2}{\tilde{\gamma}}\right), \tag{3.34}$$

which indeed can be much bigger than that of all the other M_j. Defining for convenience

$$\epsilon \equiv N \frac{g^2}{4\pi}, \tag{3.35}$$

and using eq. (3.23), we find a finite spacing between the Polyakov loop phases ϕ_1 and ϕ_0,

$$\phi_0 - \phi_1 \simeq -\epsilon \log\left(\frac{4e^2}{\tilde{\gamma}}\right), \tag{3.36}$$

which is ≥ 0 in our limit $\frac{4e^2}{\tilde{\gamma}} < 1$. As a result, the saddle point solution in eq. (3.31) describes a distribution of Polyakov line phases with a gap, and thus the centre symmetry is broken, indicating that this is indeed the deconfined phase. The gap closes as $4e^2/\tilde{\gamma} \to 1$. As we will see in subsection 3.2.3, $4e^2/\tilde{\gamma} = 1$ can be regarded as the GWW transition point.

The rest of the distribution behaves as follows. The solution $X(t)$ starts at zero when $t = -\frac{1}{2}$, goes all the way up to $\frac{\tilde{\gamma}}{16} > 1$ when $t = 0$, and then comes down to zero when $t = \frac{1}{2}$. As a result, as t increases $\ln(X(t))$ is initially negative, then at some point turns positive, and then becomes negative again. If $X(t) < 1$ then $\phi_j - \phi_{j+1} < \frac{2\pi}{N}$, namely the distribution is more dense. If $X(t) > 1$ then $\phi_j - \phi_{j+1} > \frac{2\pi}{N}$, namely the distribution is more sparse. In short, the Polyakov phases grow sparser as j increases.

As mentioned below eq. (3.25), this saddle-point solution assumed all the M_j are real, and hence CP symmetry is not spontaneously broken. Correspondingly, the V in eq. (3.29) or (3.32) does not depend on θ at all. As a result, $\frac{\partial V}{\partial \theta} = 0$, and hence our order parameter for CP symmetry breaking vanishes, $\langle \mathrm{tr}(F_{\mu\nu}\tilde{F}^{\mu\nu}) \rangle = 0$.

3.2.3 Partial phase

In this subsection, we will find new solutions of the effective theory with action V in eq. (3.19) that describe a partial phase. We will begin with the Abelian large-N limit, and with $\theta = 0$, where we will find an unstable partial phase connecting the confined and deconfined phases. Of course, when $\theta = 0$ in this theory, CP symmetry is unbroken in both the confined and deconfined phases. We will find that CP symmetry is unbroken in the partial phase as well. We then consider $\theta = \pi$, where CP symmetry is broken in the confined phase and restored in the deconfined phase. We will find that when $\theta = \pi$, CP symmetry is broken in the partial phase.

We will then perform numerical computations with finite N, although we restrict to numerically large values $N \geq 30$. Our finite-N results are similar to those of the Abelian large-N limit. In particular, we will identify a partial phase that connects the confined and deconfined phases and, when $\theta = \pi$, exhibits spontaneous breaking of

CP symmetry. Our numerical results thus support our conjecture that the partial phase can be distinguished from both confined and deconfined phases by global symmetries, even at finite N.

3.2.3.1 Abelian large-N limit

We begin with the Abelian large-N limit, where we will use the continuous time parameter t and $M_j \to X(t)$, as defined in sec. 3.2.2.2. We will begin with $\theta = 0$, and will assume the M_j are all real, so that CP symmetry is unbroken. The large-N continuum limit of eq. (3.20) can then be written as

$$X''(t) = \frac{X(-1/2)}{X(t)}\left(X''(-1/2) + \frac{\tilde{\gamma}}{2}\right) - \frac{\tilde{\gamma}}{2}, \tag{3.37}$$

where for convenience we choose $X(-1/2)$ to be the minimum of the configuration. We must find solutions of eq. (3.37) that are periodic, $X(t) = X(t+1)$, and that obey the continuum version of the constraint in eq. (3.12),

$$\int_{-1/2}^{+1/2} dt \log X(t) = i\theta, \tag{3.38}$$

with $\theta = 0$.

For given initial values $X(-1/2)$ and $X''(-1/2)$, we solve eq. (3.37) numerically by the second-order Taylor method, reviewed in appendix 3.A. Actually, we numerically solve an equivalent equation, obtained by multiplying eq. (3.37) by $2X'(t)$, integrating from time 0 to t, and then taking the square root:

$$X'(t) = \pm\sqrt{X(-1/2)\log\left(\frac{X(t)}{X(-1/2)}\right)(2X''(-1/2) + \tilde{\gamma}) - \tilde{\gamma}(X(t) - X(-1/2))}, \tag{3.39}$$

where we used $X'(-1/2) = 0$ to set the integration constant. This is a consequence of our convention $M_j = M_{N-j}$ and the smoothness of the solution. Since we chose $X(-1/2)$ as the minimum, we use the $+$ branch of the root in eq. (3.39) in all of our computations.

For a particular choice of $X(-1/2)$ and $X''(-1/2)$ we check for the periodicity condition by integrating eq. (3.39) numerically to obtain the half-period τ,

$$\tau = \int_{X(-1/2)}^{X_{\max}} \frac{dX}{\sqrt{X(-1/2)\log\left(\frac{X}{X(-1/2)}\right)(2X''(-1/2) + \tilde{\gamma}) - \tilde{\gamma}(X - X(-1/2))}}. \tag{3.40}$$

A solution with the required periodicity will have $\tau = \frac{1}{2}$. For fixed $X(-1/2)$, we use Newton's method to find $X''(-1/2)$ such that $\tau = \frac{1}{2}$ is satisfied to high precision.

For a given value of $X(-1/2)$, therefore, we finally need to satisfy the constraint in eq. (3.38). To do so, we use the bisection method, varying upper and lower bounds on $X(-1/2)$ until the corresponding solution $X(t)$ satisfies eq. (3.38) to high precision. By choosing the initial upper and lower bounds on $X(-1/2)$ to be between 0 and 1, we are able to avoid the confined and deconfined solutions reviewed in subsection 3.2.2.

Given a numerical solution for $X(t)$, we can straightforwardly compute the on-shell action V. Fig. 3.2 shows our numerical results for NV as a function of the "temperature" $\tilde{\gamma}$, together with the results for NV in the confined phase eq. (3.22) and in the deconfined phase from eq. (3.32). (Appendix 3.A describes in detail how we determine the numerical uncertainties in V and $X(-1/2)$.) In fig. 3.2 we observe the "swallow-tail" shape characteristic of a first-order phase transition, with the partial phase as the unstable branch connecting the confined and deconfined branches.

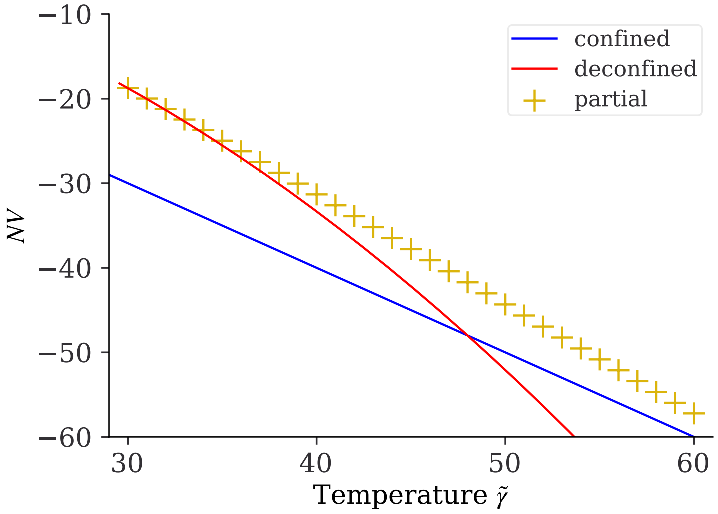

FIGURE 3.2: Free energy V times N versus "temperature" $\tilde{\gamma}$ in the Abelian $N = \infty$ limit, for any θ. We show NV of the confined phase from eq. (3.22) (blue line), the deconfined phase from eq. (3.32) (red line), and our numerical results for the partial phase (gold plus signs). We find the "swallow-tail" shape characteristic of a first-order phase transition, with the partial phase as the unstable branch connecting the confined and deconfined branches.

When $\theta = 0$, CP symmetry is preserved in all three phases. To study the spontaneous breaking of CP symmetry we need to set $\theta = \pi$, and compute our order parameter, $\frac{\partial V}{\partial \theta} \propto \langle \mathrm{tr}(F_{\mu\nu}\tilde{F}^{\mu\nu}) \rangle$. Crucially, however, in the Abelian large-N limit, generically $V \sim N^{-1}$, while $\frac{\partial V}{\partial \theta} \sim N^{-3}$, as we saw for example in the confined phase of sec. 3.2.2.1, and as we will find for the partial phase below. In other words, our results for NV in fig. 3.2 are in fact the leading contribution in the Abelian large-N limit for *any* value of

θ. We therefore do not need to re-compute NV for $\theta = \pi$: the result is the same as in fig. 3.2.

For $\theta = 0$ we assumed the M_j were real-valued, hence $\frac{\partial V}{\partial \theta} = 0$. If $\theta \neq 0$, then we expect $\frac{\partial V}{\partial \theta} \sim N^{-3}$. Generically, the magnitudes $|M_j| \sim N^0$, hence their leading contribution to $\frac{\partial V}{\partial \theta}$ will be unchanged in going from $\theta = 0$ to $\theta = \pi$. In other words, to compute $\frac{\partial V}{\partial \theta}$ when $\theta \neq 0$, we can use our existing solutions for the magnitudes $|M_j|$. By extension, if $\theta \neq 0$, then $\frac{\partial V}{\partial \theta}$ can be non-zero only due to the *phases* of the M_j. We thus need to compute the phases of the M_j, in the Abelian large-N limit.

Writing $M_j = |M_j| e^{i\varphi_j}$, from V in eq. (3.19) we find

$$\frac{\partial V}{\partial \varphi_j} = |M_j| \left(2|M_{j+1}| \sin(\varphi_j - \varphi_{j+1}) + 2|M_{j-1}| \sin(\varphi_j - \varphi_{j-1}) + \gamma \sin(\varphi_j)\right), \tag{3.41}$$

while the constraint in eq. (3.12) becomes

$$\sum_{j=0}^{N-1} \varphi_j = \theta. \tag{3.42}$$

The confined phase satisfies this constraint with $\varphi_j = \theta\, N^{-1}$ for all j, while in the deconfined phase all of the θ dependence is in $\varphi_0 = \theta$. Generically, the partial phase satisfies this constraint with all φ_j being different, but with $\varphi_j \sim N^{-1}$ for all j. Using the constraint, we can write the equation of motion of each φ_j as

$$\frac{\partial V}{\partial \varphi_j} = \frac{\partial V}{\partial \varphi_0}, \tag{3.43}$$

that is, because of the constraint, all $\partial V / \partial \varphi_j$ take the same value, namely $\partial V / \partial \varphi_0$. Large-$N$ counting in this equation of motion provides another way to see $\varphi_j \sim N^{-1}$ for all j, assuming $\tilde{\gamma}$ is an order N^0 distance from the GWW transition, so that $|M_j| \sim N^0$.

As mentioned above, when $\theta \neq 0$, to compute $\frac{\partial V}{\partial \theta}$ we can use the solutions for the $|M_j|$ at $\theta = 0$, so the only new contribution is from the φ_j. We can thus write

$$\frac{\partial V}{\partial \theta} = \sum_j \frac{\partial \varphi_j}{\partial \theta} \frac{\partial V}{\partial \varphi_j}. \tag{3.44}$$

Taking $\partial / \partial \theta$ of the constraint in eq. (3.42) gives us

$$\sum_j \frac{\partial \varphi_j}{\partial \theta} = 1. \tag{3.45}$$

Using eqs. (3.43) and (3.45), we can re-write eq. (3.44) as

$$\frac{\partial V}{\partial \theta} = \frac{\partial V}{\partial \varphi_j}, \tag{3.46}$$

that is, to obtain $\frac{\partial V}{\partial \theta}$ we can just compute $\partial V / \partial \varphi_j$ for any one value of j. If we choose $j = 0$, then

$$\frac{\partial V}{\partial \theta} = |M_0| \left(2|M_1| \sin(\varphi_0 - \varphi_1) + 2|M_{N-1}| \sin(\varphi_0 - \varphi_{N-1}) + \gamma \sin(\varphi_0)\right). \tag{3.47}$$

From eq. (3.47) we can argue that the order parameter will jump discontinuously at the GWW transition, as we expect for a first-order transition. In general, as we approach the GWW transition we expect $\phi_0 \to \pi$ and $\phi_{\pm 1} \to 0$, so that the partial phase matches onto the deconfined phase. In eq. (3.47), as we approach the GWW transition, naïvely we expect each sine function to approach zero, and hence $\frac{\partial V}{\partial \theta} \to 0$, indicating restoration of CP symmetry, as expected. Additionally, as we approach the GWW transition, we expect $|M_0| \to 0$ tends towards zero, further suppressing $\frac{\partial V}{\partial \theta}$. Our finite-$N$ results in the next subsection will indeed exhibit such behaviour, although $|M_0|$ will never precisely reach zero (but will decrease at the GWW transition as N increases). However, as mentioned above, in the Abelian large-N limit, $\varphi_j \sim N^{-1}$ for all j, including $j = 0$, so as we approach the GWW transition we will not see $\varphi_0 \to \pi$ smoothly. Instead, in the GWW transition, φ_0 will jump discontinuously from $\varphi_0 \sim N^{-1}$ in the partial phase to $\varphi_0 = \pi$ in the deconfined phase, and correspondingly $\frac{\partial V}{\partial \theta}$ will jump discontinuously. In the Abelian large-N limit, the CP symmetry restoration transition at the GWW point will therefore be first order.

To solve for the φ_j in the Abelian large-N limit, we expand the sine functions in eq. (3.41) to linear order, and then take the continuum limit and introduce the time parameter t from sec. 3.2.2.2, with $\varphi_j \to \varphi(t)$, so that eq. (3.43) becomes a differential equation for $\varphi(t)$. In this equation, $X(t)$ and its derivatives appear. To leading order in N we can use our existing $\theta = 0$ solutions for these, which allows us to write $\varphi(t)$'s equation of motion as

$$\varphi''(t) = \frac{-4XX'\varphi' + 2X(-1/2)^2\varphi''(-1/2) + \tilde{\gamma}(X\varphi - X(-1/2)\varphi(-1/2))}{2X^2}. \tag{3.48}$$

A solution $\varphi(t)$ must also be periodic, $\varphi(t+1) = \varphi(t)$, and obey the continuum version of the constraint in eq. (3.42)

$$\int_{-1/2}^{1/2} dt\, \varphi(t) = \theta. \tag{3.49}$$

For given values of $\varphi(-1/2)$ and $\varphi''(-1/2)$, we solve eq. (3.48) numerically using the second-order Taylor method, in analogy to what we did for $X(t)$ above (and reviewed in Appendix 3.A). To guarantee that $\varphi(t)$ is periodic in t and obeys the constraint in eq. (3.49), we fix values of $\varphi(-1/2)$ and $\varphi''(-1/2)$, as follows. We first choose $\varphi(-1/2) = 1$, and use the bisection method to determine $\varphi''(-1/2)$ such that the extreme values of $\varphi(t)$ occur at the terminating values of t, i.e. $\varphi'(\pm\frac{1}{2}) = 0$. This guarantees that the solution $\varphi(t)$ will be periodic. To guarantee that the solution obeys the constraint in eq. (3.49), we observe that eq. (3.48) is linear in $\varphi(t)$, and hence remains unchanged under a re-scaling of $\varphi(t)$. We thus simply re-scale $\varphi(-1/2)$ and $\varphi''(-1/2)$ until the constraint in eq. (3.49) is satisfied. Explicitly, if $c \equiv \int dt\, \varphi(t)$, then we re-scale $\varphi(-1/2) \to \varphi(-1/2)\frac{\theta}{c}$ and $\varphi''(-1/2) \to \varphi''(-1/2)\frac{\theta}{c}$.

For a given solution $\varphi(t)$, we computed $\frac{\partial V}{\partial \theta}$ in two different ways, as a cross-check. The first way was using the continuum version of eq. (3.46). The second way begins by observing that if we re-scale $\theta \to \xi\, \theta$ then we can obtain the new solution for $\varphi(t)$ simply by re-scaling $\varphi(t) \to \xi \varphi(t)$. Furthermore, we observe that in the continuum version of V, in the terms involving an integral over t, φ and φ' enter quadratically,

$$V \ni V_\varphi \equiv \int dt \left(X^2 \varphi'^2 + \frac{1}{2}\, \tilde{\gamma} X \varphi^2 \right). \tag{3.50}$$

We can thus evaluate $\partial V / \partial \theta$ at any θ by extracting the coefficient of the φ terms, V_φ, evaluated at θ, as

$$\frac{\partial V}{\partial \theta} = \frac{2}{\theta}\, V_\varphi \big|_\theta . \tag{3.51}$$

We have checked that numerical results obtained from eq. (3.46) or eq. (3.51) agree to great numerical accuracy.

Fig. 3.3 shows our numerical results for $\frac{\partial V}{\partial \theta}$ times N^3 at $\theta = \pi$ as a function of the "temperature" $\tilde{\gamma}$ in the partial phase. We see clearly that $\partial V / \partial \theta \propto \langle \mathrm{tr}(F_{\mu\nu} \tilde{F}^{\mu\nu}) \rangle \neq 0$, indicating spontaneous CP symmetry breaking. We also see that as we approach the GWW transition point, $\tilde{\gamma} \to 4e^2 \approx 29.556\ldots$, the order parameter $\frac{\partial V}{\partial \theta}$ does not approach zero, indicating a first-order CP symmetry restoring transition, as mentioned above. Fig. 3.3 also shows our finite-N numerical results, which we describe in the next subsection.

3.2.3.2 Finite N numerics

In this subsection we will perform numerical calculations in the effective theory with action V in eq. (3.19), with finite $N \geq 30$. Our goal will be to identify a partial phase. However, as mentioned in sec. 1.3, our definition of the partial phase is valid in the large-N limit ('t Hooft, Abelian, or otherwise), where we have a continuous distribution of Polyakov phases. Namely, we define the partial phase from the breaking of centre symmetry plus no gap in the distribution. Our numerics have finite N, and hence a discrete distribution. How then do we define the partial phase? Our working definition is the following. Eq. (3.23) allows us to write the eigenvalue density around any given ϕ_j as $\left(2\pi - Ng^2/(4\pi) \log |M_j|\right)^{-1}$. A gap occurs if the minimum of this eigenvalue density is zero. Using centre symmetry permutations we will always make M_0 the smallest of the M_j, so any gap will occur at

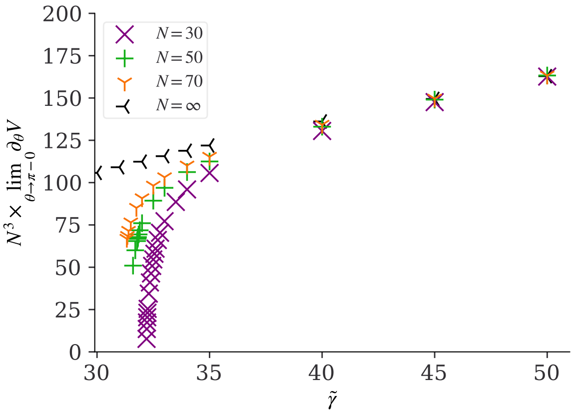

FIGURE 3.3: Numerical results in the partial phase for $\frac{\partial V}{\partial \theta} \propto \langle \mathrm{tr}(F_{\mu\nu}\tilde{F}^{\mu\nu})\rangle$ times N^3 in the limit $\theta \to \pi - 0$ as a function of "temperature" $\tilde{\gamma}$, for $N = 30$ (purple crosses), 50 (green plus signs), 70 (orange 3-point star), and ∞ (black 3-point star). The error bars are invisibly small on the scale of the plot. In all cases, we see clearly that $\langle \mathrm{tr}(F_{\mu\nu}\tilde{F}^{\mu\nu})\rangle \neq 0$ and hence CP symmetry is spontaneously broken in the partial phase. We also see that the finite-N results smoothly approach the $N = \infty$ result as $\tilde{\gamma}$ increases.

$\left(2\pi - Ng^2/(4\pi)^2 \log|M_0|\right)^{-1}$. This can vanish only if $|M_0|$ becomes exponentially small. In our new solutions we will explicitly find that $|M_0| < 1$, but that $|M_0|$ is not exponentially small at a finite distance from the GWW transition point. As a result, the distribution of the Polyakov line phases will not be gapped, which we use to identify a partial phase.

As further evidence that our numerical solutions describe a partial phase, we will also check the eigenvalues of the Hessian of V, whose components are $\frac{\partial^2 V}{\partial M_j \partial M_k}$, $\frac{\partial^2 V}{\partial M_j^* \partial M_k}$, and $\frac{\partial^2 V}{\partial M_j^* \partial M_k^*}$. At minima of V, all eigenvalues of the Hessian are positive, as occurs for the confined and deconfined phase solutions. We expect the partial phase solution to be a local maximum of V, with one negative eigenvalue in the Hessian, and all others positive. This is because in the partial phase at fixed temperature, when we change the energy we expect the free energy to decrease. In all the solutions we present below, we confirmed this expectation numerically, as we will discuss.

In appendix 3.B we collect some numerical data useful for anyone who wishes to reproduce our results.

Finite N numerical methods

We will use a combination of two numerical methods to find finite-N solutions for the M_j. The first is to solve the saddle-point equation in eq. (3.20), $\frac{\partial V}{\partial M_j} = 0$, via gradient descent. To do so, we define a function $\Phi_1(M_1, \cdots, M_{N-1})$ as

$$\begin{aligned}\Phi_1(M_1, \cdots, M_{N-1}) &\equiv \sum_{j=1}^{N-1} \left| \frac{\partial V}{\partial M_j} \right|^2 \\ = \sum_{j=1}^{N-1} &\left| 2M_j^* - M_{j+1}^* - M_{j-1}^* + \frac{M_0}{M_j}(M_1^* - M_0^*) + \frac{M_0}{M_j}(M_{N-1}^* - M_0^*) - \frac{\gamma}{2} + \frac{\gamma}{2}\frac{M_0}{M_j} \right|^2 .\end{aligned} \tag{3.52}$$

Solving eq. (3.20) is then equivalent to solving $\Phi_1(M_1, \cdots, M_{N-1}) = 0$. To do so, we minimise $\Phi_1(M_1, \ldots, M_{N-1})$ via gradient descent. Specifically, we choose some initial conditions for the M_j and then iteratively update them as $M_j \to M_j - \epsilon \frac{\partial \Phi_1}{\partial M_j^*}$, with some small step size ϵ. A drawback of this method is that generic initial conditions lead to the confined or deconfined solutions reviewed in subsection 3.2.2. We thus combine this first method with a second method that can generate suitable initial conditions for the first method, to avoid this problem.

The second method starts with V in eq. (3.19), and implements the constraint in eq. (3.12) not by replacing $M_0 = e^{i\theta}/(M_1 \ldots M_{N-1})$, as we have done so far, but by introducing a Lagrange multiplier κ, so that instead of extremising V we extremise $V + \kappa \left(\sum_j \log M_j - i\theta \right)$. This is equivalent to solving

$$M_j \frac{\partial V}{\partial M_j} = M_j \left(2M_j^* - M_{j-1}^* - M_{j+1}^* - \frac{\gamma}{2} \right) = -\kappa, \tag{3.53}$$

and simultaneously solving

$$\sum_{j=0}^{N-1} \log M_j - i\theta = 0. \tag{3.54}$$

The confined and deconfined solutions have $\kappa = \frac{\gamma N}{2} e^{i\theta/N}$ and $\kappa = 0$, respectively. Clearly, κ measures the size of the confined sector. Intuitively, fixed-γ gives the canonical ensemble, while fixed-κ gives the microcanonical ensemble. By re-writing eq. (3.53) as

$$2M_j^* - M_{j+1}^* - M_{j-1}^* - \frac{\gamma}{2} = -\frac{\kappa}{M_j}, \tag{3.55}$$

and then taking a sum over j and solving for γ, we find

$$\gamma = \frac{2\kappa}{N} \sum_{j=0}^{N-1} M_j^{-1}. \tag{3.56}$$

We then use the following strategy to find partial-phase solutions. We begin with $\theta = 0$, and we choose values for N and κ. As an initial condition, we use a discretised version of the deconfined solution in eq. (3.31), at the GWW transition point. In that solution, both the M_j and κ are real-valued, and together with N, determine γ via eq. (3.56). We then solve eq. (3.55) via gradient descent. In particular, we define a function

$$\begin{aligned}\Phi_2(M_1,\cdots,M_N) &\equiv \frac{1}{2}\sum_j\left(2M_j-M_{j+1}-M_{j-1}-\frac{\gamma}{2}+\frac{\kappa}{M_j}\right)^2+\frac{1}{2}\left(\sum_{j=1}^N\log M_j\right)^2\\ &=\frac{1}{2}\sum_j\left(2M_j-M_{j+1}-M_{j-1}-\frac{\kappa}{N}\sum_{k=1}^N M_k^{-1}+\frac{\kappa}{M_j}\right)^2+\frac{1}{2}\left(\sum_{j=1}^N\log M_j\right)^2\\ &=\frac{1}{2}\sum_j\left(2M_j-M_{j+1}-M_{j-1}+\frac{\kappa}{M_j}\right)^2\\ &\qquad-\frac{\kappa^2}{2N}\left(\sum_{j=1}^N M_j^{-1}\right)^2+\frac{1}{2}\left(\sum_{j=1}^N\log M_j\right)^2,\end{aligned}\tag{3.57}$$

so that eq. (3.55) is equivalent to $\Phi_2(M_1,\cdots,M_N)=0$, and we solve this latter equation via gradient descent. We found that if our initial κ is to large, then the gradient descent converges to the confined solution in eq. (3.21), but if we start with sufficiently small κ we find partial-phase solutions. With one solution for the partial phase, we can increase κ slightly, and use the solution as an initial condition for a new gradient descent. By iterating this procedure, we obtain solutions for a range of κ values. We then turn on a small θ for fixed N and γ, and use the $\theta=0$ partial-phase solution as an initial condition for the first method. By combining the two methods in this way, we found partial-phase solutions for a range of N, γ, and θ, including $\theta=0$ and $\theta=\pi$.

As mentioned above, to provide additional evidence that our solutions describe a partial phase, we also numerically computed the Hessian of V, whose explicit components are

$$\frac{\partial^2 V}{\partial M_j\partial M_k}=-\frac{M_0}{M_k}\left(M_1^*+M_{N-1}^*-2M_0^*+\frac{\gamma}{2}\right)\left(\frac{\delta_{jk}}{M_k}+\frac{1}{M_j}\right),\tag{3.58a}$$

$$\frac{\partial^2 V}{\partial M_j^*\partial M_k}=2\delta_{kj}-\delta_{k,j+1}-\delta_{k,j-1}+\frac{M_0}{M_k}(\delta_{1j}+\delta_{N-1,j})+\frac{M_0^*}{M_j^*}(\delta_{1k}+\delta_{N-1,k})+2\frac{M_0M_0^*}{M_kM_j^*},\tag{3.58b}$$

and a similar expression for $\frac{\partial^2 V}{\partial M_j^*\partial M_k^*}$. At minima of the free energy V, all eigenvalues of the Hessian are positive, as occurs for the confined and deconfined solutions in eqs. (3.21) and (3.31), respectively. We expect the partial phase solution to be a local maximum of V, with one negative eigenvalue in the Hessian, and all the other eigenvalues positive. For all numerical solutions used below, we confirmed this expectation explicitly.

Finite-N numerical results at $\theta = 0$

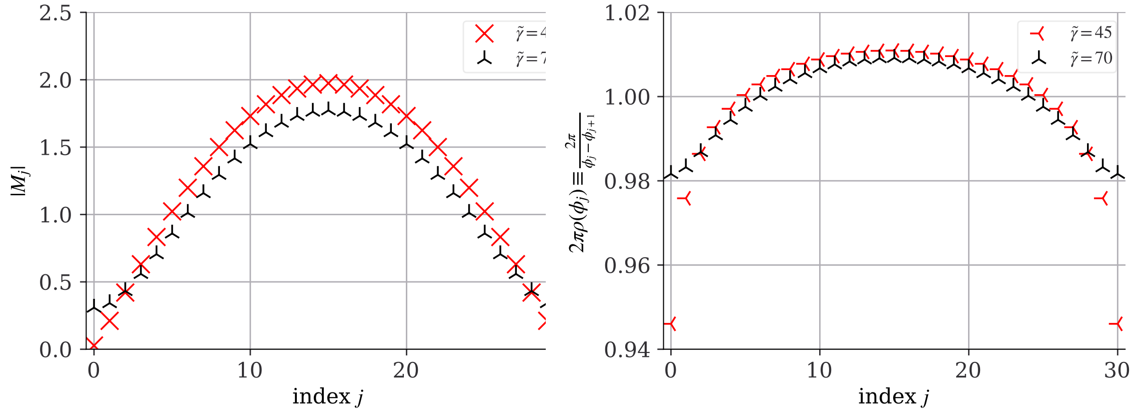

(A)

(B)

FIGURE 3.4: (a) $\theta = 0$ numerical results for the $|M_j|$ versus j for $N = 30$ in the partial phase, for $\tilde{\gamma} = 45$ (red crosses) and 70 (black 3-point stars). Notice that $|M_0|$ is small but non-zero. (b) Using eq. (3.23), with $g^2 = 0.1$, we converted the results of (a) into the Polyakov loop eigenvalue distribution $2\pi\rho(\phi_j) = \frac{2\pi}{\phi_j - \phi_{j+1}}$ versus j. The eigenvalue distribution is not flat, indicating spontaneous breaking of centre symmetry, and is not gapped, indicating that the phase is not deconfined. We thus identify these as partial phase solutions.

For $\theta = 0$, fig. 3.4 shows typical numerical solutions for the M_j and the corresponding distribution of Polyakov loop eigenvalues, $2\pi\rho(\phi_j) = \frac{2\pi}{\phi_j - \phi_{j+1}}$, in the partial phase, with $\tilde{\gamma} = 45$ and 70. For both values of $\tilde{\gamma}$, the eigenvalue distribution is not flat, indicating spontaneous breaking of the centre symmetry, and is not gapped, indicating that this phase is not deconfined. In particular, at $\tilde{\gamma} = 45$, observe that M_0 is small, but non-zero. We will explore $|M_0|$ in more detail momentarily.

Fig. 3.5 shows our numerical results for the free energy V times N as a function of $\tilde{\gamma}$ with $N = 30$ and $\theta = 0$. We see the swallow-tail shape characteristic of a first-order phase transition, with the partial phase appearing as the unstable branch connecting the confined and deconfined branches. In particular, the partial phase always has the highest free energy, and hence is always thermodynamically dis-favoured.

The phase diagram fig. 3.5, which has $N = 30$, is qualitatively similar to the phase diagram in fig. 3.2, which has $N = \infty$, suggesting that as we increase N, fig. 3.5 may evolve continuously into fig. 3.2. In other words, our numerical results suggest that the $N \to \infty$ limit of V is smooth. We provide additional evidence for this in fig. 3.6, which shows NV versus $1/N$ for several values of $\tilde{\gamma}$, and strongly suggests that as N increases, NV smoothly approaches the $N = \infty$ result. This also provides further

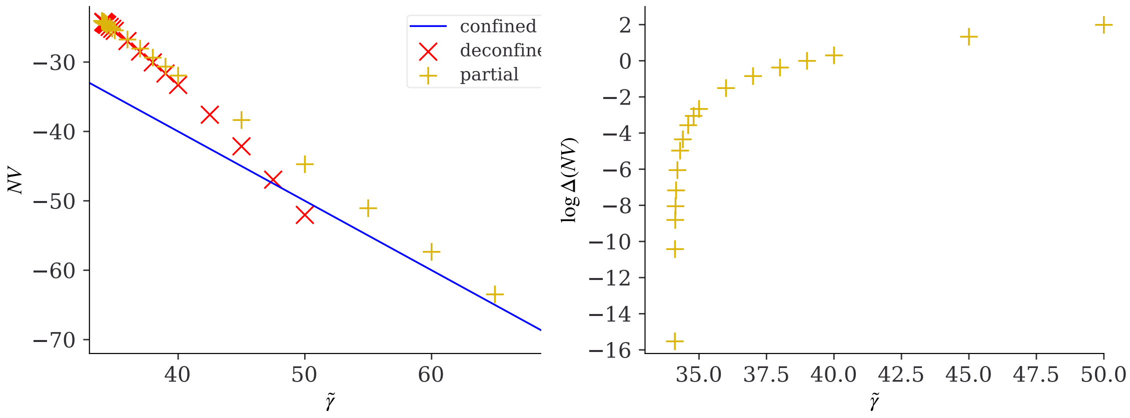

(A) (B)

FIGURE 3.5: (a) $\theta = 0$ numerical results for N times the free energy V as a function of $\tilde{\gamma}$ for $N = 30$, showing the confined phase (blue line), deconfined phase (red crosses), and partial phase (gold plus signs). We clearly observe a first-order transition, with the partial phase as the unstable branch connecting the confined and deconfined phases. (b) $\theta = 0$ numerical results for $\log(\Delta NV)$ versus $\tilde{\gamma}$ for $N = 30$, where ΔNV is the difference in NV between the partial and deconfined phases, $\Delta NV \equiv N(V|_{\text{partial}} - V|_{\text{deconf}})$. Clearly the partial phase has higher free energy than the deconfined phase near the transition between them (which at $N = \infty$ is the GWW transition).

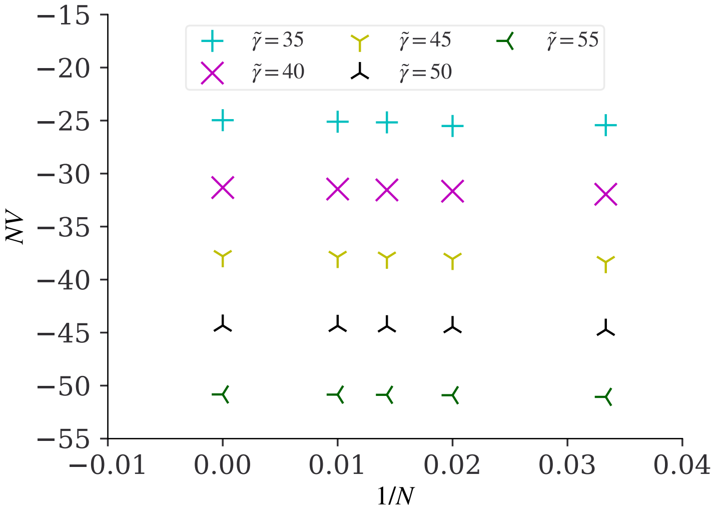

FIGURE 3.6: Our $\theta = 0$ numerical results for N times the tree energy V versus $1/N$ for $N = 30, 50, 70, 100, \infty$, or equivalently $1/N = 0.0333\ldots, 0.02, 0.0142\ldots, 0.01, 0$, for several values of $\tilde{\gamma}$. These results suggest that the $N \to \infty$ limit of V is smooth at each fixed $\tilde{\gamma}$.

evidence that our numerical solutions describe a partial phase, since they appear to connect smoothly to our $N = \infty$ partial phase solutions.

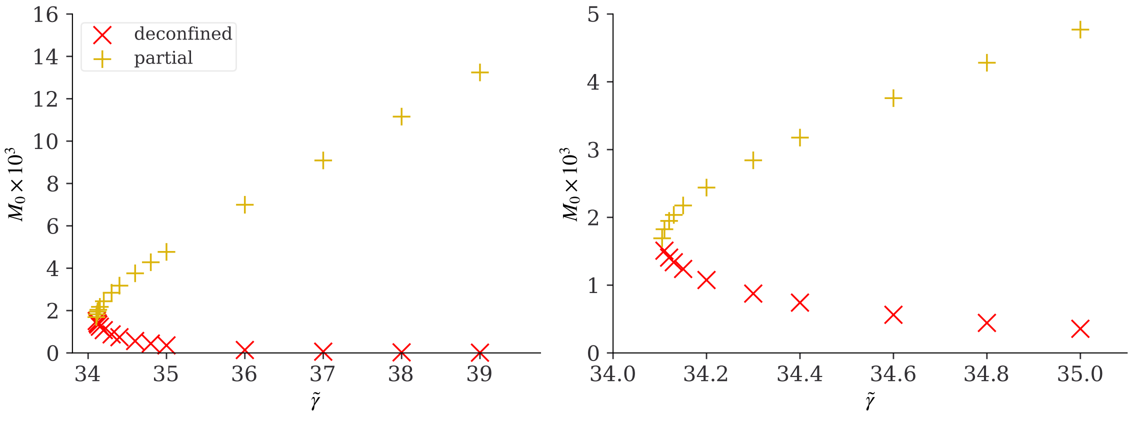

(A)

(B)

FIGURE 3.7: (a) $\theta = 0$ numerical results for $|M_0|$, magnified by a factor of 10^3 for clarity, as a function of $\tilde{\gamma}$, for $N = 30$, in the deconfined phase (red crosses) and partial phase (gold plus signs). $|M_0|$ in the deconfined phase becomes zero in the large-N limit. The gold plus signs have larger values, showing that our solutions indeed describe a partial phase. (b) Close-up of (a) near the transition point.

Fig. 3.7 shows $|M_0|$, magnified by a factor of 10^3 for clarity, as a function of $\tilde{\gamma}$ near the transition to the deconfined phase (which at $N = \infty$ is the GWW transition). Clearly, $|M_0|$ is small, but not exponentially small, near the transition point. In particular, $|M_0|$ is non-zero, justifying our interpretation of these solutions as the partial phase.

When $\theta = 0$ all the M_j are real and CP symmetry is preserved in all phases. As a result, our order parameter for CP symmetry breaking, $\frac{\partial V}{\partial \theta} \propto \langle \mathrm{tr}(F_{\mu\nu}\tilde{F}^{\mu\nu}) \rangle$, vanishes in all phases when $\theta = 0$. To see the spontaneous breaking of CP symmetry in the partial phase, we turn next to $\theta = \pi$.

Finite-N numerical results at $\theta = \pi$

For $\theta = \pi$, fig. 3.8 shows typical numerical solutions for the $|M_j|$ and the corresponding distribution of Polyakov loop eigenvalues, in the partial phase, with $\tilde{\gamma} = 45$ and 70. The results are qualitatively similar to the $\theta = 0$ case in fig. 3.4, although a key difference is that when $\theta = \pi$, the M_j's can have non-zero phases and hence CP symmetry can be spontaneously broken, as we will discuss in detail momentarily.

We next want to calculate V and $\frac{\partial V}{\partial \theta}$, both at $\theta = \pi$. To do so numerically, we calculated V at three values of θ near π, namely $\theta = 3.14159, 3.14155$, and 3.14149, and then extrapolated to $\theta = \pi$ by fitting to a form $V(\theta) = a \cdot (\theta - \pi) + b$ and numerically

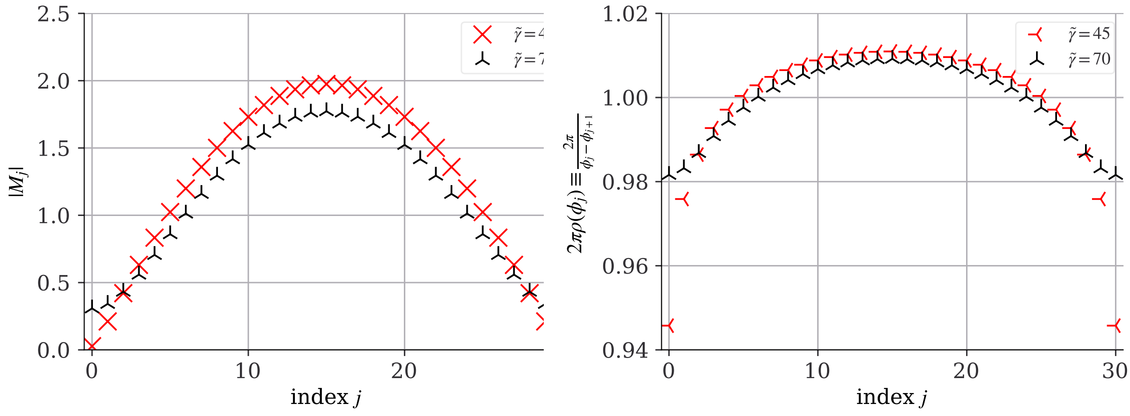

(A)

(B)

FIGURE 3.8: (a) $\theta = \pi$ numerical results for the $|M_j|$ versus j for $N = 30$ in the partial phase, for $\tilde{\gamma} = 45$ (red crosses) and 70 (black 3-point stars). Notice that $|M_0|$ is small but non-zero. (b) Using eq. (3.23), with $g^2 = 0.1$, we converted the results of (a) into the Polyakov loop eigenvalue distribution $2\pi\rho(\phi_j) = \frac{2\pi}{\phi_j - \phi_{j+1}}$ versus j. These results are qualitatively similar to those at $\theta = 0$ in fig. 3.4.

extracting the coefficients a and b. In this was we obtained V and $\frac{\partial V}{\partial \theta} = a$ at $\theta = \pi$. We performed a similar extrapolation for $|M_0|$ as well.

Fig. 3.9 shows our numerical results for the free energy V times N as a function of $\tilde{\gamma}$ with $N = 30$ and $\theta = \pi$. We again see the swallow-tail shape characteristic of a first-order phase transition, with the partial phase appearing as the unstable branch connecting the confined and deconfined branches. Again the partial phase always has the highest free energy, and hence is always thermodynamically dis-favoured.

Fig. 3.10 shows $|M_0|$, magnified by a factor of 10^3 for clarity, as a function of $\tilde{\gamma}$ near the transition to the deconfined phase (which at $N = \infty$ is the GWW transition). Similar to the $\theta = 0$ case in fig. 3.7, we again see that $|M_0|$ is small, but not exponentially small, near the transition point, and in particular $|M_0|$ is non-zero, justifying our interpretation of these solutions as the partial phase.

Of course, a key difference between the $\theta = 0$ and $\theta = \pi$ cases is that in the former all of the M_j were real-valued while in the latter the M_j acquire non-zero phases, indicating spontaneous breaking of CP symmetry. Fig. 3.11 illustrates this difference, showing our numerical results for both $|M_j|$ and $\arg(M_j) = \varphi_j$ as a function of j in the partial phase, for $\theta = \pi$ and various $\tilde{\gamma}$. The evolution of the $|M_j|$ is consistent with what we observed in figs. 3.4 and 3.8. However, we now see that in the partial phase with $\theta = \pi$, generically all the $\arg(M_j) = \varphi_j$ are non-zero. We also see that as we approach the deconfined phase, all of the $\arg(M_j)$ approach zero except for $\arg(M_0)$, which approaches $\arg(M_0) = \theta = \pi$, so that the partial solutions connect to the deconfined solution (recall eq. (3.33)).

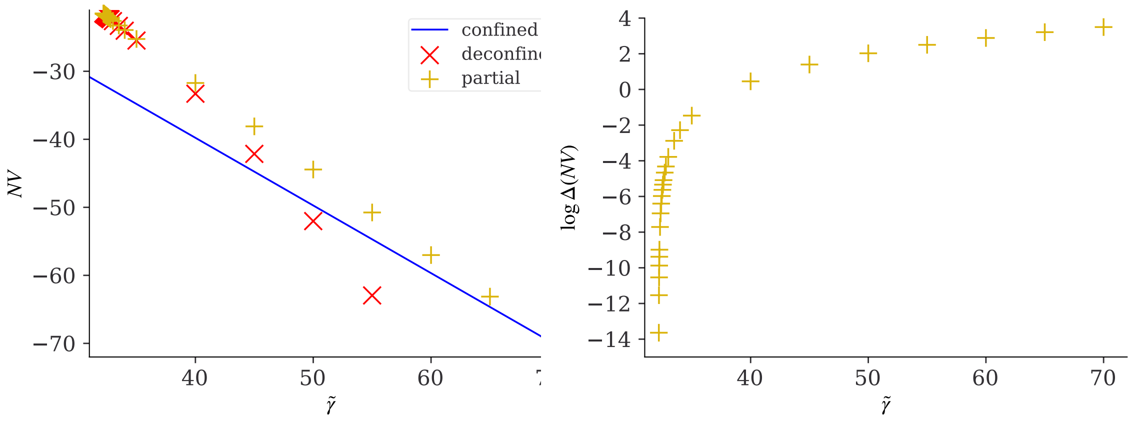

(A)

(B)

FIGURE 3.9: (a) $\theta = \pi$ numerical results for N times the free energy V as a function of $\tilde{\gamma}$ for $N = 30$, showing the confined phase (blue line), deconfined phase (red crosses), and partial phase (gold plus signs). We find a first-order transition, similar to the $\theta = 0$ case in fig. 3.5. (b) Our $\theta = \pi$ numerical results for $\log(\Delta NV)$ versus $\tilde{\gamma}$ for $N = 30$, with ΔNV defined as in fig. 3.5. Clearly the partial phase has higher free energy than the deconfined phase near the transition between them (which at $N = \infty$ is the GWW transition).

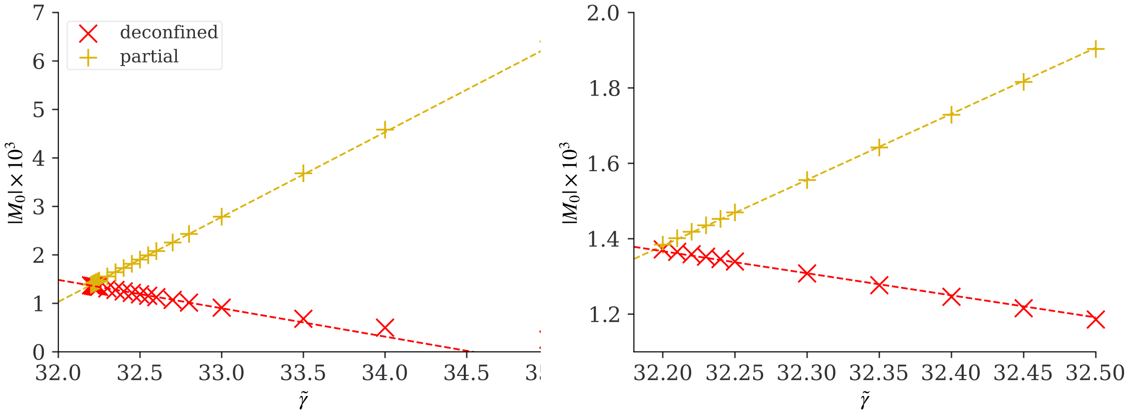

(A)

(B)

FIGURE 3.10: (a) $\theta = \pi$ numerical results for $|M_0|$, magnified by a factor of 10^3 for clarity, as a function of $\tilde{\gamma}$, for $N = 30$, in the deconfined phase (red crosses) and partial phase (gold plus signs). $|M_0|$ in the deconfined phase becomes zero in the large-N limit. The gold plus signs have larger values, showing that our solutions indeed describe a partial phase. (b) Close-up of (a) near the transition point.

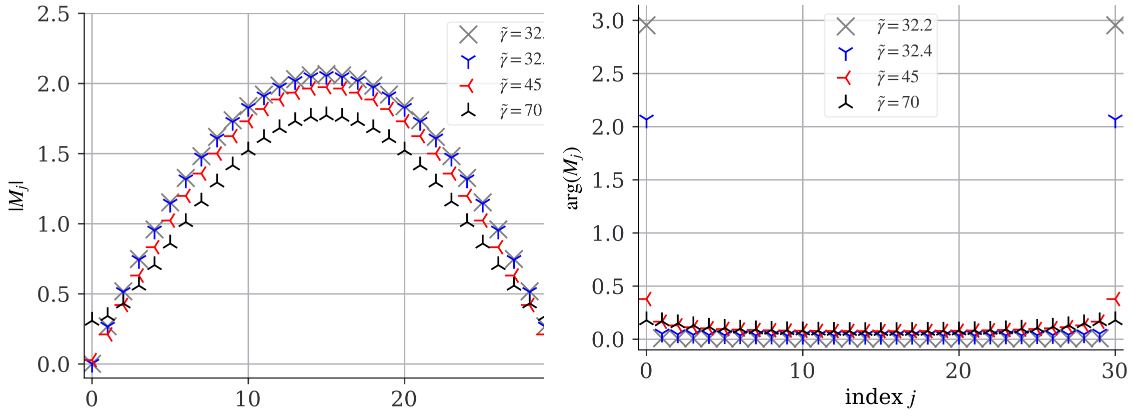

(A) (B)

FIGURE 3.11: (a) $\theta = \pi$ numerical results for $|M_j|$ as functions of j, in the partial phase, at $\tilde{\gamma} = 32.2$ (gray crosses) 32.4 (blue 3-pont star), 45 (red 3-point star), and 70 (black 3-point star). (b) $\theta = \pi$ numerical results for $\arg(M_j)$ as functions of j, in the partial phase, at the same $\tilde{\gamma}$ as in (a). Generically the M_j have non-zero phases, indicating spontaneous breaking of CP symmetry. As we decrease $\tilde{\gamma}$ we see that $\arg(M_0)$ grows, to meet the value of the deconfined phase, $\arg(M_0) = \theta = \pi$.

Our numerical results for $\frac{\partial V}{\partial \theta} \propto \langle \mathrm{tr}(F_{\mu\nu}\tilde{F}^{\mu\nu})\rangle$ (times N^3) with $\theta = \pi$ and $N = 30, 50, 70$ appear in fig. 3.3, alongside our $N = \infty$ results from subsection 3.2.3.1. In all cases we see that $\frac{\partial V}{\partial \theta} \neq 0$ in the partial phase, indicating spontaneous breaking of CP symmetry. This is our main result, that CP symmetry distinguishes the partial and deconfined phases, even at finite N. Moreover, at large N we saw that $\frac{\partial V}{\partial \theta}$ was finite at the GWW transition, and hence jumped discontinuously between the partial and deconfined phases, indicating a first-order transition. In contrast, at finite N we see in fig. 3.3 that $\frac{\partial V}{\partial \theta}$ smoothly approaches zero at the transition to the deconfined phase, suggesting a second-order transition. However, as N increases we observe that the slope of $\frac{\partial V}{\partial \theta}$ increases, strongly suggesting that the slope diverges as $N \to \infty$, thus connecting the finite- and large-N calculations.

In summary, we have demonstrated that, in weakly-coupled, softly-broken $\mathcal{N} = 1$ SYM on $\mathbb{S}^1 \times \mathbb{R}^3$, at both infinite and finite N a partial phase exists that connects the confined and deconfined phases, and has broken centre and CP symmetries. As a result, order parameters exist that can distinguish the partial phase from both the confined and deconfined phases. In particular, $\frac{\partial V}{\partial \theta} \propto \langle \mathrm{tr}(F_{\mu\nu}\tilde{F}^{\mu\nu})\rangle$ can distinguish the partial and deconfined phases, a phenomenon that to our knowledge is novel.

3.3 Chiral symmetry in strongly-coupled lattice gauge theory

In this section, we consider $U(N)$ YM theory on an anisotropic lattice, with $d = 3$ spatial dimensions with lattice spacing a_s, and a compact Euclidean time direction with lattice spacing a_t. We will use the same setup as described in Chapter 2, specifically the lattice action (3.59), which we repeate here,

$$S = \frac{N}{2a} \sum_{\mu=1}^{d} \sum_{t=1}^{n_t} \mathrm{Tr} \left(\mathbf{1}_N - U_{\mu,t} V_t U^{\dagger}_{\mu,t+1} V^{\dagger}_t \right) + \text{h.c.}, \tag{3.59}$$

This describes Eguichi-Kawai-reduced lattice-regularised $U(N)$ YM theory in the strong coupling limit, dropping magnetic terms, in the large N 't Hooft limit. The validity of Eguichi-Kawai (EK) equivalence requires two other conditions: unbroken discrete spatial translational symmetry in the large-volume theory, and centre symmetry unbroken by a Wilson line in a spatial direction in the single-site theory.

This setup come with some subtleties. For example, since we reduce to a single site, our results are valid only in the 't Hooft large-N limit. However, to do numerics we must use link variables of finite size, hence we must work with finite N. We will use large but finite N, namely $N = 8, \ldots, 32$. Notice this is qualitatively different from our finite-N results for softly-broken $\mathcal{N} = 1$ SYM in sec. 3.2.3.2: those were genuinely finite N, while here our starting point, namely the action in eq. (3.59), is an accurate description of the large-volume YM theory only at $N = \infty$. We will discuss other subtleties with our limits in what follows.

Our order parameter for the confinement/deconfinement transition will be the Polyakov loop, P, defined on the lattice as $P = \frac{1}{N}\mathrm{Tr}\mathcal{P}$, where

$$\mathcal{P} = V_1 V_2 \cdots V_{n_t}. \tag{3.60}$$

Although P can be complex, the complex phase can be shifted by a centre symmetry transformation, which acts on the Polyakov loop as $P \to e^{i\alpha} P$, where in the large-N limit, α is an arbitrary real number. In the following, we will use the centre symmetry to make P real-valued and non-negative, so strictly speaking, our $P = \left|\frac{1}{N}\mathrm{Tr}\mathcal{P}\right|$. Using this order parameter, we will observe a first-order transition as T increases, from a confined to a deconfined phase. In this transition the centre symmetry will be spontaneously broken. We will also find an unstable partial phase connecting the confined and deconfined phases. In the partial phase the centre symmetry will be spontaneously broken.

We will add to this model fermions in the fundamental representation, i.e. quarks. In general, fundamental-representation fields explicitly break centre symmetry. To suppress this explicit breaking, we will take a fourth limit, namely the probe limit: we will introduce a number N_f of quarks, keep N_f fixed as $N \to \infty$, and work only to leading order in N_f/N. In the probe limit, the explicit breaking of centre symmetry is invisible in the pure glue sector, so the confinement/deconfinement transition will be unchanged. However, as in ordinary YM theory, the probe quarks exhibit chiral symmetry breaking in the confined phase, and chiral symmetry restoration in the deconfined phase. The order parameter for this transition is the chiral condensate. We will numerically compute the eigenvalue distribution of the probe Dirac operator and use the Banks-Casher relation [60] to extract the value of the chiral condensate. Our main result in this section will be that chiral symmetry is broken in the partial phase, and hence the chiral condensate provides an order parameter that can distinguish the partial and deconfined phases.

In sec. 3.3.1 we present our numerical results for the confinement/deconfinement transition in this model, including novel results for the partial phase. In sec. 3.3.2 we present our numerical results for the probe Dirac operator's eigenvalue spectrum, where our main result is that chiral symmetry is spontaneously broken in the partial phase.

We acknowledge here that the use of fermion eigenvalue distributions in quenched lattice gauge theory to detect chiral symmetry breaking and a chiral condensate is a controversial topic. Some arguments have been advanced suggesting that a significant contribution to the accumulation of near-zero eigenvalues is can sometimes be attributed to finite-volume topological effects, specifically instantons and anti-instantons, rather than indicating a true chiral condensate [61; 62; 63; 64]. Therefore, the density of eigenvalues near zero cannot be naively trusted as a signature of a chiral symmetry breaking in the continuum-limit, infinite-volume theory. Introducing full dynamical quarks, or using a different implementation of probe fermion (such as staggered fermions instead of overlap fermions), can cause the peak of low-value eigenvalues to vanish, revealing the apparent chiral symmetry breaking to be an artifact of the quenched, finite-volume approximation. Consequently, it is not always entirely clear whether one is truly measuring a property of the underlying gauge configuration or merely a property of the probe itself.

3.3.1 Confinement/deconfinement transition

We will apply the Hybrid Monte Carlo method [42] to the single-site lattice action in eq. (3.59). Without probe quarks, the cost for configuration generation is not so large, unless we make N and/or n_t large. We will work with $N = 8, \ldots, 32$ and $n_t = 24$.

As we will show shortly, for the current theory in the canonical ensemble the confinement/deconfinement transition is first order. As a result, the partial phase is the maximum of the free energy, and therefore has the *smallest* weight in the ensemble, and hence is not efficiently sampled using the standard Monte Carlo method. To sample configurations at fixed values of P efficiently, we performed a constrained simulation, in which we fixed the value of the Polyakov loop. Specifically, we modified the action S in eq. (3.59) by adding a term, $S \to S + \Delta S$, where

$$\Delta S = \begin{cases} \frac{g_{\rm P}}{2}\left(P - (P_{\rm fix} + \delta)\right)^2 & (P > P_{\rm fix} + \delta) \\ 0 & (P_{\rm fix} - \delta \le P \le P_{\rm fix} + \delta) \\ \frac{g_{\rm P}}{2}\left(P - (P_{\rm fix} - \delta)\right)^2 & (P < P_{\rm fix} - \delta) \end{cases} , \tag{3.61}$$

where we chose the dimensionless constant $g_{\rm P}$ to be large enough that the value of P is fixed to a small window $P_{\rm fix} - \delta \le P \le P_{\rm fix} + \delta$.

Ideally, to study the partial phase we should find the maximum of the free energy as a function of T. If we fix P, then as P in the partial phase decreases, T increases slightly. We instead fixed T near the confinement/deconfinement transition temperature T_c, and then dialed the value of P. In particular, we studied the distribution of the Polyakov line phases at $T = 0.29$, 0.30, and 0.31, and did not see significant T-dependence in the distribution of Polyakov line phases.

As mentioned above, EK reduction requires both translational symmetry in spatial directions, and unbroken centre symmetry in spatial directions. As also mentioned above, a subtlety arise with EK reduction, in the partial phase. To see why, consider taking the infinite-volume limit of the spatial directions in our theory. In this limit, the confined and deconfined phases preserve spatial translational symmetry, hence they pose no problem for the EK reduction. However, the partial phase is a local maximum of the free energy, hence a state in which the partial phase uniformly fills all of space is unstable, even in the micro-canonical ensemble: such a state should in principle separate into regions of confined or deconfined phase, thus breaking spatial translational symmetry. Since we will use the single-site approximation, we will be blind to this effect, that is, we will study states with fixed energy that, in the continuum and infinite-volume limits, correspond to the partial phase uniformly filling all of space.

In the strong-coupling limit, centre symmetry in spatial directions is not spontaneously broken, hence EK reduction is valid. To confirm this, we numerically computed Wilson loops in spatial directions, and verified that they approach zero as N increases. To be explicit, the action in eq. (3.59) is invariant under a global (i.e. t-independent) centre symmetry transformation in each spatial direction, which at large N is a $U(1)$ transformation for each spatial direction. These leave V_t untouched but act on $U_{\mu,t}$ as $U_{\mu,t} \to e^{i\alpha_\mu} U_{\mu,t}$ with each α_μ an arbitrary real number. If centre symmetry in all spatial directions is unbroken, then the Wilson lines $\mathrm{Tr}\, U_{\mu,t}$ will be zero in all directions. For EK reduction to be valid, this must be the case at least at large N. We numerically calculated

$$W \equiv \frac{1}{3Nn_t} \sum_{\mu=1}^{3} \sum_{t=1}^{n_t} |\mathrm{Tr} U_{\mu,t}|, \tag{3.62}$$

for all the solutions we use below, and verified that W approaches zero as N increases.

We now present our results for the confinement/deconfinement transition in this theory. As shown in ref. [32], for this theory with arbitrary spatial dimension d, simple state counting reveals a first-order phase transition around $T_c = \frac{1}{2\log(2d-1)}$, which in our $d = 3$ case is $T_c = \frac{1}{2\log(5)} \simeq 0.31$. We easily confirmed this numerically. Fig. 3.12 shows our numerical results for the Polyakov loop, P. In particular, Fig. 3.12 (a) shows our numerical results for P as a function of T, for $N = 32$ and $n_t = 24$. We observe a strong hysteresis, consistent with a first-order transition at $T_c =\simeq 0.31$. Fig. 3.12 (b) shows the simulation history of P at $T = 0.31$, for $N = 32$ and $n_t = 24$. We see that the confined and deconfined phase both exist rather stably, which also indicates a first-order phase transition. Fig. 3.12 (c) shows P at $T = 0.25$, in the confined phase, for $n_t = 24$ and $N = 8, 16, 24$ and 32. We see that P approaches zero as N increases, as expected for the confined phase.

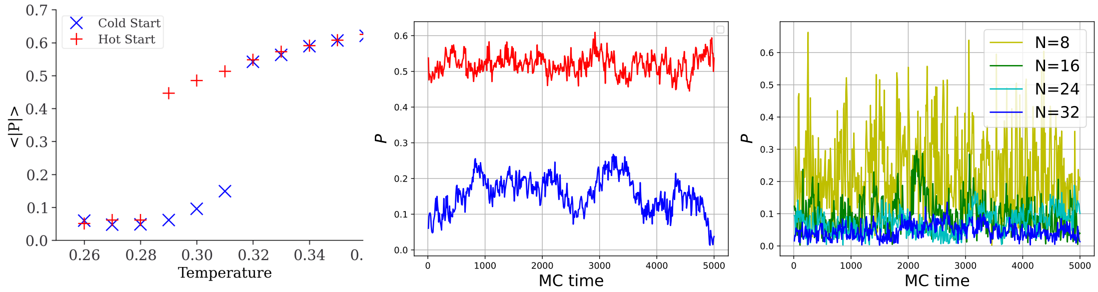

(A) (B) (C)

FIGURE 3.12: Numerical results for the Polyakov loop, P, in the theory with action in eq. (3.59). As discussed below eq. (3.60), our P is always real and non-negative. (a) Mean Polyakov loop versus temperature T, for $N = 32$ and $n_t = 24$. We observe strong hysteresis around $T_c \simeq 0.31$, consistent with a first-order transition. The cold start (blue crosses) and hot start (red plus signs) simulations had initial temperatures $T = 0.2$ and $T = 0.45$, respectively. The simulations were then thermalised before 200 configurations taken for data collection. (b) The simulation history of P for $N = 32$ and $n_t = 24$ at $T = 0.31$, for a cold start (blue) and hot start (red). The horizontal axis is the Monte Carlo time. We observe that tunneling between the two phases is strongly suppressed. The fluctuations are larger in the confined phase because $T = 0.31$ is close to the endpoint of the confined phase. (c) The simulation history of P for $N = 8, 16, 24$ and 32, with $n_t = 24$, at $T = 0.25$. As N becomes larger, P approaches zero.

Fig. 3.13 shows our numerical results for the distribution of Polyakov line phases, $\rho(\psi)$, versus ψ, for $N = 32$ and $n_t = 24$. Fig. 3.13 (a) shows our results for $\rho(\psi)$ in the deconfined phase, as we lower T through $T_c \simeq 0.31$ and towards the GWW transition. We observe a gap that shrinks and approaches zero as T approaches the GWW transition, as expected. We also observed that in the confined phase $\rho(\psi)$ is uniform, up to $1/N$-corrections. Fig. 3.13 (b) shows the evolution of $\rho(\psi)$ in fixed-P simulation at $T = 0.29$, the lowest T of the deconfined phase, i.e. near the GWW transition. As P decreases, we see that the gap closes at $P \simeq 0.35$, and for $P < 0.35$ the gap is gone, but

$\rho(\psi)$ is not uniform. We thus identify these $P \leq 0.35$ configurations as partial phase solutions.

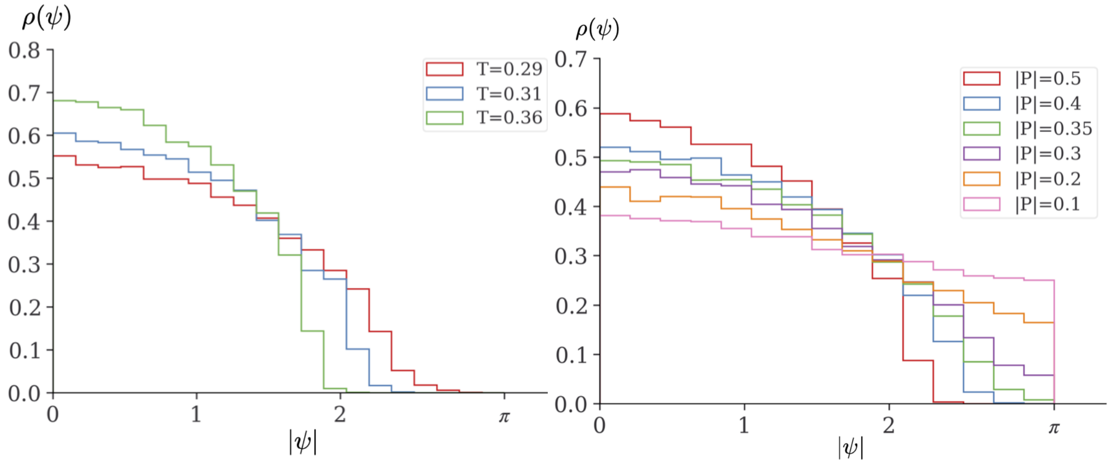

(A) (B)

FIGURE 3.13: Numerical results for the distribution of Polyakov loop phases, $\rho(\psi)$, as a function of $|\psi|$, in the theory with action in eq. (3.59), for $N = 32$ and $n_t = 24$. We use $|\psi|$ because, if the number of samples is sufficiently large, $\rho(\psi)$ is symmetric about $\psi = 0$. (a) The deconfined phase, as T decreases through the confinement/deconfinement transition temperature $T_c \simeq 0.31$, where the free energies of confined and deconfined phases coincide. We see a gap at $\psi = \pi$ that shrinks as T decreases, as expected. (b) Fixed-P simulations at the lowest T in the deconfined phase, $T = 0.29$, i.e. near the GWW transition. Specifically, we fixed P with $\delta = 5 \times 10^{-3}$ in eq. (3.61), with 400 configurations for each P. We see that as P decreases, the gap closes at $P \simeq 0.35$, so we identify $P \leq 0.35$ as the partial phase.

All of our results above are consistent with a first-order confinement/deconfinement transition in which the partial phase appears as the unstable branch connecting the confined and deconfined branches, similar to what we saw for softly-broken $\mathcal{N} = 1$ SYM in sec. 3.2.

3.3.2 Chiral symmetry

We now introduce a massless probe quark and study chiral symmetry breaking. We use the naïve lattice fermion, with action[2]

$$S_f = \frac{1}{2}\sum_{t=1}^{n_t}\left[\frac{1}{a}\left(\bar{\psi}_t\gamma^t V_t\psi_{t+1} - \bar{\psi}_{t+1}\gamma^t V_t^\dagger\psi_t\right) + \sum_\mu\left(\bar{\psi}_t\gamma^\mu U_\mu\psi_t - \bar{\psi}_t\gamma^\mu U_\mu^\dagger\psi_t\right)\right]. \quad (3.63)$$

Let us write this action as $S_f = \bar{\psi}D\psi$, where D is the Dirac operator. The eigenvalues of D are purely imaginary, with two-fold degeneracy. Specifically, they have the form $\pm i\lambda$, where λ is real and non-negative. We want to compute the distribution of

---

[2] Notice we have no reason to worry about doublers for our current purposes.

eigenvalues of the Dirac operator, which we denote $\rho^{(\mathrm{D})}(\lambda)$. We normalise this density as $\int_0^\infty d\lambda \rho^{(\mathrm{D})}(\lambda) = 4Nn_t$.

As mentioned above, fields in the fundamental representation explicitly break the centre symmetry, but we suppress this effect by working in the probe limit, i.e. working in the 't Hooft large-N limit with N_f fixed, and keeping the leading order in $N_f/N \ll 1$. In that case, roughly speaking the quark is influenced by the pure glue sector, but the pure glue sector is unaffected by the quark, i.e. the quark's "back-reaction" on the pure glue sector is suppressed. As a result, introducing the probe quark does not affect the results of sec. 3.3.1.

Our quarks are massless, hence the quark sector classically has $U(N_f) = U(1) \times SU(N_f)$ chiral symmetry. When N is finite the $U(1)$ factor is anomalous, however the one-loop diagram that produces this anomaly is suppressed in the probe limit. We expect the chiral symmetry to be spontaneously broken in the confined phase and restored in the deconfined phase. The corresponding order parameter is the chiral condensate, $\langle\bar{\psi}\psi\rangle$, which we expect to be non-zero in the confined phase and zero in the deconfined phase.

As discussed in ref. [18], anomaly-matching arguments suggest that chiral symmetry is spontaneously broken also in the partial phase, and specifically in its confined subsector. Our goal here is to compute $\langle\bar{\psi}\psi\rangle$ in the partial phase solutions of sec. 3.3.1, to determine whether chiral symmetry is indeed spontaneously broken. To do so, we will numerically compute $\rho^{(\mathrm{D})}(\lambda)$, and use the Banks-Casher relation [60], which states that $\rho^{(\mathrm{D})}(0) \propto \langle\bar{\psi}\psi\rangle$.

Computing D's eigenvalues, and hence $\rho^{(\mathrm{D})}(\lambda)$, is the most computationally-demanding part of our numerical calculations for this theory. We calculated D's eigenvalues using the linear algebra package LAPACK.

When the centre symmetry breaks spontaneously, the eigenvalues of D are sensitive to the complex phase of the Polyakov loop. Because we want to interpret our probe quarks as an approximation to dynamical (i.e. non-probe) quarks, we have no reason to pick a specific phase. Instead, we need to perform a centre-symmetry transformation $V_t \to e^{i\alpha} V_t$ and average over α. In our simulation, for each configuration we chose ten random values of α from $[0, 2\pi)$, and used $e^{i\alpha} V_t$ instead of V_t to calculate D's eigenvalues.[3]

Fig. 3.14 shows our numerical results for $\frac{1}{N}\rho^{(\mathrm{D})}(\lambda)$ for various T in the deconfined phase for $N = 8$, 12 and 16. For all of these N, we clearly observe that $\rho^{(\mathrm{D})}(0) = 0$, and

---

[3] Because configurations related by the U(1) centre symmetry transformation have the same path-integral weight, such an averaging is, in principle, automatic. In our simulation, because we used the same step size for the $U(1)$ and $SU(N)$ directions, the auto-correlation along the $U(1)$ direction is large. We therefore used such a trick to average over the $U(1)$ direction with a reasonable number of configurations.

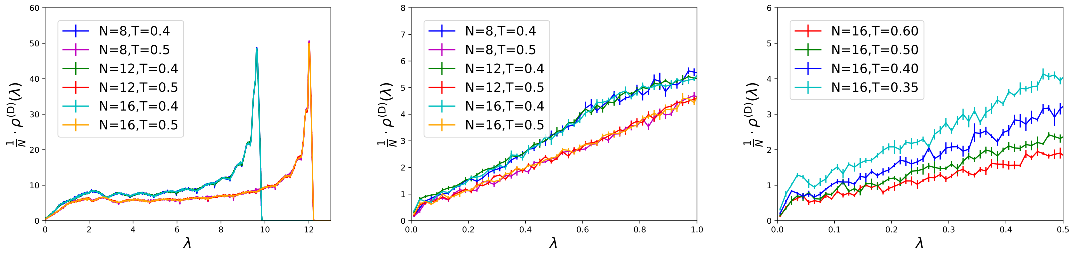

(A) (B) (C)

FIGURE 3.14: The density of Dirac eigenvalues, $\rho^{(\mathrm{D})}(\lambda)$, divided by N, for $N = 8$, 12, and 16, $n_t = 24$, and $T = 0.4$ and 0.5, i.e. in the deconfined phase, with 500 configurations (5000 sets of eigenvalues) for each. Error bars are estimated by using 5-bin Jackknife with bin width 0.02. We see in all cases that $\rho^{(\mathrm{D})}(\lambda) \to 0$ as $\lambda \to 0$, indicating $\langle\bar{\psi}\psi\rangle = 0$ and hence that chiral symmetry is preserved, as expected. (b) Close-up of (a), showing that the slope near $\lambda = 0$ increases as T increases. (c) The same, but for $T = 0.35$, 0.40, 0.50, and 0.60, showing again that the slope near $\lambda = 0$ increases as T increases.

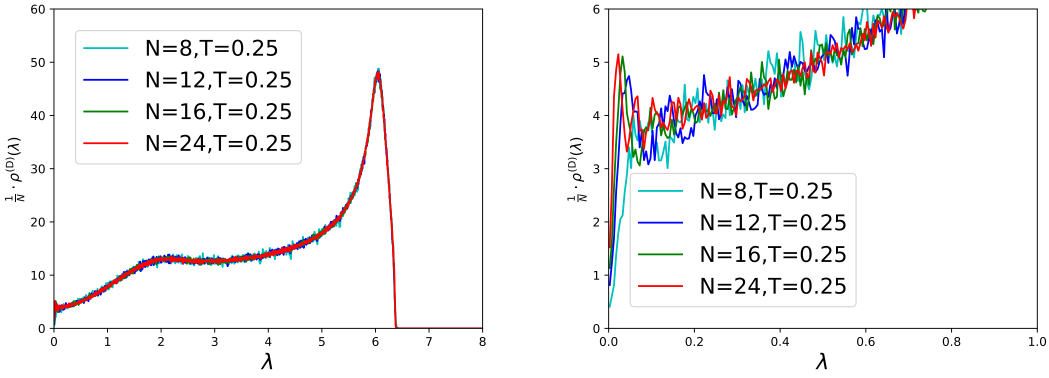

(A) (B)

FIGURE 3.15: (a) The density of Dirac eigenvalues, $\rho^{(\mathrm{D})}(\lambda)$, divided by N, for $N = 8$, 12, 16, and 24, $n_t = 24$, and $T = 0.25$, i.e. in the confined phase. We see in all cases that $\rho^{(\mathrm{D})}(\lambda)$ approaches a non-zero value as $\lambda \to 0$, indicating $\langle\bar{\psi}\psi\rangle \neq 0$ and hence that chiral symmetry is spontaneously broken, as expected. (b) Close-up of (a).

hence $\langle\bar{\psi}\psi\rangle = 0$ and chiral symmetry is preserved, as expected. Furthermore, by comparing $\frac{1}{N}\rho^{(\mathrm{D})}(\lambda)$ for $N = 8$, 12 and 16, we find no significant N-dependence, so in the $N \to \infty$ limit we again expect $\frac{1}{N}\rho^{(\mathrm{D})}(\lambda) = 0$, and hence $\langle\bar{\psi}\psi\rangle = 0$ and chiral symmetry restoration. Notice the slope of $\frac{1}{N}\rho^{(\mathrm{D})}(\lambda)$ as $\lambda \to 0$ increases as T approaches the GWW-point.

Fig. 3.15 shows our numerical results for $\frac{1}{N}\rho^{(\mathrm{D})}(\lambda)$ at $T = 0.25$ in the confined phase. In contrast to the deconfined phase, here we find that $\frac{1}{N}\rho^{(\mathrm{D})}(0) \neq 0$, and hence $\langle\bar{\psi}\psi\rangle \neq 0$ and chiral symmetry is spontaneously broken, as expected. In fact, $\frac{1}{N}\rho^{(\mathrm{D})}(\lambda)$

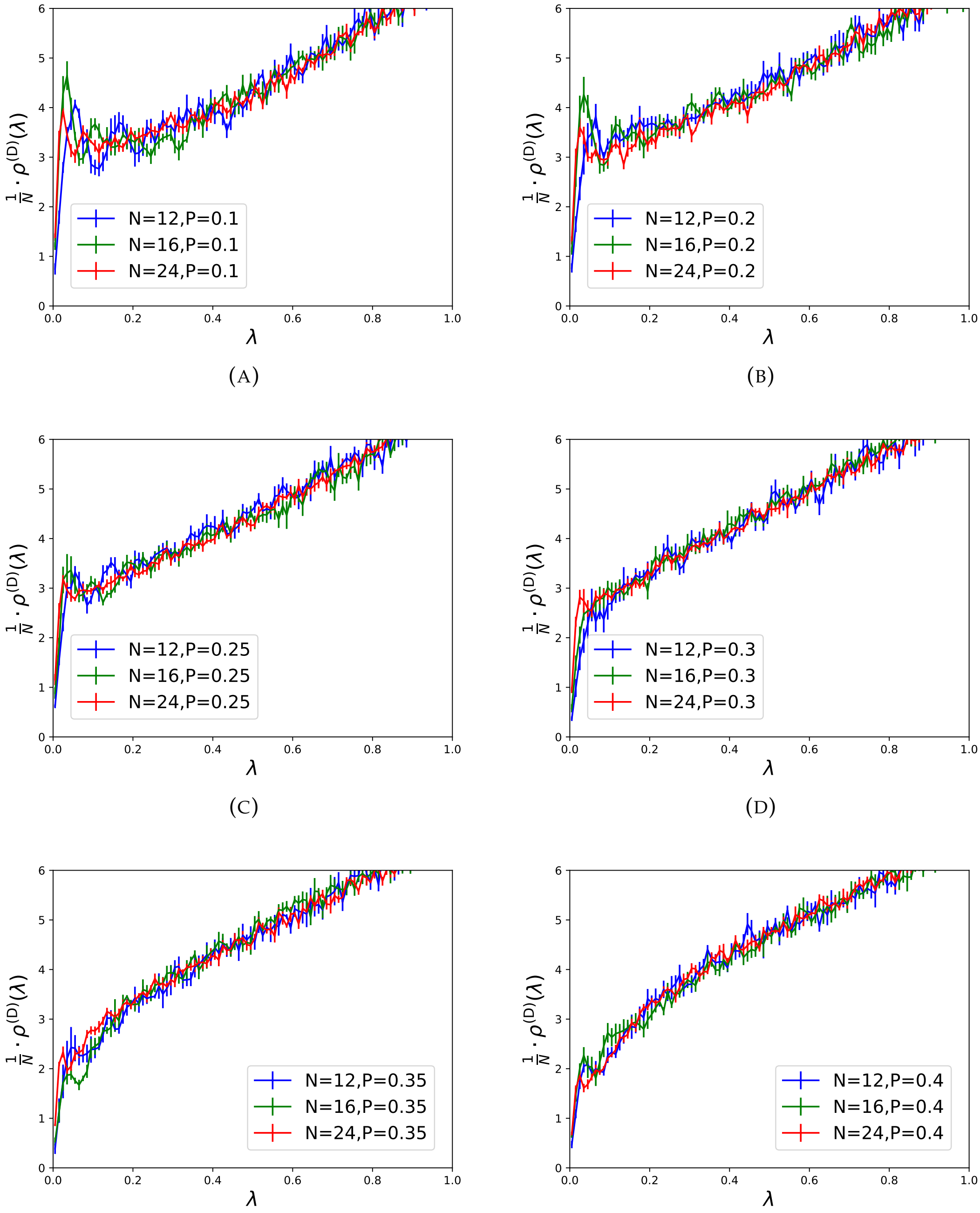

(A)

(B)

(C)

(D)

(E)

(F)

FIGURE 3.16: The density of Dirac eigenvalues, $\rho^{(\mathrm{D})}(\lambda)$, divided by N, for $N = 12$, 16, and 24, $n_t = 24$, and $T = 0.29$, for various fixed values of P: (a)-(d) have $P = 0.1$, 0.2, 0.25, 0.3, respectively, which are all in the partial phase, while (e) and (f) have $P = 0.35$ and 0.4, respectively, which are in the deconfined phase. In the partial phase, the behaviour is qualitatively similar to the confined phase in fig. 3.15.

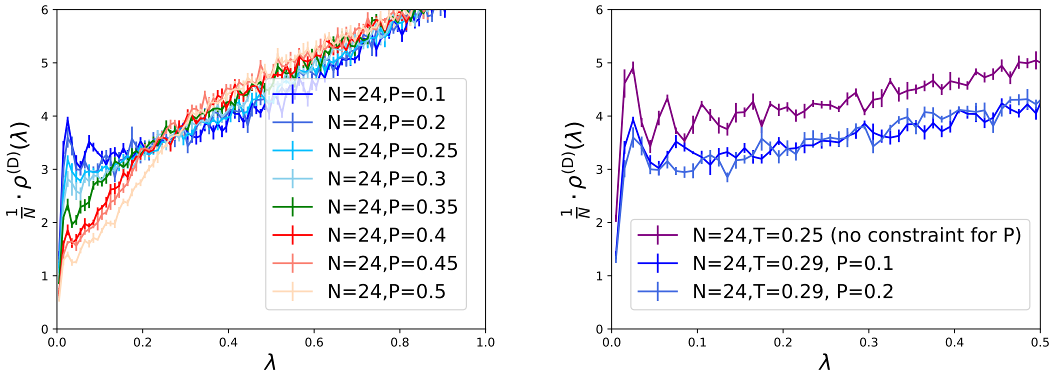

(A) (B)

FIGURE 3.17: (a) The density of Dirac eigenvalues, $\rho^{(\mathrm{D})}(\lambda)$, divided by N, for $N = 24$, $n_t = 24$, $T = 0.29$, and various P above and below the GWW point, $P \simeq 0.35$. In the partial phase, $P \lesssim 0.35$, the behaviour is similar to the confined phase in fig. 3.15, whereas when $P \gtrsim 0.35$, the behaviour is similar to that in the deconfined phase in fig. 3.14. (b) The same, but for $P = 0.1$ and 0.2 only, and now including $T = 0.25$ with no P-constraint, i.e. the confined phase, to highlight the similarity.

exhibits a small maximum and then a steep slope down as $\lambda \to 0$, both of which increase as N increases.

Fig. 3.16 shows our numerical results for $\frac{1}{N}\rho^{(\mathrm{D})}(\lambda)$ at $T = 0.29$, near the GWW transition, for $N = 12$, 16, and 24, and various P below and above the GWW point at $P \simeq 0.35$. Figs. 3.17 shows the same, for a larger range of P, and also shows $T = 0.25$, which is the confined phase.

In fig. 3.16 we see a clear difference as P increases through $P \simeq 0.35$. When $P \lesssim 0.35$, which is the partial phase, our results are similar to those of the confined phase in fig. 3.15. In particular, $\frac{1}{N}\rho^{(\mathrm{D})}(\lambda)$ exhibits a small maximum and a steep slope near $\lambda = 0$, and most importantly, $\frac{1}{N}\rho^{(\mathrm{D})}(0) \neq 0$, hence $\langle\bar{\psi}\psi\rangle \neq 0$ and chiral symmetry is spontaneously broken. This is our main result. In contrast, when $P \gtrsim 0.35$, which is the deconfined phase, our results are qualitatively more similar to those in fig. 3.14, including a less pronounced maximum and slope near $\lambda = 0$. Moreover, as P increases we see that $\frac{1}{N}\rho^{(\mathrm{D})}(0)$ approaches zero, suggesting chiral symmetry restoration.

Our results are insufficient to determine whether, as we increase P, the GWW transition and chiral symmetry breaking occur simultaneously, although that is a natural expectation. In any case, we have shown that complete confinement is not necessary for chiral symmetry breaking. Most importantly, we have demonstrated our main point in this section: for at least some range of P in the partial phase, chiral symmetry is spontaneously broken, and hence $\langle\bar{\psi}\psi\rangle$ is an order parameter that can distinguish the partial and deconfined phases.

3.4 Conclusion and discussion

In this chapter, we studied the partially-deconfined phase in two large-N YM theories, namely weakly-coupled, softly-broken $\mathcal{N} = 1$ SYM with $\theta = \pi$ and strongly-coupled lattice YM. In each case, we showed that in the partial phase both centre symmetry and a second global symmetry, either CP symmetry or chiral symmetry, respectively, are spontaneously broken. As a result, in each case an order parameter exists that can distinguish the partial phase from both the confined and deconfined phases. For $\mathcal{N} = 1$ SYM we also presented finite-N numerical evidence for the same phenomenon.

Our results raise some immediate questions for the two YM theories we studied. For example, in $\mathcal{N} = 1$ SYM the adiabatic continuity conjecture [52] proposes that the phase transitions that occur in the softly-broken $\mathcal{N} = 1$ SYM theory are smoothly connected to those in the pure YM theory, i.e. that the phase structure is preserved with respect to increasing the gaugino mass. Do our results for the partial phase extend to larger gaugino masses? Could we find the same global symmetry breaking pattern and a GWW point at large gaugino mass values, or infinite gaugino mass, i.e. in pure YM with $\theta = \pi$? If so, then such agreement would provide a more stringent test of the adiabatic continuity conjecture than the existing tests, many of which could just be coincidences.

Looking farther afield, our numerical results, combined with anomaly-based arguments such as those in refs. [45; 49], motivate the conjecture that the partial phase can be defined by spontaneous breaking of global symmetries in general, and in particular may apply for any N, not just for large N. Indeed, our results suggest that the novel phase found in ref. [49], for the weakly-coupled, softly-broken $\mathcal{N} = 1$ SYM with $\theta = \pi$ with gauge group $SU(2)$, is a partial phase. Spontaneous breaking of global symmetries may provide a definition of the GWW transition beyond the large-N limit, and a definition that, in practical terms, may be easier to calculate in many theories.

Spontaneous breaking of global symmetries also means the partial phase's spectrum will be distinct from both the confined or deconfined phases, implying the existence of a either a Nambu-Goldstone boson, if the global symmetry is continuous (like chiral symmetry in our lattice YM example), or domain walls if the global symmetry is discrete (like CP symmetry in our $\mathcal{N} = 1$ SYM example). An obvious and important task is thus to formulate effective field theory descriptions of partial phases, and to explore their physical consequences.

The partial flux tubes and possible bound states in the confined sector discussed in Chapter 2 fits well with the idea that chiral symmetry is spontaneously broken at the complete deconfinement/partial deconfinement phase transition point. We expect the bound states to induce a chiral condensate in the confined sector, which should be sufficient to break the chiral symmetry.

An especially important question is whether global symmetries can be used to identify partial phases in theories closer to QCD, including $N = 3$, $\theta = 0$, and physical quark masses. If a partial phase exists, then a crucial question is what observable effects it may have for the quark-gluon plasma created in heavy ion collider and the early universe, as well as for neutron stars and many other systems. The observable effects of a global symmetry breaking could be very important for this.

Recall that the partial phase has been proposed to explain the field theory AdS/CFT dual to certain phases in the bulk gravity, such as the small black hole phase in global AdS_5, differentiated from the big black hole by its negative specific heat. Following the findings of this chapter, an obvious question is whether probe fermions added to the dual $\mathcal{N} = 4$ SYM exhibit any global symmetry breaking at the point at which the specific heat becomes negative. This could provide compelling evidence for the conjecture, and a better understanding of the holographic mapping in general. A closely related question is whether a partial phase appears in the deconfinement transition observed in the index of $\mathcal{N} = 4$ SYM on $\mathrm{S}^1 \times \mathrm{S}^3$ [65].

3.A Second order Taylor method for softly-broken $\mathcal{N} = 1$ SYM large-N numerical calculations

The second order Taylor method of solving an initial value problem is the natural extension of the Euler method to a second order Taylor expansion. That is, using analytic expressions for the first and second derivatives at the i-th iteration, $X'_i \equiv X'(X_i)$ and $X''_i \equiv X''(X_i)$, from eqs. (3.37) and (3.39) respectively, we find the value of the $(i+1)$-th iteration by second order Taylor expansion,

$$X_{i+1} = X_i + X'_i \delta t + X''_i \frac{\delta t^2}{2}, \tag{3.64}$$

for small δt. The local truncation error is $\mathcal{O}(\delta t^3)$, rather than the $\mathcal{O}(\delta t^2)$ associated with Euler's method, and we avoid incurring large errors near the minimum, $X_i = X(-1/2)$, where X' is zero but X'' is very large. Moreover, in our case, near the GWW transition point, typical solutions exhibit a sharp gradient. To handle these sharp gradients, we limit the maximum change $\delta X(t)$ at each step of the Taylor method to 1% of the current magnitude of $X(t)$ by decreasing the step size δt as necessary.

Numerical uncertainties in V and M_0 (as reported for large N in appendix 3.B.1), arise from three places: from errors in the numerical integration of the constraint eq. (3.38), from the numerical integration of the continuum limit of eq. (3.19) when calculating V, and from the approximations made by the second order Taylor method. Uncertainties in the numerical integrals are calculated using concave and convex properties of the integrands. Below, we discuss how we determine uncertainties arising from the second order Taylor approximation and compose these with the errors from numerical integration. We assume throughout that floating point precision errors are negligible.

We can write the exact relation,

$$X_{i+1}^{\text{exact}} = X_i + X_t' \delta t_i + \int_{t_i}^{t_{i+1}} ds \int_{t_i}^{s} du\, X''(u) \tag{3.65}$$

By differentiating eq. (3.37) we find that the third derivative is always negative between the start and end points (defined by $X' = 0$). We therefore have $X''(t_i) \geq X''(t) \geq X''(t_{i+1})$ for $t_i \leq t \leq t_{i+1}$, and from this we can derive upper and lower bounds, X_{i+1}^{UB} and X_{i+1}^{LB}, on X_{i+1}^{exact}, namely

$$X_{i+1}^{\text{UB}} \equiv X_i + X_i' \delta t_i + X_i'' \frac{\delta t_i^2}{2} \geq X_{i+1}^{\text{exact}} \tag{3.66a}$$

$$X_{i+1}^{\text{LB}} \equiv X_i + X_i' \delta t_i + X_{i+1}'' \frac{\delta t_i^2}{2} \leq X_{i+1}^{\text{exact}} \tag{3.66b}$$

These hold even if δt is not small. The upper bound X^{UB} coincides with our definition eq. (3.64). The approximate value of X_{i+1} found at each iteration of our original computation is thus an overestimate. Since the terminating value of X will be reached sooner, the parameter $\tau = \sum_i \delta t_i$ evaluated in this way is underestimated. More precisely, for the choices of $X_0 = X(-1/2)$ and $X_0'' = X''(-1/2)$ that give the correct solution as $\delta t \to 0$, the maximum of X is obtained slightly below $\tau = 1/2$ due to the discretisation effect at finite δt.

To obtain lower bounds on X_i, and subsequently an upper bound on the value of τ, we use eq. (3.66b). We use the values of X_i obtained in our first computation, and solve the quadratic equation to obtain values of δt_i at each iteration i such that eq. (3.66b) is satisfied. For any given X_0 and X_0'', each δt_i, and hence their sum τ, will be overestimated by this procedure. We thus have a lower bound on $X(t)$ and upper bound on τ.

We can find bounds on our evaluation of the second constraint, eq. (3.38), by feeding both the upper and lower bounds on X_i into the numerical integration, and compounding each result with the uncertainty introduced by the integration.

Next, we find the uncertainty in X_0 and X_0''. For any given value of X_0 and X_0'', we have a range of uncertainty around the computed values of τ and the constraint. If we can obtain values of X_0 and X_0'' such that the most pessimistic part of these uncertainty ranges lies just around the target values ($1/2$ for τ and 0 for the constraint), then we obtain bounds on X_0 and X_0''. We must do this for each of the four combinations of signs, i.e. above and below $1/2$ and 0 for τ and the constraint, respectively.

We achieve this using the 2D Newton-Raphson method, as follows. We define

$$c \equiv \int_{-1/2}^{1/2} dt \log X(t), \tag{3.67}$$

so that the constraint in eq. (3.38) is satisfied when $c = i\theta$, which for us means $c = 0$. We then compute the values $\frac{\partial \tau}{\partial X_0}$, $\frac{\partial \tau}{\partial X_0''}$, $\frac{\partial c}{\partial X_0}$, and $\frac{\partial c}{\partial X_0''}$, and construct the matrix,

$$\hat{M} = \begin{pmatrix} \frac{\partial c}{\partial X_0''} & -\frac{\partial \tau}{\partial X_0''} \\ -\frac{\partial c}{\partial X_0} & \frac{\partial \tau}{\partial X_0} \end{pmatrix}.$$

We can then calculate ΔX_0 and $\Delta X_0''$ as

$$\begin{pmatrix} \Delta X_0 \\ \Delta X_0'' \end{pmatrix} = \frac{1}{(\det \hat{\mathrm{M}})} \hat{M} \begin{pmatrix} \tau - \frac{1}{2} \\ \mathcal{N} \end{pmatrix}.$$

We then update the values of X_0 and X_0'' as $X_0 \to X_0 - \Delta X_0$ and $X_0'' \to X_0'' - \Delta X_0''$, respectively. We repeat this such that X_0 and X_0'' approach the solution of $\tau = 1/2$ and $c = 0$, until sufficiently good precision is achieved. We repeat this for all four combinations of signs for $\tau - 1/2$ and c. We thus obtain upper and lower values of X_0 and X_0''.

Finally, we find errors on V by combining all the previous uncertainties with the uncertainties from the numerical integration, which are calculated using concave and convex properties of the integrand.

3.B Numerical data for the partial phase in softly-broken $\mathcal{N} = 1$ SYM

In this appendix we summarise the numerical data that we used for the partial-phase saddle in mass-deformed $\mathcal{N} = 1$ SYM. For finite N, we performed the minimisation procedure described in sec. 3.2.3.2 until the values cease to change within the machine precision. One should not take last few digits too seriously, because there can be round-off errors.

3.B.1 $\theta = 0$

$\tilde{\gamma}$	N	V

35	30	-0.8478043903335438
	50	-0.5102166657650717
	70	-0.3595906166171574
	100	-0.25107574410395184
40	30	-1.0649718464701392
	50	-0.6332206873888775
	70	-0.45061468574478286
	100	-0.3145884066304803
45	30	-1.2785511307705075
	50	-0.761118429321458
	70	-0.5420426727252557
	100	-0.3787049502744858
50	30	-1.4907670060318092
	50	-0.8894724152036553
	70	-0.6342449477861769
	100	-0.44359705462577126
55	30	-1.702131639184869
	50	-1.0181099952602852
	70	-0.7266752877179159
	100	-0.5084837953775918

$N = 30, 50, 70$ and 100, partial phase, $\theta = 0$

$\tilde{\gamma}$	V	M_0
34.105	-0.8077784649468457	$1.6912265451456194 \times 10^{-3}$
34.11	-0.808006900961617	$1.825013252705753 \times 10^{-3}$
34.12	-0.8084628031642389	$1.9478656004707329 \times 10^{-3}$
34.13	-0.8089179187701646	$2.036195524651749 \times 10^{-3}$
34.15	-0.8098264888913062	$2.1755532782433296 \times 10^{-3}$
34.2	-0.8120911012726231	$2.4397435964616405 \times 10^{-3}$
34.3	-0.8166006952471729	$2.8419172665191623 \times 10^{-3}$
34.4	-0.8210917533707988	$3.1768860264097065 \times 10^{-3}$
34.6	-0.8300338142941242	$3.759119403517365 \times 10^{-3}$
34.8	-0.8389351432399467	$4.281329673944455 \times 10^{-3}$
35.0	-0.8478043903335438	$4.7702137949790195 \times 10^{-3}$
36.0	-0.8918117613679025	$6.995520728491199 \times 10^{-3}$
37.0	-0.9354339738397822	$9.08813053438817 \times 10^{-3}$
38.0	-0.9787946802571408	$1.1156329329176953 \times 10^{-2}$
39.0	-1.0219599197166551	$1.3242392404282448 \times 10^{-2}$
40.0	-1.0649718464701392	$1.5370757634584244 \times 10^{-2}$
45.0	-1.2785511307705075	$2.722990757508838 \times 10^{-2}$
50.0	-1.4907670060318092	$4.288292912186151 \times 10^{-2}$
55.0	-1.702131639184869	$6.710582512934164 \times 10^{-2}$
60.0	-1.9116692104565214	0.10823277553764502
65.0	-2.1161089139314724	0.18747909204305171
70.0	-2.311793371129293	0.3079225504046863

$N = 30$, partial phase, $\theta = 0$

$\tilde{\gamma}$	NV	M_0
30	$-18.74626162(8)$	$6.3142(0) \times 10^{-49}$
31	$-19.98133943(4)$	$5.55392(3) \times 10^{-16}$
32	$-21.2204182(5)$	$5.20898(7) \times 10^{-10}$
33	$-22.4637859(1)$	$1.62375(1) \times 10^{-7}$
34	$-23.711824(6)$	$3.72298(3) \times 10^{-6}$
35	$-24.9650239(7)$	$2.64232(4) \times 10^{-5}$
36	$-26.2238647(7)$	$1.0095981(8) \times 10^{-4}$
37	$-27.4886645(9)$	$2.6907652(0) \times 10^{-4}$
38	$-28.7595114(5)$	$5.726169(6) \times 10^{-4}$
39	$-30.0362787(7)$	$1.04973585(9) \times 10^{-3}$
40	$-31.3186700(6)$	$1.7345736(7) \times 10^{-3}$
41	$-32.6062631(6)$	$2.6581096(1) \times 10^{-3}$
42	$-33.8985461(4)$	$3.8491581(7) \times 10^{-3}$
43	$-35.1949437(6)$	$5.3352114(3) \times 10^{-3}$
44	$-36.4948366(6)$	$7.1430956(1) \times 10^{-3}$
45	$-37.7975750(8)$	$9.2994790(6) \times 10^{-3}$
46	$-39.1024887(4)$	$1.183127(7) \times 10^{-2}$
47	$-40.4088940(9)$	$1.47659901(3) \times 10^{-2}$
48	$-41.7160994(9)$	$1.81319999(2) \times 10^{-2}$

49	$-43.0234090(4)$	$2.19588494(7) \times 10^{-2}$
50	$-44.3301255(2)$	$2.62775163(4) \times 10^{-2}$
51	$-45.6355526(2)$	$3.11206952(7) \times 10^{-2}$
52	$-46.9389962(8)$	$3.65231002(2) \times 10^{-2}$
53	$-48.2397661(0)$	$4.25217969(9) \times 10^{-2}$
54	$-49.5371762(1)$	$4.91565774(0) \times 10^{-2}$
55	$-50.8305458(6)$	$5.64703882(0) \times 10^{-2}$
56	$-52.1191999(9)$	$6.4509830(3) \times 10^{-2}$
57	$-53.4024695(7)$	$7.3325746(4) \times 10^{-2}$
58	$-54.6796918(6)$	$8.2973921(7) \times 10^{-2}$
59	$-55.9502105(9)$	$9.3515928(8) \times 10^{-2}$
60	$-57.2133759(5)$	$0.105020155(6)$

Large N, partial phase, $\theta = 0$

3.B.2 $\theta \sim \pi$

$\tilde{\gamma}$	θ	V	ReM_0	ImM_0
32.2	3.14159	-0.7170743511036082	$-1.3600120580223471 \times 10^{-3}$	$2.5812519554220423 \times 10^{-4}$
	3.14155	-0.7170743628838336	$-1.3609155565518565 \times 10^{-3}$	$2.4784827954029973 \times 10^{-4}$
	3.14149	-0.7170743795687697	$-1.3624561102521084 \times 10^{-3}$	$2.2927790368880996 \times 10^{-4}$
32.21	3.14159	-0.717533767794569	$-1.3321141681612805 \times 10^{-3}$	$4.350584609566822 \times 10^{-4}$
	3.14155	-0.7175337879330195	$-1.3326243195853749 \times 10^{-3}$	$4.3165909238074365 \times 10^{-4}$
	3.14149	-0.717533817841014	$-1.3334057063425766 \times 10^{-3}$	$4.264017413306071 \times 10^{-4}$
32.22	3.14159	-0.7179929889543566	$-1.3043571146458457 \times 10^{-3}$	$5.57310975551346 \times 10^{-4}$
	3.14155	-0.7179930147641919	$-1.3047479039944685 \times 10^{-3}$	$5.552750211788038 \times 10^{-4}$
	3.14149	-0.717993053301827	$-1.305339812640364 \times 10^{-3}$	$5.5217786311380666 \times 10^{-4}$
32.23	3.14159	-0.7184520170186798	$-1.276726078298016 \times 10^{-3}$	$6.562673111173997 \times 10^{-4}$
	3.14155	-0.7184520473852677	$-1.2770527104979121 \times 10^{-3}$	$6.5481765509790115 \times 10^{-4}$
	3.14149	-0.7184520928099734	$-1.2775455721013584 \times 10^{-3}$	$6.526246943145053 \times 10^{-4}$
32.24	3.14159	-0.7189108543080747	$-1.2492167707726551 \times 10^{-3}$	$7.413419732325752 \times 10^{-4}$
	3.14155	-0.7189108885694004	$-1.2495016117582143 \times 10^{-3}$	$7.402186698172351 \times 10^{-4}$
	3.14149	-0.7189109398649564	$-1.2499306258614793 \times 10^{-3}$	$7.385239606680516 \times 10^{-4}$
32.25	3.14159	-0.7193695030812562	$-1.2218263069640964 \times 10^{-3}$	$8.169019109646184 \times 10^{-4}$
	3.14155	-0.719369540783399	$-1.2220810489925724 \times 10^{-3}$	$8.159864591338513 \times 10^{-4}$
	3.14149	-0.719369597258429	$-1.2224643426274118 \times 10^{-3}$	$8.146073893530602 \times 10^{-4}$
32.3	3.14159	-0.721659994897846	$-1.0865777302750799 \times 10^{-3}$	$1.1133356734658564 \times 10^{-3}$
	3.14155	-0.7216600459096133	$-1.0867518649578847 \times 10^{-3}$	$1.112865030557661 \times 10^{-3}$
	3.14149	-0.7216601223879526	$-1.08701339135787 \times 10^{-3}$	$1.1121579353577529 \times 10^{-3}$
32.35	3.14159	-0.7239460866385014	$-9.539872225466342 \times 10^{-4}$	$1.336510099405864 \times 10^{-3}$
	3.14155	-0.7239461474331051	$-9.541226194560151 \times 10^{-4}$	$1.3361958057500578 \times 10^{-3}$
	3.14149	-0.7239462385992684	$-9.543258607049511 \times 10^{-4}$	$1.3357239597633632 \times 10^{-3}$
32.4	3.14159	-0.7262280139802966	$-8.238336317452523 \times 10^{-4}$	$1.5198967085948667 \times 10^{-3}$

	3.14155	-0.7262280826292161	$-8.239449058808901 \times 10^{-4}$	$1.519661261553193 \times 10^{-3}$
	3.14149	-0.7262281855836519	$-8.241119012794183 \times 10^{-4}$	$1.5193078955209953 \times 10^{-3}$
32.45	3.14159	-0.7285059915660974	$-6.95920795442486 \times 10^{-4}$	$1.6772622461292543 \times 10^{-3}$
	3.14155	-0.7285060668033074	$-6.960151327319915 \times 10^{-4}$	$1.6770737855282707 \times 10^{-3}$
	3.14149	-0.7285061796442005	$-6.96156691043507 \times 10^{-4}$	$1.67679098903428 \times 10^{-3}$
32.5	3.14159	-0.7307802155542057	$-5.700733563845978 \times 10^{-4}$	$1.815922434919294 \times 10^{-3}$
	3.14155	-0.7307802964681885	$-5.701549451005102 \times 10^{-4}$	$1.8157648292755948 \times 10^{-3}$
	3.14149	-0.7307804178268624	$-5.702773652676167 \times 10^{-4}$	$1.8155283552895594 \times 10^{-3}$
32.55	3.14159	-0.7330508657711814	$-4.46133941861139 \times 10^{-4}$	$1.9403360418338673 \times 10^{-3}$
	3.14155	-0.7330509516677158	$-4.462054880739285 \times 10^{-4}$	$1.940200026377375 \times 10^{-3}$
	3.14149	-0.7330510805020409	$-4.463128344139536 \times 10^{-4}$	$1.9399959606733754 \times 10^{-3}$
32.6	3.14159	-0.7353181075532847	$-3.2396082753576216 \times 10^{-4}$	$2.0534664742781557 \times 10^{-3}$
	3.14155	-0.7353181978832048	$-3.240242052503035 \times 10^{-4}$	$2.053346256161984 \times 10^{-3}$
	3.14149	-0.7353183333689319	$-3.2411929223816873 \times 10^{-4}$	$2.05316590012776 \times 10^{-3}$
32.7	3.14159	-0.7398429640031353	$-8.441353218502272 \times 10^{-5}$	$2.2536927081194666 \times 10^{-3}$
	3.14155	-0.7398430619362288	$-8.446433117245173 \times 10^{-5}$	$2.2535937029615045 \times 10^{-3}$
	3.14149	-0.7398432088284732	$-8.454054168750659 \times 10^{-5}$	$2.2534451813331 \times 10^{-3}$
32.8	3.14159	-0.7443558729386548	$1.4945625418492055 \times 10^{-4}$	$2.427763658793177 \times 10^{-3}$
	3.14155	-0.7443559772114889	$1.4941476202572692 \times 10^{-4}$	$2.427677878174378 \times 10^{-3}$
	3.14149	-0.7443561336144284	$1.4935251527640314 \times 10^{-4}$	$2.42754919912249 \times 10^{-3}$
33.0	3.14159	-0.7533494785206036	$6.029864611902578 \times 10^{-4}$	$2.722097577747968 \times 10^{-3}$
	3.14155	-0.7533495928971548	$6.029579386735867 \times 10^{-4}$	$2.722026565347336 \times 10^{-3}$
	3.14149	-0.7533497644568607	$6.029151504548835 \times 10^{-4}$	$2.721920043916067 \times 10^{-3}$
33.5	3.14159	-0.7756774553170565	$1.6768822556210576 \times 10^{-3}$	$3.2794358050263086 \times 10^{-3}$
	3.14155	-0.7756775865578464	$1.6768711746605895 \times 10^{-3}$	$3.2793770628401324 \times 10^{-3}$
	3.14149	-0.7756777834149097	$1.6768545514918272 \times 10^{-3}$	$3.2792889492241932 \times 10^{-3}$
34.0	3.14159	-0.7978302202388292	$2.6962105102698835 \times 10^{-3}$	$3.707440095081149 \times 10^{-3}$
	3.14155	-0.7978303624083353	$2.6962083806895687 \times 10^{-3}$	$3.707383288903868 \times 10^{-3}$
	3.14149	-0.797830575658689	$2.696205185554002 \times 10^{-3}$	$3.707298079813313 \times 10^{-3}$
35.0	3.14159	-0.8417550290603878	$4.652679404706676 \times 10^{-3}$	$4.397709927810709 \times 10^{-3}$
	3.14155	-0.8417551856349794	$4.652686740494166 \times 10^{-3}$	$4.397650104350867 \times 10^{-3}$
	3.14149	-0.8417554204929414	$4.652697743717927 \times 10^{-3}$	$4.397560369302386 \times 10^{-3}$
40.0	3.14159	-1.0573792156622257	$1.4412981881233673 \times 10^{-2}$	$7.189654944745767 \times 10^{-3}$
	3.14155	-1.0573794090113	$1.441300645625501 \times 10^{-2}$	$7.189564703253496 \times 10^{-3}$
	3.14149	-1.0573796990302957	$1.4413043318185594 \times 10^{-2}$	$7.189429340916259 \times 10^{-3}$
45.0	3.14159	-1.2699610845858604	$2.580531090072105 \times 10^{-2}$	$1.0251017087791112 \times 10^{-2}$
	3.14155	-1.2699613031848664	$2.580534712424157 \times 10^{-2}$	$1.025088921290766 \times 10^{-2}$
	3.14149	-1.2699616310781705	$2.5805401458661206 \times 10^{-2}$	$1.0250697400390536 \times 10^{-2}$
50.0	3.14159	-1.4812961563094476	$4.094947544666873 \times 10^{-2}$	$1.4243699194655928 \times 10^{-2}$
	3.14155	-1.4812963972886606	$4.0949524558640515 \times 10^{-2}$	$1.424352143939323 \times 10^{-2}$
	3.14149	-1.4812967587517454	$4.094959822543871 \times 10^{-2}$	$1.42432548062422 \times 10^{-2}$
55.0	3.14159	-1.6918402420861214	$6.4604328760748135 \times 10^{-2}$	$2.0052826308490346 \times 10^{-2}$
	3.14155	-1.691840503923804	$6.460439236308307 \times 10^{-2}$	$2.0052575094367473 \times 10^{-2}$
	3.14149	-1.6918408966740976	$6.460448770552378 \times 10^{-2}$	$2.00521982780708 \times 10^{-2}$
60.0	3.14159	-1.9005649352418637	0.10809898207091294	$2.8902218845528007 \times 10^{-2}$

	3.14155	-1.9005652175955352	0.10809905918554755	$2.890185488245071 \times 10^{-2}$
	3.14149	-1.9005656411193246	0.10809917465036076	$2.890130889764398 \times 10^{-2}$
65.0	3.14159	-2.104169423293366	0.18387620479734793	$4.060558125607354 \times 10^{-2}$
	3.14155	-2.1041697270523865	0.18387629641317327	$4.060506857755586 \times 10^{-2}$
	3.14149	-2.104170182683694	0.18387643368075676	$4.060429953799894 \times 10^{-2}$
70.0	3.14159	-2.298983857096773	0.30372551405890685	$5.480071091863914 \times 10^{-2}$
	3.14155	-2.29898418298924	0.30372562079881626	$5.480001782656032 \times 10^{-2}$
	3.14149	-2.298984671820188	0.30372578090795543	$5.4798978188303415 \times 10^{-2}$

$N = 30$, partial phase at finite θ

$\tilde{\gamma}$	θ	V	ReM_0	ImM_0
31.6	3.14159	-0.4155123088833649	$-1.8782005991409765 \times 10^{-4}$	$6.330578970860719 \times 10^{-4}$
	3.14155	-0.4155123251919556	$-1.8784922965670887 \times 10^{-4}$	$6.330043923677622 \times 10^{-4}$
	3.14149	-0.4155123496523715	$-1.878929966005143 \times 10^{-4}$	$6.32924113843514 \times 10^{-4}$
31.7	3.14159	-0.4181552328004205	$-4.600790872308327 \times 10^{-5}$	$7.559655923117715 \times 10^{-4}$
	3.14155	-0.41815525200604925	$-4.602804756640492 \times 10^{-5}$	$7.559296156993012 \times 10^{-4}$
	3.14149	-0.4181552808128721	$-4.605826079233592 \times 10^{-5}$	$7.558756446524675 \times 10^{-4}$
31.78	3.14159	-0.4202649022150887	$6.326245956469611 \times 10^{-5}$	$8.332766036474448 \times 10^{-4}$
	3.14155	-0.42026492316425357	$6.324671926096537 \times 10^{-5}$	$8.332471502032584 \times 10^{-4}$
	3.14149	-0.4202649545866925	$6.322310593859195 \times 10^{-5}$	$8.33202967268706 \times 10^{-4}$
31.802	3.14159	-0.42084439582102184	$9.275084219401403 \times 10^{-5}$	$8.522634299284915 \times 10^{-4}$
	3.14155	-0.420844417187829	$9.273606185621027 \times 10^{-5}$	$8.522352193851644 \times 10^{-4}$
	3.14149	-0.4208444492367917	$9.271388887576544 \times 10^{-5}$	$8.521929013447016 \times 10^{-4}$
31.82	3.14159	-0.4213183239133828	$1.1671237306609559 \times 10^{-4}$	$8.671909558256232 \times 10^{-4}$
	3.14155	-0.4213183456054398	$1.1669831738462748 \times 10^{-4}$	$8.671636395208687 \times 10^{-4}$
	3.14149	-0.4213183781423188	$1.1667723159806762 \times 10^{-4}$	$8.671226631305268 \times 10^{-4}$
31.85	3.14159	-0.42210780928338515	$1.5633301651780533 \times 10^{-4}$	$8.909669581169569 \times 10^{-4}$
	3.14155	-0.4221078314876758	$1.5632006291092861 \times 10^{-4}$	$8.909409280614963 \times 10^{-4}$
	3.14149	-0.42210786479296847	$1.5630063057297492 \times 10^{-4}$	$8.909018814793864 \times 10^{-4}$
31.9	3.14159	-0.42342256294940883	$2.215471299404181 \times 10^{-4}$	$9.278918024374619 \times 10^{-4}$
	3.14155	-0.4234225859345137	$2.2153576841864933 \times 10^{-4}$	$9.278674695536766 \times 10^{-4}$
	3.14149	-0.4234226204111069	$2.2151872465800584 \times 10^{-4}$	$9.278309692573936 \times 10^{-4}$
32.5	3.14159	-0.4391174957274477	$9.496371234248153 \times 10^{-4}$	$1.2294221709574773 \times 10^{-3}$
	3.14155	-0.43911752431471013	$9.496345451950141 \times 10^{-4}$	$1.229403158143993 \times 10^{-3}$
	3.14149	-0.4391175671948034	$9.496306776463555 \times 10^{-4}$	$1.2293746389938343 \times 10^{-3}$
34.0	3.14159	-0.4779612628170003	$2.601455269143662 \times 10^{-3}$	$1.653288813560361 \times 10^{-3}$
	3.14155	-0.4779612968106036	$2.601457687671169 \times 10^{-3}$	$1.6532672341409855 \times 10^{-3}$
	3.14149	-0.4779613478001801	$2.6014613153755284 \times 10^{-3}$	$1.6532348650414865 \times 10^{-3}$
45.0	3.14159	-0.7592450724009824	$1.734899931471533 \times 10^{-2}$	$4.515391915490412 \times 10^{-3}$
	3.14155	-0.7592451200935519	$1.7349010423645999 \times 10^{-2}$	$4.5153349993345975 \times 10^{-3}$
	3.14149	-0.7592451916312689	$1.734902708674579 \times 10^{-2}$	$4.515249625049745 \times 10^{-3}$
50.0	3.14159	-0.8874198012140362	$3.0056225594155026 \times 10^{-2}$	$6.954488692854987 \times 10^{-3}$
	3.14155	-0.887419853467416	$3.005624166450025 \times 10^{-2}$	$6.954400874243307 \times 10^{-3}$
	3.14149	-0.887419931846239	$3.0056265769649566 \times 10^{-2}$	$6.954269146282227 \times 10^{-3}$

$N = 50$, partial phase at finite θ

$\tilde{\gamma}$	θ	V	ReM_0	ImM_0
31.325	3.14159	-0.2918407654541345	$7.98026871679131 \times 10^{-5}$	$4.424333155597573 \times 10^{-4}$
	3.14155	-0.291840773245185	$7.979585621482465 \times 10^{-5}$	$4.42420336394707 \times 10^{-4}$
	3.14149	-0.29184078493135135	$7.978560880788008 \times 10^{-5}$	$4.42400866869941 \times 10^{-4}$
31.35	3.14159	-0.2923040923705275	$1.0278346984026125 \times 10^{-4}$	$4.550621221981385 \times 10^{-4}$
	3.14155	-0.29230410035776927	$1.0277720816889515 \times 10^{-4}$	$4.550497714063126 \times 10^{-4}$
	3.14149	-0.29230411233824344	$1.0276781494419844 \times 10^{-4}$	$4.5503124467492855 \times 10^{-4}$
31.4	3.14159	-0.29323011303276025	$1.4803076391381091 \times 10^{-4}$	$4.78144033280332 \times 10^{-4}$
	3.14155	-0.29323012137172827	$1.4802545804784515 \times 10^{-4}$	$4.781326262086492 \times 10^{-4}$
	3.14149	-0.29323013387982394	$1.480174987299652 \times 10^{-4}$	$4.781155153336815 \times 10^{-4}$
31.5	3.14159	-0.29507983238035607	$2.360576804307633 \times 10^{-4}$	$5.175995910049874 \times 10^{-4}$
	3.14155	-0.2950798412980503	$2.3605377995782924 \times 10^{-4}$	$5.175893000261233 \times 10^{-4}$
	3.14149	-0.2950798546742728	$2.360479289004306 \times 10^{-4}$	$5.175738634434299 \times 10^{-4}$
31.75	3.14159	-0.29969279644826335	$4.455054068316847 \times 10^{-4}$	$5.921697420074003 \times 10^{-4}$
	3.14155	-0.29969280636979745	$4.455035033503333 \times 10^{-4}$	$5.921603720842227 \times 10^{-4}$
	3.14149	-0.29969282125181285	$4.45500648040117 \times 10^{-4}$	$5.921463172458622 \times 10^{-4}$
32.0	3.14159	-0.30429298401236626	$6.449889616569478 \times 10^{-4}$	$6.4801563646402665 \times 10^{-4}$
	3.14155	-0.30429299459764153	$6.449881034089653 \times 10^{-4}$	$6.480063166785355 \times 10^{-4}$
	3.14149	-0.3042930104752741	$6.449868159820404 \times 10^{-4}$	$6.479923370314297 \times 10^{-4}$
32.5	3.14159	-0.3134658092525986	$1.0279762018595526 \times 10^{-3}$	$7.34053348582117 \times 10^{-4}$
	3.14155	-0.313465820704502	$1.0279764159264388 \times 10^{-3}$	$7.340435347025221 \times 10^{-4}$
	3.14149	-0.31346583788207316	$1.0279767369974029 \times 10^{-3}$	$7.340288139099266 \times 10^{-4}$
33.0	3.14159	-0.3226126313086142	$1.4010179461914722 \times 10^{-3}$	$8.042442954538322 \times 10^{-4}$
	3.14155	-0.322612643339618	$1.4010187169395665 \times 10^{-3}$	$8.042338161760316 \times 10^{-4}$
	3.14149	-0.3226126613858309	$1.4010198732807868 \times 10^{-3}$	$8.04218097538276 \times 10^{-4}$
34.0	3.14159	-0.3408572002751646	$2.142071796713208 \times 10^{-3}$	$9.269612602029794 \times 10^{-4}$
	3.14155	-0.3408572131130061	$2.1420731847348127 \times 10^{-3}$	$9.269493944101995 \times 10^{-4}$
	3.14149	-0.34085723236945964	$2.142075266736319 \times 10^{-3}$	$9.269315957258254 \times 10^{-4}$
35.0	3.14159	-0.3590631133644247	$2.895574207226948 \times 10^{-3}$	$1.042688775208161 \times 10^{-3}$
	3.14155	-0.3590631268061734	$2.8955759853564587 \times 10^{-3}$	$1.0426755056744041 \times 10^{-3}$
	3.14149	-0.3590631469684751	$2.8955786523457916 \times 10^{-3}$	$1.0426556014402968 \times 10^{-3}$
40.0	3.14159	-0.45000014388659393	$7.225957517480029 \times 10^{-3}$	$1.6925857932954413 \times 10^{-3}$
	3.14155	-0.45000015953462313	$7.225960775567354 \times 10^{-3}$	$1.6925643698951656 \times 10^{-3}$
	3.14149	-0.45000018300629346	$7.225965662618408 \times 10^{-3}$	$1.6925322347811091 \times 10^{-3}$
45.0	3.14159	-0.5413574476911213	$1.3626015882620472 \times 10^{-2}$	$2.697613400021317 \times 10^{-3}$
	3.14155	-0.5413574651378426	$1.3626021051768908 \times 10^{-2}$	$2.6975792579866846 \times 10^{-3}$
	3.14149	-0.5413574913075072	$1.3626028805361086 \times 10^{-2}$	$2.6975280449202055 \times 10^{-3}$
50.0	3.14159	-0.6334972947003091	$2.6550506491932127 \times 10^{-2}$	$4.66305021094182 \times 10^{-3}$
	3.14155	-0.6334973137359372	$2.6550514317777956 \times 10^{-2}$	$4.662991057611511 \times 10^{-3}$
	3.14149	-0.6334973422889246	$2.6550526056381325 \times 10^{-2}$	$4.662902327597171 \times 10^{-3}$

$N = 70$, partial phase at finite θ

Chapter 4

Holography and RG flows on Wilson Loops and Defects

In this chapter, we will make use of an especially fertile and adaptable method of approaching strongly coupled field theories known as gauge/gravity duality [66; 67; 68]. This allows us to represent certain strongly coupled field theories as equivalent, or dual, theories of weakly coupled gravity in one dimension higher. While this duality remains a conjecture, there is bountiful evidence in its support, and we will assume its reliability. We will exclusively use the best-understood example of AdS/CFT, namely the equivalence between ten-dimensional type IIB supergravity (SUGRA) on $AdS_5 \times S^5$ and $(3+1)$-dimensional $\mathcal{N}=4$ supersymmetric (SUSY) Yang-Mills theory (SYM), with gauge group $SU(N_c)$, in the 't Hooft large-N_c limit, and with large 't Hooft coupling [66; 69; 70].

We will employ this duality to analyse $2+1$-dimensional spherical defects, $\mathbb{R} \times S^2$, in strongly-coupled $\mathcal{N}=4$ SYM. We will demonstrate that these run under renormalisaton group (RG) flow to spherically-symmetric $(0+1)$-dimensional gapless fields that, when integrated out of the $\mathcal{N}=4$ SYM path integral, produce straight superconformal Wilson or Wilson-'t Hooft loops. We deduce, therefore, that these spherical defects furnish a new UV completion of the Wilson and Wilson-'t Hooft loops [39; 71; 72; 73; 74; 75; 76], thereby offering an entirely new description of Wilson loops as the IR limit of such defects. Our results also suggest that, generically in gauge theories, conformal line operators may appear in the IR when defect matter on a sphere supports spherically-symmetric zero-energy states.

We speculate that, as new descriptions of Wilson loops, these defects themselves might act as useful probes and order parameters in some situations. In particular, we might hope to use them in future work to learn more about the partially confined phase and its holographic manifestation.

While the above is of intrinsic interest for understanding strongly coupled gauge theories and Wilson loops, there is an additional motivation for this construction that concerns the physics of graphene and fullerenes.

Calculations attempting to elucidate the physics of graphene using various techniques have been performed in refs. [77; 78; 79; 80; 81; 82; 83; 84]. The main result agreed upon in all of these is that free, massless Dirac fermions on $\mathbb{R} \times S^2$ with $B = 0$ are gapped, while a magnetic monopole producing $B \neq 0$ normal to the S^2 give gapless modes.

However, a fundamental problem is that graphene and similar materials do not give rise to *free* $(2+1)$-dimensional Dirac fermions, but rather to $(2+1)$-dimensional Dirac fermions coupled to $(3+1)$-dimensional Maxwell theory. In other words, such materials are codimension-one "defects" in Maxwell theory. The resulting interactions can generate energy gaps, break degeneracies, and/or trigger fermion pairing, producing condensates that may break symmetries.

"Traditional" methods for answering such questions are often practically useless. For example, in graphene the effective fine structure constant is order one [85], making perturbation theory unreliable. For questions about physics with $Q > 0$ and/or out of equilibrium, such as electronic transport, the sign problem [86] makes quantum Monte Carlo and similar numerical methods unreliable. In short, for many important questions about these materials, currently *no reliable method exists* to calculate the answers.

We therefore turn to AdS/CFT. Like $(3+1)$-dimensional Maxwell theory, $(3+1)$-dimensional $\mathcal{N} = 4$ SYM is a CFT: the 't Hooft coupling is exactly marginal for any N. We will be able to introduce a $(2+1)$-dimensional spherical defect in this theory to which Dirac fermions accompanied by scalar superpartners (thus forming hypermultiplets) are restricted. These fields couple to the gauge field and one or more adjoint scalars of $\mathcal{N} = 4$ SYM, or more precisely, to their pullbacks to the $(2+1)$-dimensional defect [87; 88; 89; 90]. Such defect flavor fields have global $U(N_f)$ flavor symmetry, of which the overall diagonal $U(1) \subset U(N_f)$ is the hypermultiplet number. We will introduce non-zero charge density Q and magnetic field B for this $U(1)$, as well as a hypermultiplet mass, M.

In this way, we hope to model spherical graphene and fullerenes, capturing the consequences of Dirac fermions being strongly coupled to gauge fields of the surrounding CFT, in the presence of a magnetic field and non-zero charge density.

Before we introduce the AdS/CFT correspondence, we will explain the field theory description of the problem in more detail. We consider Dirac fermions and their scalar superpartners consigned to a sphere of two spatial dimensions, placed in the background of a strongly-coupled $\mathcal{N} = 4$ $SU(N)$ SYM theory at large N, to which the hypermultiplet on the sphere is coupled. We introduce N_f flavours of this hypermultiplet, all sharing the same mass, to the sphere. The theory therefore has a $U(N_f)$ flavour symmetry. We split $U(N_f) = U(1) \times SU(N_f)$. This $U(1)$ symmetry is the quark number (equivalently, the baryon number multiplied by N_f). We introduce a non-zero quark number-density (or quark charge) to the sphere. We also add a radial, non-dynamical background magnetic field, proportional to the field's volume form. Our calculations remain at zero temperature throughout. We perform RG flow on this system to arrive at the IR description, which we find to be various kinds of Wilson-'t Hooft loops depending on the initial quark number density and magnetic field strength.

4.1 AdS/CFT

We will now introduce the duality between $\mathcal{N} = 4$ $SU(N)$ SYM and Type IIB superstring theory in $AdS_5 \times S^5$ [66; 67; 68]. This relation is usually motivated by considering a stack of a number N parallel D3 branes, embedded in flat ten dimensional space. In the low energy ($E \ll 1/\sqrt{\alpha'}$, where α' is the squared string length, $\alpha' = l_s^2$) and weakly coupled (perturbative) region, D branes can be fully characterised as objects on which open strings end, and their dynamical behaviour inferred from that of open strings. Each end of an open strings can end on different branes on the stack, and we thus obtain a $U(N)$ symmetry, with open strings transforming adjointly. The effective string coupling for a stack is $g_s N$, and we therefore demand $g_s N \ll 1$ for the validity of this description.

Since closed strings form naturally in a theory with open string and D branes, the full action for the D brane involves that of open strings, closed strings, and the interactions between open and closed strings. We may write the effective action as,

$$S = S_{\text{open}} + S_{\text{closed}} + S_{\text{int}} \tag{4.1}$$

In analogy with the Nambu-Goto action for fundamental strings, the local contribution to the bosonic part of the open string action for the D brane can be written,

$$S_{\text{DBI}} = -T_{\text{D3}} \int \mathrm{d}^4\xi \, \mathrm{STr} \sqrt{-\det(g + 2\pi\alpha' F)}, \tag{4.2}$$

where STr denotes the symmetric trace over the gauge indices, g is the induced metric on the brane, F is the $U(N)$ gauge field on the stack of branes, and the integral is over the worldvolume coordinates ξ. The prefactor is the tension of the brane, $T_{\text{D3}} = \frac{1}{(2\pi)^3(\alpha')^2 g_s}$.

There are also topological contributions to the bosonic part of the open string action known as the Wess-Zumino action. This term allows strings and D branes to be dissolved in another D brane, thus sourcing charge in the brane. It won't be crucial for the current discussion, but will be important later.

We now consider the low energy limit, which can be obtained by expanding the action in α' and then taking $\alpha' \to 0$. The closed strings decouple from the open strings, while the closed string action becomes that of free gravitons. Meanwhile, (4.2) becomes the action of 4D $\mathcal{N} = 4$ SYM. We thus have a field theory in 4D, and a decoupled theory of free gravtitons in flat 10D.

We now consider a different description of the stack of D branes. It has also been shown that the D branes are solitonic solutions of supergravity, and that an alternative description of their dynamics can be given in terms of supergravity. The supergravity perspective is valid when $g_s \ll 1$ and the energy scale $E \ll 1/\sqrt{\alpha'}$, such that only massless modes are relevant.

The supergravity solution describing this stack of D3 branes is then given by,

$$ds^2 = f^{-1/2}(-dt^2 + dx_1^2 + dx_2^2 + dx_3^2) + f^{1/2}(dr^2 + r^2 d\Omega_5^2) \tag{4.3}$$

$$C_4 = (1 - f^{-1}) dx_0 \wedge dx_1 \wedge dx_2 \wedge dx_3 + \cdots \tag{4.4}$$

$$f = 1 + L^4/r^4 \tag{4.5}$$

where C_4 is an RR 4-form potential with associated self-dual field strength $F_5 = dC_4$, the ellipsis denotes terms in the potential that ensure this self-duality and which we do not show, $d\Omega_5$ is the unit metric on a 5-sphere, and L is a length scale linked to the number of branes in the stack, N, by,

$$L^4 = 4\pi g_s \alpha'^2 N. \tag{4.6}$$

To compare this to the low energy open string description that we outlined above, we should take the strict low energy limit again. We must be careful with the meaning of this in a theory with nontrivial metric. An observer held at constant coordinate r measures an energy E_r related to that measured by an observer at infinity by,

$$E_r = f^{1/4} E \tag{4.7}$$

It is the energy at infinity that matches the notion of energy used in the field theory. Therefore, we now consider taking the low energy limit as perceived by an observer at infinity. We can again achieve a low energy limit by keeping E fixed while taking $\alpha' \to 0$.

Strings are redshifted according to (4.7), and so high energy strings sufficiently close to the D3 branes will not decouple under this limit. In fact, as we take the low energy limit carefully, we can see two sectors of closed strings that decouple from one another[1]: firstly, free massless strings in flat spacetime, and secondly, strings arbitrarily close to the D3 branes that can have arbitrarily high energies, described by a full Type IIB string theory. A precise calculation shows that the absorption cross section of the D3 brane stack with respect to the strings approaching from large r with energy ω goes as $\sigma \sim \omega^3 L^8$, and so vanishes as we take $\omega \to 0$ [67]. (This, in turn, is because the wavelength of the scattering strings becomes much larger than the gravitational curvature exerted, which, in this supergravity description, is how the interaction of the D brane is represented.) Also, of course, as the energy scale E is reduced, strings of a certain energy must lie ever closer to $r = 0$ in order not to be integrated out.

This motivates us to consider a *near-horizon* limit, 'zooming in' to the region around $r \sim 0$ so that we can make sense of the sector of the theory close to the horizon. We consider values of $r \ll L$. We want to keep the energy in this region fixed under this process (in string units), so that we can continue to have a full string theory here and keep this sector of the theory intact. This means we must keep $E_p\sqrt{\alpha'}$ fixed. We also want to keep the energy at infinity fixed, since this is the the notion of energy corresponding to that used in the open string picture and will permit us to compare both theories. From (4.7), at small α' we have $E \sim E_p r/\sqrt{\alpha'}$. Together, therefore, this demands we perform the near-horizon limit by taking $r \to 0$ with $\frac{r}{\alpha'}$ held fixed. This is the Maldacena limit. Taking this limit, the metric and RR potential become,

$$\begin{aligned} ds^s &= \frac{r^2}{L^2}\eta_{\mu\nu}dx^\mu dx^\nu + \frac{L^2}{r^2}dr^2 + L^2 d\Omega_5^2 \\ C_4 &= \frac{r^4}{L^4} + \cdots \end{aligned} \tag{4.8}$$

The metric describes $AdS_5 \times S^5$, with radius of the S^5 and radius of curvature for AdS_5 each of L.

For this description to be accurate, we require that the AdS radius of curvature, L, be must larger than the string length, $l_s = \sqrt{\alpha'}$. Using (4.6), we see that this implies,

$$\frac{L^4}{l_s^4} \sim g_s N \gg 1. \tag{4.9}$$

Since we also require g_s to be small, we must take N to be large.

Therefore, we have a theory of IIB string theory in $AdS_5 \times S^5$, combined with a decoupled free gravity theory in flat space. Recall that the first description consisted of an $\mathcal{N} = 4$ SYM theory and a decoupled free gravity theory in flat space. These should both describe the same theory, but in different regions of the 't Hooft coupling, $g_s N$. It is natural to suppose that we can remove the decoupled gravity theories from each description and retain an equivalence. This then implies that we can describe

---

[1] with a caveat regarding the decoupling of the diagonal $U(1)$, mentioned below

$\mathcal{N} = 4$ SYM theory at strong ('t Hooft) coupling by a theory of supergravity at weak coupling. This 'strong to weak' aspect of the duality is a very useful feature, making computations on strongly coupled field theories tractable.

This construction cannot be considered a proof since it dealt with string theory only in a perturbative way. It therefore remains a conjecture, though it has survived many tests for consistency.

It is important to note that the gauge group of $\mathcal{N} = 4$ SYM is $SU(N)$, not $U(N)$. The reason for this was not made clear in the above argument. It turns out that, in the large N and Maldacena limits, the diagonal $U(1)$ of $U(N)$ decouples from the $SU(N)$ degrees of freedom in the SYM theory. Commonly in field theory, couplings corresponding to different irreducible representations in the theory have different runnning behaviour under renormalisation group flow. In this case, the coupling corresponding to the $U(1)$ representation does not share the property of asymptotic freedom, and so decouples from the theory as we take the near-horizon (i.e. infrared) limit. From the perspective of the gravity theory, the $U(1)$ degrees of freedom correspond to non-propagating boundary modes. Regardless, in the large N limit, the difference between $SU(N)$ and $U(N)$ theories becomes negligible, differing only by terms suppressed by powers of N.

The lower-dimensional gauge theory will be referred to as 'the field theory', or, for reasons to be explained below, 'the boundary theory', while the higher-dimensional theory containing gravity will sometimes be referred to as 'the bulk'.

4.1.1 UV/IR connection

A very important aspect of the AdS/CFT duality is revealed when we inquire as to how the extra dimension of the bulk theory is encoded in the field theory. The answer is suggested already by the need, when taking the low energy limit of the field theory, to correspondingly take the near horizon limit. That is, the extra dimension in the bulk theory represents the energy scale of the boundary theory.

We can see this more explicitly. At a given value of the radial direction r, according to 4.8, the time at the boundary τ in terms of the local proper time t is,

$$d\tau = \frac{r}{R} dt \tag{4.10}$$

From this, we can infer the relation between the local energy in the bulk, E_{local}, and the energy in the boundary theory, E_{YM}, to be,

$$E_{\text{YM}} = \frac{r}{R} E_{\text{local}} \tag{4.11}$$

Consider processes in the bulk that share the same local energy scale but that differ in the radial depth at which they occur. The greater this radial depth, the lower is the energy of the corresponding boundary theory process being described. We can examine the extreme limits. Approaching the boundary of AdS space, we see

$$r \to \infty \implies E_{\text{YM}} \to \infty, \tag{4.12}$$

showing that the UV of the field theory is described close to the boundary in the bulk. In contrast, as we approach the stack of D3 branes near the Poincaré horizon,

$$r \to 0 \implies E_{\text{YM}} \to 0, \tag{4.13}$$

and so we probe lower energies in the field theory by approaching the horizon in the bulk, far from the boundary.

This association between the depth of the bulk process and the energy of the field theory is known as the UV/IR connection. It is a very salient feature of AdS/CFT and will be extremely useful for us. It allows us to consider motion in the radial direction as an RG-flow on the field theory. We will use this aspect of AdS/CFT later to infer the IR effective theory that emerges from a strongly coupled gauge theory that we have defined in the UV. This is often a very difficult task using only field theory techniques and without the benefit of AdS/CFT.

The UV/IR connection is also why we can think of the full UV field theory as 'living at the boundary' of AdS. This is an image that proves very fruitful at encapsulating the details of the AdS/CFT correspondence.

4.2 Field-operator correspondence and symmetry representations

The AdS/CFT correspondence constructed above proposes an exact equivalence between the boundary and bulk theories. This implies the existence of a bijective map between the physical degrees of freedom of each theory. Since a CFT has no asymptotic states or an S-matrix, the most natural proposal is to relate operators in the boundary theory to fields in the bulk theory.

The physical symmetries of each side of the duality must be identical. Both theories have $PSU(2,2|4)$ symmetry. The bosonic part of this is $SO(6) \times SO(4,2)$. In the field theory, the $SO(6)$ is the R symmetry of $\mathcal{N} = 4$ SYM, while the $SO(4,2)$ is composed of Lorentz transformations, $SO(3,1)$, enhanced by conformal transformations. Meanwhile, in the gravity theory, the AdS space is invariant under $SO(4,2)$

isometries, while the S^5 is invariant under $SO(6)$ rotations. We also have supersymmetry on each side.

We should expect corresponding fields and operators to be in matching representations of the symmetries. This principleallows us to deduce the precise dictionary between fields and operators.

Scalar, vector and tensor operators in the boundary theory will map, respectively, to scalar, vector, and tensor fields in the bulk theory. In $\mathcal{N} = 4$ SYM and its dual, it can be shown that the $SO(6)$ R symmetry currents of the field theory map to gauge field fluctuations that result from Kaluza-Klein reduction of the S^5, while the energy-momentum tensor of the field theory maps to metric fluctuations in the AdS.

As another example, we can decompose scalar fields in the bulk into irreducible representations of $SO(6)$ by Kaluza-Klein reduction and expansion in spherical harmonics on the S^5. We can then associate these to (composite) gauge-invariant operators in the boundary theory whose symmetries and representations are known from field theory analysis. If, for example, we find the duals of $1/2$ BPS scalar operators in this way, we can subsequently associate all the superconformal descendants of the operators with appropriate descendants in the gravity theory.

We can formalise this field-operator correspondence with the proposal that deforming the field theory by

$$\int d^d x \phi_0(x) \mathcal{O}(x), \tag{4.14}$$

for field theory operator $\mathcal{O}$ and classical source field values $\phi_0(x)$, should correspond to solving the gravity equations in the bulk for the corresponding field $\phi(r, x)$ with (appropriately-renormalised) boundary value $\phi_0(x)$. If we allow the extension of AdS/CFT to hold for the full string theory, beyond the supergravity limit, we can express this as

$$\left\langle \exp\left(\int d^d x \mathcal{O} \phi_0 \right) \right\rangle_{\text{CFT}} = \mathcal{Z}_{\text{string}}\big|_{\phi(x,r) \xrightarrow{r\to\infty} \phi_0(x)} \tag{4.15}$$

relating expectation values in the field theory to the partition functions of the bulk. In fact, this equation could be considered the most concise and complete expression of the AdS/CFT correspondence.

The asymptotic limit of this relation as we approach the boundary will suffice for our purposes. Consider, therefore, any bulk field ϕ, in any representations of the symmetries, that obeys the bulk equations of motion. Since these equations of motion are typically second-order differential equations (such as the Klein-Gordon equation), the asymptotic solution near the boundary generically has two independent solutions. Here, we introduce the radial parameter z, defined as $z = 1/r$, such that $z \to 0$ takes us to the boundary of AdS. Then, as $z \to 0$, we will have a solution of the form,

$$\phi(x,z) \sim \phi_0(x) z^{\Delta_-} + \phi_+ z^{\Delta_+} + ... \tag{4.16}$$

where we take $\Delta_+ \geq \Delta_-$ by definition. For any bulk field denoted by ϕ, we will be able to deduce by dimensional analysis that ϕ_0 can be identified as the source for the corresponding field theory operator, while ϕ_+ can be recognised as the vacuum expectation value for the operator.[2]. This prescription will need only minor modification when we consider insertions of probe branes and boundary defects below.

4.3 Probe D branes

We would like to learn how to extend the AdS/CFT correspondence to introduce more matter content into the field theory. Introducing more D branes of some dimension, p, *after* having taken the near-horizon limit is one method of achieving this.

Recall that open strings are able to end on D branes. Consider placing a set of N_f parallel Dp brane close to the stack of D3 branes. We can now imagine that states of open strings stretching between the D3 stack and the Dp branes, 3-p and p-3 strings, can be excited. We can also expect string states that begin and end on the new Dp branes, p-p strings. Each end of an open string transforms in the fundamental or anti-fundamental representation. From the perspective of the stack, then, and ultimately the field theory, the strings that have one end on the D3 stack might appear to be introducing fundamental matter to our theory.

This vague impression can be substantiated [91; 92]. If we stay within the probe limit, defined by ensuring $N_f/N \to 0$ as we take $N \to \infty$, then we do not have to consider the back-reaction of the new Dp branes on the geometry, nor consider the consequences of the RR fields they source. This is a very useful simplification. We can then describe the above proposal rigorously. We take the near horizon limit as before by replacing the stack with the background (4.8). Into this background, we insert the new Dp branes. Its dynamics will be described by the DBI and Wess-Zumino actions. Now, however, the induced metric is non-trivial, and because of the background RR field, the Wess-Zumino term is also generally non-trivial. Analogous to the stack of D3 branes, the N_f coincident D branes will introduce a $U(N_f)$ symmetry into the theory. This is then akin to introducing N_f flavours of fundamental representation matter, or quarks, to our theory. To more easily differentiate the number N_f of Dp branes describing flavour from the number N of D3 branes in the stack, we shall often denote

---

[2] We will not encounter bulk fields with negative mass and so do not need to discuss the Breitenlohner-Freedman bound

the latter by $N_c \equiv N$, where the subscript denotes that we can think of N_c as the number of colours in the gauge theory.

Solving for the dynamics of any new matter that we have introduced amounts to solving the equations of motion for for the Dp-brane in this background.For $p > 3$, p-p strings are found to decouple and become nondynamical in the Maldacena limit, which removes additional dynamics from the theory, leaving the fundamental matter introduced by the p-3 and 3-p strings. Since we are in Type IIB string theory, it is most straightforward to restrict to $p = 3$, 5, and 7.

The exact set of matter representations introduced to our boundary theory depends on the dimension p and the embedding that we select for the Dp branes, and can be deduced from the symmetries and representations of fluctuations. If we choose to align the Dp branes to extend along all the four dimensions spanned by the D3 brane, we can expect open strings to be able to be excited between the stack and the Dp branes at any point along the stack, and thus at any point in the boundary field theory. If, however, there is a direction along the stack that we do not also wrap with the Dp branes, the dimensions along which 3-p and p-3 strings can be excited will accordingly be reduced. Then, we can expect the boundary theory to have fundamental matter restricted to some region of lower dimension, depending on the exact embedding. Likewise, if we choose an embedding solution that increases the separation between the Dp and the D3 branes, we increase also the excitation energy for the 3-p and p-3 strings, corresponding to a greater mass for the corresponding matter in the boundary theory. Both these properties of the D brane embeddings can vary with respect to the radial coordinate of the bulk theory.

Solving for the profile of the D brane embedding at different radial distances in the bulk amounts to performing RG flow on the field theory. In particular, in Poincaré coordinates, we can consider the IR limit of the theory as taking place at the Poincaré horizon. If we expect the matter introduced by our theory to be massless in this IR limit, we can expect the D brane to reach all the way to the Poincaré horizon. Open strings of arbitrarily small length and energy can then be excited, implying that the field theory is gapless. Alternatively, if we expect this matter to be massive, the D brane should terminate at some finite radial distance from the Poincaré horizon. Open strings representing the fundamental matter then have a minimum excitation energy, and the corresponding matter in the field theory must be massive.

Similarly, the region of the field theory over which the the fundamental matter can be excited can change under RG flow. This corresponds to varying the embedding of the D branes along the dimensions over which the D3 stack extends. It could even be possible for the dimension of this region to change. Indeed, we present an example below of a $2 + 1$ dimensional defect in the UV, described by a D5 brane in the bulk, flowing to a $0 + 1$ dimensional object in the IR, as seen by the narrowing of the D5 brane along the non-radial AdS dimensions. Furthermore, the fact that this brane reaches the Poincaré horizon will demonstrate that the theory living on this defect is gapless.

4.4 Maldacena-Wilson loops

Since we are dealing with gauge theories, we would especially like to know how to compute the Wilson loops in the gravitational dual picture. As noted in Chapter 1, the fundamental Wilson loop can be thought of as the holonomy associated to a very massive quark taken along a designated path, $\mathcal{C}$. We can introduce a massive fundamental particle, which we regard as a quark, to an $\mathcal{N}=4$ SYM theory by Higgsing the theory. This will be shown to be the same as introducing fundamental matter via a D3 probe brane in the sense discussed in the previous section [39; 71; 67].

4.4.1 Fundamental Maldacena-Wilson loops

We start by considering $N+1$ coincident D3 branes in the stack, giving us $U(N+1)$ SYM as the worldvolume theory. We now place one of the D3 branes at some radial distance U (in string units) from the stack, and at some arbitrary point on the S^5. This 'breaks the gauge symmetry' $U(N+1) \to U(N) \times U(1)$. Open strings can now exist between the stack of N D3 branes and the isolated D3 brane, with an associated excitation mass of $m = U/2\pi$. This appears, therefore, to describe the Higgs mechanism in terms of D branes, with open strings behaving as W bosons that have gained a mass. These 'W bosons' transform in the fundamental representation of the gauge group and source the gauge field, and can thus take the role of quarks in our Wilson line. To render these quarks nondynamical, we can take $m \to \infty$, which will mean moving the isolated D3 brane to the boundary of AdS.

The open strings do not just source the gauge field, however, as they can also pull on the D3 brane stack in transversal directions. Transverse displacements are described by scalar fields. Therefore, there is also a coupling of the W bosons to these scalar fields. Writing out the full $U(N+1)$ Lagrangian shows that the stretched open strings couple to the operator,

$$W(\mathcal{C}) = \mathrm{Tr}\left[\mathcal{P}\exp\left(\oint_{\mathcal{C}} iA_\mu \dot{x}^\mu + \vec{n}\cdot\vec{\Phi}\sqrt{\dot{x}^2}\right)\right] \tag{4.17}$$

where $\vec{n}$ is a unit vector on the S^5, $\vec{\Phi}$ encodes the six scalar fields in the field theory, $\mathcal{C}$ is our choice of path over which we take the values of the integral x, and the derivative is respect to the path parameter. This is known as the Maldacena-Wilson loop.

When we take the near horizon limit, we again replace the stack of D3 branes by the background (4.8). The Maldacena-Wilson loop is then described in the bulk by open strings ending at the boundary along $\mathcal{C}$ and obeying the Nambu-Goto action in the bulk under this $AdS_5 \times S^5$ background.

Applying (4.15) to this situation implies that we can deduce the vacuum expectation value of the Maldacena-Wilson loop by evaluating the partition function, or action, of the corresponding bulk description. In the supergravity regime, with large 't Hooft coupling $g_s N$, the leading contribution to the action is made by the area of the worldsheet of the open strings as measured according to the AdS metric. In our limits, $g_s \to 0$ and $\alpha' \to 0$, we neglect nontrivial worldsheet topologies and fluctuations away from saddle point approximations. The dominant contribution to the action is therefore the worldsheet that solves the classical equations of motion in the bulk, or equivalently the worldsheet with minimal area, and that ends on $\mathcal{C}$ at the boundary.

To calculate the Wilson loop expectation value, we would therefore calculate something like,

$$\langle W(\mathcal{C})\rangle \sim e^{-S_{\text{cl}}[\partial\Sigma=\mathcal{C}]} \tag{4.18}$$

where S_{cl} is the classical action, proportional to the minimal area, of the string worldsheet Σ with boundary $\mathcal{C}$ on the boundary of AdS. However, since the area of a worldsheet that reaches to the boundary of AdS diverges, this expression is also divergent. This can generally be resolved by taking the Legendre transform of the action, following arguments that we should properly be giving the open string end Neumann, rather than Dirichlet, boundary conditions [93]. However, it is often sufficient to regularise and subtract the action given by a different embedding ending on the same $\mathcal{C}$.

We can easily extend this discussion to describe not just Wilson loops, but also 't Hooft loops and Wilson-'t Hooft loops. Whereas a Wilson loop describes the path of an electrically-charged quark sourcing gauge fields, a 't Hooft loop can be thought of as describing the path of magnetically charged monopole. A Wilson-'t Hooft loop describes the path of a dyonic particle, carrying both electric and magnetic charge. We can describe Wilson-'t Hooft loops by replacing fundamental strings in the above discussion with (p,q)-strings, which is a bound state of p fundamental strings and q D1 branes.

In this chapter, we will focus on straight, infinitely long Maldacena-Wilson lines. These are gauge invariant when we include the point at infinity. In the bulk, these describe a single string with one endpoint on the AdS_5 boundary, hanging straight down into the bulk. More precisely, the string is extended along an AdS_2 subspace of AdS_5, thus breaking $SO(4,2) \to SO(1,2) \times SO(3)$, where $SO(1,2)$ comes from conformal transformations that preserve the straight line and $SO(3)$ comes from rotations around the straight line. The string sits at a point on the S^5, thus breaking $SO(6)_R \to SO(5)_R$. These straight strings also have the property of being maximally superconformal, retaining half of the Poincaré supersymmetries and half of the superconformal supersymmetries, making them 1/2-BPS. In the next subsection, we will describe Wilson lines valued in higher representations of the gauge group that share all these same symmetries.

4.4.2 Symmetric-representation Maldacena-Wilson loops and D3 branes

The above discussion concerned Wilson and Wilson-'t Hooft loops in the fundamental representation. It is possible to obtain dual descriptions of Wilson loops in higher representations. One might imagine that higher representations can be formed by layering multiple fundamental strings on top of each other, or winding the string multiple times along the same path to obtain multiply-wound Wilson loops. However, it is difficult to know how to calculate such an object: the Nambu-Goto action applies only to a single string, and computing interactions become infeasible when the worldsheets lie coincident. However, it is known that multiple fundamental strings can polarise, or 'blow up', into a D brane with fundamental strings dissolved in it via the Myers effect [94]. It might therefore be proposed that D branes, such as D3 branes, with the correct embedding might describe higher representations of Wilson loops, and indeed this has been verified explicitly in [76; 95; 72].

In this section we review the D3-brane solutions that are holographically dual to symmetric-representation, maximally-superconformal Wilson lines and which will emerge in the IR of our defect RG flows. There are similar solutions for D5-branes describing anti-symmetric representations, but these will not appear in our defect RG flows and so we will not review them here. We will work in a gauge in which the $AdS_5 \times S^5$ solution of type IIB supergravity is

$$\begin{aligned} \mathrm{d}s^2 &= \frac{L^2}{z^2}\left(-\mathrm{d}t^2 + \mathrm{d}r^2 + r^2 \mathrm{d}s^2_{S^2} + \mathrm{d}z^2\right) + L^2\left(\mathrm{d}\theta^2 + \sin^2\theta\, \mathrm{d}s^2_{S^4}\right), \\ C_4 &= \frac{L^4}{z^4} r^2 \mathrm{d}t \wedge \mathrm{d}r \wedge \omega(S^2) + L^4 f(\theta)\,\omega(S^4), \\ f(\theta) &= \frac{3}{2}\theta - \sin(2\theta) + \frac{1}{8}\sin(4\theta), \end{aligned} \tag{4.19}$$

where $\omega(S^2) = \sin\phi_1\, \mathrm{d}\phi_1 \wedge \mathrm{d}\phi_2$ is the volume form on the field theory S^2, $\omega(S^4)$ is the volume form on the internal S^4 appearing in the metric, and $\theta \in [0, \pi]$. Notice that we have chosen a gauge in which the component of C_4 with legs on the S^5 vanishes at the north pole $\theta = 0$. This is appropriate for configurations wrapping an S^4 that can collapse at the north pole. For configurations that wrap an S^4 that can collapse at the south pole $\theta = \pi$, the components of the C_4 on the S^5 would be

$$f(\theta) \to \tilde{f}(\theta) = \frac{3}{2}(\theta - \pi) - \sin(2\theta) + \frac{1}{8}\sin(4\theta). \tag{4.20}$$

Each gauge choice is smooth over different patches of the S^5 surrounding the north and south poles respectively. At the intersection they are equivalent up to a gauge transformation

$$C_4 \to C_4 - \frac{3\pi}{2}\omega(S^4). \tag{4.21}$$

A Wilson-'t Hooft line in a totally symmetric representation of $SU(N_c)$ is dual to a probe D3-brane solution that wraps an S^2 inside AdS_5, is point-like on the S^5, and carries both fundamental string and D1-brane charges [72; 75; 76]. Here we review the construction of these solutions.

The relevant terms in the D3-brane action are

$$S_{\mathrm{D3}} = -T_{\mathrm{D3}} \int \mathrm{d}^4\xi \sqrt{-\det(g + 2\pi\alpha' F)} + T_{\mathrm{D3}} \int P[C_4], \tag{4.22}$$

where $T_{\mathrm{D3}} = (2\pi)^{-3}\alpha'^{-2}g_s^{-1}$ is the D3-brane tension with g_s the string coupling, ξ are the coordinates on the brane, F is the field strength for a $U(N_f)$ world-volume gauge field A, STr is a symmetrised trace over gauge indices, and g and $P[C_4]$ are the pullbacks of the bulk metric and C_4, respectively. We parameterise the D3-brane by $\xi = (t, z, \phi^i)$, where ϕ^i are the coordinates on S^2 appearing in equation (4.19), and make the ansatz that the D3-brane sits at a constant location on the S^5, has $r = r(z)$, and has world-volume field strength

$$F = \frac{L^2}{2\pi\alpha'}\mathcal{E}(z)\,\mathrm{d}t \wedge \mathrm{d}z + \frac{L^2}{2\pi\alpha'}\mathcal{B}\,\omega(S^2), \tag{4.23}$$

where $\omega(S^2) = \sin\phi_1\,\mathrm{d}\phi_1 \wedge \mathrm{d}\phi_2$ is the volume form on the S^2, $\mathcal{E}(z)$ is proportional to a radial electric field sources by the dissolved fundamental string charge, and $\mathcal{B}$ is proportional to a constant radial magnetic field sourced by the dissolved D1-brane charge.

Substituting the ansatz into the D3-brane action and integrating over the angles on the S^2 we obtain

$$S_{\mathrm{D3}} = -\mathcal{N}_3 \int \mathrm{d}z\,\frac{1}{z^4}\left[\sqrt{(1 + r'^2 - z^4\mathcal{E}^2)\,(r^4 + z^4\mathcal{B}^2)} - r^2 r'\right]. \tag{4.24}$$

where $\mathcal{N}_3 = \frac{2}{\pi}N_c \int \mathrm{d}t$. The equations of motion for A_{ϕ_i} are solved automatically by the ansatz, while if we write the D3-brane action (4.24) as $S_{\mathrm{D3}} = \mathcal{N}_3 \int \mathrm{d}r\,\mathcal{L}$, then the equation of motion for A_t implies that $\partial\mathcal{L}/\partial\mathcal{E} = Q$ for some integration constant Q.

Solving for the electric field, we obtain

$$\mathcal{E} = \frac{Q\sqrt{1+r'^2}}{\sqrt{r^4 + z^4(Q^2+\mathcal{B}^2)}}. \tag{4.25}$$

Here, Q determines the number k of dissolved fundamental strings, while the magnetic field $\mathcal{B}$ is proportional to the number n_1 of dissolved D1-branes,

$$k = \int_{S^2} \frac{\delta S_{\mathrm{D3}}}{\delta E} = \frac{4N_c}{\sqrt{\lambda}} Q, \qquad n_1 = \frac{1}{2\pi}\int_{S^2} F = \frac{\sqrt{\lambda}}{\pi}\mathcal{B}, \tag{4.26}$$

where $E = \sqrt{\lambda}\,\mathcal{E}/2\pi$ is the canonical world volume electric field.

We now Legendre transform the action (4.24) to eliminate $\mathcal{E}$ in favour of Q, yielding an action for $r(z)$ only

$$\tilde{S}_{\mathrm{D3}} \equiv S_{\mathrm{D3}} - \mathcal{N}_3 \int \mathrm{d}z\, Q\mathcal{E} = -\mathcal{N}_3 \int \mathrm{d}z\, \frac{1}{z^4}\left[\sqrt{(1+r'^2)\left[r^4 + z^4(Q^2+\mathcal{B}^2)\right]} - r^2 r'\right]. \tag{4.27}$$

The equation of motion for $r(z)$ following from $\tilde{S}_{\mathrm{D3}}$ admits the solution

$$r = \kappa z, \qquad \kappa = \sqrt{Q^2+\mathcal{B}^2} = \sqrt{\frac{\lambda^2}{16N_c^2}k^2 + \frac{\pi^2}{\lambda}n_1^2}, \tag{4.28}$$

where in the final equality we have used equation (4.26) to rewrite the proportionality coefficient κ in terms of the dissolved string and D1-brane charges. This is the solution that describes the Wilson-'t Hooft line in a totally symmetric representation of $SU(N_c)$. The resulting induced brane metric is $AdS_2 \times S^2$, with AdS radius of curvature $L\sqrt{\kappa^2+1}$.

4.5 Defect D5-branes

We will conduct our investigation of spherical defects by employing D5-branes. The D3-D5 model, in which the probe D5-branes are dual to a flat, planar $(2+1)$-dimensional defect carrying an $\mathcal{N}=2$ hypermultiplet was one of the first holographic defect models constructed [96; 87].

In the 10-dimensional flat space limit, a stack of the N_c D3-branes and N_f D5-branes are arranged as shown in Table 4.1. The D3-D5 intersection is $ND = 4$, and as a result, the system preserves $\mathcal{N}=2$ SUSY. Turning on a mass for the multiplet corresponds to separating the branes in the 7-9 directions.

In the decoupling limit, the D3-brane spacetime is $AdS_5 \times S^5$, as in (4.19). The probe D5-branes spans a flat (2+1)-dimensional plane in the boundary space, the radial direction, and an $S^2 \subset S^5$.

	0	1	2	3	4	5	6	7	8	9
N_c D3	x	x	x	x						
N_f D5	x	x	x		x	x	x			

TABLE 4.1: The embedding of the D3 and defect flavor D5-branes in the flat space limit.

Here we are interested in spherical, rather than planar, defects. We parameterise $AdS_5 \times S^5$ (4.19) using spherical coordinates in the AdS and write the S^5 in terms of two S^2s:

$$\begin{aligned}
\mathrm{d}s^2 &= \frac{L^2}{z^2}\left(-\mathrm{d}t^2 + \mathrm{d}r^2 + r^2 \mathrm{d}s^2_{S^2} + \mathrm{d}z^2\right) + L^2\left(\mathrm{d}\vartheta^2 + \sin^2\vartheta\, \mathrm{d}s^2_{\hat{S}^2} + \cos^2\vartheta\, \mathrm{d}s^2_{S^2_\perp}\right), \\
C_4 &= \frac{L^4}{z^4} r^2 \mathrm{d}t \wedge \mathrm{d}r \wedge \omega(S^2) + L^4 g(\vartheta)\, \omega(\hat{S}^2) \wedge \omega(S^2_\perp),
\end{aligned}$$

The function $g(\vartheta)$ is determined by the condition $\mathrm{d}C_4 = *\mathrm{d}C_4$. We will not need the explicit function in what follows. We have distinguished the two internal S^2s by a hat and a perpendicular symbol. The D5-brane wraps the hatted two-sphere, $\hat{S}^2$, and is a point on the transverse two-sphere $S^2_\perp$. The relevant terms in the D5-brane action are

$$S_{\mathrm{D5}} = -T_{\mathrm{D5}} \int \mathrm{d}^6\xi\, \mathrm{STr}\sqrt{-\det(g + 2\pi\alpha' F)} + 2\pi\alpha' T_{\mathrm{D5}} \int \mathrm{Tr}\left(P[C_4] \wedge F\right), \tag{4.29}$$

where $T_{\mathrm{D5}} = (2\pi)^{-5}\alpha'^{-3} g_s^{-1}$ is the D5-brane tension, ξ are the coordinates on the D5-brane, F is the field strength for a $U(N_f)$ world-volume gauge field A, STr is a symmetrised trace over gauge indices, and g and $P[C_4]$ are the pullbacks of the bulk metric and C_4, respectively.

We parameterise the stack of D5-branes with six of the bulk spacetime coordinates $\xi \in (t, z, \phi^i, \phi^\alpha)$, where ϕ^i are the two angles on the S^2 inside AdS_5 and ϕ^α are the two angles on the $\hat{S}^2$ inside the S^5. The embedding of the stack of D5-branes is then specified by the two $N_f \times N_f$ matrices $r(\xi)$ and $\vartheta(\xi)$.

We will take as our ansatz that these embedding functions depend only on z and are proportional to the identity matrix,

$$r = r(z)\, \mathbb{1}_{N_f}, \qquad \vartheta = \vartheta(z)\, \mathbb{1}_{N_f}. \tag{4.30}$$

For the gauge field strength we make the ansatz

$$F = \frac{L^2}{2\pi\alpha'}\mathcal{E}(z)\, \mathbb{1}_{N_f}\, \mathrm{d}t \wedge \mathrm{d}z + \frac{L^2}{2\pi\alpha'}\mathcal{B}\, \mathbb{1}_{N_f}\, \omega(S^2) + \frac{L^2}{2\pi\alpha'} q\, \mathbb{1}_{N_f}\, \omega(\hat{S}^2). \tag{4.31}$$

This consists of three pieces: a radial electric field proportional to $\mathcal{E}(z)$ sourced by dissolved fundamental strings, a constant radial magnetic field proportional to $\mathcal{B}$ sourced by dissolved D3-branes, and an internal flux proportional to q also sourced by dissolved D3-branes. We denote the number of D3-branes sourcing the magnetic field by $\hat{n}_3$ and the number sourcing the internal flux by n_3. We have chosen the naming scheme so that $\hat{n}_3$ is the number of D3-branes wrapping the $\hat{S}^2$, while n_3 is the number wrapping the S^2. They are related to the flux (4.31) by

$$\hat{n}_3 = \frac{1}{2\pi}\int_{S^2} \mathrm{Tr} F = \frac{\sqrt{\lambda} N_f}{\pi}\mathcal{B}, \qquad n_3 = \frac{1}{2\pi}\int_{\hat{S}^2} \mathrm{Tr} F = \frac{\sqrt{\lambda} N_f}{\pi} q. \tag{4.32}$$

There are also D1-branes sourced by the Chern-Simons term $C_2 \wedge F \wedge F$. This term vanishes for our background and was omitted from (4.29). The number of D1-branes is given by

$$n_1 = \frac{1}{8\pi^2}\int_{S^2 \times \hat{S}^2} \mathrm{Tr}(F \wedge F) = \frac{\lambda N_f}{2\pi^2}\mathcal{B} q = \frac{n_3 \hat{n}_3}{2N_f}. \tag{4.33}$$

Evaluated on the ansatz in equations (4.30) and (4.31), the D5-brane action (4.29) becomes

$$S_{\mathrm{D5}} = -\mathcal{N}_5 \int \mathrm{d}z \left[\frac{1}{z^2}\sqrt{1 + r'^2 + z^2 \vartheta'^2 - z^4 \mathcal{E}^2}\sqrt{\frac{r^4}{z^4} + \mathcal{B}^2}\sqrt{\sin^4(\vartheta) + q^2} - \frac{r^2 r'}{z^4} q\right], \tag{4.34}$$

where $\mathcal{N}_5 = (4\pi)^2 L^6 N_f T_5 \int \mathrm{d}t$.

We write the D5-brane action (4.34) as $S_{\mathrm{D5}} = \mathcal{N}_5 \int \mathrm{d}z\, \mathcal{L}$ and introduce the integration constant Q defined by $\partial\mathcal{L}/\partial\mathcal{E} = Q$, which determines $\mathcal{E}$ as

$$\mathcal{E} = \frac{Q\sqrt{1 + r'^2 + z^2\vartheta'^2}}{z^2\sqrt{(\sin^4(\vartheta) + q^2)\left(\frac{r^4}{z^4} + \mathcal{B}^2\right) + Q^2}}. \tag{4.35}$$

The integration constant Q is proportional to the number k of dissolved fundamental strings, given by Gauss' law

$$k = \int_{S^2}\int_{\hat{S}^2} \frac{\delta S_{\mathrm{D5}}}{\delta E} = \frac{4 N_f N_c}{\pi} Q, \tag{4.36}$$

where $E = \sqrt{\lambda}\,\mathcal{E}/2\pi$ is the canonical world volume electric field. It is also common to make use of a parameter known as the filling fraction, which we simply define here as,

$$\nu = \frac{4Q}{\mathcal{B}\sqrt{\lambda}}. \tag{4.37}$$

We now perform a Legendre transform $\tilde{S}_{\mathrm{D5}} = S_{\mathrm{D5}} - \mathcal{N}_5 \int \mathrm{d}r\, Q\mathcal{E}$ to eliminate $\mathcal{E}$ from the action in favour of Q, yielding an action for just the scalar fields $r(z)$ and $\vartheta(z)$. The Legendre transformed action is

$$\tilde{S}_{\mathrm{D5}} = -\mathcal{N}_5 \int \frac{\mathrm{d}z}{z^2}\left(\sqrt{(\sin^4\vartheta + q^2)\left(\frac{r^4}{z^4} + \mathcal{B}^2\right) + Q^2}\sqrt{1 + r'^2 + z^2\vartheta'^2} - \frac{q r^2 r'}{z^2}\right). \tag{4.38}$$

Extremizing $\tilde{S}_{\text{D5}}$ with respect to r and ϑ leads to the equations of motion

$$\left(\frac{\Sigma}{z^2}r' - \frac{qr^2}{z^4}\right)' = \frac{2(\sin^4\vartheta + q^2)r^3}{z^6\Sigma} - \frac{2qrr'}{z^4}, \tag{4.39a}$$

$$(\Sigma\,\vartheta')' = \frac{2\sin^3\vartheta}{z^2\Sigma}\left(\frac{r^4}{z^4} + \mathcal{B}^2\right)\cos\vartheta, \tag{4.39b}$$

where we have defined

$$\Sigma(z) \equiv \sqrt{\frac{(\sin^4\vartheta + q^2)\left(\frac{r^4}{z^4} + \mathcal{B}^2\right) + Q^2}{1 + r'^2 + z^2\vartheta'^2}}. \tag{4.40}$$

The equations of motion following from (4.38) admit solutions near the conformal boundary at $z \to 0$ with asymptotic expansions,

$$\begin{aligned} r(z) =& R + qz - \frac{1+q^2}{3R}z^2 + \frac{q(2+2q^2+3M^2R^2)}{6R^2}z^3 \\ &- \frac{(5+22q^4+9q^2(3+2M^2R^2) - 54MqR^3C)}{54R^3}z^4 + \frac{2q(1+q^2)^2}{135R^4}z^5\log z \\ &+ \mathcal{D}z^5 + \dots \\ \vartheta(z) =& \frac{\pi}{2} - Mz - \mathcal{C}z^2 + \dots, \end{aligned} \tag{4.41}$$

with the integration constants $(R, \mathcal{D}, M, \mathcal{C})$. R is the spherical radius of the dual spherical defect. The constant $\mathcal{D}$ is related to the expectation value of the displacement operator. The integration constants M and $\mathcal{C}$ appearing in the near-boundary expansion of $\vartheta(z)$ are related to the source for and expectation value of an operator with the canonical dimensions of a fermion bilinear in the defect theory.

The deep IR admits a wide range of asymptotic expansions and we focus on solutions corresponding to point-like defects, such as the Wilson and Wilson-'t Hooft lines of section 4.4. We categorise the different types of solutions by their behaviour in the deep IR ($z \to \infty$), i.e. as the D5-branes approach the Poincaré horizon of AdS_5:

- Type 3: The D5-branes approach a profile similar to a D3-brane dual to a symmetric representation Wilson-'t Hooft line, discussed in section 4.4.2.
- Type 1: The D5-branes approach a profile similar to a (p, q) string dual to a dyonic Wilson line in the fundamental representation, discussed in section 4.4.1.
- Type $\hat{3}$: The D5-branes approach a profile of a D3-brane wrapping the internal two-sphere $\hat{S}^2$.

Solution type (IR D-brane)	AdS_5	S^5
$\tilde{\mathbf{3}}$ (D3-brane)	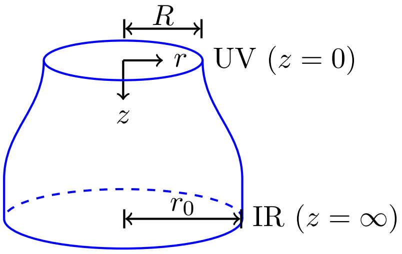	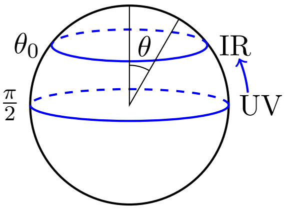
1 (D1-brane)	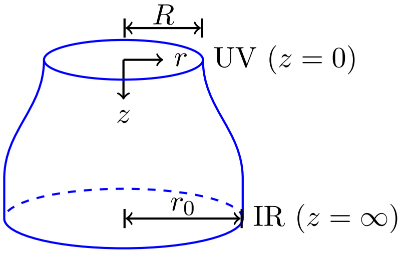	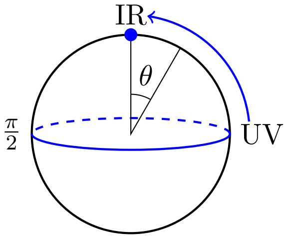
3 (D3-brane)	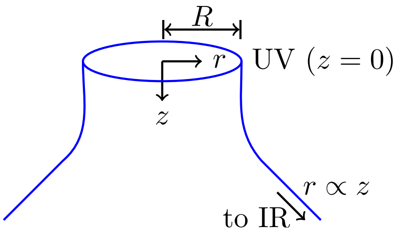	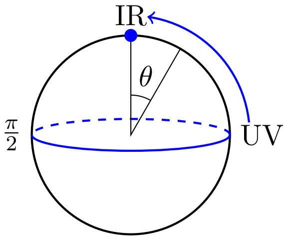

TABLE 4.2: Cartoons of the different classes of probe D5-brane embeddings discussed in this chapter. The D5-branes wrap an S^2 inside AdS_5, and an S^2 inside S^5, represented by the blue circles in the right-hand column. The cartoons show how these wrapped spheres evolve as we move from the UV region near the boundary of AdS_5 to the IR region near the Poincaré horizon.

4.5.1 Type 3: D5-branes flowing to symmetric representation Wilson lines

The D3-branes of section 4.4.2 corresponding to symmetric representations are characterized by a scaling relation of the form $r = \kappa z$, with the D3-brane a point on the internal S^5. We find solutions in the deep IR which asymptote to these D3-brane embeddings, with the asymptotic expansions in the variable $s = [\log(z/z_0)]^{-1/2} \ll 1$,

$$\begin{aligned} \frac{r}{z} &= \kappa + \frac{\kappa}{4}(\kappa^2+1)\left(1 - \sqrt{1 - \frac{q^2\kappa^4}{(\mathcal{B}^2+\kappa^4)^2}}\right) s^2 + O(s^4) \\ \vartheta &= \frac{q\kappa}{2\sqrt{\mathcal{B}^2+\kappa^4}} s + O(s^3), \end{aligned} \tag{4.42}$$

with higher terms involving powers of s and $\log s$ and we have introduced

$$\kappa = \sqrt{(Q/q)^2 + \mathcal{B}^2}. \tag{4.43}$$

Real solutions exist only for $\mathcal{B}^2 + \kappa^4 \geq q\kappa^2$. Up to a choice of the sign (and selection of the reference value z_0), all coefficients are fixed by the equations of motion.

Solutions corresponding to Wilson lines have no magnetic charge, $n_1 = 0$. This is achieved by setting $\mathcal{B} = 0$. The condition for real solutions simplifies to $Q^2 \geq q^3$.

Solutions corresponding to 't Hooft lines have no electric charge, $k = 0$. This is achieved by setting $Q = 0$. The condition for real solutions simplifies to $q^2 \leq (1 + B^2)^2$.

For such solutions, in the deep IR the induced metric on the world-volume of the D5-branes becomes approximately that of $AdS_2 \times S^2$, warped with an S^2 that shrinks to zero size as $z \to \infty$,

$$g_{ab}\,\mathrm{d}\xi^a \mathrm{d}\xi^b \approx \frac{L^2}{z^2}\left[-\mathrm{d}t^2 + \left(\kappa^2 + 1\right)\mathrm{d}z^2\right] + L^2\kappa^2 \mathrm{d}s^2_{S^2} + \frac{L^2\kappa^2 q^2}{4(\mathcal{B}^2 + \kappa^4)\log(z/z_0)}\mathrm{d}s^2_{S^2}, \tag{4.44}$$

where the radius of curvature of the AdS_2 is $L\sqrt{\kappa^2+1}$. To determine the one-dimensional scaling dimensions of the operators dual to r and θ we consider small fluctuations about the fixed point,

$$r(z) = \kappa z + \left[(Q/q)^2 + \mathcal{B}^2 + 1\right]^{1/2} z\,\delta r(z), \qquad \theta(z) = \delta\theta(z). \tag{4.45}$$

The Legendre transformed action (4.38) quadratic in the fluctuations is then[3]

$$\tilde{S}^{(2)}_{\text{D5}} = -\frac{1}{2}\kappa q \mathcal{N}_5 \int \mathrm{d}z\left[\delta r'^2 + \delta\theta'^2 + \mathcal{O}(z^{-3})\right]. \tag{4.46}$$

This is proportional to the canonically normalised action for two massless scalar fields in AdS_2, and so r and θ are dual to marginal operators on the symmetric representation Wilson-'t Hooft line.

A second class of solutions with collapsing S^2 in the IR, similar to (4.42), can be written as,

$$\begin{aligned} \frac{r}{z} &= \kappa + \frac{\kappa}{4}(\kappa^2+1)\left(1 + \sqrt{1 - \frac{q^2\kappa^4}{(\mathcal{B}^2+\kappa^4)^2}}\right)s^2 + r_{\text{IR}}s^\gamma + O(s^3) \\ \vartheta &= \frac{q\kappa}{2\sqrt{\mathcal{B}^2+\kappa^4}}s + r_\theta s^{\gamma+1} + O(s^3), \end{aligned} \tag{4.47}$$

where r_{IR} is a free parameter, r_θ is determined by r_{IR} and the equations of motion, and

$$\gamma = 2 + 2\sqrt{1 - \frac{\kappa^4 q^2}{\left(\mathcal{B}^2+\kappa^4\right)^2}} \tag{4.48}$$

---

[3] We have dropped a boundary term $-z^{-1}\delta r^2$ from the action.

Again, real solutions exist only for $\mathcal{B}^2 + \kappa^4 \geq q\kappa^2$. This covers a broad set of solutions due to the free parameter, r_{IR}.

4.5.2 Type 1: D5-branes flowing to (p, q)-strings

The equations of motion (4.39) also admit solutions for which both the internal $\hat{S}^2$ inside the S^5 and the S^2 wrapped by the brane in AdS_5 collapse at the Poincaré horizon, thus asymptoting to a (p, q) string. The IR expansion for this set of solutions is,

$$\begin{aligned} r &= r_0 + \frac{r_0^2}{z_0} e^{-1/s^2} \left(\frac{q}{\sqrt{\mathcal{B}^2 q^2 + Q^2}} + s^4 \frac{q\sqrt{\mathcal{B}^2 q^2 + Q^2}}{32\mathcal{B}^2} \right) \\ &+ \frac{r_0^3}{z_0^2} e^{-2/s^2} \left(\frac{q^2}{\mathcal{B}^2 q^2 + Q^2} - s^4 \frac{4\mathcal{B}^2 q^2 - Q^2}{80\mathcal{B}^4} \right) + O(s^5) + O(e^{-3/s^2}) \\ \vartheta &= \frac{\sqrt{\mathcal{B}^2 q^2 + Q^2} s}{2\mathcal{B}} + s^3 c_3 + s^3 \log(s) \frac{\sqrt{\mathcal{B}^2 q^2 + Q^2}(\mathcal{B}^2(6 + q^2) + Q^2)}{8\mathcal{B}^3} \\ &+ e^{-4/s^2} \left(s^3 \frac{r_0^4}{z_0^4} \frac{\sqrt{\mathcal{B}^2 q^2 + Q^2}}{80\mathcal{B}^3} \right) + O(s^5) + O(e^{-5/s^2}) \end{aligned} \tag{4.49}$$

where r_0 is a free positive parameter. Although c_3 is undetermined by the local equations of motion, we find that its effect is merely to vary the scale z_0, and it can therefore be set to any value without influencing the physics.

This corresponds to type **1** solutions, as depicted in Table 4.2, which are dual to Wilson-'t Hooft lines in the fundamental representation. Solutions corresponding to Wilson lines, which have no magnetic charge, are obtained by setting $\mathcal{B} = 0$, while 't Hooft lines, which have no electric charge, can be achieved by setting $Q = 0$.

4.5.3 Type $\hat{\mathbf{3}}$: D5-branes flowing to D3-branes wrapping $\hat{S}^2$

For $\mathcal{B} \neq 0$ with the ansatz $r = r_0 + O(1/z)$, $\vartheta = \vartheta_0 + O(1/z)$, we require $\vartheta_0 = 0, \pm\pi/2$. The solution with constant $\vartheta = \pi/2$ gives,

$$r = r_0 - \frac{1}{z} \frac{q r_0^2}{\sqrt{\mathcal{B}^2(1 + q^2) + Q^2}} + \frac{1}{z^2} \frac{(1 + 5q^2) r_0^3}{5(\mathcal{B}^2(1 + q^2) + Q^2)} + O(1/z^3) \tag{4.50}$$

where r_0 is a constant of integration.

This solution describes a D5 brane for which the S^2 wrapped by the brane in AdS_5 is collapsing near the Poincaré horizon. The wrapping of the internal $\hat{S}^2$ remains constant and on the equator of S^5 at all radial values. The D5 brane is thus asymptoting to a D3 brane wrapping an internal $\hat{S}^2$. This is an example of a Type $\hat{\mathbf{3}}$

solution, as depicted in Table 4.2. Since ϑ is constant, the value MR, which is multiplied by $\vartheta'(z)$, always vanishes for such solutions.

4.5.4 Constructing explicit flows

We construct explicit numerical solutions for D5-brane embeddings of the different types discussed in the previous subsections by continuing the large-z expansions (4.42), (4.47), (4.49), or (4.50) to higher order in $1/z$. We then use these expansions to set boundary conditions for the equations of motion (4.39) which we then integrate to small z. We can then perform a fit to the small-z asymptotics (4.41) to determine the UV coefficients $(R, \mathcal{D}, M, \mathcal{C})$ for a given solution.

In figure 4.1 we show some example solutions for fixed values of the charges $q = 1$, $\mathcal{B} = 1$ (corresponding to a flux $\Phi = 2\sqrt{\lambda}$), and vanishing filling fraction $\nu = Q = 0$. The dotted blue, purple, and green curves show solutions of type **3**, as described in section 4.5.1, for which the D5-brane flows to a D3-brane that becomes a point on the internal S^5 in the IR. The green curve corresponds to the special solution (4.42), while the other colours correspond to different values of r_{IR} in the large-z expansion (4.47). The dashed red, orange, and yellow curves show solutions of type **1**, as described in section 4.5.2, for which the D5-brane flows to a (p, q)-string in the IR. The different colours correspond to different values of the parameter r_0 appearing in the large-z expansion (4.49). The solid black line shows a solution of type $\bar{\mathbf{3}}$, described in section 4.5.3, for which the D5-brane flows to a D3-brane wrapping the internal $\hat{S}^2$ in the IR. The UV of each solution generally corresponds to a different value of the dimensionless combination MR.

In figure 4.2 we show the range of values of MR spanned by the different types of solutions described here, for $\mathcal{B} = 1$, corresponding to a magnetic flux $\Phi = 2\sqrt{\lambda}$, and two different values of the internal charge, $q = 1$ and $q = 5/2$. We can always choose orientation of the $\hat{S}^2$ within the S^5 such that the value of MR is nonnegative.

For sufficiently small q we find that there is a solution of one of the types we describe for any given value of MR and any filling fraction ν. The solutions of types **1** and **3** each span a range of MR since their IR expansions (4.49) and (4.47) both contain a free parameter, r_{IR} and r_0, respectively.

For sufficiently large q we find that there is a region of the (MR, ν) plane not covered by any of the solutions we have found. This region appears when the filling fractions are such that the IR expansions for the type **3** solutions contain complex terms. Concretely, the IR expansions in equations (4.42) and (4.47) contain terms proportional to

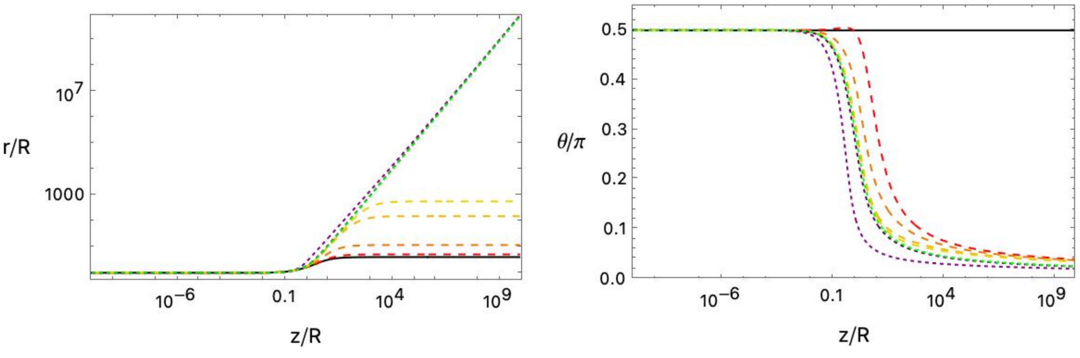

(A) r embeddings (B) θ embeddings

FIGURE 4.1: Example D5 embeddings for magnetic flux $\Phi = 2\sqrt{\lambda}$, $q = 1$, and vanishing filling fraction, $\nu = 0$. Each curve corresponds to a different value of the dimensionless combination MR. The solid black curve shows a solution of type $\bar{\mathbf{3}}$, which flows to a D3-brane wrapping the internal S^2 in the IR. The dashed curves show a solution of type **1**, which flow to (p, q) strings dual to fundamental representation Wilson-'t Hooft loops in the IR. The dotted lines show solutions of type **3**, which flow to D3 brane dual to symmetric representation Wilson-'t Hooft line. Amongst these, the green dotted line corresponds to the special solution (4.42).

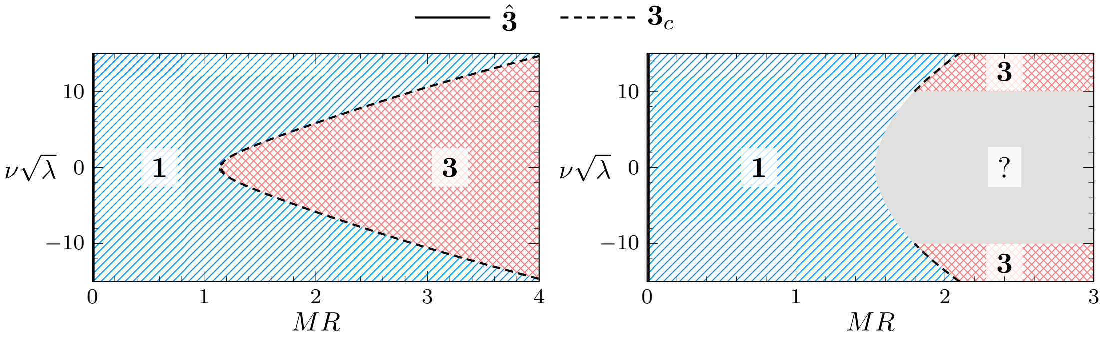

FIGURE 4.2: Partial phase diagrams for the D5-brane flows for fixed value of the flux, $\Phi = 2\sqrt{\lambda}$ (corresponding to $\mathcal{B} = 1$), and internal charges $q = 1$ (left) and $q = 5/2$ (right). Cartoons of the different embeddings corresponding to these phases are shown in table 4.2. The grey region in the figure on the right covers a region for which we have not found solutions.

$$\sqrt{1 - \frac{q^2\kappa^4}{(\mathcal{B}^2 + \kappa^4)^2}}. \tag{4.51}$$

When q is sufficiently large and Q sufficiently small, i.e. when

$$q^2 > \frac{(\mathcal{B}^2 + \kappa^4)^2}{\kappa^4} \tag{4.52}$$

the argument of this square root becomes negative, causing the type **3** solutions to become complex and therefore unphysical. For $\mathcal{B} = 1$, $q = \frac{5}{2}$, this corresponds to $|Q| < \frac{5}{2}$, or equivalently to $|\nu| < \frac{10}{\sqrt{\lambda}}$. This region is shown in grey in the right panel of Fig. 4.2.

4.6 Conclusion and discussion

We began with strongly-coupled $SU(N_c)$ $\mathcal{N} = 4$ supersymmetric Yang-Mills (SYM) theory at large N_c on $(3+1)$-dimensional Minkowski space, $\mathbb{R}^{1,3}$. We introduced a number $N_f \ll N_c$ of $(2+1)$-dimensional hypermultiplets containing Dirac fermions and their scalar superpartners in the fundamental representation of $SU(N_c)$ on $\mathbb{R} \times S^2$, and subjected these to non-zero charge density Q and magnetic field B. Using holographic techniques, we then deduced the IR effective theory, finding $(0+1)$-dimensional gapless defect fields that, when integrated out, give rise to superconformal Wilson or Wilson-'t Hooft lines of $\mathcal{N} = 4$ SYM in the fundamental or totally symmetric representations of $SU(N_c)$.

Our results demonstrate the interesting phenomenon of a defect changing dimensions under RG flow, along with the holographic description of this process. Our calculations suggest that, generically in gauge theories, conformal line operators may appear in the IR when defect matter on a sphere supports spherically-symmetric zero-energy states. Moreover, we can hope to apply our findings to spherical graphene and fullerenes, giving evidence that gapless Dirac fermions exist at nonzero-magnetic fields and charge density even when strongly coupled to gauge fields in the surrounding four dimensional theory.

The spherical defects considered here provide a new UV completion of Wilson loops, introducing an entirely new description of Wilson loops as IR limits of these defects. This suggests that these defects themselves might serve as useful probes or order parameters for phases of gauge theories. Surface defects in the field theory and their corresponding expressions in the bulk have recently been proposed as proper substitutes for the Polyakov loop as an order parameter for the deconfinement transition in supersymmetry-preserving theories [97]. It is possible that the spherical defects we have introduced here could be used in AdS/CFT as probes to investigate the holographic manifestations of partial confinement.

It would be interesting to examine these D5 brane embeddings at finite temperature, building a more complete phase diagram. An open problem remains as to the missing D5-brane embedding solutions in some region of the boundary parameters, leaving lacunae in the zero-temperature phase diagrams, as in Fig. 4.2.

Similar computations for the case of a spherical defect described by D7 branes have been performed and are awaiting publication alongside the results for the D5 brane set forth in this chapter.

Chapter 5

Concluding remarks

In this thesis, we have used a variety of techniques to investigate the physics of strongly coupled Yang-Mills theories. Here, we summarise our findings and suggest some outlook for the future.

In Chapter 2, we argued that the colour space of a partially confined phase can separated into a confining sector and a deconfining sector, and that linear confinement is exhibited within the confining sector. This needs further investigation to confirm that this is a general property of the partially confined phase and not simply an artefact of the strong coupling limit of our lattice. We would also like to extend our results to finite N. However, our results raise the prospect of very interesting, measurable dynamical behaviour in QCD, perhaps suggesting a new kind of bound state in the spectrum. Moreover, our findings stimulate more interest in the holographic description of the partially confined phase, particularly concerning the holographic calculation of the Wilson loop in the partially confined phase.

In Chapter 3, we argued that spontaneous breaking of global symmetries may provide a definition of the partial/complete deconfinement transition. As a result, the partially confined phase can be distinguished from the confined and deconfined phases by an order parameter. This characterisation can also be applied at finite N, offering the first known examples of the partially confined phase outside of the large N limit. An especially important question remaining is whether global symmetries can be used to identify partial phases in theories closer to QCD, including $N = 3$, $\theta = 0$, and physical quark masses. The observable effects of global symmetry breaking could be very important for understanding physical consequences of the partial phase in QCD. Global symmetry breaking might also be employed to identify the partially confined phase in the dual gravity description.

Clearly, the partially confined phase deserves further study and needs to be understood in greater detail, with the ultimate goal being a comprehensive understanding of any exhibition of the partially confined phase in QCD.

Finally, in Chapter 4, we used holographic duality to show that gauge fields in flat space coupled to certain matter fields on a spherical defect admit defect-localized renormalisation group flows to superconformal line operators in the infra-red, arguing that this might be a generic feature of some classes of spherical defects in gauge theories. We consequently found a new UV completion of Wilson-'t Hooft loops. It is natural to seek other defects that flow to Wilson-'t Hooft lines in the IR, and to explore whether a complete classification of all such objects can be established. Moreover, it is easy to multiply intriguing suggestions for new defects to examine. For example, the renormalization group flows of a defect shaped like a circle, $S^1 \times \mathbb{R}$, or a torus, $S^1 \times S^1 \times \mathbb{R}$, merit investigation. We can also consider much more complicated shapes in a higher-dimensional field theory using a setting such as $AdS_7 \times S^4$.

It would be valuable to strengthen the connection between our results and real-world spherical graphene and fullerenes to allow us to form predictions that could be measured experimentally. It would also be intriguing to explore whether we can use these new defects as probes in other settings, perhaps using them to investigate partial confinement and its holographic dual.

Analysis of strongly coupled gauge theories continues to be highly fruitful and surprising, even after decades of research. Not only is the solution to known conundrums, such as colour confinement and the constitution of neutron stars, known to be hidden behind mastery of strongly coupled gauge theories, but our findings here suggest that there is much remaining to be discovered that might not have been anticipated. We can expect further study of strongly-coupled gauge theories to continue to yield interesting results and surprises.

References

[1] M. D. Schwartz, *Quantum Field Theory and the Standard Model*. Cambridge University Press, 3, 2014.

[2] G. 't Hooft, *The Conceptual Basis of Quantum Field Theory*, pp. 661–729. 2007.

[3] V. P. Nair, *Quantum field theory: A modern perspective*. Springer New York, NY, 2005.

[4] J. Greensite, *An introduction to the confinement problem*, vol. 821. 2011.

[5] M. Shifman, *Advanced Topics in Quantum Field Theory*. Cambridge University Press, 4, 2022.

[6] J. B. Kogut and M. A. Stephanov, *The phases of quantum chromodynamics: From confinement to extreme environments*, vol. 21. Cambridge University Press, 12, 2004.

[7] A. M. Polyakov, *Gauge Fields and Strings*, vol. 3. 1987.

[8] N. Seiberg and E. Witten, "Electric - magnetic duality, monopole condensation, and confinement in N=2 supersymmetric Yang-Mills theory," *Nucl. Phys. B* **426** (1994) 19–52, `arXiv:hep-th/9407087`. [Erratum: Nucl.Phys.B 430, 485–486 (1994)].

[9] A. M. Polyakov, "Quark confinement and topology of gauge theories," *Nuclear Physics B* **120** no. 3, (1977) 429–458.

[10] S. Weinberg, *Cosmology*. OUP Oxford, 2008.

[11] E. Witten, "Anti-de Sitter space, thermal phase transition, and confinement in gauge theories," *Adv. Theor. Math. Phys.* **2** (1998) 505–532, `arXiv:hep-th/9803131`.

[12] B. Sundborg, "The Hagedorn transition, deconfinement and N=4 SYM theory," *Nucl. Phys. B* **573** (2000) 349–363, `arXiv:hep-th/9908001`.

[13] O. Aharony, J. Marsano, S. Minwalla, K. Papadodimas, and M. Van Raamsdonk, "The Hagedorn - deconfinement phase transition in weakly coupled large N gauge theories," *Adv. Theor. Math. Phys.* **8** (2004) 603–696, `arXiv:hep-th/0310285`.

[14] M. Hanada and J. Maltz, "A proposal of the gauge theory description of the small Schwarzschild black hole in $AdS_5 \times S^5$," *JHEP* **02** (2017) 012, `arXiv:1608.03276 [hep-th]`.

[15] D. Berenstein, "Submatrix deconfinement and small black holes in AdS," *JHEP* **09** (2018) 054, `arXiv:1806.05729 [hep-th]`.

[16] M. Hanada, G. Ishiki, and H. Watanabe, "Partial Deconfinement," *JHEP* **03** (2019) 145, `arXiv:1812.05494 [hep-th]`. [Erratum: JHEP 10, 029 (2019)].

[17] M. Hanada, A. Jevicki, C. Peng, and N. Wintergerst, "Anatomy of Deconfinement," *JHEP* **12** (2019) 167, `arXiv:1909.09118 [hep-th]`.

[18] M. Hanada and B. Robinson, "Partial-Symmetry-Breaking Phase Transitions," *Phys. Rev. D* **102** no. 9, (2020) 096013, `arXiv:1911.06223 [hep-th]`.

[19] M. Hanada, G. Ishiki, and H. Watanabe, "Partial deconfinement in gauge theories," *PoS* **LATTICE2019** (2019) 055, `arXiv:1911.11465 [hep-lat]`.

[20] M. Hanada, H. Shimada, and N. Wintergerst, "Color confinement and Bose-Einstein condensation," *JHEP* **08** (2021) 039, `arXiv:2001.10459 [hep-th]`.

[21] H. Watanabe, G. Bergner, N. Bodendorfer, S. Shiba Funai, M. Hanada, E. Rinaldi, A. Schaefer, and P. Vranas, "Partial Deconfinement at Strong Coupling on the Lattice," `arXiv:2005.04103 [hep-th]`.

[22] D. J. Gross and E. Witten, "Possible Third Order Phase Transition in the Large N Lattice Gauge Theory," *Phys. Rev. D* **21** (1980) 446–453.

[23] S. R. Wadia, "A Study of U(N) Lattice Gauge Theory in 2-dimensions," `arXiv:1212.2906 [hep-th]`.

[24] M. Hanada, "Bulk geometry in gauge/gravity duality and color degrees of freedom," *Phys. Rev. D* **103** no. 10, (2021) 106007, `arXiv:2102.08982 [hep-th]`.

[25] J. B. Kogut and L. Susskind, "Hamiltonian Formulation of Wilson's Lattice Gauge Theories," *Phys. Rev. D* **11** (1975) 395–408.

[26] A. M. Polyakov, "Thermal Properties of Gauge Fields and Quark Liberation," *Phys. Lett. B* **72** (1978) 477–480.

[27] L. Susskind, "Lattice Models of Quark Confinement at High Temperature," *Phys. Rev. D* **20** (1979) 2610–2618.

[28] M. Hanada, "Large-N limit as a second quantization," `arXiv:2103.15873 [hep-th]`.

[29] V. Gautam, M. Hanada, A. Jevicki, and C. Peng, "Matrix Entanglement," `arXiv:2204.06472 [hep-th]`.

[30] K. Langfeld, B. Lucini, and A. Rago, "The density of states in gauge theories," *Phys. Rev. Lett.* **109** (2012) 111601, `arXiv:1204.3243 [hep-lat]`.

[31] G. Aarts *et al.*, "Phase Transitions in Particle Physics – Results and Perspectives from Lattice Quantum Chromo-Dynamics," in *Progress in Particle and Nuclear Physics*. 1, 2023. `arXiv:2301.04382 [hep-lat]`.

[32] M. Hanada, J. Maltz, and L. Susskind, "Deconfinement transition as black hole formation by the condensation of QCD strings," *Phys. Rev. D* **90** no. 10, (2014) 105019, `arXiv:1405.1732 [hep-th]`.

[33] T. Eguchi and H. Kawai, "Reduction of Dynamical Degrees of Freedom in the Large N Gauge Theory," *Phys. Rev. Lett.* **48** (1982) 1063.

[34] D. Mason, B. Lucini, M. Piai, E. Rinaldi, and D. Vadacchino, "The density of state method for first-order phase transitions in Yang-Mills theories," *PoS* **LATTICE2022** (2023) 216, `arXiv:2212.01074 [hep-lat]`.

[35] J. Skilling, "Nested sampling," in *Aip conference proceedings*, vol. 735, pp. 395–405, American Institute of Physics. 2004.

[36] J. Buchner, "Nested Sampling Methods," *arXiv e-prints* (Jan., 2021) arXiv:2101.09675, `arXiv:2101.09675 [stat.CO]`.

[37] J. Buchner, "UltraNest - a robust, general purpose Bayesian inference engine," *The Journal of Open Source Software* **6** no. 60, (Apr., 2021) 3001, `arXiv:2101.09604 [stat.CO]`.

[38] A. Sokal, *Monte Carlo Methods in Statistical Mechanics: Foundations and New Algorithms*, pp. 131–192. Springer US, Boston, MA, 1997. `https://doi.org/10.1007/978-1-4899-0319-8_6`.

[39] J. M. Maldacena, "Wilson loops in large N field theories," *Phys. Rev. Lett.* **80** (1998) 4859–4862, `arXiv:hep-th/9803002`.

[40] E. Rinaldi, X. Han, M. Hassan, Y. Feng, F. Nori, M. McGuigan, and M. Hanada, "Matrix-Model Simulations Using Quantum Computing, Deep Learning, and Lattice Monte Carlo," *PRX Quantum* **3** no. 1, (2022) 010324, `arXiv:2108.02942 [quant-ph]`.

[41] E. Berkowitz, E. Rinaldi, M. Hanada, G. Ishiki, S. Shimasaki, and P. Vranas, "Precision lattice test of the gauge/gravity duality at large-N," *Phys. Rev. D* **94** no. 9, (2016) 094501, `arXiv:1606.04951 [hep-lat]`.

[42] S. Duane, A. D. Kennedy, B. J. Pendleton, and D. Roweth, "Hybrid Monte Carlo," *Phys. Lett. B* **195** (1987) 216–222.

[43] M. Hanada and S. Matsuura, *MCMC from scratch — a practical introduction to Markov Chain Monte Carlo method*. Springer, 2022.

[44] C. T. Asplund and D. Berenstein, "Small AdS black holes from SYM," *Phys. Lett. B* **673** (2009) 264–267, `arXiv:0809.0712 [hep-th]`.

[45] D. Gaiotto, A. Kapustin, Z. Komargodski, and N. Seiberg, "Theta, Time Reversal, and Temperature," *JHEP* **05** (2017) 091, `arXiv:1703.00501 [hep-th]`.

[46] **Particle Data Group** Collaboration, J. Beringer *et al.*, "Review of Particle Physics (RPP)," *Phys. Rev. D* **86** (2012) 010001.

[47] E. Poppitz, T. Schäfer, and M. Ünsal, "Universal mechanism of (semi-classical) deconfinement and theta-dependence for all simple groups," *JHEP* **03** (2013) 087, `arXiv:1212.1238 [hep-th]`.

[48] R. F. Dashen, "Some features of chiral symmetry breaking," *Phys. Rev. D* **3** (1971) 1879–1889.

[49] S. Chen, K. Fukushima, H. Nishimura, and Y. Tanizaki, "Deconfinement and $\mathcal{CP}$ breaking at $\theta = \pi$ in Yang-Mills theories and a novel phase for SU(2)," *Phys. Rev. D* **102** no. 3, (2020) 034020, `arXiv:2006.01487 [hep-th]`.

[50] E. Witten, "Constraints on Supersymmetry Breaking," *Nucl. Phys. B* **202** (1982) 253.

[51] E. Witten, "Supersymmetry and Morse theory," *J. Diff. Geom.* **17** no. 4, (1982) 661–692.

[52] E. Poppitz, T. Schäfer, and M. Ünsal, "Continuity, Deconfinement, and (Super) Yang-Mills Theory," *JHEP* **10** (2012) 115, `arXiv:1205.0290 [hep-th]`.

[53] N. M. Davies, T. J. Hollowood, V. V. Khoze, and M. P. Mattis, "Gluino condensate and magnetic monopoles in supersymmetric gluodynamics," *Nucl. Phys. B* **559** (1999) 123–142, `arXiv:hep-th/9905015`.

[54] N. M. Davies, T. J. Hollowood, and V. V. Khoze, "Monopoles, affine algebras and the gluino condensate," *J. Math. Phys.* **44** (2003) 3640–3656, `arXiv:hep-th/0006011`.

[55] M. M. Anber, E. Poppitz, and B. Teeple, "Deconfinement and continuity between thermal and (super) Yang-Mills theory for all gauge groups," *JHEP* **09** (2014) 040, `arXiv:1406.1199 [hep-th]`.

[56] E. Poppitz, "Notes on Confinement on $\mathbf{R}^3 \times \mathbf{S}^1$: From Yang-Mills, super-Yang-Mills, and QCD(adj) to QCD(F)," `arXiv:2111.10423 [hep-th]`.

[57] E. Poppitz and M. Unsal, "Index theorem for topological excitations on R**3 x S**1 and Chern-Simons theory," *JHEP* **03** (2009) 027, `arXiv:0812.2085 [hep-th]`.

[58] M. Unsal, “Magnetic bion condensation: A New mechanism of confinement and mass gap in four dimensions,” *Phys. Rev. D* **80** (2009) 065001, `arXiv:0709.3269 [hep-th]`.

[59] D. J. Gross, R. D. Pisarski, and L. G. Yaffe, “QCD and Instantons at Finite Temperature,” *Rev. Mod. Phys.* **53** (1981) 43.

[60] T. Banks and A. Casher, “Chiral Symmetry Breaking in Confining Theories,” *Nucl. Phys. B* **169** (1980) 103–125.

[61] R. G. Edwards, U. M. Heller, J. E. Kiskis, and R. Narayanan, “Chiral condensate in the deconfined phase of quenched gauge theories,” *Phys. Rev. D* **61** (2000) 074504, `arXiv:hep-lat/9910041`.

[62] T. A. DeGrand and A. Hasenfratz, “Low lying fermion modes, topology and light hadrons in quenched QCD,” *Phys. Rev. D* **64** (2001) 034512, `arXiv:hep-lat/0012021`.

[63] J. E. Kiskis and R. Narayanan, “Quenched divergences in the deconfined phase of SU(2) gauge theory,” *Phys. Rev. D* **64** (2001) 117502, `arXiv:hep-lat/0106018`.

[64] R. V. Gavai, S. Gupta, and R. Lacaze, “Quenched QCD at finite temperature with chiral fermions,” *Phys. Rev. D* **65** (2002) 094504, `arXiv:hep-lat/0107022`.

[65] S. Choi, J. Kim, S. Kim, and J. Nahmgoong, “Comments on deconfinement in AdS/CFT,” `arXiv:1811.08646 [hep-th]`.

[66] J. M. Maldacena, “The Large N limit of superconformal field theories and supergravity,” *Int. J. Theor. Phys.* **38** (1999) 1113–1133, `arXiv:hep-th/9711200 [hep-th]`. [Adv. Theor. Math. Phys.2,231(1998)].

[67] O. Aharony, S. S. Gubser, J. M. Maldacena, H. Ooguri, and Y. Oz, “Large N field theories, string theory and gravity,” *Phys. Rept.* **323** (2000) 183–386, `arXiv:hep-th/9905111`.

[68] M. Ammon and J. Erdmenger, *Gauge/gravity duality: Foundations and applications*. Cambridge University Press, Cambridge, 4, 2015.

[69] S. Gubser, I. R. Klebanov, and A. M. Polyakov, “Gauge theory correlators from noncritical string theory,” *Phys. Lett. B* **428** (1998) 105–114, `arXiv:hep-th/9802109`.

[70] E. Witten, “Anti-de Sitter space and holography,” *Adv. Theor. Math. Phys.* **2** (1998) 253–291, `arXiv:hep-th/9802150`.

[71] S.-J. Rey and J.-T. Yee, “Macroscopic strings as heavy quarks in large N gauge theory and anti-de Sitter supergravity,” *Eur. Phys. J. C* **22** (2001) 379–394, `arXiv:hep-th/9803001`.

[72] N. Drukker and B. Fiol, "All-genus calculation of Wilson loops using D-branes," *JHEP* **02** (2005) 010, `arXiv:hep-th/0501109`.

[73] S. A. Hartnoll and S. P. Kumar, "Multiply wound Polyakov loops at strong coupling," *Phys. Rev. D* **74** (2006) 026001, `arXiv:hep-th/0603190`.

[74] S. Yamaguchi, "Wilson loops of anti-symmetric representation and D5-branes," *JHEP* **05** (2006) 037, `arXiv:hep-th/0603208`.

[75] J. Gomis and F. Passerini, "Holographic Wilson Loops," *JHEP* **08** (2006) 074, `arXiv:hep-th/0604007`.

[76] J. Gomis and F. Passerini, "Wilson Loops as D3-Branes," *JHEP* **01** (2007) 097, `arXiv:hep-th/0612022`.

[77] J. Gonzalez, F. Guinea, and M. A. H. Vozmediano, "Continuum approximation to Fullerene molecules," *Phys. Rev. Lett.* **69** no. 1, (1992) 172.

[78] J. Gonzalez, F. Guinea, and M. A. H. Vozmediano, "The Electronic spectrum of fullerenes from the Dirac equation," *Nucl. Phys. B* **406** (1993) 771–794, `arXiv:cond-mat/9208004`.

[79] F. Guinea, J. Gonzalez, and M. A. H. Vozmediano, "Electronic interactions in fullerene spheres," *Phys. Rev. B* **47** (1993) 6576, `arXiv:cond-mat/9212022`.

[80] A. Jellal, "Anomalous quantum Hall effect on sphere," *Nucl. Phys. B* **804** (2008) 361–382, `arXiv:0709.4126 [hep-th]`.

[81] J. Schliemann, "Graphene in a strong magnetic field: Massless dirac particles versus skyrmions," *Physical Review B* **78** no. 19, (Nov, 2008) . `https://doi.org/10.1103%2Fphysrevb.78.195426`.

[82] K.-I. Imura, Y. Yoshimura, Y. Takane, and T. Fukui, "Spherical topological insulator," *Physical Review B* **86** no. 23, (Dec, 2012) . `https://doi.org/10.1103%2Fphysrevb.86.235119`.

[83] T. Neupert, S. Rachel, R. Thomale, and M. Greiter, "Interacting surface states of three-dimensional topological insulators," *Phys. Rev. Lett.* **115** no. 1, (2015) 017001, `arXiv:1412.2766 [cond-mat.str-el]`.

[84] M. Greiter and R. Thomale, "Landau level quantization of Dirac electrons on the sphere," *Annals Phys.* **394** (2018) 33, `arXiv:1807.05816 [cond-mat.str-el]`.

[85] A. H. C. Neto, F. Guinea, N. M. R. Peres, K. S. Novoselov, and A. K. Geim, "The electronic properties of graphene," *Reviews of Modern Physics* **81** no. 1, (Jan, 2009) 109–162. `https://doi.org/10.1103%2Frevmodphys.81.109`.

[86] C. Gattringer and K. Langfeld, "Approaches to the sign problem in lattice field theory," *Int. J. Mod. Phys. A* **31** no. 22, (2016) 1643007, `arXiv:1603.09517 [hep-lat]`.

[87] O. DeWolfe, D. Z. Freedman, and H. Ooguri, "Holography and defect conformal field theories," *Phys. Rev. D* **66** (2002) 025009, `arXiv:hep-th/0111135`.

[88] J. Erdmenger, Z. Guralnik, and I. Kirsch, "Four-dimensional superconformal theories with interacting boundaries or defects," *Phys. Rev. D* **66** (2002) 025020, `arXiv:hep-th/0203020`.

[89] J. L. Davis, P. Kraus, and A. Shah, "Gravity Dual of a Quantum Hall Plateau Transition," *JHEP* **11** (2008) 020, `arXiv:0809.1876 [hep-th]`.

[90] S.-J. Rey, "String theory on thin semiconductors: Holographic realization of Fermi points and surfaces," *Prog. Theor. Phys. Suppl.* **177** (2009) 128–142, `arXiv:0911.5295 [hep-th]`.

[91] A. Karch and E. Katz, "Adding flavor to AdS / CFT," *JHEP* **06** (2002) 043, `arXiv:hep-th/0205236`.

[92] M. Kruczenski, D. Mateos, R. C. Myers, and D. J. Winters, "Meson spectroscopy in AdS / CFT with flavor," *JHEP* **07** (2003) 049, `arXiv:hep-th/0304032`.

[93] H. Ooguri, "Wilson loops in large N theories," *Class. Quant. Grav.* **17** (2000) 1225–1233, `arXiv:hep-th/9909040`.

[94] R. C. Myers, "Dielectric branes," *JHEP* **12** (1999) 022, `arXiv:hep-th/9910053`.

[95] J. Gomis, S. Matsuura, T. Okuda, and D. Trancanelli, "Wilson loop correlators at strong coupling: From matrices to bubbling geometries," *JHEP* **08** (2008) 068, `arXiv:0807.3330 [hep-th]`.

[96] A. Karch and L. Randall, "Open and closed string interpretation of SUSY CFT's on branes with boundaries," *JHEP* **06** (2001) 063, `arXiv:hep-th/0105132`.

[97] Y. Chen, M. Heydeman, Y. Wang, and M. Zhang, "Probing Supersymmetric Black Holes with Surface Defects," `arXiv:2306.05463 [hep-th]`.